



Design and development of a new high nitrogen bearing steel, for offshore wind turbine with improved surface fatigue, wear and corrosion properties for in service life increment

(SteelWind)

The background of the slide features abstract, flowing blue and white lines and waves, suggesting motion and energy, which are fitting for a wind energy project.

EUR 30458 EN

Design and development of a new high nitrogen bearing steel, for offshore wind turbine with improved surface fatigue, wear and corrosion properties for in service life increment (Steelwind)

European Commission

Directorate-General for Research and Innovation

Directorate D – Clean Planet

Unit D.3 — Low Emission Future Industries

Contact Hervé Martin

E-mail RTD-PUBLICATIONS@ec.europa.eu

European Commission

B-1049 Brussels

Manuscript completed in 2019.

This document has been prepared for the European Commission however it reflects the views only of the authors, and the Commission cannot be held responsible for any use which may be made of the information contained therein.

More information on the European Union is available on the internet (<http://europa.eu>).

Luxembourg: Publications Office of the European Union, 2020

PDF ISBN 978-92-76-25390-7 ISSN 1831-9424 doi: 10.2777/1334 KI-NA-30-458-EN-N

© European Union, 2020.

Reuse is authorised provided the source is acknowledged. The reuse policy of European Commission documents is regulated by Decision 2011/833/EU (OJ L 330, 14.12.2011, p. 39).

For any use or reproduction of photos or other material that is not under the EU copyright, permission must be sought directly from the copyright holders.

All pictures, figures and graphs © Rina Consulting – Centro Sviluppo Materiali S.p.A. (CSM), RFCR-CT-2014-00018 Steelwind

Research Fund for Coal and Steel

Design and development of a new high nitrogen bearing steel, for offshore wind turbine with improved surface fatigue, wear and corrosion properties for in service life increment

(SteelWind)

Claudio GUARNASCHELLI (Project Coordinator)

F. ARCOBELLO VARLESE, C. COSTA, R. PILEGGI

Rina Consulting – Centro Sviluppo Materiali S.p.A. (CSM)

Via di Castel Romano 100 - 00128 Rome, ITALY

F. BATTISTELLA, N. BOZZATO, R.RIGON, L. SMIDERLE, D. STOCCHI

ECOR Research S.P.A. (ECOR)

Via Friuli 11 - 36015 Schio (Vicenza), ITALY

A.M. CABRAL, M.A. GOMES, M.A. ESTRELA

Instituto de Soldadura e Qualidade (ISQ)

Av. Do Professor Doutor Cavaco Silva Parque Das Tecnologias 33 2740 120 Porto Salvo, PORTUGAL

K. VINTER DAHL, T.L. CHRISTIANSEN

Technical University of Denmark (DTU)

Produktionstorvet 425 - 2800 Kgs. Lyngby, DENMARK

J.R. GONZALEZ GARCIA

Sidenor Investigacion y Desarrollo (SIDENOR)

Barrio Ugarte s/n - 48970 Basauri, SPAIN

T. BLASS, D. MERK

Schaeffler Technologies AG & Co. KG (SCH)

Industriestrasse 1-3 - 91074 Herzogenaurach, GERMANY

M. SCHYMURA, C. HELLWIG

Energietechnik Essen GmbH (ESSEN)

Westendstraße 15 - 45143 Essen, GERMANY

N. BELFIORE

DIMA

Rome, ITALY

Grant Agreement RFSR-CT-2014-00018

31/07/2014 -30/06/2018

Final Report

Table of contents

Final summary	5
Scientific and technical description of the results.....	15
Objectives of the project	15
Description of activities and discussion	16
1. WP1 - Failure analysis of steel bearings for wind turbines	16
1.1. Definition of steel bearing working conditions (Task 1.1).....	16
1.2. Failure analysis: modes and causes of the large dimension steel bearings (Task 1.2)	21
1.3. Functional characterization design (Task 1.3).....	33
2. WP2. High Nitrogen Austenitic Steel (HNAS): alloy and process design	42
2.1. Alloy and bulk heat treatment design (Task 2.1).....	42
2.2. Process design and HNAS lab manufacturing by production route 1 (casting by VIM) and production route 2 (casting by VIM followed by secondary remelting) (Task 2.2 - Task 2.3)	56
3. WP3. HNAS thermo-mechanical treatments	60
3.1. Hot workability tests and hot rolling/forging of test ingots (Task 3.1).....	60
3.2. Laboratory bulk heat treatments (Task 3.2)	67
3.3. Laboratory test rig construction (Task 3.3)	69
4. WP4. HNAS prototype characterization.....	70
4.1. Metallurgical characterization of prototype (Task 4.1).....	70
4.2. Design of deep rolling process of prototype HNAS (Task 4.2).....	80
4.3. Test rig set up and FE8 tests (Task 4.3)	89
5. WP5. Design and set up of functional laboratory tests	104
5.1. Preliminary considerations (Task 5.4. Selection of the steel grade).....	104
5.2. Design of the test plan (Task 5.1)	104
5.3. Mechanical characterization of prototype HNAS (Task 5.2)	108
5.4. Corrosion and tribological characterization (Task 5.3).....	117
6. WP6. Bearing prototyping and Full-Scale Tests, Life Cycle Assessment (LCA), cost analysis	128
6.1. Manufacturing of final HNAS electrodes/ingots (Task 6.1)	128
6.2. Production of full scale prototype HNAS (Task 6.2).....	135
6.3. Full scale tests, Lab analysis and Life Cycle Assessment (Task 6.4-6.6)	142
Conclusions	153
Exploitation and impact of the research results	153
List of figures	154
List of tables.....	160
List of acronyms and abbreviations	162
List of references	163
APPENDIX - D1.1 Report with dynamic and kinetic analyses	166

Final summary

Bearings are considered the most critical component in drivetrains of Wind Turbines (WT), due to maintenance costs and decrease of service lifetime. The problem is enhanced in offshore working conditions. The aim of the project is to increase the reliability of WT, improving tribological, fatigue, surface fatigue and corrosion properties of steel bearings by the development of a new steel functional grade.

The 100Cr6 steel is usually used for steel bearings production. The introduction of a new high nitrogen austenitic steel can improve the critical properties of the steel component and reduce its cost by the increment of the service lifetime. In fact nitrogen enhances fatigue strength, wear and fatigue resistance, resistance to crevice corrosion and to pitting corrosion of austenitic steels. Moreover, nitrogen addition helps to refine the microstructure, it increases the steel strength and it can be used instead of nickel as an austenite-forming

Objectives of the project

The objectives of the project are:

Development of a new nitrogen added austenite steel (HNAS) for the application in offshore wind turbine with improved surface fatigue, wear and corrosion properties.

Reduction of the total costs and improvement of the overall efficiency by advanced production techniques (including steelmaking, processing and heat treatment).

Development of a HNAS with improved hot/cold workability.

Optimization of a Deep Rolling Process for mechanical surface improvement and fatigue strength enhancement.

Development of a functional test rig for the simultaneous evaluation of steel surface fatigue and corrosion properties.

Identification of testing methodologies to simulate damage of steel bearings in service conditions.

WP1. Failure analysis of steel bearings for wind turbine

The activities of this WP included primarily the definition of the working conditions, in terms of loads and environment, as well as the identification of the main failure modes of the bearings adopted in the wind turbines, through an extensive failure analysis. Secondly, on the basis of the mentioned analyses, the design of a specific functional test rig has been performed.

Task 1.1. Definition of steel bearing working conditions

The IEC standard defines many situations for the analysis of design load cases: Power production under normal conditions, Power production with an operational fault, Start up, Normal shut down, Emergency stop, Parked (Rotor stopped or idling), Parked with operational fault, Transport, maintenance and repair.

For extreme loads IEC 61400-1 rules specify the gust duration should be 5 and 3 seconds respectively and the gust value is according to a certain return period in years.

Wind turbines operate in a unique environment that influence their duration. The environment inside the gearbox, during in-service condition, is very complex. There are quite a number of aspects that have to be taking into account as: atmosphere composition, temperature, lubrication conditions, residuals deposited on gearbox components due to thermal-humidity cycling, presence of particles as debris and foreign particles.

The climate conditions in which the WT facilities can be installed are different and severe as well. It is possible to define three different climate areas:

- Standard: Temperature for operation: -20 to +30°C; Temperature for structure: -20 to +50°C
- Tropical: Temperature for operation: -20 to +40°C; Temperature for structure: -20 to +50°C
- Artic: Temperature for operation: -30 to +30°C; Temperature for structure: -40 to +50°C

Maritime environments, especially offshore and coastal, present an additional challenge as NaCl salt accelerates the corrosion of metals and degradation of the lubricating oil. Corrosion results in pitting, leakage, weakening, and breaking of parts, and release of abrasive particles into the oil (such as iron oxide, better known as rust).

Lubrication has a very important role in the correct bearing operation and life expectancy, lubrication prevents corrosion, reduces the effects of sliding friction and cools heavily loaded bearings.

Task 1.2. Failure analysis: modes and causes of the large dimension steel bearings

The bearing failure analysis, herein described, namely characterization and analysis of failed bearings, is an important tool that can support and aid the development of new alloys for the application in offshore wind turbine bearings with improved surface characteristics. The analysis of the macro-failure on fracture and/or damaged surfaces of following mechanical parts supplied by Schaeffler have been done on the following parts:

- a new shaft washer (SW) from axial cylindrical roller bearing FAG 81212
- a no-failed shaft washer from a cylindrical roller bearing FAG 81212 tested for 461h in good oil
- SW from a failed cylindrical roller bearing FAG 81212 (axial)
- OR from *failed* cylindrical roller bearing NU222, namely two 'as tested' microcuts in axial and circumferential direction and two corresponding sections

All the parts are manufactured out of 100Cr6 martensitic steel according to ISO 683-17.

A failure analysis was performed on failed and no-failed FAG81212/NU222 bearings made in 100Cr6 martensitic steel and tested at Schaeffler labs by means of R4G and FE8 test rigs.

A new FAG 81212 bearing was the reference sample for the microstructural analysis and hardness of 100Cr6 steel.

First, failed samples were studied by SEM surface analysis to assess the damage due to wear and better evidence the worn areas in an attempt of giving a rough classification of the bearing damage tipology. Surface analysis evidenced typical damage due to pitting in the race of OR (outer ring of NU222), originated from subsurface and signs of edge run in the load zone. On the raceway cracks spalling and flaking of material were found, together with evidence of plastic deformation. This kind of damage could on principle be due to both fatigue or sub-surface initiated fatigue.

Analysis of cross sections was then performed on FAG81212 and NU222 microcuts. In both NU 222-14 and FAG 81212-14 tested bearings many cracks were evidenced. For NU222-14 few cracks were located close to the inner surface, while in FAG 81212-14 lots of cracks were found in the mid-thickness area. Inside the cracked zones of each sample WEA phases were always present.

The comparative SEM analysis showed that no substantial modification of 100Cr6 steel microstructure seems to take place during testing outside the zone of WEAs formation. In fact martensitic structure appears to be unmodified far from WEAs and close to these phases both in failed and in no-failed bearings. Sharp boundary separates the WEA structures from the unaffected steel matrix.

Etching with Nital 2% and 3% allowed to better highlight WEAs both by OM analysis where they appear white as visible light reflects off the relatively smooth surface and by SEM imaging. WEAs resisted etching so their supposed microstructure (or nano-structure) needs to be further investigated by means of others technique.

Microscopy investigation after etching evidenced typical subsurface cracks WEC, with WEAs (white etching areas), pitting and metallic inclusions (MnS) with cracks and (sometimes) points close to the inclusion.

Some authors assert that Butterflies (BFs) do not originates from metallic inclusions, namely MnS, but only from non-metallic ones like Al₂O₃ (or generally oxides) where MnS is encapsulated: under these circumstances the oxide acts as initiation site. MnS/Al₂O₃ inclusions weren't found, while a lot of sulphide of Mn were present in the analysed bearings.

SEM documentation with EDS microanalysis were performed on the steel matrix, on 'single' carbide particles and on the smooth surface of WEAs.

Comparative results on Cr and C content sometimes seemed to indicate the effect of the coalescence and 'dissolution' of carbides inside WEAs structures, but this need to be further confirmed.

Lots of WEAs were evidenced in all the analysed cross sections, while Butterflies (BFs) were no found (or doubtless recognized).

Neither DERs (dark etching regions) nor 30° and 80° oriented WEBs (white etching bands) were detected in all the analysed samples.

Hardness and micro-hardness measurements gave the 'as expected' results with WEAs hardness 30-50% higher than steel 100Cr6 matrix as suggested by others authors in literature.

Task 1.3. Functional characterization design

The activities of this task concern the design of a functional test rig for the laboratory testing of bearings machined from the new steels developed in the project.

The main innovative characteristics of the tribometer consists mainly in the possibility to carry out tests in which a set of three variables can be simultaneously involved:

- Load
- Induced currents
- Water injection in the oil circuit.

The design has led to the preliminary configuration of the test rig. The dimension of the components and their typology has been defined.

Some modifications to the designed model could be made in the future depending on the necessity:

- to modify some details
- to adapt some configurations at small scale
- to optimise some assembly parts of the test rig in the most suitable way to ensure proper working conditions.

The design has led to the final configuration of the test rig. The dimensions of the components and their typology have been defined.

WP2. High Nitrogen Austenitic Steel (HNAS): alloy and process design

Alloy and process design focused on new nitrogen added austenitic steel (HNAS), expected to guarantee elevated surface fatigue resistance, wear and corrosion properties respect to reference solutions for bearings (high-carbon, chromium-added 100Cr6).

In terms of process, two production routes have been considered: vacuum induction melting (VIM) and VIM followed by Pressure-Electro Slag Remelting (PESR).

Task 2.1. Alloy and bulk heat treatment design

The target mechanical properties were considered – in terms of hardness, up to 58 HRC in a surface layer and around 30 HRC in the bulk. The expected advantages for new HNAS with respect to reference solutions for are related to the properties typical of austenitic matrix, as for example: high nitrogen solubility, potentially resulting in resistance to localized corrosion, the work hardening, potentially enabling to achieve high mechanical resistance.

The identification of the suitable compositions was essentially based on the assessment of the following properties:

- Austenite stability, by means of thermodynamic calculations.
- Nitrogen solubility, through empirical models from the literature and thermodynamic calculations.
- Mechanical strength, by means of empirical models from the literature.

Further information were collected from a preliminary experimental activity based on the production of small ingots in order to select the HNAS composition to be taken into account for the following work.

The results show that a N amount of at least 0.80 % is needed to achieve the mechanical strength required for the bulk (UTS = 1000 MPa). So, a composition with N = 0.90 % has been considered as a base. To obtain such nitrogen level, the manufacturing route VIM + PESR (Manufacturing Route MR2) is needed:

	C	N	Cr	Mn	Mo	Si	V	Cu	Ni
MR2	0.05	0.90	18.0	11.0	2.0	0.60	0.10	0.20	0.20

Two compositions have also been selected, to be obtained by means of Manufacturing Route 1 (only VIM in nitrogen atmosphere):

	C	N	Cr	Mn	Mo	Si	V	Cu	Ni
MR1/1	0.40	0.60	18.0	19.0	1.0	0.30	0.10	0.20	0.20
MR1/2	0.05	0.60	18.0	18.0	2.0	0.30	0.10	0.20	0.20

The compositions MR1/1 is belonging to the so-called CARNIT alloys, based on the addition of carbon and nitrogen. According to the literature, UTS levels higher than 1000 MPa can be achieved with such composition.

The design of the heat treatments aimed at obtaining an austenitic microstructure, maintaining nitrogen in solid solution and avoiding nitride and carbide precipitation. In order to comply with such requirements, the following criteria should be respected:

1. Soaking temperatures must fall in the austenite stability range, avoiding formation of δ -phase.
2. Soaking temperatures must be out of the range of carbide and nitride precipitation (solubilization).
3. Cooling rate must be suitable to prevent precipitation of carbides and nitrides.

From considerations based mainly on thermodynamic calculations, a suitable set of solubilization temperature to be adopted in the heat treatment has been selected for the three alloys:

Alloy	Composition	Solubilization temperature (°C)
MR1/1	CARNIT	1110
MR1/2	Medium N (0.60 %)	1030
MR2	High N (0.90 %)	1110

The soaking time at the solubilization temperature depends on the size of the sample or the component to be treated. For a thickness of 5 mm, it has been approximately considered 30 minutes. The cooling rate has to be set in order to avoid precipitation of nitrides, and carbides in CARNIT alloy. Water quenching was selected as a proper cooling, at least for the treatment of the experimental samples.

Task 2.2 / 2.3. Process design and HNAS lab manufacturing

At the end of the alloy and process design, two ingots have been cast for each selected alloy/process route:

Composition of CARNIT alloy ingots (MR1/1). Mass %.

Range	C	N	Cr	Mn	Mo	Si	S	P	Cu	Ni
min	0.35	0.55	17.50	18.50	0.80	0.25	-	-	0.18	0.18
max	0.45	0.65	18.50	19.50	1.20	0.35	0.015	0.015	0.22	0.22
Ingot	C	N	Cr	Mn	Mo	Si	S	P	Cu	Ni
VM2947	0.38	0.59	17.85	18.70	0.88	0.25	0.007	<0.015	0.20	0.21
VM2950	0.40	0.60	17.75	18.71	0.96	0.30	0.006	<0.015	0.18	0.22

Composition of medium N alloy ingots (MR1/2). Mass %.

Range	C	N	Cr	Mn	Mo	Si	S	P	Cu	Ni
min	0.040	0.55	17.50	17.50	1.80	0.25	-	-	0.18	0.18
max	0.060	0.65	18.50	18.50	2.20	0.35	0.015	0.015	0.22	0.22
Ingot	C	N	Cr	Mn	Mo	Si	S	P	Cu	Ni
VM2948	0.060	0.59	17.50	17.60	1.90	0.27	0.006	<0.015	0.19	0.21
VM2951	0.050	0.58	17.85	18.13	1.90	0.29	0.006	<0.015	0.19	0.21

Composition of high N alloy ingots (MR2). Mass %.

Range	C	N	Cr	Mn	Mo	Si	S	P	Cu	Ni
min	0.040	0.85	17.50	10.50	1.80	-	-	-	0.18	0.18
max	0.060	0.95	18.50	11.50	2.20	0.65	0.015	0.015	0.22	0.22
Ingot	C	N	Cr	Mn	Mo	Si	S	P	Cu	Ni
PESR073	0.060	0.56	17.80	10.50	1.89	0.37	<0.015	<0.015	0.25	0.25
PESR074	0.050	0.83	18.00	10.90	1.93	0.33	<0.015	<0.015	0.22	0.20

WP3. HNAS thermo-mechanical treatments

This WP included the determination of the hot workability of the steels, in order to perform properly the hot forging of the ingots, and the following laboratory heat treatments.

Task 3.1. Hot workability tests and hot forging of test ingots

The hot workability of the High-Nitrogen Alloyed Steels produced in WP2 has been assessed from measurements of hot ductility (Reduction of Area %) by means of Gleeble testing. As a reference, a 100Cr6 steel commonly used for the bearing manufacturing ($C = 0.96\%$; $Cr = 1.44\%$) has been characterised, produced via Ingot Casting and hot rolled to a bar of 62 mm diameter.

In general, the steel grades that exhibit a reduction of area higher than 60% have a good hot workability with absence of cracks. Below this value, the steel can still be forged but with moderate reductions and strain rates in order to avoid cracks. Values of less than 20 % in RA are generally considered unacceptable for hot forming operations.

The alloys identified as Medium-N (0.60%) show a progressive decrease of Reduction of Area with the temperature from the maximum preheat temperature, but in general maintains a reduction of area higher than 40%. The CARNIT C+N alloy exhibits a remarkable drop in hot ductility at temperature lower than 1100°C, with Reduction of Area lower than 40%, and an embrittlement region (RoA lower than 20%) in the temperature range 850-950°C.

High-N steel (0.90%) exhibits values of reduction of area in the range of 40% to 20%, meaning a very poor hot workability. This alloy when forged is very prone to the appearance of cracks, so small reductions and few passes per heating are required.

On the basis of the results of the hot workability tests, the ingots cast in medium-N (0.60%) and Carnit-C+N alloys have been forged at ETE.

Task 3.2. Laboratory bulk heat treatment

Laboratory heat treatments have been carried out in order to optimize the industrial heat treatments to get the desired structures and properties. Mainly attention has been paid to avoid the precipitation of carbides and nitrides. The purpose of this work is to investigate the effect of annealing heat treatment on the microstructure characteristics of the HNS. CARNIT C+N and medium-N ($N=0.60\%$) steel grades were used in the study, considering the solubilization temperatures determined in WP2. The temperature ranges were 1050-1200 °C and 930-1200 °C for Carnit and medium-N alloys respectively.

Some analyses of the the microstructure have been performed just after heat treatment tests, while a deeper metallurgical characterization has been carried out and presented in WP4. In general, the Carnit C+N steel as received contains porosity, likely related to N_2 formation and/or a low forging reduction. The major part of the formed precipitates have a morphology normally related to "nitrogen pearlite", Cr_2N as indicated in the rest of the micrographs. Cr_2N normally forms during cooling, however as these samples have been water quench it's possible that they were formed during the heating process. The medium-N steel microstructure also contains porosity, likely related to N_2 formation and probably due to a low forging reduction. Moreover, the samples contain delta ferrite and sigma intermetallic phase, indicating that the microstructure achieved in these laboratory treatments was not completely austenitic.

Task 3.3. Laboratory test rig construction

Based on the configuration defined through the design activities reported in WP1, the functional test rig has been built.

WP4. HNAS prototype characterization

Task 4.1. Metallurgical characterization of prototype HNAS

The materials from the experimental heats in Carnit C+N steel and Medium-N ($N=0.60\%$) steel, heat treated according to what reported in WP3, have been characterized by means of optical microscopy (RLM), SEM-EDX and X-Ray diffraction (XRD)..

For the medium-N steel, the results showed the following:

- The as forged sample contained porosity, likely related to N_2 formation
- The as forged sample contained δ -ferrite that is enriched in Cr and Mo
- For samples heat treated at 930°C and 970°C, the δ -ferrite decomposed and intermetallic σ -phase also rich in Cr and Mo formed instead
- For the sample heat treated at 1010°C both σ -phase and δ -ferrite is found
- For samples heat treated at 1050°C and 1090°C δ -ferrite was found, XRD indicates that the amount of δ -ferrite after heat treatment at 1090°C is increased in comparison to the as forged condition
- XRD indicates that the material has a clear texture

In conclusion, there was none of the heat treatments that resulted in a fully austenitic structure, in the low temperature region intermetallic was formed and at higher temperatures, δ -ferrite was present.

The behavior may be coupled to a too low nitrogen level and therefore not sufficient stabilizing effect of nitrogen on FCC but there may also be a kinetic factor influencing especially the σ -phase formation. σ -phase formation may be accelerated and (meta)stabilized through the presence of δ -ferrite at the beginning of the heat treatment.

For the Carnit C+N steel, the following findings can be summarized:

- The as forged sample contained porosity, likely related to N₂ formation
- The as forged sample has likely experienced dynamic recrystallization during forging resulting in variance in grain-size
- XRD revealed only presence of austenite and indicates that the material also has a clear texture.
- LOM and SEM show precipitation that is taking place in and from the grain-boundaries of the fine grains. No precipitation was revealed from XRD, likely due to low volume fraction.
- The major part of the formed precipitates have a morphology normally related to "nitrogen pearlite", FCC+Cr₂N, which forms through a discontinuous precipitation reaction FCC(N) -> FCC+Cr₂N
- Precipitation decreased at higher temperature commensurate with the disappearance of the fine grained zones due to grain growth.

Task 4.2. Design of deep rolling process of prototype HNAS

The design of the deep rolling process has been performed in this WP. Deep rolling combines three main physical effects in cold work hardening of the surface. Through a hydraulically pumping system, a pressure is transferred to a rolling element, roller, which passes the pressure onto the component surface. The rolling element produces an elastic and plastic deformation of the surface layer, which is controlled by the rolling force and results in cold work hardening and residual compressive stresses. Furthermore, the treatment has a smoothing effect on the surface. This depends strongly on the previous surface quality of the component and the finishing quality of the rolling body. All of the three effects: the cold work hardening of the surface, the introducing of residual compressive stresses and the reduction of the roughness, are expected to have a positive effect on the fatigue strength of components.

The two High Nitrogen Steel grades: MR1/1, CARNIT C+N and MR1/2, medium-N N=0.60% were used in this tests. An ECOROLL deep rolling equipment and tools with integrated sensors and a software for process monitoring were employed.

The results were evaluated in terms of surface hardness and surface roughness. Further evaluations have also been made by means of hardness profiles on cross sections and residual stresses by XRD. A number of tests have also been carried out to evaluate the effect of a "tempering" at temperatures up to 600 °C to medium-N steel subjected to different deep rolling surface treatments.

- The best conditions found are a tool angle of 90° and a pressure of 600 bar.
- In such conditions, a surface hardness increase of 30-40 % is found.
- Some evaluations of hardness profile through the thickness and residual stresses measurement (XRD) are in substantial agreement. A reduction up to about 2/3 of the surface hardness is occurring in the first 250 μ m of depth.
- Tempering from 300 °C up to 500 °C on Deep Rolled samples have a very small influence on hardness on deep rolled samples.

Task 4.3. Test rig set up and FE8 tests

In this WP, the set up of the functional test rig (ECOR) was also performed, as well as of FE8 bearing test at Schaeffler.

The activities have been concentrated on the set up of the developed test rig for the laboratory characterisation and simulation of White Etching Cracks damage of the bearings will be machined from the new steels developed in the research proposal.

The main test rig characteristics have been defined taking in account the following boundary conditions:

- Failure modes
- Mechanical working conditions
- Environment
- Input data from SCHAEFFLER.

A specific bearing typology has been identified in collaboration with SCH. The bearing type is identified by the code NU207-E-MP1A. The material is the martensitic steel 100Cr6.

The bearings are subject to failure characterised by the so called "White Etched Cracks".

The following findings can be summarized:

- The investigation, performed at Schaeffler obtained, that no White Etching Cracks were generated in the bearings, tested at ECOR.
- All the rings, affected with damages after test showed surface initiated fatigue due to mixed friction conditions and/or contaminated environment. The amount of contamination significantly decreased from test to test. Nevertheless, there were some contaminations with hard particles, even in the latest two test runs.
- Via SEM analysis, the occurrence of electrical current flow (as the applied additional load, which should provoke the WEC-formation) could at least be proven on samples of the test No. 15.
- The prototype testing system is able to induce the development of butterfly defect, which is often found in WEC damage.
- Suitable test parameters for developing butterfly defects have been established.
- Once established suitable parameters, the butterfly density seems to depend on test duration.
- The concurrence between Alumina induced damage and butterflies' development has been unfortunately favourable to the first one. This condition has reduced the possibility of further test duration as required to obtain WECs.

WP5. Design and set up of functional laboratory tests

Preliminary considerations – (Task 5.3. Selection of the steel grade)

This WP originally included the characterization of the experimental materials in terms of mechanical properties, fatigue properties, corrosion and tribology, and the selection of the most promising steel grade.

At the end of the phases described in the previous sections, it was possible to identify the best temperature ranges for the heat treatments (solubilization) of the medium-N and Carnit C+N alloy. In particular, it was found that only Carnit alloy possessed a range of austenite stability, even though a further optimization is required in order to face the issues related to the presence of second phases (precipitates). Accordingly, a C+N austenitic steel (Carnit) alloyed with chromium and manganese (Carnit) has been selected as the alloy to produce some industrial material, complete the experimental activities (in particular, mechanical testing, corrosion and tribological testing) planned in WP5, and then manufacture the prototypes and perform full-scale / functional testing planned in the WP6.

The choice of Carnit steel has been based on the need to withstand both dynamic loads – achieving high levels of strength - and corrosion attack of water, especially sea water when used in offshore applications. The development of the Carnit composition was based on the investigation results of earlier projects (Riedner, 2010). Despite the results of the thermodynamic calculations, it was found that larger parts would not be able to manufacture without unwanted precipitations like N-perlite.

To improve the microstructure it has been necessary to further change the composition of the alloy, substantially in the balance of C and N, and in the content of added elements as Mo. The recent investigations suggest that the change of the composition not only improves the microstructure after solution annealing but also improves the fatigue strength and the resistance against surface breakdown (Schymura, 2014; Niederhofer, 2013), which are important properties for bearing steels. The grade selected has been the Carnit 90.

Bars in different diameters – according to the needs of experimental activities and prototype manufacturing – have been forged from an industrial heat of Carnit 90 steel (actual composition: C = 0.33 %, Mn = 18.6 %, Cr = 18.2 %, N = 0.44 %) and made available for the completion of experimental testing planned in WP5 and for the activities planned in WP6 (prototype manufacturing and full-scale tests). A campaign of laboratory heat treatments, followed by a basic characterization (evaluation of microstructure and steel cleanliness), has been preliminary performed on the bars:

- The material is characterized by a good quality in terms of absence of porosity.
- The steel cleanliness (non-metallic inclusions) is good according to the usual specifications given for bearing steel bars.
- A temperature of 1120 °C can be selected as the condition for the industrial heat treatment (solubilization annealing): at that temperature, a complete recrystallization and absence of undesired precipitates are found.
- The hardness level is 300-320 HV. According to a first estimation, the hardness target of 500 HV for bearing parts (which enables to perform scale test on FE8 with a Hertzian pressure of 2000 MPa) can be achieved by means of the operations included in the component manufacturing

process: cold deformation (to be adjusted even on the basis of some preliminary tests) and deep rolling.

Task 5.1. Design of the test plan

A specific test bench has been designed in order to get available a reliable test on a small laboratory scale. Such test bench should allow to involve a large set of damage variables, whose modulation allows us to prepare some experimental tests which accelerate sliding wear and pressure (related to the so-called "PV limit" of the tribo-system), while maintaining also a small component of rolling. The attempt consists, instead of simulating exactly the contact physical conditions in the real systems, that would take a very long experimental time, in trying to obtain simulated damage within a reasonable time. A Universal Micro Tribometer CETR UMT-3 has been modified in order to detect the damage on a sample with alternative sliding combined with a small grade of rolling. The combined dynamic actions of the alternate motion of the holder, which sustains the sample by means of an elastic media, the tangential traction due to friction and the normal load applied through a spherical pin, induce a torque with periodic oscillations of amplitude and, consequently, alternative rotations on the sample.

Offshore wind turbines are characterized by the presence of a large generator which induces a electromagnetic field which is crossed by the bearings. Some of them belong to an epicyclic gear-drive and therefore are mounted on floating shaft. For example, currents around the inner and outer rings, and also between two rollers. A circulation of alternating current is therefore necessary to simulate the physical state holding in a bearings employed in Off Shore Wind Turbines. A suitable electric circuit has been designed, where the passage of the current is guaranteed thanks to the pins connected to the loading system and the sample holder respectively.

A first set of tests have been carried out on a reference material, a high-C Cr-added steel (100Cr6 QT), with current flowing through the sliding contact. In this set of experiments the applied load has been set using the Hertz formulae to adjust the acceleration degree of the test due to pressure, taking into account the spherical pin radius of the test stand and the real roller principal radii. A load of 8 N was applied, with a 3 Hz alternating cycling, for a time of 2.5 h. A second set of tests have been performed on Carnit 90 steel. The main attention has been paid to the effect of the electric current. The wear tracks have been evaluated in terms of width and depth, by means of optical microscope and optical profilometer.

The effect of the current seems to affect mainly the width of the wear tracks, while the depth tends to remain quite constant. The lower wear track width observed on the reference material (almost negligible in absence of current, up to 600 µm with 10 A) with respect to Carnit 90 (210-320 µm without current, 640-650 µm with 4 A) may be attributed to the higher surface hardness of the former (650 HV). It should be noted that the samples taken from Carnit 90 had a surface hardness equal to that of the bulk (about 300 HV) as in the given condition it has not been possible to subject them to the operations designed to enhance surface hardness, as deep rolling. In the future tests with such equipment, it will be necessary to take into account this issue and find a way to obtain experimentally the required surface hardness of the samples

Task 5.2. Mechanical characterization

Tests performed:

- Hardness
- Impact toughness (RT, 0°C, -15°C, -25°C, -35°C)
- Tensile tests at RT, 200°C, 400°C.
- Fatigue tests (uniaxial)

Results in summary:

- Hardness around 300 HV (vs. 650-700 HV of 100Cr6 QT)
- UTS @ RT 900-1000 MPa (vs 1500 MPa of 100Cr6 QT – *NOTE: that sounds lower than expected*). In any case, 900-100 MPa are quite in line with the initial requirement.
- Impact toughness: more than 200 J (vs. 10 J of 100Cr6 QT).
- Fatigue: the new grade steel has an average value of 546 MPa was considered as the yield stress for all conditions and the stress levels for the fatigue tests set-up on this basis. The center of the D160 bar seems to have a behavior similar to the reference material without HT whereas the periphery exhibited a considerably higher fatigue resistance

Task 5.3. Corrosion and tribological characterization

A tribo-electrochemical test apparatus was realised at CSM laboratory modifying a pin-on-disc tribometer (RTM, Italy) by installing a 3 electrode electrochemical cell. To assess tribocorrosion behaviour of 100Cr6 (Q&T) martensitic steel in marine environment, corrosion/tribological first tests were carried out by means of a modified tribometer. The activity also aimed at testing the experimental setup. 100Cr6 steel

in Q&T state will be used as 'reference' in future activities involving tribocorrosion of new HNAS alloys (comparative analysis). A series of experiments in potentiodynamic and potentiostatic mode, namely electrochemical without sliding, 'tribo-electrochemical' with sliding and sliding wear, were carried out. For sliding tests under controlled load (contact load: 150 N) and speed conditions, an insulating holder carrying a Al_2O_3 ball slider was used.

The results of first experiments on 100Cr6 steel (in the described experimental conditions) seemed to evidence that sliding in saline electrolyte modifies the corrosion potential of the material by significantly lowering. This makes 100Cr6 more susceptible to corrosion phenomena, but does not change its corrosion rate significantly. These results were confirmed during the campaign on Carnit, when a couple of tests on 100Cr6 were repeated.

Investigations on Carnit steel compared to 100Cr6 evidenced a better behaviour in terms of corrosion and a reversed situation in sliding or corrosion-sliding, whenever the load is applied (tribometer). The wear-corrosion tracks for CARNIT resulted wider and deeper if compared to 100Cr6 a confirmation that Carnit is less wear resistant with respect to 100Cr6 in the adopted conditions. In all the typologies of test with sliding a track cross section area measurable and in some cases the material loss evaluable by weighing, unlike happens for 100Cr6.

WP6. Bearing prototyping and full scale tests, LCA and cost analysis

Task 6.1. Manufacturing of final HNAS electrodes/ingots

A cast ingot (\varnothing 630 mm) in Carnit 90 alloy previously selected in WP5 has been first hot rolled to a 230 mm x 230 mm square shaped, the final hot deformation was induced by means of forging, up to the final dimensions of the forged bars of \varnothing 60 mm, \varnothing 120 mm and \varnothing 160. The composition is the following:

C	Mn	Si	P	S	Cr	Ni	Mo	V	Cu	Al	N
0.33	18.6	0.87	0.016	0.001	18.0	0.08	0.03	0.025	0.04	0.006	0.44

The sum of C+N is actually 0.77 %, lower than that planned for Carnit 90 (C+N = 0.90 %).

As previously described (WP5, selection of material) a campaign of laboratory heat treatments, followed by a basic characterization (evaluation of microstructure and steel cleanliness), has been preliminary performed on the bars, allowing to determine the proper solubilizing temperature and check that an acceptable condition exists in terms of porosity and steel cleanliness.

Task 6.2. Production of full scale prototype HNAS bearing

The full-scale production includes the following steps: casting of the alloy and forging to final dimension, solution heat treatment, turning in a soft condition, surface hardening via cold deformation and hard machining to final geometry.

The full-scale production of bearings was performed on axial cylindrical roller bearings type FAG81212, whereas the washers were made of the Carnit material, cage made of polymer and rollers made from ceramic Si_3N_4 .

The soft annealing of the material was already performed at ETE. So, a set of 20 housing washers and 20 shaft washers were produced out of 120 mm raw material bars. As described in the Technical Annex, those bearings parts (washers) were cold deformed at Sidenor via deep rolling to achieve an appropriate hardness level, enabling the parts to withstand the loads applied in the assigned FE8 test.

The hardness values, measured in a depth of 0.1 mm are about 450 HV1, so extrapolating this value towards the surface a hardness of 500 HV1 can be expected. This means that in comparison with the core hardness (about 250 HV1) an increase of about 100 % was reached. But nevertheless, this value was somewhat lower, than desired.

The results of the geometrical measurement showed that the deviation in the geometry from the required dimension can be seen. There was a plastic deformation of the washers up to 0.23 mm measurable. Therefore, it was not meaningful to apply the last step of production (hard machining), since it was impossible to reach the geometry, required to fit in the full-scale test FE8 without removing the cold deformed surface area.

In alternative, another production route was created, aiming to apply the cold deformation in the FE8 test rig. The plastic deformation was then applied using the test rig FE8. This way to produce the test bearings should reach two goals: elimination of one production step and avoiding of macroscopic deformations, since the washers were clamped in the bearings seats during the deformation steps.

The hardness in 0.1 mm was measured to be about 420 HV1, so a hardness of 450 HV1 can be extrapolated with both the variants. A differentiation in between the two variants can be seen in the hardness at higher depth, e.g. 0.5 mm. Here is the influence of cold deformation more effective using the higher force (higher pressure) level

Task 6.4- 6.6. Full scale tests and related Lab analysis – LCA / cost analysis

The alloy Carnite 0.77 had an initial hardness of 330 HV10. Due to basic compression and tension tests, a max. hardness increase to 590 HV10 was expected.

The full scale production (following the route according to Technical Annex) with a cold deformation applied via deep rolling process was performed without success. This process resulted in a noticeable hardness increase to about 480 HV1 at the surface, but also in massive geometrical deformation of the whole bearing parts (washers).

An alternative production route was performed, accompanied by numerical simulation. During this production route, the cold deformation was deployed in the same FE8 device, in which the later full-scale tests were completed. This production lead to a max. hardness of about 450 HV1. This lower hardness required an adapted test procedure on FE8. So, the tests were performed at 1600 MPa only. Nevertheless, even this relatively low pressure resulted in early failures of the washers made of Carnit steel. The failure mode was surface initiated fatigue in each test. This leads to the assumption that the hardness level was not high enough, even for this low Hertzian pressures. The influence of other features of the alloy, e.g. the big grain size can also not be excluded.

The Life Cycle impact Assessment shows that the manufacturing of both types of bearings do not show significant differences in terms of environmental impact. The main difference between the two processes is the absence of the thermal treatment step in the bearings produced with the new steel. The new steel grade offers the promise of longer life cycle and thus the greater advantage of using such steel will be on extending the working time of the turbines where the bearings will be used. The potential environmental benefits will thus most probably be on the use stage of the bearings.

Conclusions

A High Nitrogen Austenitic Steel has been developed for the application in bearings in wind turbines. After the experimental phase, the C+N Carnit 90 steel has been selected, which has a sufficient hot workability to be forged without cracks and porosity, and after a suitable heat treatment possesses a completely austenitic microstructure, free from precipitates (as N-pearlite). The mechanical properties substantially comply with the requirements established for the bulk (300 HV, 900-1000 MPa), with an excellent level of toughness in comparison with the reference materials (i.e. high-C Cr-added as 100Cr6/AISI 52100)

The deep rolling process – aiming at increasing the surface hardness up to the level required for the application – has been optimized through a number of experimental trials and the prototypal bearings have been manufactured.

A number of prototypes (axial washer) have been manufactured from the bars of the developed Carnit steel, through two distinct process routes (surface hardness increase obtained by deep rolling or, in alternative, in-situ cold rolling) aimed at obtaining components suitable to be tested on the full-scale test rig FE8 (Schaeffler). The operations of surface strengthening – included an in-situ cold deformation applied on the test rig – were not able to achieve the required hardness levels, which resulted in early failures of the prototypes in the full-scale tests.

The failure mechanisms of the bearings have been deeply investigated and a specific functional test rig for the simultaneous evaluation of steel surface fatigue and corrosion properties has been developed, as well the testing methodologies to simulate damage of steel bearings in service conditions. The testing system is able to induce the development of typical butterfly defect, which are often found coupled to WEC damage

Scientific and technical description of the results

Bearings are considered the most critical component in drivetrains of Wind Turbines (WT), due to maintenance costs and decrease of service lifetime. The problem is enhanced in offshore working conditions. [1-4]

Conventional materials for bearings are either through hardened steels of the 100Cr6 (SAE52100) – family, hardened to a martensitic or bainitic microstructure, or carburizing steels like 17MnCr5 or 17CrNiMo6 in case hardened condition with a carbon concentration at the surface in the range between 0.6 to 1.1% Carbon. The Carbon generates a sufficient strength for normal over-rolling conditions, but the structures offer only a limited resistance against shock loading, sliding, particle over-rolling and reverse bending stresses. Other alternatives, Cronidur30®, are restricted by the poor formability and costs, due to a complex manufacturing cycle based on sophisticated forging and rolling techniques and a final heat treatment also comprising deep-freezing before tempering. [5-20]

HNAS steels offer better chances of application in gearbox for WT. Nitrogen as an alloying element has been known and used in technical applications since the 1940s, initially under the premise for nickel substitution in stainless grades. Alloys high in chromium (Cr) and manganese (Mn) but low in Ni and Mo are much more attractive to the present world market. N, Ni and Mo are alloying elements that play an important role in stainless steels. Nonetheless, N is inexpensive when compared with Ni and Mo, especially if it is added in its gaseous form into the steel. N is easily available, its price is not subject to large fluctuations and therefore do not suffer from market speculation. [21-25]

Objectives of the project

The objectives of the project are:

- development of new nitrogen added austenitic steel (HNAS) for the application in offshore wind turbine bearings with improved surface fatigue, wear and corrosion properties
- reduction of the total costs and improvement of the overall efficiency by advanced production techniques (including steel making, processing and heat treatment)
- development of a HNAS with improved hot/cold workability
- optimization of a Deep Rolling Process for mechanical surface improvement and fatigue strength enhancement
- development of a functional test rig for the simultaneous evaluation of steel surface fatigue and corrosion properties
- identification of testing methodologies to simulate damage of steel bearings in service conditions

Description of activities and discussion

1. WP1 - Failure analysis of steel bearings for wind turbines

1.1. *Definition of steel bearing working conditions (Task 1.1)*

Bearing loads

Due to constant wind changes bearing loads and rotor speeds have a wide range of values. The rotor shaft can idle (in case of wind speeds below minimum wind speed required for power generation – cut in speed) resulting in low-speed, low-load operation, oppositely wind speeds above cut-in speed will imply average speeds and loads, this is the nominal operating regime. One other case is large loads on the rotor shaft bearings exerted by the blades and rotor due to wind gusts. Wind turbine bearing requirements are proper operating at high speeds and high operating temperatures, efficient lubrication and cooling, large ΔT_{IR-OR} , ability to operate correctly under vibrations and idling under light wind. Wind turbine loads can be divided into two groups:

- Static loads: – These loads are due to the weight of the turbine or during its steady rotation e.g. gravitational.
- Dynamic loads – These loads can be transients (e.g. start/stop manoeuvres, accelerations), stochastic (e.g. turbulence) and cyclic /periodic (e.g. wind shear, tower shadow, blade mass).

The IEC takes all these loads into account and defines eight situations for the analysis of design load cases [26]:

- Power production under normal conditions
- Power production with an operational fault
- Start up
- Normal shut down
- Emergency stop
- Parked (Rotor stopped or idling)
- Parked with operational fault
- Transport, maintenance and repair.

For extreme loads IEC 61400-1 rules specify the gust duration should be 5 and 3 seconds respectively and the gust value is according to a certain return period in years. Figure 1.1 shows the wind speed for design loads according to IEC 61400-1, this wind speed extreme load is for extreme rising and falling gust with 50 year return period for steady wind of 25 m/s and category A turbulence.

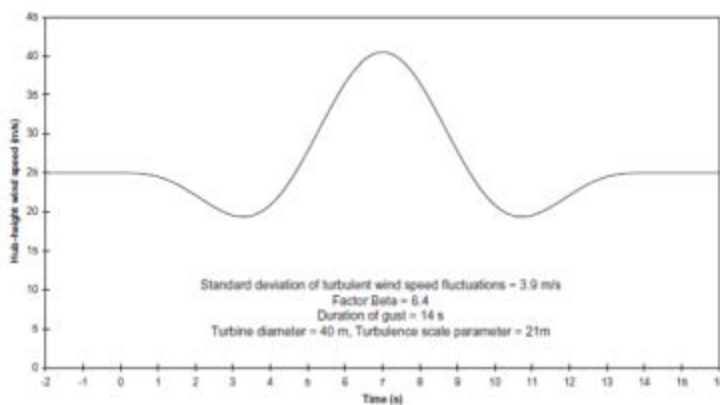


Figure 1.1. Gust Wind speed according to IEC 61400-1 [27].

Loads and moments exerted on the rotor shaft bearing are presented in Figure 1.2 (left side) and Figure 1.3, these variable forces can be observed in the two plots in the right side of Figure 1.2, providing an easier understanding of the effort changes over time. These graphs are from a wind turbine at speeds of 24m/s which causes load fluctuation and thence rotor shaft bearings repeat start, stop, accelerate, decelerate operations irregularly.

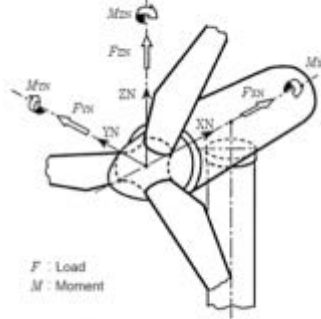


Fig. 2 Rotor load schematic

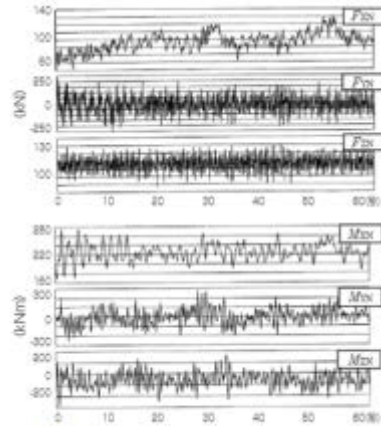


Fig. 3 Measurements of rotor load and moment

Figure 1.2. Rotor load schematic (left); Measurements of rotor load and moment (right)[28]

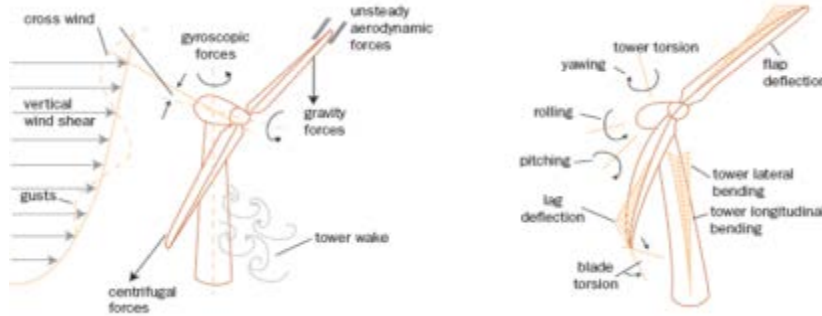


Figure 1.3. Loads on a turbine (DFVLR).

In order to ensure that the bearing will fulfil the above requirements and operate as desired, certain critical measurements must be known. The knowledge of motion, forces, moments on shaft & mounts, radial load distribution along each bearing, bearing inner ring to outer ring relative motions, bearing slip or skidding and temperature of bearing inner and outer rings will provide necessary inputs to design or choose the correct bearing. Figure 1.4 shows the slow speed shaft torsion during normal-shut down breaking, in the figure can be seen the several shut down stages such as the aero tips deployment, generator offline and the registered torsion range that is very broad.

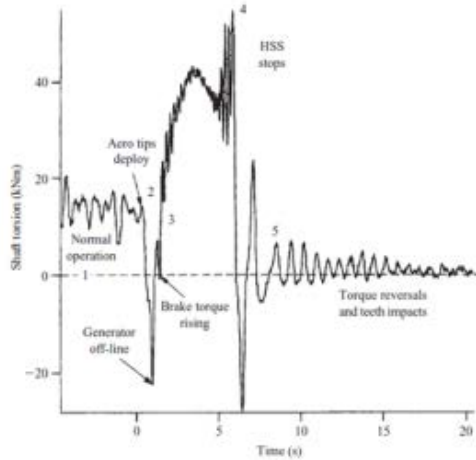


Figure 1.4. Low-speed shaft torque during normal shut-down [27].

Some of the parameters and forces that affect bearings life, according to Timken are:

RPM

The bearing speed will affect the development of the film thickness (lambda ratio, the ratio of the film thickness to the surface finish) and ultimately affect the predicted bearing life.

Radial Load, F_z

The radial load is relatively constant as a result of the weights of the rotor hub, blades, and generator.

Axial Load, F_x

In many cases the axial load is relatively constant for most condition in the duty cycle. A small number of coarse bins can be used.

Radial Load, F_y

The yaw loads are small compared to the pitch loads and are not as critical to the bearing fatigue life depletion.

Pitch Moment, M_y

The pitch moments contribute significantly bearing life reduction. Wind speed vertical distributions create these high moments and adjust the loading on the bearing rows in the XZ-plane that are a result of the rotor mass.

Yaw Moment, M_z

The yaw moments are perpendicular to the pitch moments and may be either clockwise or counter clockwise with respect to the tower axis. Consideration of the yaw moments can be simplified into absolute values without having a large effect on the bearing fatigue life calculation. [29]

The next case study was a 3MW electrical power, 90m rotor diameter, three point support, two planetary gear stages and one helical gear stage (Figure 1.5).

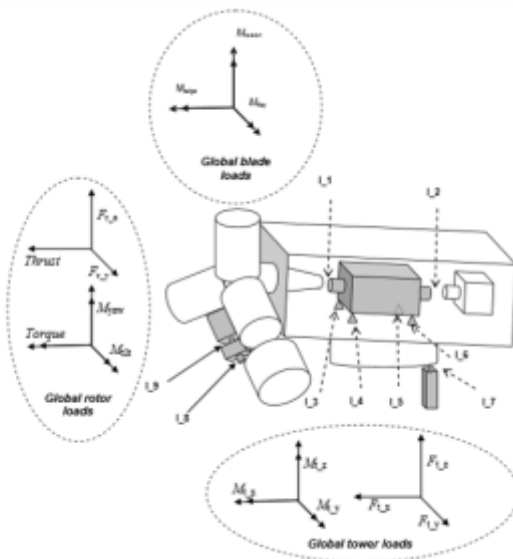


Figure 1.5. Global and local turbine loads [30].

Analysis of the environment inside the gearbox and bearings

Wind turbines operate in a unique environment that influence their duration. The environment inside the gearbox, during in-service condition, is very complex. There are quite a number of aspects that have to be taking into account as: atmosphere composition, temperature, lubrication conditions, residuals deposited on gearbox components due to thermal-humidity cycling, presence of particles as debris and foreign particles.

The climate conditions in which the WT facilities can be installed are different and severe as well. It is possible to define three different climate areas:

- Standard: Temperature for operation: -20 to +30°C; Temperature for structure: -20 to +50°C
- Tropical: Temperature for operation: -20 to +40°C; Temperature for structure: -20 to +50°C
- Artic: Temperature for operation: -30 to +30°C; Temperature for structure: -40 to +50°C.

Wind turbines can also operate extremes such as 100% humidity and ambient temperatures from -40°C to 85°C, provided that precautions are taken when assessing and choosing the correct equipment and lubrication oil. [31].

Maritime environments, especially offshore and coastal, present an additional challenge as NaCl salt accelerates the corrosion of metals and degradation of the lubricating oil. Corrosion results in pitting, leakage, weakening, and breaking of parts, and release of abrasive particles into the oil (such as iron oxide, better known as rust).

With moderate temperatures, food, and free water the microbial growth becomes an issue, especially in tropical conditions where the conditions to grow and multiply microbes are more easily met.

Microorganisms such as bacteria and moulds thrive if free water is present and temperatures ranging 15–52°C as they can metabolize gear oil. The metabolism of the oil leads to the accumulation of acids which in its turn promote corrosion, and formation of biological slimes that reduces flow and clogs moving parts.

Bearing lubrication

Lubrication has a very important role in the correct bearing operation and life expectancy, lubrication prevents corrosion, reduces the effects of sliding friction and cools heavily loaded bearings.

Gear oil recirculates through wind turbine gearboxes and bearings, lubricating mating surfaces and removing heat. Unfortunately, contaminant particles suspended in the gear oil, as well as water can significantly degrade the performance and reliability of the components. Especially when winds are light, sometimes the turbine is simultaneously operating under a medium-sized load at low speeds and with low load at high speed. This may lead to an insufficient thickness of the lubricating film that's necessary for long bearing life. With high loads, due to wind gusts and inner turbine vibrations, intermediate bearing bodies, such as balls and rollers, vibrate against the outer and inner rings causing the grease to squeeze out of highly loaded contact areas, then the lubricant is not able to re-enter. In this lubricant-free and unprotected area tiny corrosion pits appear as elliptical or rectangular footprints at the roller or roller spacing, leading to bearing failure.

Lubrication methods such as drip, splash or mist (pressure-fed oil only) and by the use of lubricators (oil or grease) are used in the main shaft bearings. Besides the means of lubrication there is one other important issue which is the effective lubrication. For an effective lubrication it is necessary a consistent oil film thickness, however this film cannot be achieved in slow or intermittently/oscillating grease. It is of the upmost importance to have clean grease that provides a good lubrication boundary, a seal system is in fact essential for a satisfactory lubrication. Raceway fretting-corrosion is commonly caused by an uneven and discontinuous oil film. Common considerations for the grease selection process include:

- higher viscosity (ISOVG 460 or 320) is better for maintaining good film strength
- synthetic base oil with high viscosity index (VI) will provide better lubrication over a larger temperature range
- excellent water, rust, oxidation and corrosion resistance is important for extended grease life
- low-temperature operation with adequate pumping may be required in some applications

The analysis of oil samples from wind turbine gearboxes supplied from Schaeffler was done to detect the presence of foreign particles (Figure 1.6). In detail: nr 6 oil samples from "Castrol BBX A320" and nr 5 oil samples from "Supplier B".



Figure 1.6. Oil samples from wind turbines gearboxes in the as received condition.
Left: Castrol BBX A320 – Right: Supplier B.

In order to check the presence of particles in the oil samples, the following procedure was applied:

- 1) the oil sample was dissolved with n-heptane, and was poured onto a filter paper (8.0µm);
- 2) after filtration, the filter paper was washed with n-heptane to remove any oil traces;
- 3) drying the filter in the oven at 100°C;
- 4) after drying, the filter paper was placed in a desiccator at environment temperature;
- 5) analysis with a stereomicroscope to check the presence of possible particles retained on the filter paper;
- 6) the particles were analysed by Scanning Electron Microscope (SEM) / Energy Dispersive X-Ray Spectroscopy (EDS) after preparation by sputter coating with gold to prevent electronic charging (example Figure 1.7).

Table 1.1 presents the chemical composition for the oil sample, from the customer Castrol BBX A320. This composition will be assumed as typical for this type of oil. The oil composition from Supplier B was not available. Some illustrative pictures from the particles analysed were obtained using SEM and are presented in Figure 1.7.

Table 1.1 – Oil chemical composition, provided from the customer Castrol BBX A320.

Compton	CH4	S	Cl	Ca	P	Zn	Na	Mg	Al
144,0 KCps 1,03	- 98,9%	12,0 KCps 0,509%	0,1 KCps 77 PPM	0,2 KCps 13 PPM	5,4 KCps 0,144%	105,9 KCps 0,150%	0,1 KCps 188 PPM	1,8 KCps 0,153%	0,0 KCps 1 PPM
	Si	K	Fe	Mo	Cd	Sn	Sb	Pb	-
	0,0 KCps 10 PPM	0,0 KCps 1 PPM	0,2 KCps 2 PPM	142,3 KCps 999 PPM	0,0 KCps 1 PPM	0,0 KCps 2 PPM	0,0 KCps 3 PPM	0,3 KCps 1 PPM	-

Observations: The analysis of CASTROL BBX A320 oil samples after filtration has shown the presence of metallic particles in samples 17-cracks, 27-cracks and 54-cracks. The other elements detected are most probably from the oil, since they are present in the oil composition. The filtered oil analysis from supplier B revealed the following features:

- a) B1- HSS rolling damage: particles of most probably a fragment of stainless steel and a particle containing aluminum.
- b) B3 - HSS bearing replacement: particle containing titanium.
- c) B4 - HSS Lagerwechsel: particle containing aluminum and silicon.
- d) B5 - HSS rolling damage: particle containing titanium and other elements that may be from the oil, since its composition is unknown. Another particle of aluminum and silicon such as the one detected in the filtered oil from B4.

In all the cases, the origin of the other detected elements especially the ones present far from isolated particles, may be the oil itself. No relationships were found between oil composition and part failure. In fact, it is visible that the functional additives from the oil are filtered out by an 8 µm mesh grid. The relation to the white etching crack failures are not proven yet, even though residues and sludge formation in the drive train and may cause a dysfunction of the oil that could be important in the white etching crack formation.

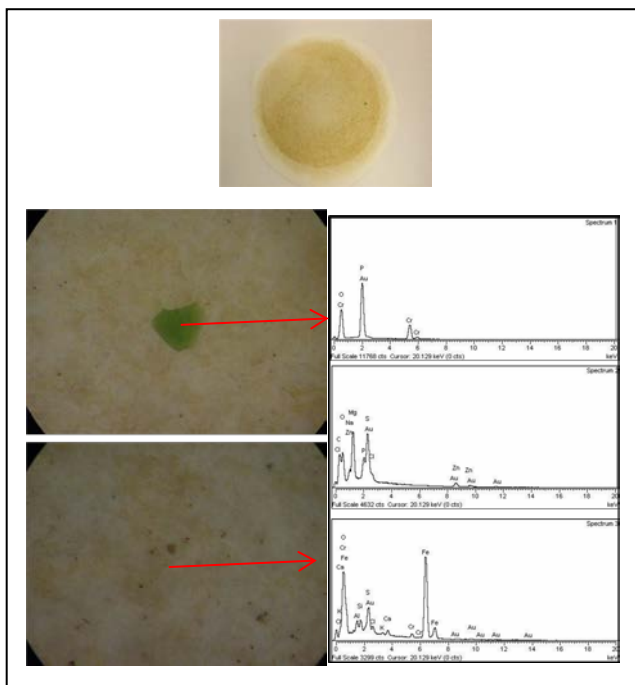


Figure 1.7. EDS spectrum of the particle side identified with the stereoscopic microscope and of the matrix in general.

1.2. Failure analysis: modes and causes of the large dimension steel bearings (Task 1.2)

The bearing failure analysis is an important tool that can support the development of new alloys for the application in offshore wind turbine bearings with improved surface characteristics. The analyses of the macro-failure on fracture and/or damaged surfaces of the following parts supplied by Schaeffler have been done on cut from FAG 81212-Reference and NU222-Reference bearings, both used in Schaeffler's test rigs (NU222 in R4G test rig and FAG 81212 in FE8 test rig). In detail:

- a new shaft washer (SW) from axial cylindrical roller bearing FAG 81212
- a no-failed shaft washer from a cylindrical roller bearing FAG 81212 tested for 461h in good oil
- SW from a failed cylindrical roller bearing FAG 81212 (axial)
- OR from *failed* cylindrical roller bearing NU222, namely two 'as tested' microcuts in axial and circumferential direction and two corresponding sections.

All the parts are manufactured in 100Cr6 martensitic steel according to ISO 683-17. FAG 81212 is a test bearing for FE8_25 test rig and NU222 is a test bearing for R4G test rig, aimed at reproducing WEC (Figure 1.8). Images of as received samples and prepared sections are shown in Figure 1.9.



Figure 1.8. Drawings of FAG81212 and NU222 type bearings, and shaft (SW).



Figure 1.9. Top left: New SW from axial cylindrical roller bearing FAG 81212. Top right: SW from cylindrical roller bearing FAG 81212 *no-failed* tested for 461h. Bottom left: SW from *failed* cylindrical roller bearing FAG 81212. Bottom right: OR from *failed* cylindrical roller bearing NU222.

Samples were investigated by SEM surface analysis to assess the damage issues due to contact between rolling parts and better evidence the worn areas [32]. Longitudinal and transverse cross sections from bearings raceway (OR) and shaft washer (SW) were also examined to reveal possible microstructural changes in martensitic 100Cr6 steel. A summary of the samples is given in Table 1.2.

Table 1.2. Schaeffler's analysed samples

Bearing	Test Type	Sample ID	SEM/EDS Analised area
NU222_14	R4G	NU222_14 A	SURFACE
		NU222_14 B	SURFACE
		NU222_14 section	SECTION
FAG 81212-14	FE8_25	FAG 81212_14 A	SURFACE
		FAG 81212_14 section	SECTION

Failed OR-NU222 raceway

Figure 1.10 shows NU222_14A and NU222_14 B samples extracted from failed OR of cylindrical roller bearing tested on R4G for a running time of 1022.4 hrs, with maximum axial load 90 kN and speed 3000 min⁻¹. Coloured circles point up the surface areas investigated by SEM.

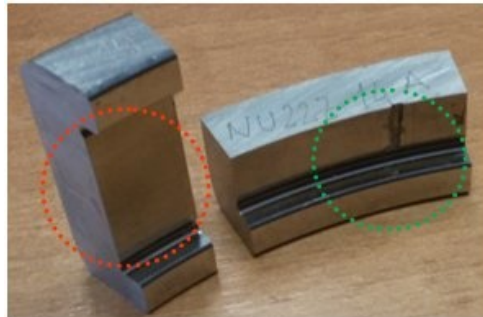


Figure 1.10. Samples labelled NU222_14 A (right) and NU222_14 B (left).

SEM images representing the damaged area are shown in Figure 1.11. The zones named 1 and 2 are shown at a higher magnification in Figure 1.12 where damaged parts in the race of OR from NU222_14A bearing are characterized by cracks and sharp spalling of material. Sample NU222_14 B was investigated close to both race edges were surface scars were evidenced. SEM analysis highlighted flaking and spalling of material (Figure 1.13).

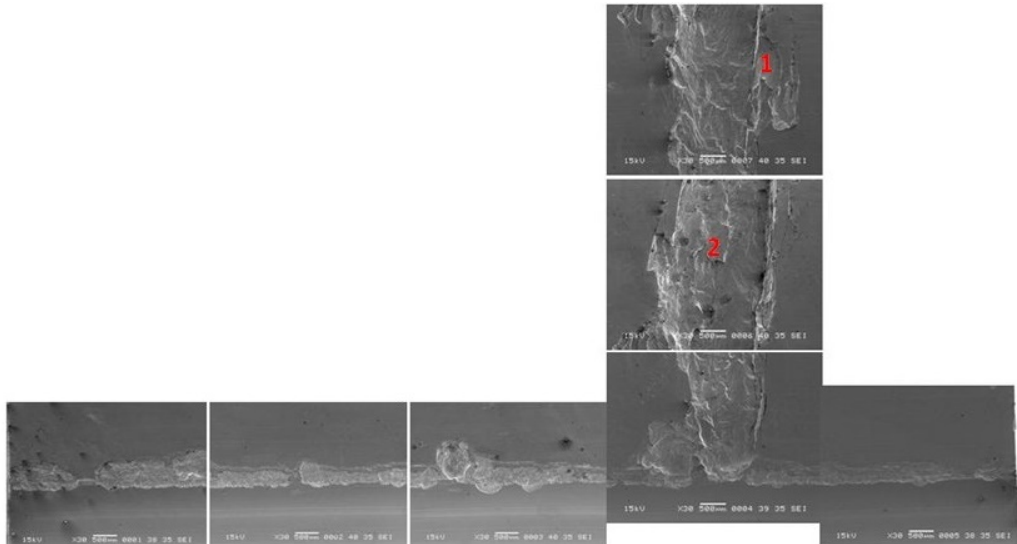


Figure 1.11. NU222_14A: SEM 'collage' of images of the damaged zone of a part of the OR pointed up in the green circle in Figure 1.10.

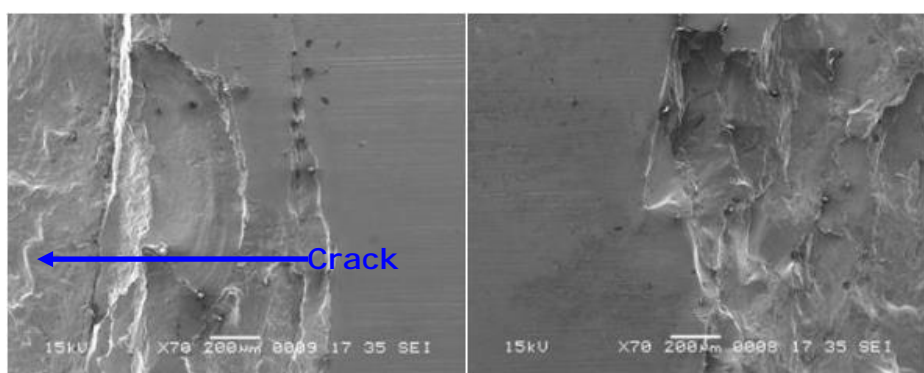


Figure 1.12. NU222_14A: SEM images of the enlarged areas of zones depicted in the previous images: left image corresponds to zone labelled 1 and right image to zone labelled 2.

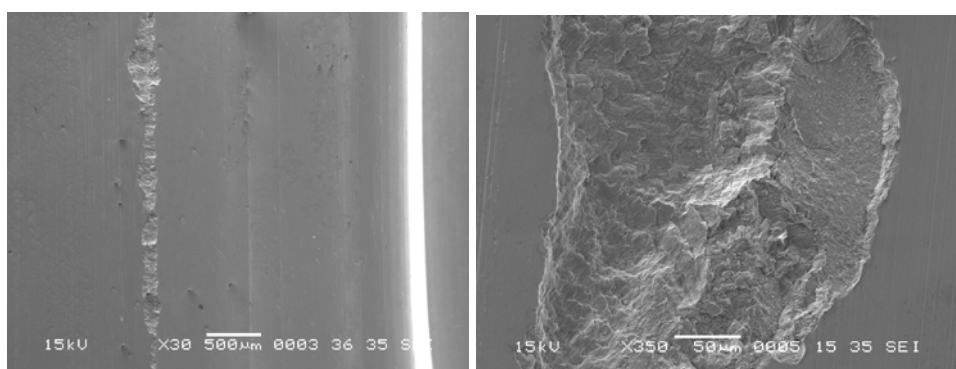


Figure 1.13. Sample NU222_14B. Left side: SEM image of edge areas evidenced by red circle in Figure 1.10 (90° rotated). On the right enlarged image of damaged zones.

Cross Section Analysis (before metallographic etching)

Samples NU222_14A

The appearance of a WEC (white etching crack) in NU222_14A sample observed by SEM is reported in Figure 1.14. MnS inclusions in 100Cr6 steel appears like dark elongated strips (red arrow). Without any etching white phases surrounding cracks, if present, are not easily detectable by SEM imaging. The presence of MnS inclusions was confirmed by means of EDS microanalysis. In NU222-14B axial section were found several WECs and cavities as shown in Figure 1.15.

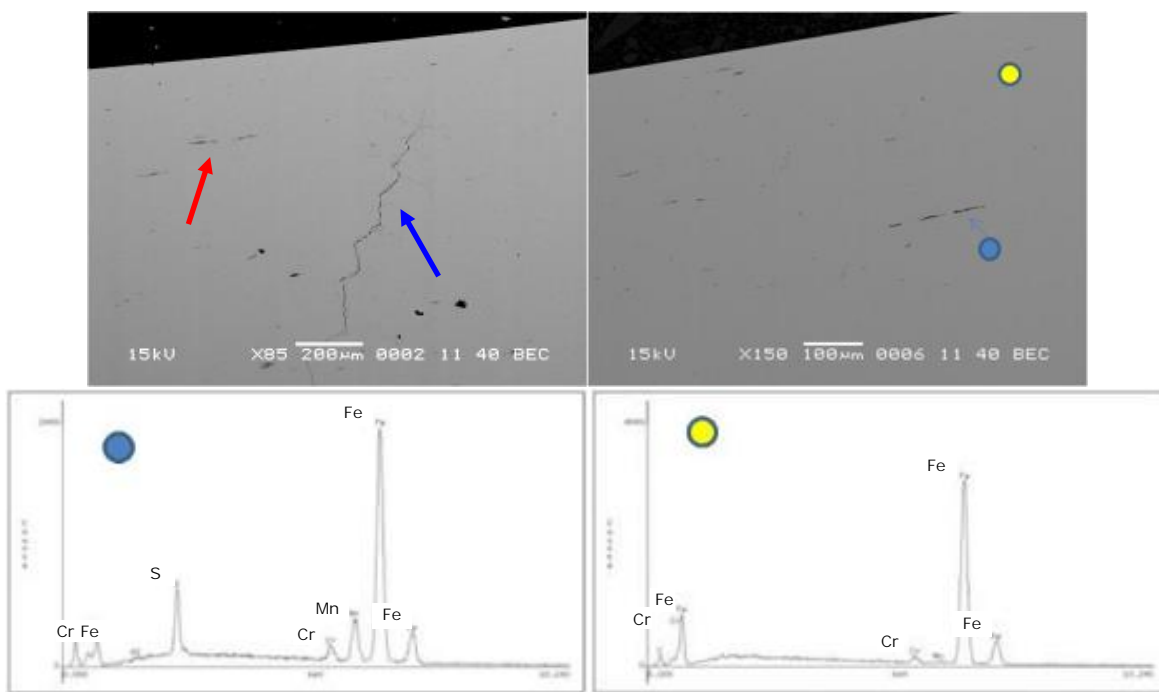


Figure 1.14. NU222_14A. SEM images with MnS (red arrow) and WECs (blue arrow). EDS spectra: Mn sulphide and steel matrix area with no visible inclusions.

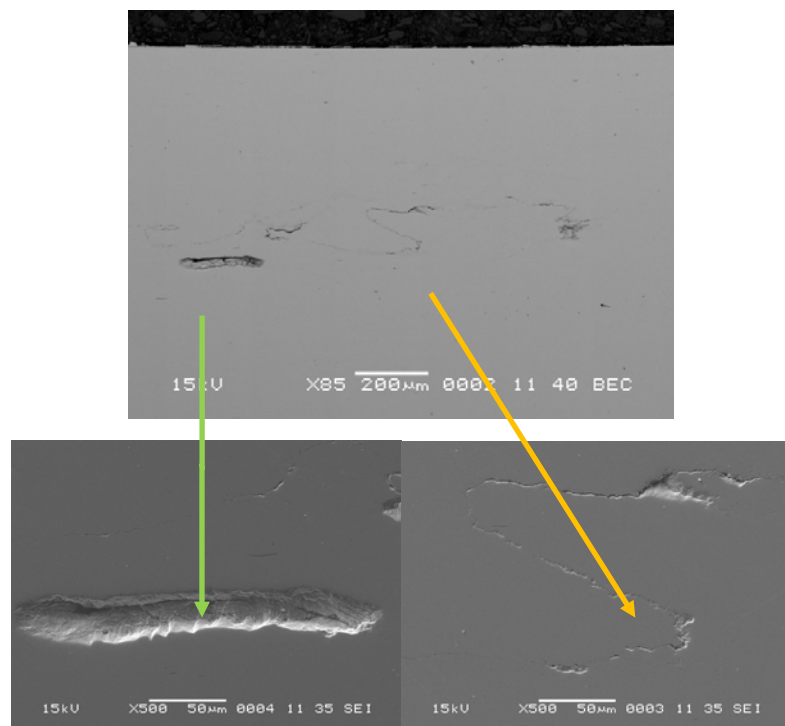


Figure 1.15. NU222_14 B: SEM BSE image and details at higher magnification (SE mode) of WECs.

Samples FAG 81212 14 A

In Figure 1.16 SEM images of a WEC and the area close to the crack appears to be affected by pitting. In the third image, a higher magnification of the second, the morphological flat surface lying between the area with pitting and the unaffected matrix (with well evident carbides) is possibly due to WEA (white etching area). The inclusion composition, MnS, was confirmed by EDS microanalysis as in the case of another zone (Figure 1.17) where the MnS is crossed by a crack close to its tip. The SEM backscattered mode helps to identify both the inclusion (that appear darker with respect to the matrix, due to the so called chemical composition contrast of back scattered electrons) and the WEA surrounding the other crack that runs in parallel with the previous.

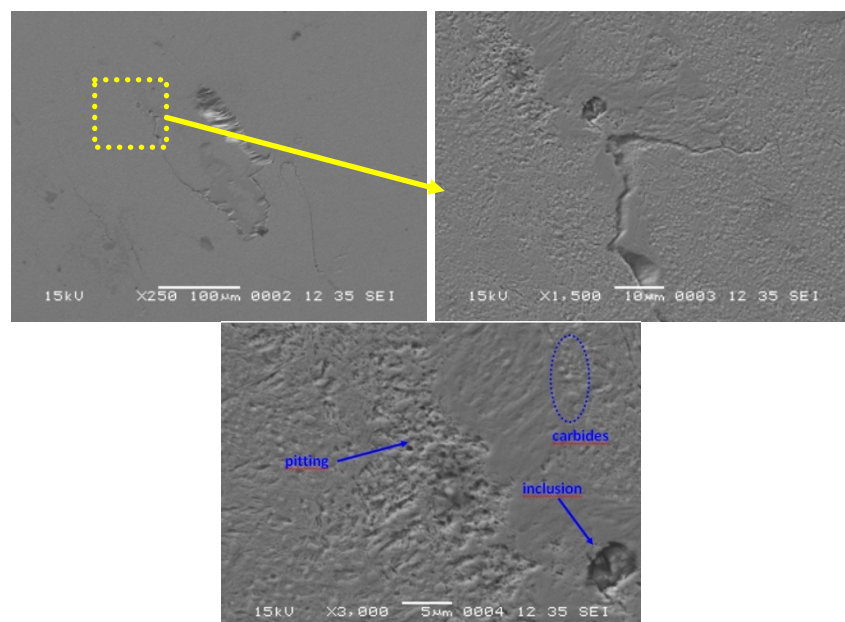


Figure 1.16. SEM (SE) images of WECs area with presence of pitting in FAG81218_14 A section sample (Circumferential - no etched sample). The third image is a detail of the second one.

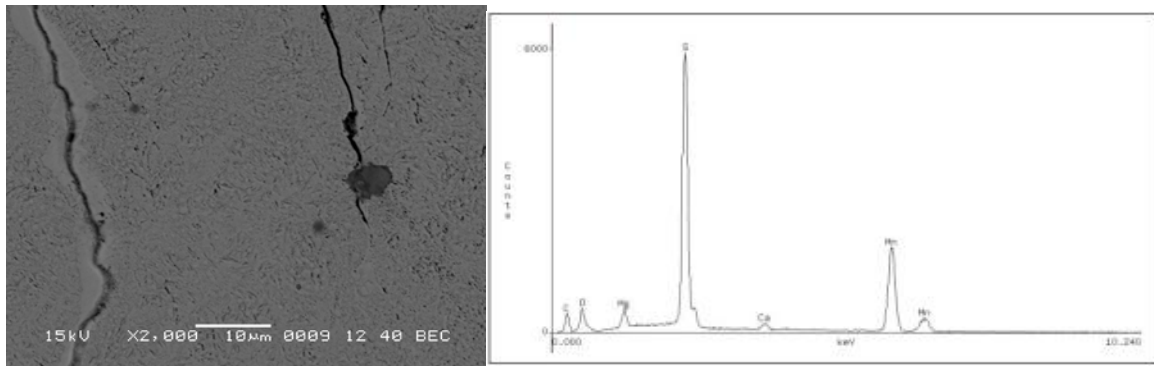


Figure 1.17. MnS inclusion (confirmed by EDS microanalysis) close to crack tip

Cross Section Analysis by Optical Microscopy after metallographic etching

The microstructure of 100Cr6 steel (Figure 1.18, transverse cross section) is characterized by a fine martensitic microstructure. Average hardness values (Table 1.3) are those expected for QT 100Cr6 steel.

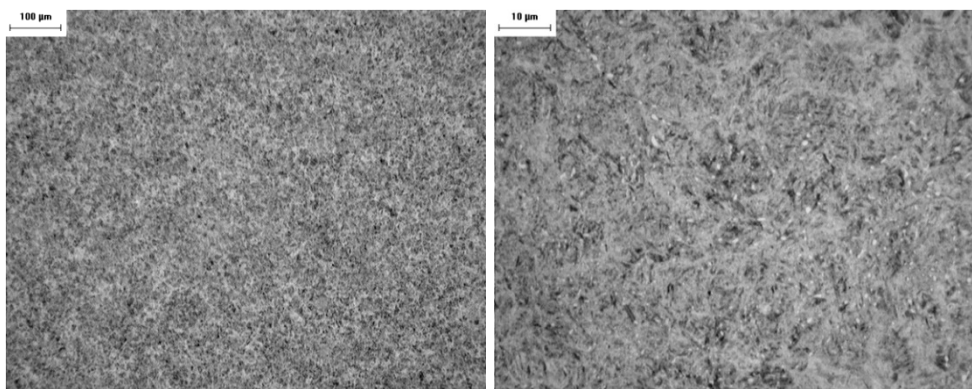


Figure 1.18. New FAG 81212-12 (Transversal section): OM images after 3% Nital etching.

Table 1.3. FAG 81212-12 new bearing hardness measurements results

Indentation	$HV_{10\text{ kg}}$	$HV_{2\text{ kg}}$
Average	718	721

Assessment of the presence of WEA phases

The presence of WEA (White Etching Area) was confirmed by OM (Optical Microscope) investigation carried out on FAG 81212_14 A sez, NU222_14 A sez and NU222_14 B from failed bearings, (Figure 1.19 and Figure 1.20). In NU222_14 A few cracks were detected close to the inner surface, while in FAG 81212_14 A lots of cracks were detected in the mid-thickness area. In the cracked zones of each sample WEA phases were always present. No evidence of 'butterflies' (BF) was found. Neither Dark Etching Zone (DEZ) nor oriented WEBs (White Etching Bands) were found. WEA appear 'white' compared with the surrounding matrix (the relatively smooth surface resists etching).

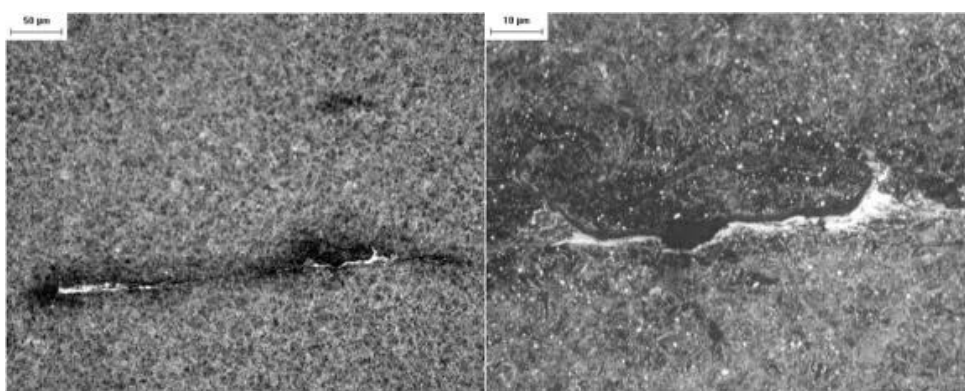


Figure 1.19. OM images for NU222_14 B after 3% Nital etching.

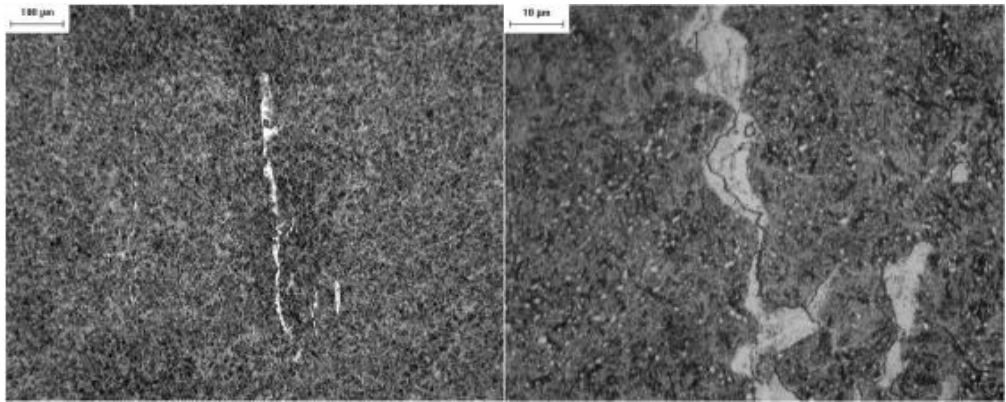


Figure 1.20. FAG 81212_14 A:OM images of WECs after 3% Nital etching.

After testing for 461 hours in FE8 test rig, FAG 81212-12 461 hrs showed no microstructural evidence of failure, since neither WEAs nor WECs were detected (Figure 1.21).

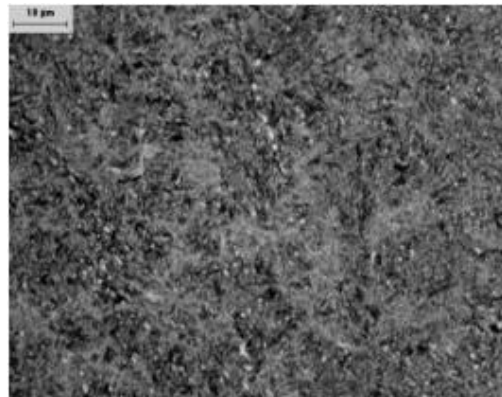


Figure 1.21. FAG 81212-12 no failed-461 hrs: OM images after 3% Nital etching.

Hardness and microhardness measurements are reported in Table 1.4. Indentations 4, 5 and 7 refer to steel matrix while the other points to the WEA structure and the surrounding adjacent matrix. A boundary zone can be attributed to indentation 6. Figure 1.22 reports the image of indentations in WEA and in steel matrix close and far from WEA. The results show that WEAs structures are harder than matrix. According to literature an increase of 30-50% is consistent with results of others authors [32, 33].

Table 1.4. FAG 81212-14 microhardness and hardness measurements results.

Indentation	HV _{10g}	HV _{50g}	HV _{2kg}
1	990		
2	960		
3	1300		
4	620		
5	640		
6		800	
7			700

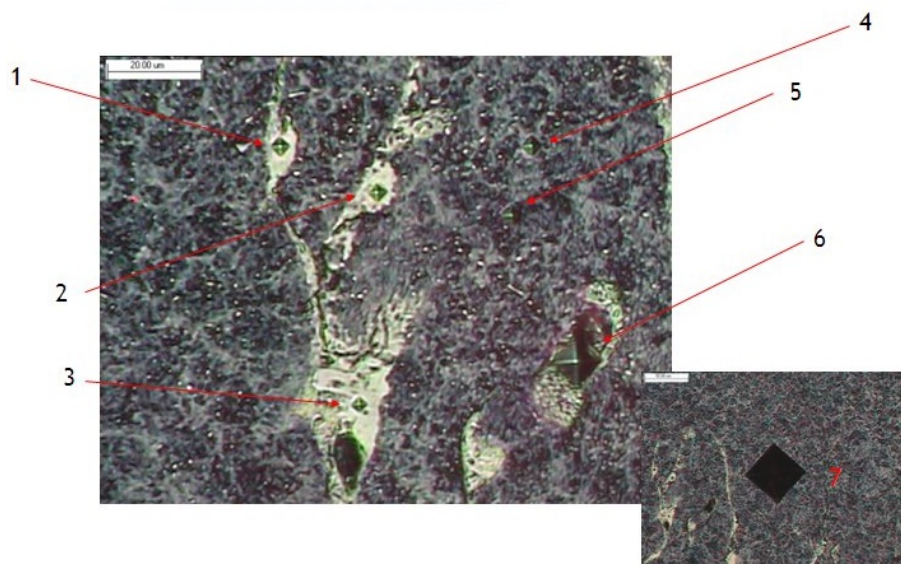


Figure 1.22. FAG 81212-14: indentations for micro-hardness and hardness measurements.

SEM Cross Section Analysis after metallographic etching

The reference microstructure after Nital etching is shown in Figure 1.23 (SEM).

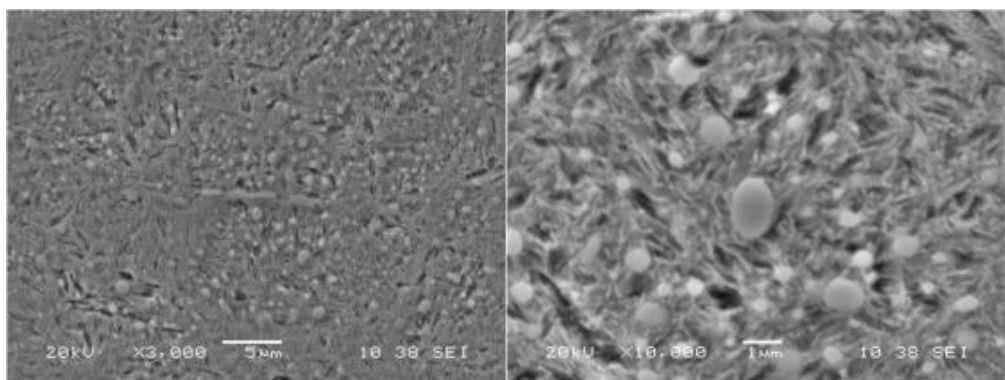


Figure 1.23. New FAG 81212-12: SEM images of 100Cr6 steel microstructure after Nital 2% etching.

Figure 1.24 shows the flat and very smooth surface of a WEA close to the crack after 3% Nital. The EDS microanalysis confirmed the qualitative composition of chromium carbides and MnS inclusions, partially evidencing a chemical modification occurring in very smooth WEA phases, where carbides 'disappear' and Cr content seems to be the same found in the steel matrix, i.e. ~1.5 % (EDS in Figure 1.25 and Figure 1.26). Chromium carbides seem to change in shape when are in the WEA phase (red circle in Figure 1.27) compared with those in the matrix. Cracks originating from MnS inclusions or passing through a MnS inclusions and close to WEA were found.

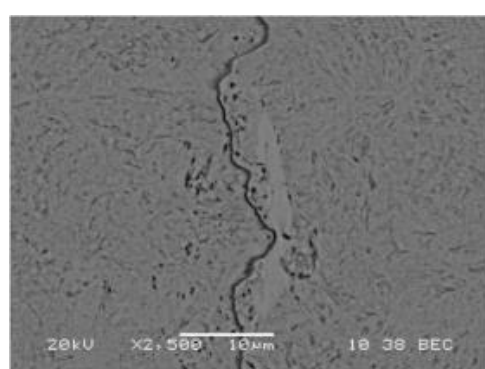


Figure 1.24. FAG 81212-14: SEM image showing a crack and a WEA.

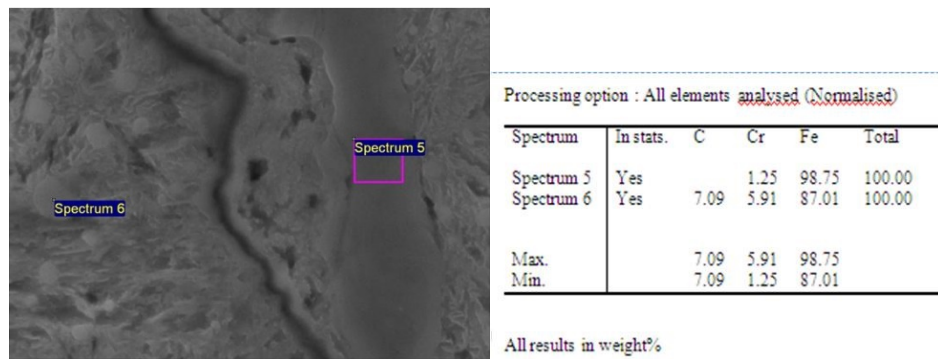


Figure 1.25. FAG 81212-14: EDS analysis on selected areas; spectrum 5 refers to a WEA; spectrum 6 to a chromium carbide.

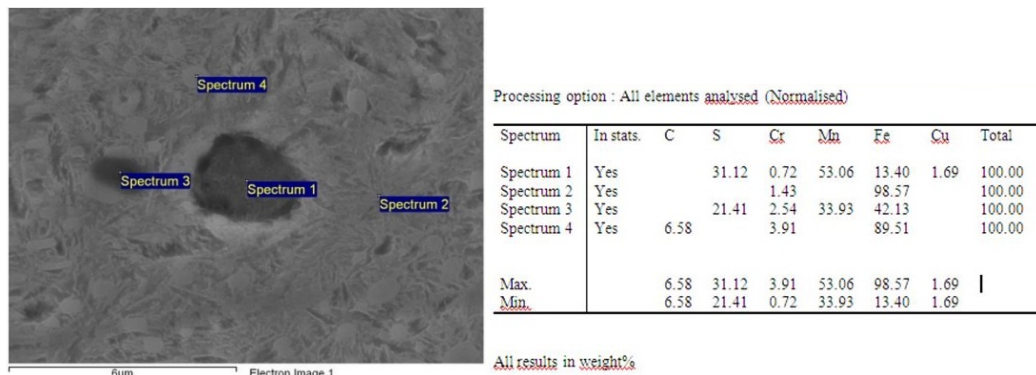


Figure 1.26. EDS analysis on selected areas: spectra 1 and 3 refer to MnS while spectrum 4 to a chromium carbide particle. Spectrum 2 to the steel matrix.

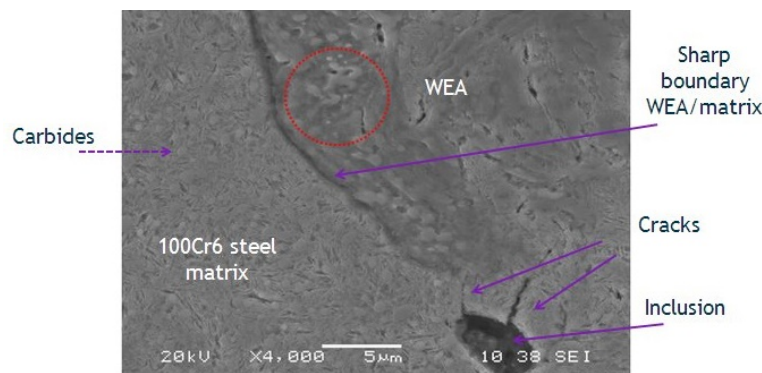


Figure 1.27. FAG 81212-14: SEM image (SE) of WEA/steel matrix sharp boundary. Inclusion, cracks and chromium carbides in steel matrix and in WEA (red circle) are highlighted.

The results of SEM analysis of NU222-14 A are comparable to those for FAG 81212-14. In Figure 1.28 an inclusion with cracks, WEA/cracks and pitting is shown. Figure 1.29 reports SEM image of subsurface branched cracks moving from the subsurface of the circumferential section of the OR from sample NU222-14 A. Depth of penetration is evidenced.

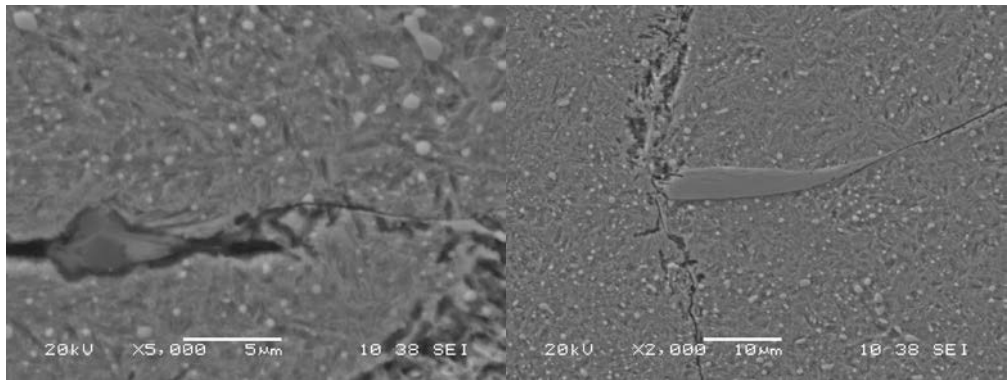


Figure 1.28. NU222-14 A sez sample after etching. SEM images. Inclusion with a crack (left); a WEA with crossing cracks and signs of pitting (right).

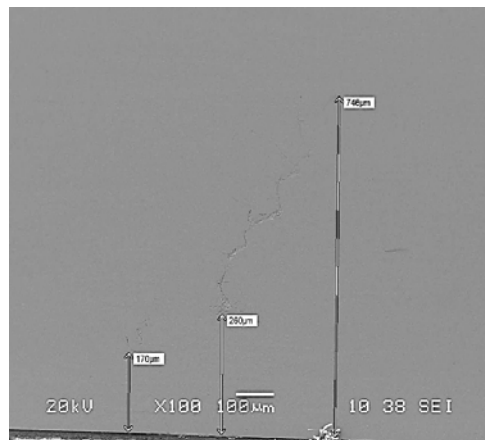


Figure 1.29. Subsurface branched cracks with distance from surface of NU222-14 A sez sample.

Further investigations of the NU222_14A bearing

Further studies of WEC in NU222_14A R4G test bearing were performed at DTU by a dual-beam FIB-SEM FEI Helios Nanolab 600 equipped with an EDAX-TSL EBSD system, in SE and BSE modes. In BSE, orientation contrast was used to reveal grain orientation differences and features inside WEC. Several large crack-systems bordered by WEA were found below the bearing raceway in the samples. Two crack systems are visible in Figure 1.30. The main cracks have a staircase-like progression with many cracks branching out from the main cracks, and the same approximate inclination indicating an influence of the stress situation during overrolling. Similar crack morphologies have been observed by Luyckx [34].

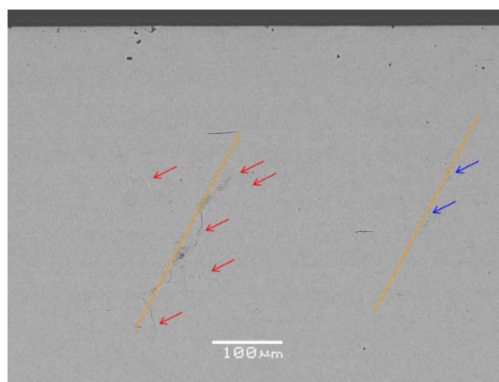


Figure 1.30. SEM-BSE image of WEC below the raceway surface.

A staircase crack is visible in Figure 1.31. Different types of locations with different morphologies of the WEA can be identified along the crack, especially at the steps where the crack changes direction. A significant amount of crack rubbing can take place during overrolling. The exact geometry of the crack can influence the morphology and also the growth/evolution of the WEA. The appearance of the WEA

depends on its positions (marked with red and green in the figure). The microstructural features appear coarser and inhomogeneous at the stair-bottom positions, marked in red, and much more homogeneous consisting of a very fine-grained white appearing microstructure at the stair-top position, marked in green, possibly related to the difference in rubbing of crack-faces at the different locations.

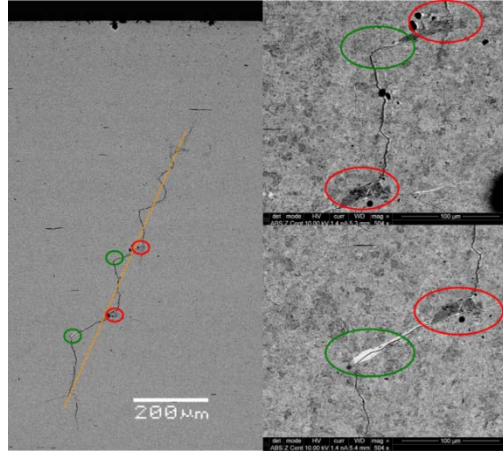


Figure 1.31. SEM-BSE images of staircase crack and local positions with different WEA morphologies.

Figure 1.32 shows one of the homogeneous WEAs shown in the lower right image in Figure 1.31 (marked in green). Where the main crack changes direction (left part of the image), there is a “chaotic” appearing inhomogeneous microstructure with multiple smaller cracks, whereas along the “crack step” a much more homogeneous (white) structure is visible. Within the homogeneous structure the line-like features that were observed in previous work [34] are clearly visible as well as defects and smaller microstructures lying aligned along these lines. In the previous work [34] these line features were taken as an indication of a cyclic crack-rubbing mechanism for the continued growth of the white etching areas. During the cyclic crack rubbing the hard WEA that has already formed is being pressed into the surrounding (softer) martensitic matrix, thus likely introducing further local deformation and evolution of the microstructure alterations.

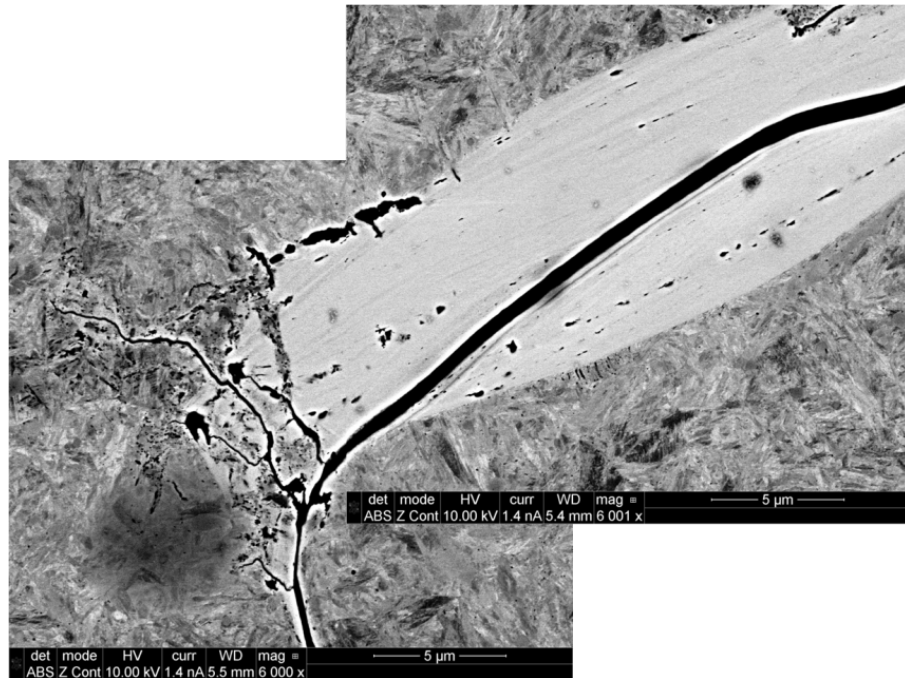


Figure 1.32. SEM-BSE image of line like features aligned with the main crack within a fine-grained homogeneous appearing WEA.

In Figure 1.33 the inhomogeneous WEA, marked red in the lower right hand image of Figure 1.31, is shown at a larger magnification. The WEA is full of defects, some parts have fallen out during preparation (black), likely due to the brittle nature of the area. The grain size in the area is on a nano-scale (up to

approximately $0.2 \mu\text{m}$). The microstructure is different from the original martensitic structure, with fine grains that have likely formed due to a refinement of the original microstructure because of continued plastic deformation. It is unclear whether recrystallization due to input of frictional heat takes place. Evidence of recrystallization within WEA was recently published [35] but it may depend on exact test/service conditions. In general, areas near to cracks are microstructurally active and that the original martensitic structure in their vicinity is being altered. In Figure 1.34 a local area with crack structures but without progressed WEA is shown. The local microstructure changed around the cracks. Possible indications of slip structures appearing during plastic deformation (dark parallel lines); the microstructure changes stop at a prior austenite grain boundary and do not penetrate into the adjacent grain indicating that the changes occur on a very local scale and possibly that the orientation of the grain matters (active slip-systems).

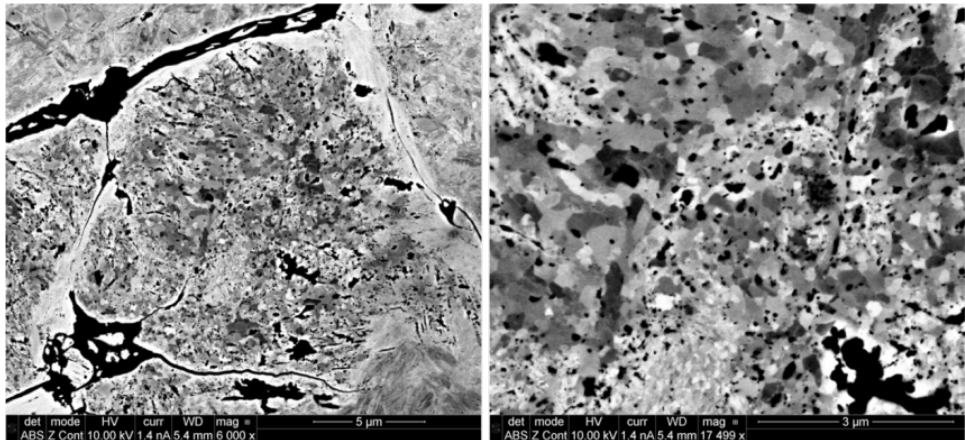


Figure 1.33. SEM-BSE image of inhomogeneous WEA with local coarser-grained homogeneous areas along the small cracks and a varied grain size in the central area with grain sizes up to approximately $0.2 \mu\text{m}$).

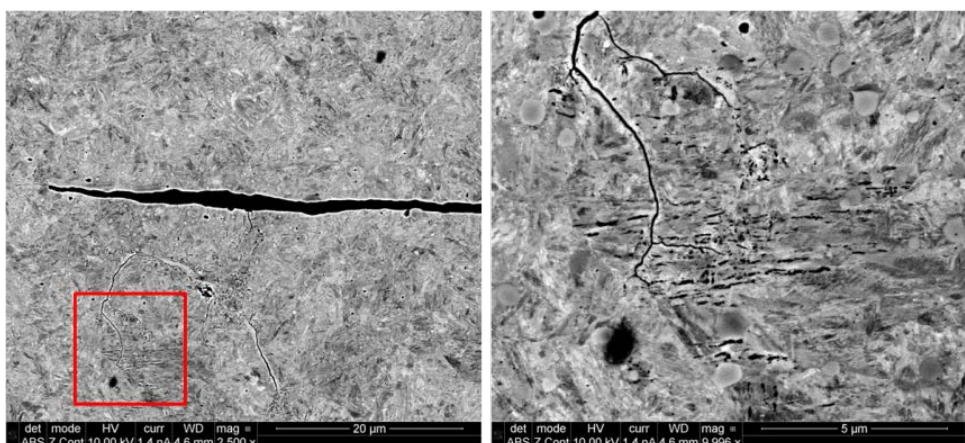


Figure 1.34. SEM-BSE image of local microstructure alterations around cracks. Indications of local plastic deformation are visible in the form of dark parallel line-like features.

Figure 1.35 and Figure 1.36 show examples of butterflies found during the investigation. The inclusions contain a crack and the crack runs into the surrounding martensitic matrix resulting in butterflies like the ones shown in. The butterflies are found to interact with the crack networks, Figure 1.37, but from the present characterization no statement can be made as to whether they are a starting point for the crack networks. Inclusions can therefore be seen as a supporting factor for WEC development.

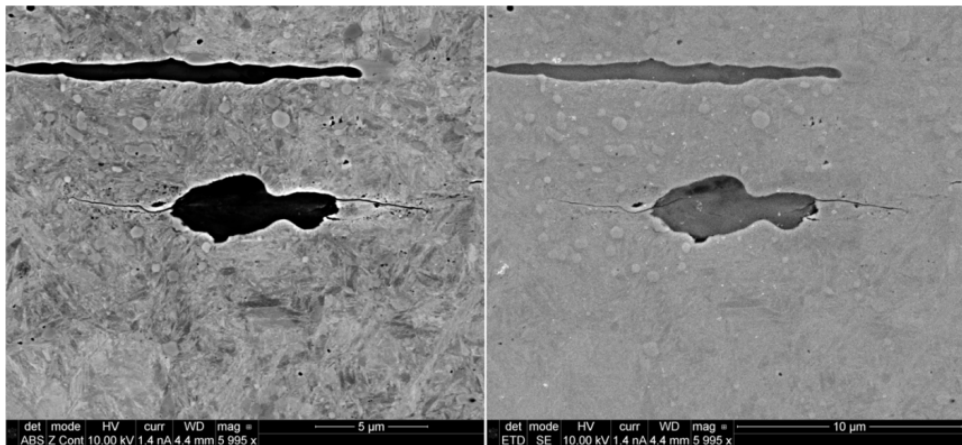


Figure 1.35. Butterflies images with SEM-BSE (left) and SEM-SE mode (right). Cracks in and next to the inclusions are visible.

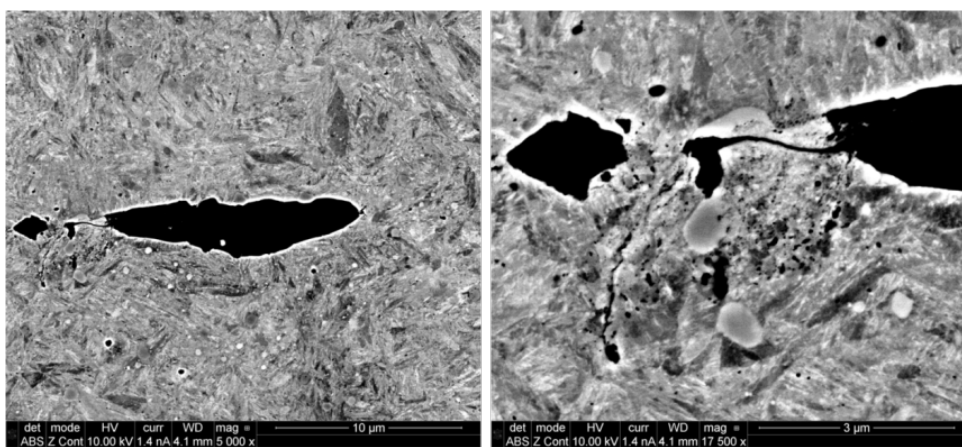


Figure 1.36. SEM-BSE image of a butterfly and local microstructure changes (WEA) at one end of the inclusion.

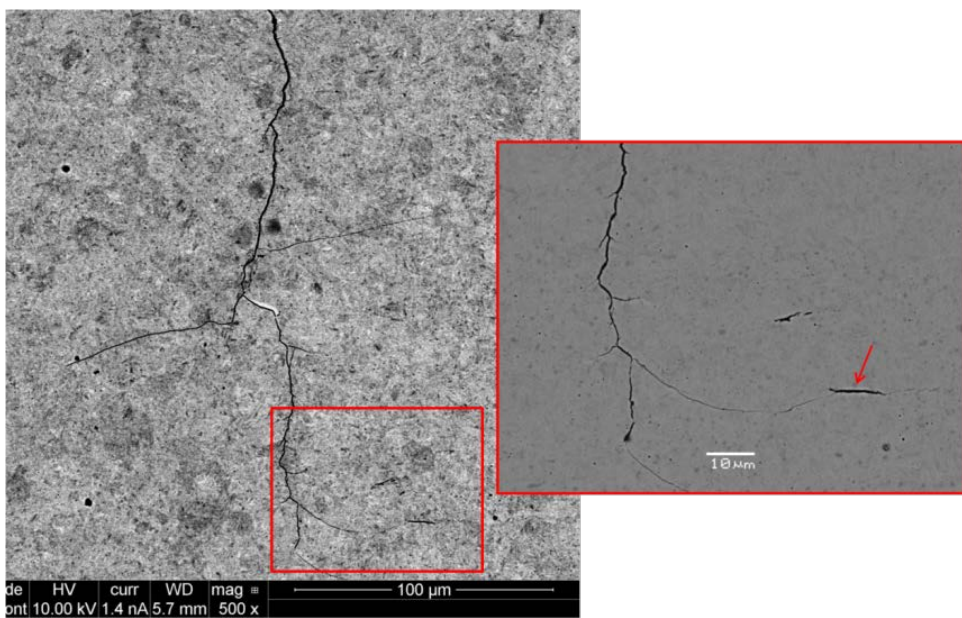


Figure 1.37. SEM-BSE images of interaction between crack network and inclusions; inclusion marked with arrow in the right image.

The continued microstructural changes that occur due to overrolling appear very local and depend on the local stress state. Furthermore, the local stress state is dependent on the overrolling parameters but also highly dependent on the local crack geometry. This indicates that the evolution of the WEA with time as a result of continued overrolling is influenced by the crack geometry and the distribution of already formed hard WEAs, which is being pressed into the surrounding matrix.

The investigated WEC revealed a striking staircase morphology. Similar crack morphology has been observed in WTG bearings as described by e.g. Luyckx [34]. The present characterization was done using SEM-BSE imaging on unetched samples. Therefore the grain structure and local features that are typically difficult to see after etching are still present; interestingly this revealed inhomogeneous grain structures and very local microstructure alterations (deformation structures) present near cracks within a single prior austenite grain. The investigations revealed butterflies that formed at MnS inclusions. The butterflies have a clear interaction with the crack networks, but from the present work it is not possible to make statements about initiation of the networks from butterflies.

Discussion

Surface analysis evidenced typical damage due to pitting in the race of OR (outer ring of NU222), originated from subsurface and signs of edge run in the load zone. On the raceway cracks spalling and flaking of material were found, together with evidence of plastic deformation. This kind of damage could on principle be due to both fatigue or sub-surface initiated fatigue.

Analysis of cross sections was performed on FAG81212 and NU222 microcuts. In both NU 222-14 and FAG 81212-14 tested bearings many cracks were evidenced. For NU222-14 few cracks were located close to the inner surface, while in FAG 81212-14 lots of cracks were found in the mid-thickness area. Inside the cracked zones of each sample WEAs phases were always present.

The comparative SEM analysis showed that no substantial modification of 100Cr6 steel microstructure seems to take place during testing outside the zone of WEAs formation. In fact martensitic structure appears to be unmodified far from WEAs and close to these phases both in failed and in no-failed bearings. Sharp boundary separates the WEA structures from the unaffected steel matrix.

Etching allowed to better highlight WEAs both by OM analysis where they appear white as visible light reflects off the relatively smooth surface and by SEM imaging. WEAs resisted etching so their supposed microstructure (or nano-structure) needs to be further investigated by means of others technique.

Microscopy investigation after etching evidenced typical subsurface cracks WEC, with WEAs (white etching areas), pitting and metallic inclusions (MnS) with cracks and (sometimes) points close to the inclusion.

Some authors assert that Butterflies (BFs) do not originate from metallic inclusions, namely MnS, but only from non-metallic ones like Al_2O_3 (or generally oxides) where MnS is encapsulated: under these circumstances the oxide acts as initiation site. MnS/ Al_2O_3 inclusions were not found, while a lot of sulphide of Mn were present in the analysed bearings.

SEM documentation with EDS microanalysis were performed on the steel matrix, on 'single' carbide particles and on the smooth surface of WEAs. Comparative results on Cr and C content sometimes seemed to indicate the effect of the coalescence and 'dissolution' of carbides inside WEAs structures, but this need to be further confirmed.

Lots of WEAs were evidenced in all the analysed cross sections, while Butterflies (BFs) were not found (or doubtless recognized). Neither DERs (dark etching regions) nor 30° and 80° oriented WEBS (white etching bands) were detected in all the analysed samples. Hardness and micro-hardness measurements gave the 'as expected' results with WEAs hardness 30-50% higher than steel 100Cr6 matrix as suggested by others authors in literature.

1.3. Functional characterization design (Task 1.3)

The activities of this task concern the design of a functional test rig for the laboratory testing of bearings machined from the new steels developed in the project. The main innovative characteristics of the tribometer consist mainly in the possibility to carry out tests in which a set of three variables can be simultaneously involved:

- Load
- Induced currents
- Water injection in the oil circuit.

The design has led to the preliminary configuration of the test rig. The dimension of the components and their typology has been defined.

Some modifications to the designed model could be made in the future depending on the necessity:

- to modify some details
- to adapt some configurations at small scale
- to optimise some assembly parts of the test rig in the most suitable way to ensure proper working conditions.

Definition of the design input parameters

The reference bearing is identified by the code NU207-E-MP1A. The main test rig characteristics have been defined taking in account the following boundary conditions:

- Failure modes
- Mechanical working conditions
- Environment
- Input data from Schaeffler.

A set of tailored characteristics have been set in order to introduce innovative capabilities of the tribometer for the laboratory testing of the components. In particular, the main innovative introduced aspect is the possibility to test involving the following damage parameters at the same time:

- Induced currents
- Corrosion (by water injection as lubricant contaminant)
- Radial loads.

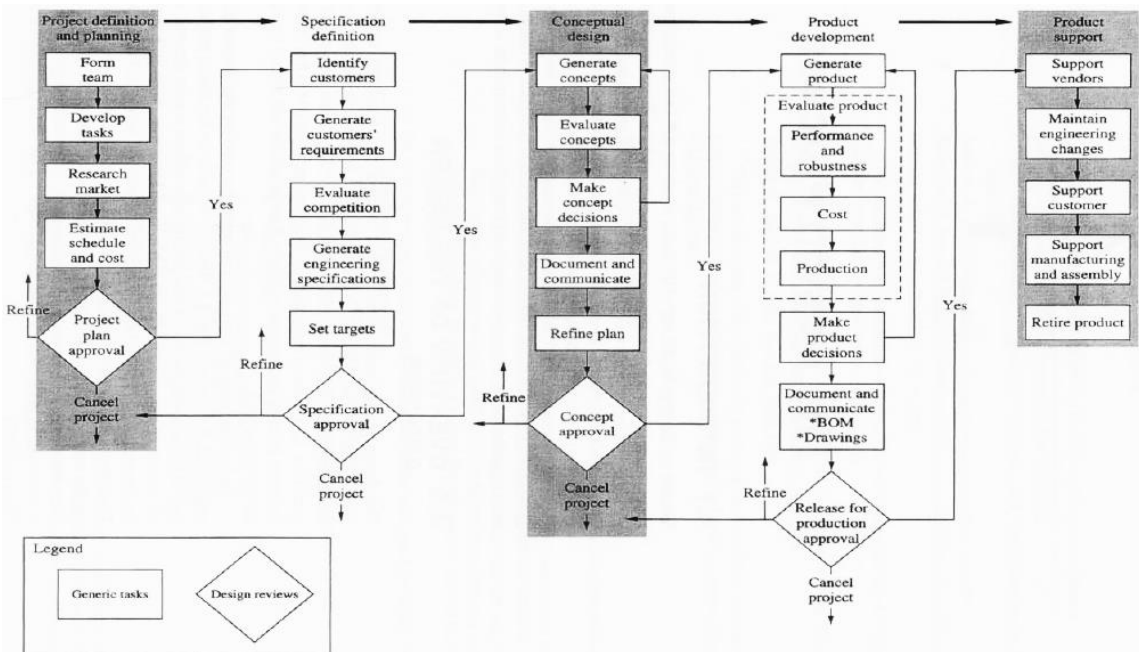


Figure 1.38. Design process flow [80].

Design activities

The working loads and required speeds have been used as input data for the design of the shafts and for the selection of the proper mechanical components in order to ensure suitable characteristics of the test rig.

Servomotor: a calculated torque value of $M_{shaft} = 0.086 \text{ Nm}$ has been used for the evaluation of the power unit for the test rig. A safety coefficient equal to 3 has been considered to ensure a suitable power level to the system. The simulation of the test rig in service operation has been carried out with the software "Motion Analyzer-Allen-Bradley-Rockwell". Then, a velocity profile has been developed in order to best define the most suitable servomotor characteristics for the tribometer.

Figure 1.39 represents the dynamic simulation of servomotor. It is provided an acceleration/deceleration of 1000 rpm/s as required specifications. The simulation allows to observe the behaviour of the motor in terms of position, speed and torque during the work cycle.

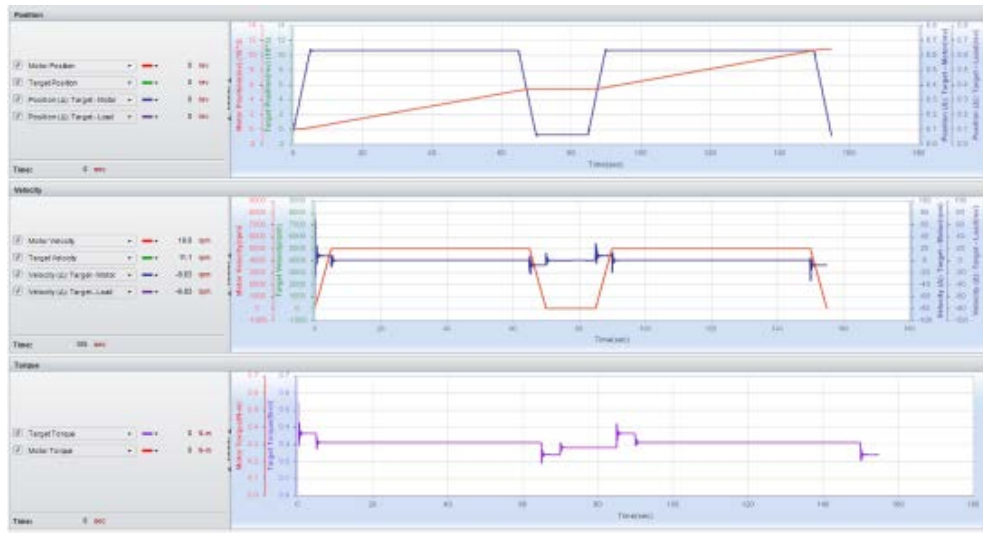


Figure 1.39. Dynamic simulation of servomotor.

Main test rig shaft: the structural analysis has been performed considering the load conditions and boundary conditions shown in Figure 1.40. The Finite Element Model (FEM) model has been developed using the ANSYS® software. The shaft data considered for the design are:

- Shaft diameter = Ø35mm
- Material = AISI431 (UTS = 800 MPa)
- Radial load = 18000 N (for each bearing)
- Angular speed = 3000 - 5000 rpm.

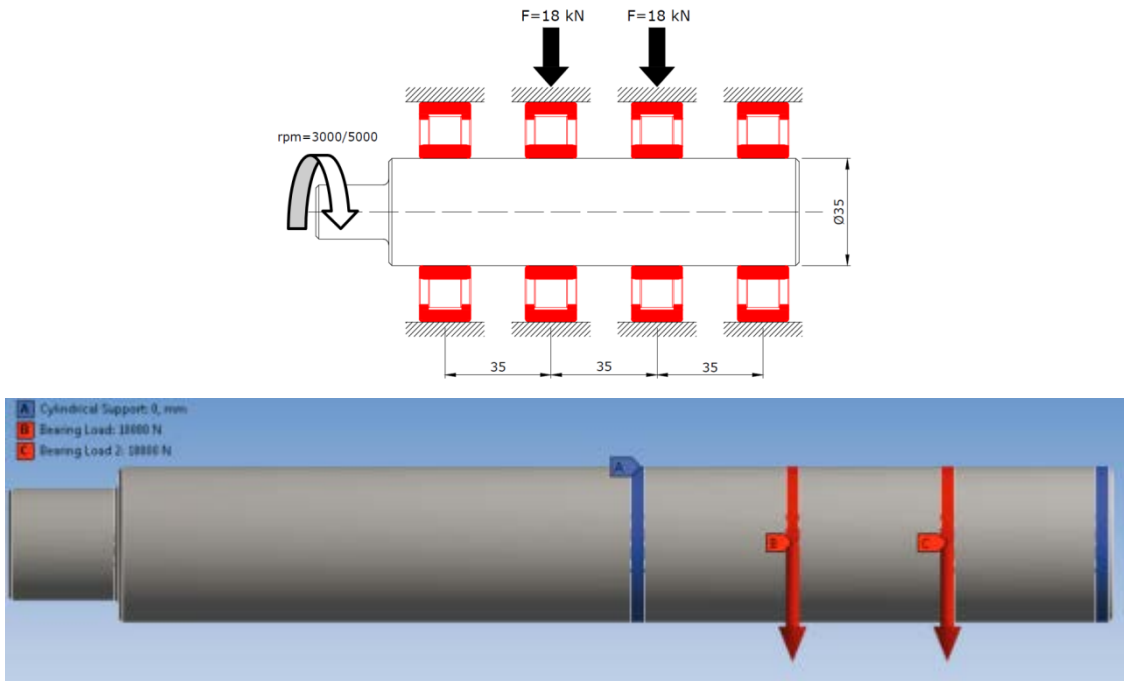


Figure 1.40. Load and boundary conditions for the structural analysis of the shaft.

The load applied on the central bearings is transferred by the equivalent one taking in account the number of nodes in the application area. The 3D model has been simplified using a constraint condition in the areas of the external bearings. This condition could lead to an over estimation of the stresses in these areas due to the imposed zero rotation on the element nodes. For this reason a second FEM model has been developed using "beam" elements (Figure 1.41). The advantage of this scheme is that it is a conservative one because of its highest intrinsic elasticity.

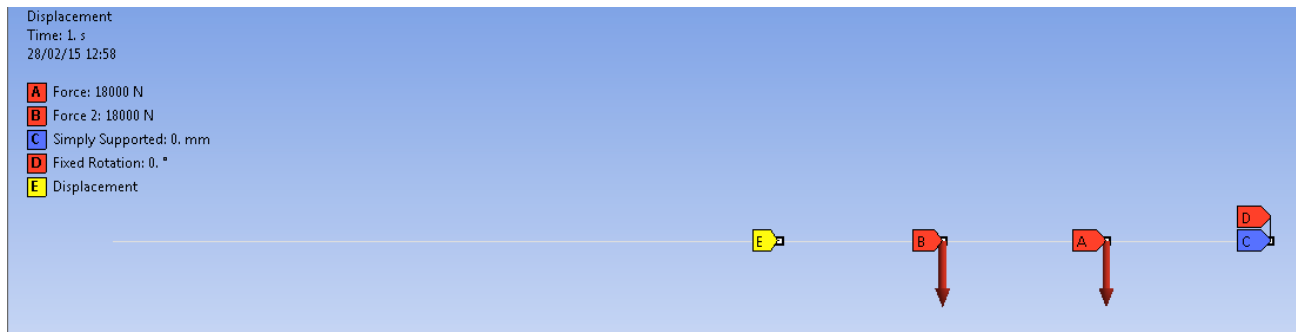


Figure 1.41. haft model with "beam" elements.

Accessory components: the components belonging to this class are the ones selected for control, measuring, safety aims. Their selection have been carried out on the basis of the rig requirements in terms of variables to be controlled and measured.

Concept design

The test rig has been developed considering the possibility to simultaneously test 4 bearings on the same shaft. The test device can be described in its main components, a simplified scheme is shown in Figure 1.42. A servomotor (1) moves the shaft (2) on which the testing bearings (3) are housed. A radial load is applied by a piston (4) whose action is controlled with an oleo-dynamic system (5). The load value is measured and controlled by a load cell (6). The torque is measured by a torsiometer (7) and the shaft angular speed is monitored by the inverter itself. The electric voltage is induced and regulated with a generator and some electric resistances (9). A recirculated bearing lubrication is ensured with a dedicated circuit (10). It allows to control the level of lubricant pollution (12) and a temperature control (11). Furthermore there is a device for oil sampling (13).

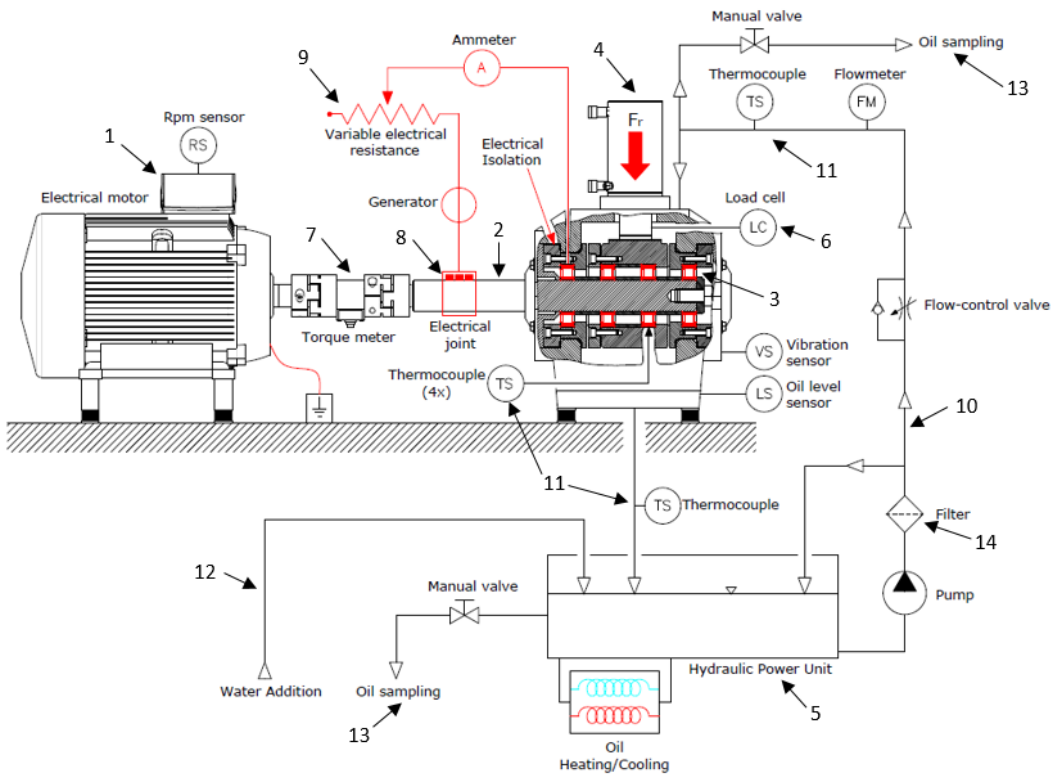


Figure 1.42. Scheme of the test rig.

The main control and controlled variables are:

- radial load ($250 \div 18000$ N for each bearing)
- rotating speed ($3000 \div 5000$ rpm). Acceleration: ± 1000 rpm/s

- adsorbed torque
- lubricant with different viscosity values (64÷320 mm²/s)
- control and measurement of the lubricant
- controlled water addition to lubricant (200÷2000 ppm)
- control and measurement of the lubricant at the of the circuit entry (50÷90 °C)
- measurement of the lubricant at the exit of the circuit
- temperature measurement of the external ring of the bearings
- control and measurement of the induced electric input (0÷10 V 0÷200 mA, DC/AC)
- vibration measurement of the system
- oil sampling for lab analyses
- lubricant filtration for debris check (5-10 µm).

The accessory components for measure and control of the system are briefly described in Table 1.5.

Table 1.5. Accessory components for control and measure.

Type	Name	Unit of Measurement	Input	Output	Range	Resolution
Mechanical	Radial Force	[N]	Oleodynamic system	Load cells	250 ÷ 18000	250
Mechanical	Time	[hr]	Time/rpm	Time/n° cycles	-	-
Mechanical	Speed rotation	[rpm]	Motor speed (inverter)	Inverter signal	3000 ÷ 5000	5
Mechanical	Torque	[Nm]	N/A	Torque meter	0 ÷ 10	± 0.2%
Mechanical	Wear	[gr]	N/A	Offline manual weight Loss	-	-
Mechanical	Cracks	[µm]	N/A	Offline lab evaluation	-	-
Mechanical	Surface defects	[µm]	N/A	Offline lab evaluation	-	-
Mechanical	General vibration	[mm/s]	N/A	Vibration sensor	0 ÷ 50	± 3%
Mechanical	Bearings vibration	[mm/s]	N/A	QASS Sensor	TBD	TBD
Thermodynamic	Temperature	[°C]	Oil temperature	Temperature sensors	50 ÷ 90	± 1.5%
Thermodynamic	OR Bearing Temperature	[°C]	N/A	Temperature sensors	0 ÷ 120	± 1.5%
Thermodynamic	Lubricant viscosity	[mm ² /s]	Oil type/viscosity	Offline lab evaluation	ISO VG 64 ÷ 320	-
Thermodynamic	Oil Particle	[µm]	N/A	Oil particle monitor	0 ÷ 24	± 1%
Thermodynamic	Pollution	[ppm]	Water addition	Offline lab evaluation	200 ÷ 2000	200
Thermodynamic	Oil humidity	[φ]	N/A	Oil humidity sensor	0 ÷ 100 %	± 1%
Electrical	Voltage	[V]	Multimeter	Multimeter	0 ÷ 10	0.5
Electrical	Current	[mA]	Multimeter	Multimeter	0 ÷ 200	5

Design of the main test rig devices: servomotor and main shaft

The results of the dynamic simulation are shown in Table 1.6. It contains the data of the selected servomotor and its drive. Figure 1.43 represents a summary of characteristics and performance of the selected servomotor and of its drive.

Table 1.6. Results of the dynamic simulation.

Motor Solution Data	Application	Motor
	RMS Torque: 0.3065 N-m	0.4981 N-m
	Peak Torque: 0.3718 N-m	1.568 N-m
	RMS Speed: 4520 rpm	
	Peak Speed: 5000 rpm	7000 rpm
	Min. Reflected Inertia: 0.0005819 kg-m ²	1.3e-005 kg-m ²
	Max. Reflected Inertia: 0.0005819 kg-m ²	1.3e-005 kg-m ²
	Average Current: 1.179 A(0-pk)	1.919 A(0-pk)
	Peak Current: 1.436 A(0-pk)	6.1 A(0-pk)
	Winding Temp: 95.83 °C	155 °C
	Minimum Inertia Ratio: 44.76	
	Maximum Inertia Ratio: 44.76	
	Motoring Peak Power: 0.1947 kW	
	Motoring Average Power: 0.1359 kW	
	Regen. Peak Power: 0 kW	
	Regen. Average Power: 0 kW	
	Brake Rating: 0.28 N-m	0.9 N-m
Drive Solution Data	Application	Drive
	Average Power: 0.1638 kW	1.018 kW
	Peak Power: 0.2367 kW	4.32 kW
	Average Current: 1.179 A(0-pk)	2.829 A(0-pk)
	Peak Current: 1.436 A(0-pk)	8.485 A(0-pk)
	Average Dump Power: 0 kW	0 kW
	Critical Velocity Segment: 1	
	Peak Bus Volts Needed: 216.6 V	509.1 V
	Critical Segment Current: 1.402 A(0-pk)	8.485 A(0-pk)
	Critical Dump Segment No: 0	
	Critical Dump Power: 0 kW	
	Critical Dump Time: 0 sec	

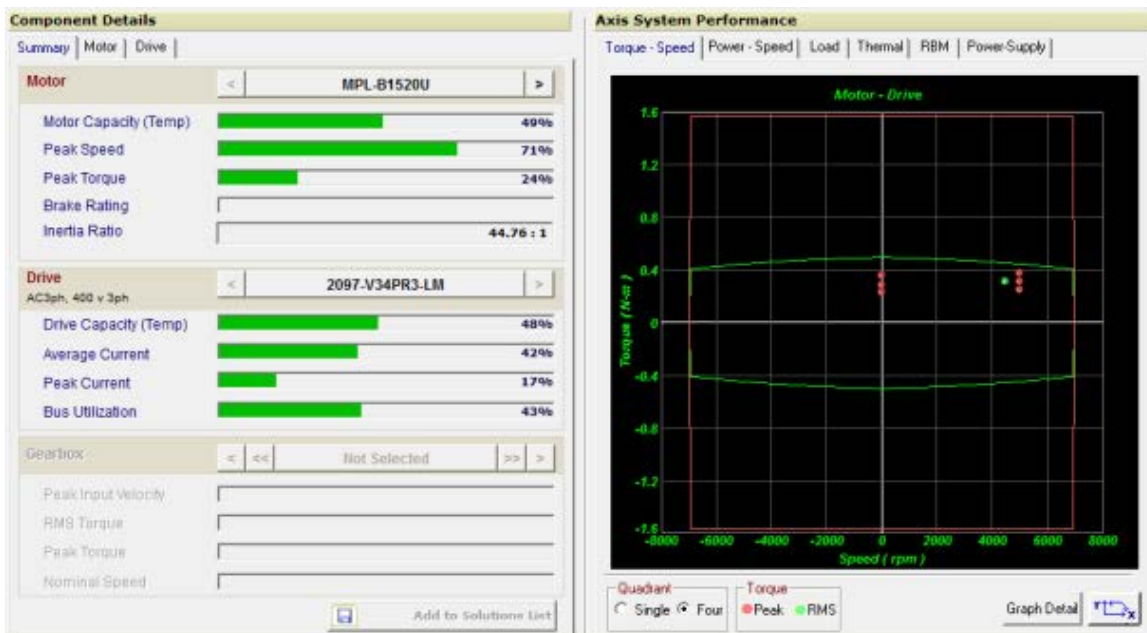


Figure 1.43. Servomotor and Drive performance summary.

The results of the FEM analyses are shown in Figure 1.44. The maximum detected values for the Von Mises stress are in the ranges 125-130 MPa. The displayed values are in fact affected by the contact effect due to the bearing considered as rigid bodies.

The maximum deflection of the shaft showed a value of 0.055 mm.

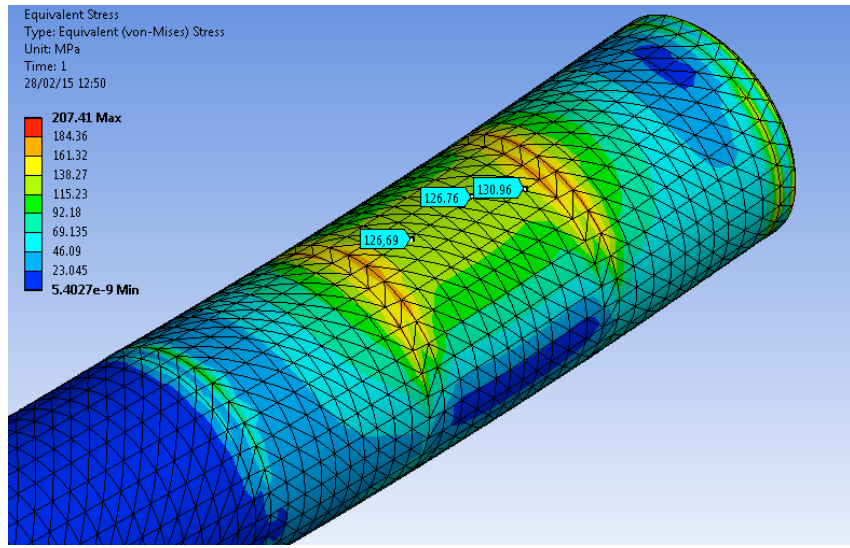


Figure 1.44. Von Mises Stresses of the main shaft.

The results from the second FEM model have been observed in a suitable agreement with the previous model both for the stress (Figure 1.45) and deformation fields. Maximum Combined Stress is combination of direct stress and maximum bending stress. Since the case is a bending problem, the maximum combined stress will be the maximum bending stress. The direct stress is the stress component due to axial load encountered by the beam element. Since there is not axial load, there is a direct stress of zero value throughout the beam. The max vertical deflection of the shaft has a value of 0.06mm in the area of the max bending (Figure 1.46 and Figure 1.47).

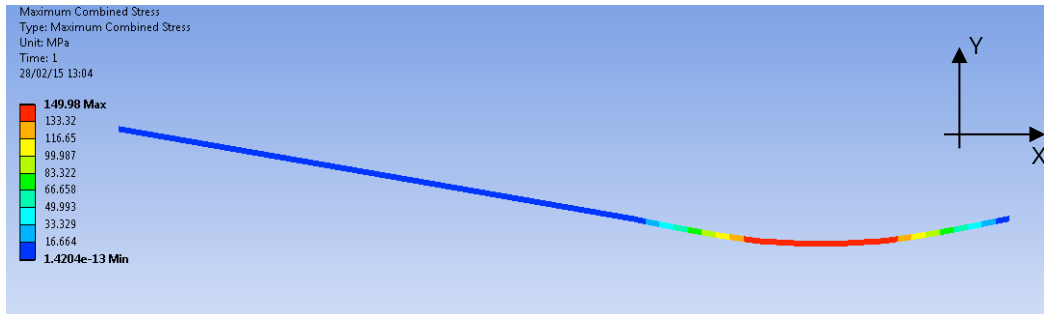


Figure 1.45. Maximum combined stresses.

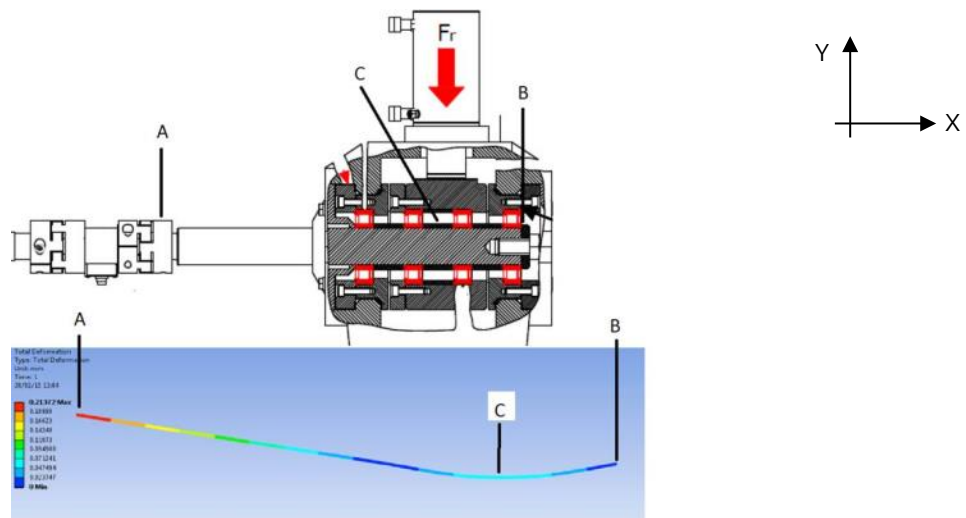


Figure 1.46. Total deformation.

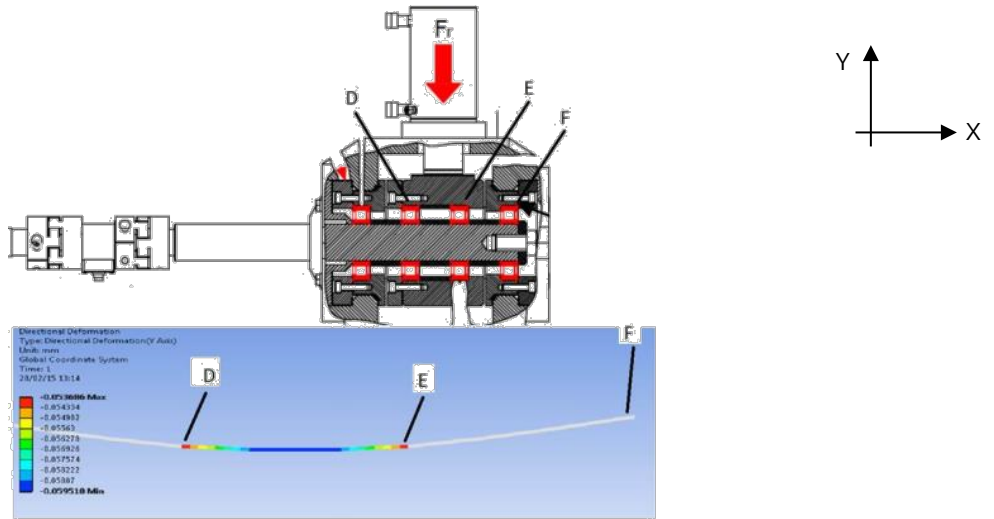


Figure 1.47. Deformation in the Y direction (between the two central bearings).

Regarding the fatigue resistance of the shaft, the estimated values for the shaft with the testing loads on the bearings show a safety coefficient at least equal to 2 (Figure 1.48).

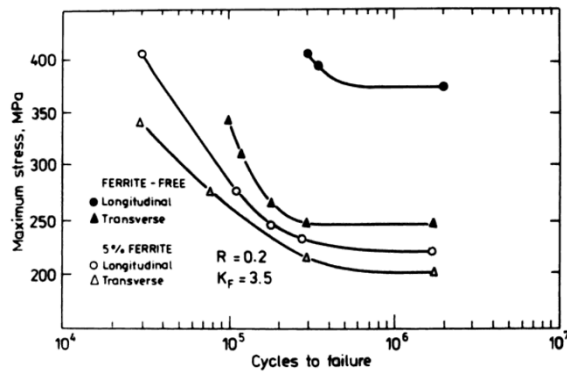


Figure 1.48. Notched fatigue strength of AISI 431 stainless steel [81].

The design has led to the preliminary configuration of the test rig. The dimensions of the components and their typology have been defined. The final configuration should be the one represented in the following pictures from the 3D CAD model (Figure 1.49, Figure 1.50).

Some differences from the designed model at present could be made in the future depending on the necessity:

- to modify some details
- to adapt some configurations at small scale
- to optimise some assembly parts of the test rig in the most suitable way to ensure proper working conditions.

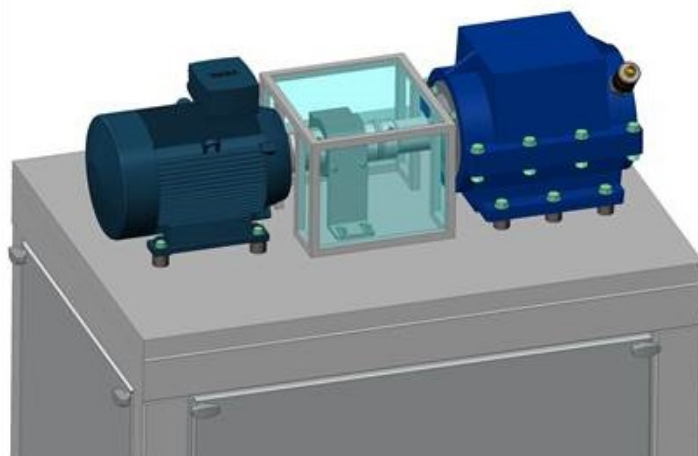


Figure 1.49. 3D model of the test rig.

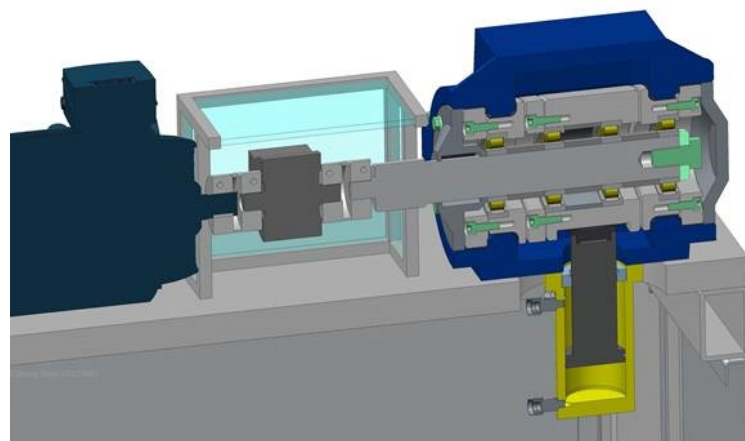


Figure 1.50. Detail of the section for the testing area.

2. WP2. High Nitrogen Austenitic Steel (HNAS): alloy and process design

2.1. Alloy and bulk heat treatment design (Task 2.1)

Preliminary considerations

Alloy design focused on high nitrogen austenitic steel (HNAS), which can guarantee high surface fatigue resistance, wear and corrosion properties with respect to reference solutions (i.e. 100Cr6). Two production routes have been considered, with and without the Pressure-Electro Slag Remelting (PESR) after Vacuum Induction Melting (VIM). The advantage of only VIM – performed in nitrogen atmosphere – is a reduced cost for manufacturing. Its criticalities are the need of a chemical balance for nitrogen solubilisation and higher costs for raw materials. On the other hand, VIM + PESR allows solubilizing higher nitrogen contents with leaner chemical balance, but with higher costs for manufacturing.

Chemical compositions and mechanical properties of reference steel grades for bearing – the common high-carbon grade 100Cr6 and a martensitic stainless steel as Cronidur 30 – are reported in Table 2.1 and Table 2.2. Target mechanical properties of new HNAS are reported in Table 2.3.

Table 2.1. Chemical compositions of reference solutions for bearings.

Steel grade	Chemical Analysis								General description
		C	Si	Mn	Cr	Ni	Mo	N	
X30CrMoN151 Cronidur® 30	min	0.25			14.0		0.85	0.30	pressure-nitrided, martensitic cold working steel
	max	0.35	1.0	1.0	16.0	0.5	1.10	0.50	
AISI/SAE 52100 (100Cr6)	min	0.95	0.15	0.25	1.40				Hardening carbon steel (martensitic or bainitic)
	max	1.10	0.35	0.45	1.60				

Table 2.2. Mechanical properties of reference solutions for bearings.

Steel grade	Mechanical Properties						Source
	Hardness [HRC]	Yield Strength [Mpa]	Tensile strength [MPa]	Fracture elongation [%]	Fracture Toughness [MPa√m]	Fatigue resistance (rotate bending) [Mpa]	
Cronidur® 30	> 58	1850	2150	3	> 20	> 1000 *	Energietech nik Essen data sheet
AISI/SAE 52100 (100Cr6)	up to 62						

Table 2.3. Target mechanical properties of new HNAS steel (source Schaeffler).

NEW HNAS steel grade	Mechanical Properties						
	Hardness [HRC]	Yield strength [Mpa]	Tensile strength [MPa]	Fracture elongation [%]	Fracture Toughness [MPa√m]	Fatigue resistance (rotate bending) [Mpa]	
Superficial layer (3mm)	> 58	> 1500	> 2000	No values	No values	> 700	
Bulk	≥ 30 *		~ 1000				

The achievement of mechanical resistance is based on high interstitial content (mainly N with limited addition of C) and work hardening. According to literature (see Figure 2.1), a minimum nitrogen content of 0.6% is expected to achieve yield strength above 1500 MPa with 40-50% cold deformation.

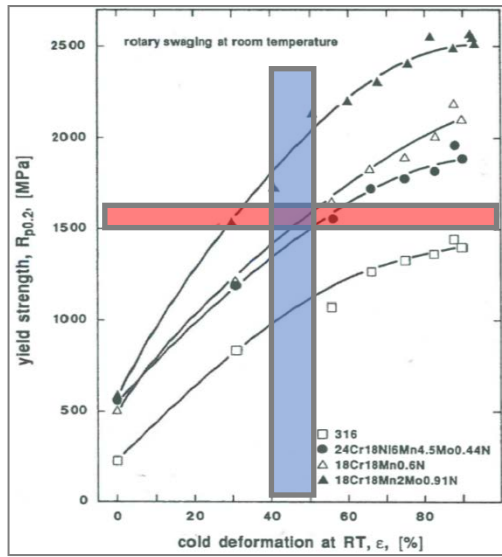


Figure 2.1. Effect of cold deformation on the yield strength of various austenitic steels [45].

The composition needs to be tuned to get a temperature range available for austenite full stability (free of chromium rich carbides, nitrides and residual δ -ferrite), allow thermomechanical and solubilizing treatments and maximizing nitrogen solubility in liquid phase and during solidification.

Alloy design

A first set of alloys for theoretical investigations is reported in Table 2.4. N = 0.3 – 0.8 %. Mn = 11 – 23 %. Cr set to 18 % in order to guarantee a resistance to salty environment comparable to Cronidur® 30. C content set to 0.05 % in order to avoid massive Cr-rich precipitation with decay of intergranular corrosion resistance and embrittling effect. Other elements were considered as typical impurities in raw materials. Amounts of Ni and Cu up to 2 % were also considered.

Table 2.4. First set of considered alloys.

Alloy	C	Cr	Cu	Mn	Ni	N	Si	Mo	V
SW1	0.05	18.0	0.2	11.0	0.2	0.30	0.3	0.2	0.1
SW2	0.05	18.0	0.2	11.0	0.2	0.60	0.3	0.2	0.1
SW3	0.05	18.0	0.2	11.0	0.2	0.80	0.3	0.2	0.1
SW4	0.05	18.0	0.2	15.0	0.2	0.30	0.3	0.2	0.1
SW5	0.05	18.0	0.2	15.0	0.2	0.45	0.3	0.2	0.1
SW6	0.05	18.0	0.2	15.0	0.2	0.60	0.3	0.2	0.1
SW7	0.05	18.0	0.2	18.0	0.2	0.30	0.3	0.2	0.1
SW8	0.05	18.0	0.2	18.0	0.2	0.60	0.3	0.2	0.1
SW9	0.05	18.0	2.0	11.0	2.0	0.30	0.3	0.2	0.1
SW10	0.05	18.0	2.0	15.0	2.0	0.30	0.3	0.2	0.1
SW11	0.05	18.0	2.0	18.0	2.0	0.30	0.3	0.2	0.1
SW12	0.05	18.0	0.2	23.0	0.2	0.60	0.3	0.2	0.1
SW13	0.05	18.0	1.0	23.0	1.0	0.60	0.3	0.2	0.1
SW14	0.05	18.0	2.0	23.0	2.0	0.60	0.3	0.2	0.1
SW15	0.05	18.0	1.0	23.0	1.0	0.45	0.3	0.2	0.1

Mechanical resistance

In high-nitrogen bearing austenitic steels, nitrogen present as interstitial solute atoms without making any nitrides, has a strengthening effect due to solution-hardening much effective than that of carbon [47]. Mechanical properties have been predicted according to empirical relationships resumed in Table 2.5.

Table 2.5. Empirical relationships for prediction of mechanical properties.

Author	Relationships	notes
IRVINE [48]	$R_{p0.2}=63.5+496N+356.5C+20.1Si+3.7Cr+14.6Mo+18.6V+4.5W+40.3Nb+26.3Ti+12.7Al+2.5\delta+7.1d^{1.2}$ $R_M=449.5+852.5N+542.5C+37.2Si-1.5Ni+18.6Mo+77.5Nb+46.5Ti+18.6Al+2.2\delta+7.1t^{1.2}$	δ is the content of δ -ferrite in vol.%, d is the grain size in m and t is the number of twins per mm.
SPEIDEL [49]	$R_{p0.2}=150+500N^{1.2}$ $R_M=500+500N^{1.2}$	
SANCHEZ [50]	$R_{p0.2}=36.7+533.7N+35.5Si+17.1Mo+11.2Cr+3.2Mn-3.3Cu-3.7Ni$ $R_M=336.9+436N+38.9Si+25.9Mo+12.4Cr+3.1Mn-2.8Cu-4.9Ni$	Valid in the following ranges: C≤0,13, Si≤0,15, Mn: 5-14,5%, Cr: 14-20%, Ni: 0,5-8%, Mo≤0,3, Cu: 0,5-4% N: 0,08-0,54%
RUFFINI [51]	$R_{p0.2}=325.1+356.79N-3.26Mn$ $R_M=591.9+272.47N+4.12Mn$	Valid in the range: C=0,06, Si=0,35, Mn: 4-12%, Cr=18,1%, Ni=3%, S<0,03%, Cu: 2,1% N: 0,15-0,55%

Predicted mechanical properties are reported in Table 2.6; for these calculations, only parameters related to chemical content of different elements have been considered. The most promising compositions are those containing higher nitrogen content (SW2, SW3, SW6, SW8, SW12, SW13, SW14).

Table 2.6. Predicted mechanical properties.

Alloy	IRVINE		SPEIDEL		SANCHEZ		RUFFINI	
	YS (MPa)	UTS (MPa)						
SW1	308	747	424	774	446	740	396	719
SW2	456	1003	537	887	606	871	503	801
SW3	556	1173	597	947	713	958	575	855
SW4	308	747	424	774	459	753	383	735
SW5	382	875	485	835	539	818	437	776
SW6	456	1003	537	887	619	884	490	817
SW7	308	747	424	774	469	762	373	748
SW8	456	1003	537	887	629	893	480	830
SW9	308	744	424	774	434	726	396	719
SW10	308	744	424	774	446	739	383	735
SW11	308	744	424	774	456	748	373	748
SW12	456	1003	537	887	645	908	464	850
SW13	456	1002	537	887	639	902	464	850
SW14	456	1000	537	887	632	894	464	850
SW15	382	874	485	835	559	837	411	809

Work hardening

An elevated work hardening can be achieved by means of a proper combination of deformation induced martensite (TRIP effect) and twins in the austenitic matrix during plastic deformation (TWIN effect).

Deformation behaviour based on TRIP or TWIN effects depends on temperature deformation and stacking fault energy (SFE), as illustrated in Figure 2.2.

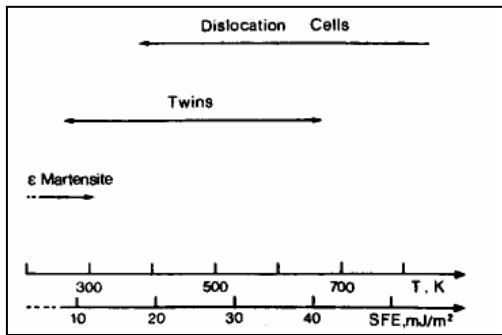


Figure 2.2. Effect of temperature and stacking fault energy on the deformation microstructures of austenite Fe-Mn-Cr-C alloys [49].

Materials with $SFE \leq 30\text{mJ/m}^2$ tend to strain induced phase transformation rather than to strain induced twinning [52]. SFE is affected by elements content, and according to different authors: C and Ni increase SFE [52, 53, 54]; Cr and Mn decrease SFE [52, 53]; the effect of N on SFE depends on Ni, Mn and C contents. As reported in Figure 2.3, in 21Cr-6Ni-9Mn-N steels SFE decreases with increasing nitrogen content up to 0.22 mass and remains almost unchanged, i.e. 30mJ/m^2 from 0.27 to 0.52% [55].

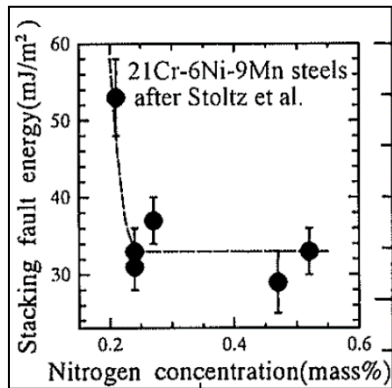


Figure 2.3. Effect of Nitrogen content temperature and stacking fault energy on the deformation microstructures of austenite Fe-Mn-Cr-C alloys [55].

To maximize work-hardening behaviour, SFE should fall in TWIP domain, in the range $20-30\text{mJ/m}^2$). SFE can be predicted according to Olson-Cohen equation. Predictions of SFE values for a Fe-based system containing 18wt% of Cr, 0.05wt% of C and variable contents of Mn and N, are reported in Figure 2.4. The most promising compositions for obtain high work-hardening should be those with lowest nitrogen contents (i.e. SW1 and SW4).

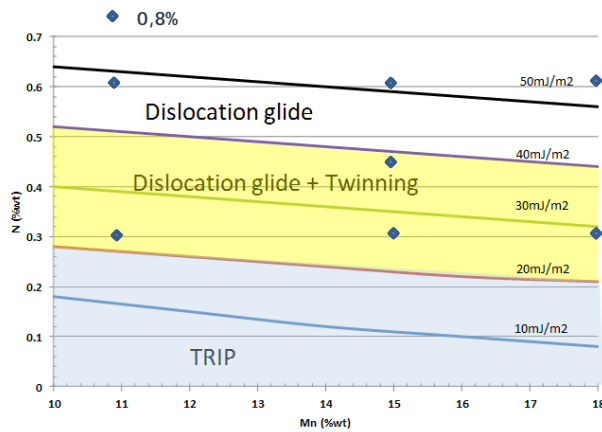


Figure 2.4. Prediction of SFE according to Olson-Cohen equation.

Austenite stability

The full stability of austenite phase at room temperature can be predicted according to positioning of candidate alloys in modified Schaeffler diagrams proposed by several authors. Candidate alloys should fall in γ domain or close to $(\delta+\gamma)$ boundary, which is represented by a line $Ni_{eq}=k*Cr_{eq}+d$. Nickel and Chromium equivalents proposed by different authors for HNAS grades, with related k and d parameters, are summarized in Table 2.7. An example is shown in Figure 2.5.

Table 2.7. Considered modified Schaeffler diagrams.

Author	Relationships	notes
UGGOWITZER [58]	$k=1.148$ $d=-11.1$ $Cr_{eq}=Cr+1.5Mo+1.5W+0.48Si+2.3V+1.75Nb+2.5Al$ $Ni_{eq}=Ni+Co+0.1Mn-0.01Mn^2+18N+30C$	Valid in the following ranges: Cr:15-18%, Mo:3-6%, Mn:10-12%, N: about 0.9%, Nickel free
SANCHEZ[48]	$k=1.309$ $d=-12.8$ $Cr_{eq}=Cr+0.7Si+1.25Mo+0.05Mn$ $Ni_{eq}=Ni+27.4C+22.7N+0.35Cu$	Valid in the following ranges: C \leq 0.13%, Si \leq 1.5%, Mn:5-14.5%, Cr:14-20%, Ni:0.5-8%, Mo \leq 3; Cu:0.5-4%, N:0.08-0.54%[48].
RECHSTEINER/SPEIDEL[43]	$k=1.2$ $d=-12.12$ $Cr_{eq}=Cr+1.5Mo+0.5Si+2.3V+2.5Al$ $Ni_{eq}=Ni+0.12Mn-0.0086Mn^2+30C+18N+0.44Cu$	Valid in the following ranges: Cr:18-25, Mn \leq 25, N:0.6-1.1, Mo \leq 7

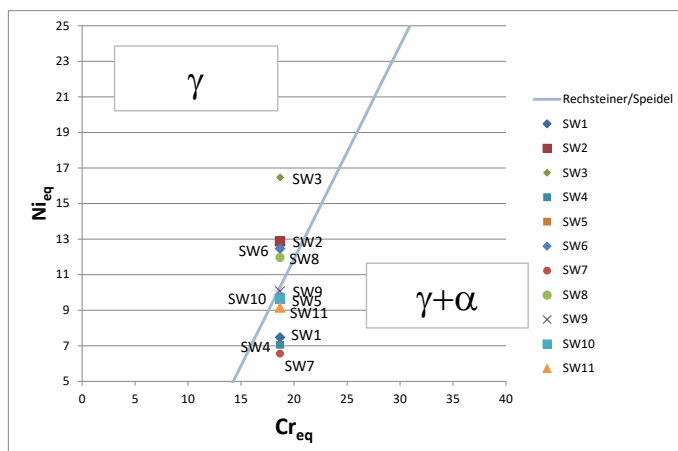


Figure 2.5. Modified Schaeffler diagram according to Rechsteiner/Speidel [43] and positioning of candidate alloys.

A fully austenitic microstructure at room temperature can be achieved only for compositions containing the highest nitrogen content (SW2, SW3, SW6, SW8, SW12, SW13, SW14). Austenite stability at high temperature has been evaluated by JMatPro and Thermo-Calc codes, which allows determination of domains of phase stability at equilibrium conditions. Austenite stability is delimited at higher temperature by $\gamma \rightarrow (\gamma+\delta)$ transformation and at lower temperature by nitrides precipitation as M(C,N) or M₂(C,N) phases. Some examples of estimations of phase stability by JMatPro are reported in Figure 2.6. Estimated temperatures of $\gamma \rightarrow (\gamma+\delta)$ transformation and nitrides precipitation according to Thermo-Calc are reported in Table 2.8.

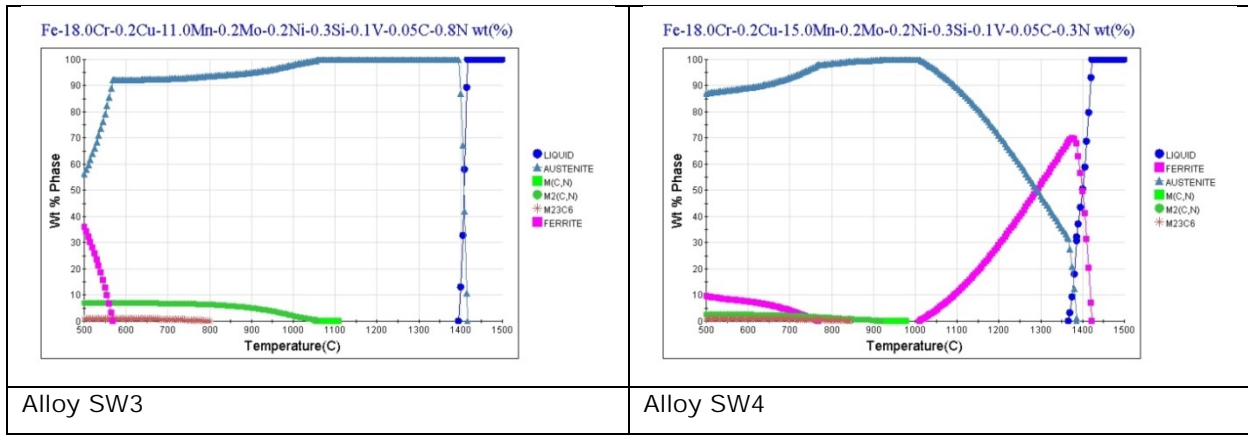


Figure 2.6. Diagrams of phase stability according to JMatPro code.

Table 2.8. Estimations of austenite stability according to Thermo-Calc.

Alloy	Temperature of Cr ₂ N precipitation (°C)	Temperature of $\gamma \rightarrow (\gamma + \delta)$ transformation	δ -ferrite at 1300°C
SW1	1041.1	1064.9	48,0%
SW2	1117.1	1302.6	0,0%
SW3	1146.1	n.d.	0,0%
SW4	1026.1	1009.7	50,8%
SW5	1069.2	1168.9	27,0%
SW6	1100.0	1275.7	5,4%
SW7	1019.0	n.d.	54,0%
SW8	1088.3	1247.7	10,8%
SW9	1138.3	1278.8	3,9%
SW10	1124.5	1248.2	8,0%
SW11	1114.8	1211.7	12,0%
SW12	1069.9	1186.2	20,3%
SW13	1123.6	1283.2	2,9%
SW14	1194.2	1295.9	0,0%
SW15	1088.6	1146.3	20,4%

Estimations according to JMatPro and Thermo-Calc generally agree and the following considerations can be made:

- Nitrogen widens austenite stability, pushing temperature of $\gamma \rightarrow (\gamma + \delta)$ transformation towards higher values; at the same time temperature of nitrides precipitation increases with Nitrogen content.
- Manganese at elevated concentrations stabilizes ferrite and reduces temperature of nitride precipitation.
- Copper and nickel stabilizes austenite respect to δ -ferrite transformation and increase temperature of nitrides precipitation.

Nitrogen solubility

Nitrogen solubility of considered alloys was evaluated according to empirical models. As mentioned before, Nitrogen limit can be calculated according to Sievert law:

$$N_{\text{limit}} = \frac{\sqrt{p_{N_2}^{1/2}}}{k f_N}$$

Where k is the constant of equilibrium for nitrogen dissolution in the liquid melt, p_{N_2} is the partial pressure of nitrogen and f_N is the Henrian activity coefficient of Nitrogen. Nitrogen solubility decreases with temperature in the liquid melt and is enhanced by high p_{N_2} values, that can be achieved, for instance, in PESR process.

Considered expression for calculation of k was the following [59]:

$$\log k = \frac{850}{T} + 0.905$$

The Henrian activity coefficient of Nitrogen depends on alloying elements' content; typically it decreases with Cr, Mn contents and increases with Ni. Empirical relationships according to different authors have been considered, taking into account interaction parameters of first, second and third order. Considered expressions are reported in Table 2.9.

Table 2.9. Empirical models for determination of N solubility based on interaction parameters for f_N .

Author	Relationships	Notes			
		Coefficients at 1600°C			
Satir-Kolorz [60]	$\log f_N = e_N[\%N] + \sum_i e_N^{xi}[\%X_i] + \sum_i r_N^{xi}[\%X_i]^2$	Cr	-0.048	3.50E-04	
		Mn	-0.024	3.20E-05	
		Mo	-0.013	7.90E-05	
		Cu	0.006		
		Ni	0.011	3.50E-05	
		Si	0.043		
		C	0.118		
		N	0.13		
		V	-0.098		
		Coefficients at 1600°C			
Medovar and Grigerenko[61]	$\log[N] = \left(-\frac{293}{T} - 1.16 \right)$ $- \left(\frac{3757}{T} - 0.81 \right) \sum_i e_N^{xi}[\%X_i]$ $+ \frac{1}{2} \left(\frac{5132}{T} - 1.48 \right) \sum_i r_N^{xi}[\%X_i]^2$ $+ \frac{1}{6} \left(\frac{8124}{T} - 3.06 \right) \sum_i q_N^{xi}[\%X_i]^3$ $+ \frac{1}{2} \log P_{N_2}$ <p>Valid in the range 1500-2100°C</p>	Cr	-0.0390	5.80E-04	-6.80E-06
		Mn	-0.0150	5.00E-06	
		Mo	-0.0103		
		Cu			
		Ni	0.0093		
		Si	0.0510		
		C	0.0720	2.15E-02	
		N	0.0440		
		V	-0.0950	2.49E-03	-4.01E-06

Alternative methods bases on chromium or carbon equivalents for determination of f_N were proposed by different authors, and are reported in Table 2.10.

Table 2.10 Empirical models for determination of nitrogen solubility based on Cr_{eq} and C_{eq} .

Author	Relationships	notes	
Satir-Kolorz[62]	$\log f_N = -0.048[\% \text{Cr}_{\text{eq}}] + 3.5 \times 10^{-4} [\% \text{Cr}_{\text{eq}}]^2 + 0.13N$	Coefficients for Cr_{eq}	
		Cr	1
		Mn	0.5
		Mo	0.27
		Cu	-0.12
		Ni	-0.22
		Si	-0.9
		C	-2.46
		N	-2.7
		V	2.05
Schurmann et Kunze[63]	$\log f_N = 0.123[\% \text{C}_{\text{eq}}] + 0.025[\% \text{C}_{\text{eq}}]^2$ (for C_{eq} between 0 and -12)	Coefficients for C_{eq}	
		Cr	-0.382
		Mn	-0.163
		Mo	-0.094
		Cu	0.0463
		Ni	0.0813
		Si	0.444
		C	1
		N	
		V	-0.85

Finally, an empirical model published by Kowanda [64] was considered, which allows prediction of nitrogen solubility in the system Fe-Cr-Mn-Ni-Mo-C-N system without overpressure, in the temperature range 1460-1560°C:

$$[\% \text{N}] = 0.067[\% \text{Cr}] + 0.0195[\% \text{Mn}] + 0.04[\% \text{Mo}] + 0.121[\% \text{V}] + 0.03[\% \text{C}] - 0.024[\% \text{Ni}] - 0.35[\% \text{Nb}] - 0.035[\% \text{Cu}] - 1.05$$

Considered methods were applied to assess nitrogen solubility limit for considered alloys at atmospheric pressure at 1600°C (with exclusion of relationship of Kowanda which is valid up to 1560°C) and therefore evaluate the risk of gas formation in the liquid melt. Results of estimations are reported in Table 2.11, compared also with evaluations by Thermo-Calc code.

Table 2.11. Predictions of nitrogen solubility according to considered empirical models
($p=1\text{ atm}$, $T=1600^\circ\text{C}$).

		SATIR-KOLORZ ⁶⁰		MEDOVAR AND GRIGERENKO ⁶¹		SATIR-KOLORZ ⁶² (CR_{EO})		SCHURMAN N AND KUNZE ⁶³ (C_{EO})		KOWANDA ⁶⁴		THERMO-CALC (TCFE7)	
ALLOY	N (%)	GAS	$N_{\text{LIMIT}}\text{ (%)}$	GAS	$N_{\text{LIMIT}}\text{ (%)}$	GAS	$N_{\text{LIMIT}}\text{ (%)}$	GAS	$N_{\text{LIMIT}}\text{ (%)}$	GAS	$N_{\text{LIMIT}}\text{ (%)}$	GAS	$N_{\text{LIMIT}}\text{ (%)}$
SW1	0.30	NO	0.40	NO	0.38	NO	0.32	NO	0.33	NO	0.38	NO	0.37
SW2	0.60	YES	0.37	YES	0.37	YES	0.28	YES	0.33	YES	0.38	YES	0.37
SW3	0.80	YES	0.35	YES	0.36	YES	0.25	YES	0.33	YES	0.38	YES	0.37
SW4	0.30	NO	0.50	NO	0.45	NO	0.37	NO	0.37	NO	0.46	NO	0.43
SW5	0.45	NO	0.48	YES	0.45	YES	0.34	YES	0.37	NO	0.46	YES	0.43
SW6	0.60	YES	0.46	YES	0.44	YES	0.32	YES	0.37	YES	0.46	YES	0.43
SW7	0.30	NO	0.59	NO	0.51	NO	0.41	NO	0.40	NO	0.52	NO	0.48
SW8	0.60	YES	0.54	YES	0.49	YES	0.36	YES	0.40	YES	0.52	YES	0.48
SW9	0.30	NO	0.38	NO	0.38	NO	0.31	NO	0.31	YES	0.27	NO	0.35
SW10	0.30	NO	0.47	NO	0.45	NO	0.35	NO	0.35	NO	0.35	NO	0.40
SW11	0.30	NO	0.55	NO	0.51	NO	0.39	NO	0.38	NO	0.41	NO	0.45
SW12	0.60	NO	0.69	NO	0.61	YES	0.42	YES	0.46	NO	0.61	YES	0.57
SW13	0.60	NO	0.68	NO	0.61	YES	0.41	YES	0.45	YES	0.57	YES	0.55
SW14	0.60	NO	0.65	NO	0.61	YES	0.40	YES	0.44	YES	0.51	YES	0.53
SW15	0.45	NO	0.71	NO	0.62	YES	0.44	YES	0.45	NO	0.57	NO	0.55

Considered methods generally agree in estimating absence of gas nucleation at 1600°C and atmospheric pressure only for alloys containing lower nitrogen contents (SW1, SW4, SW7, SW9, SW10, SW11). Achievement of higher nitrogen contents, i.e. $\geq 0.45\%$, appears critical adopting manufacturing routes at atmospheric pressure.

Further evaluations concerning Nitrogen solubility have been made by means of Thermo-Calc, which allows estimation at different pressure respect to $p=1\text{ atm}$. Estimation of Nitrogen solubility limit for compositions are reported in Figure 2.7 - Figure 2.8 respectively for $\text{Mn}=11\text{-}18\%$ and $\text{Mn}=23\%$. Increasing pressure up to 10 atm would allow solubilization of Nitrogen contents up to 0.8%. At atmospheric pressure, Nitrogen solubility is increased by increasing Mn content, by reduction of temperature and is depresses by increasing Cu and Ni content. According to Thermo-Calc evaluations, solubilization of Nitrogen at 1600°C could be feasible for Mn content of 23% only for compositions containing N up to 0.45%. Reduction of temperature from 1600°C to 1500°C would allow solubilization of N=0.6% for Mn=23% at conditions close to atmospheric pressure (Figure 2.9).

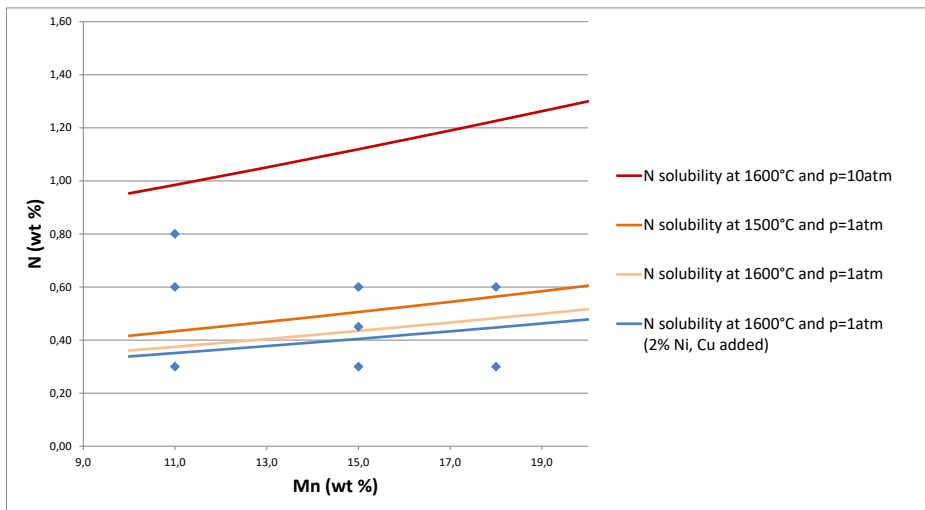


Figure 2.7. Estimation of Nitrogen solubility according to Thermo-Calc (Mn=11-18%).

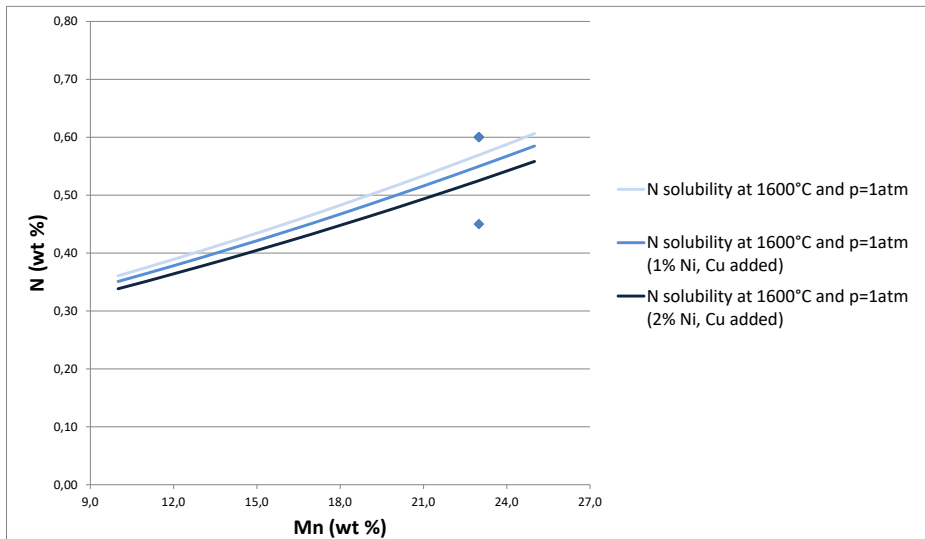


Figure 2.8. Estimation of Nitrogen solubility according to Thermo-Calc (Mn=23%).

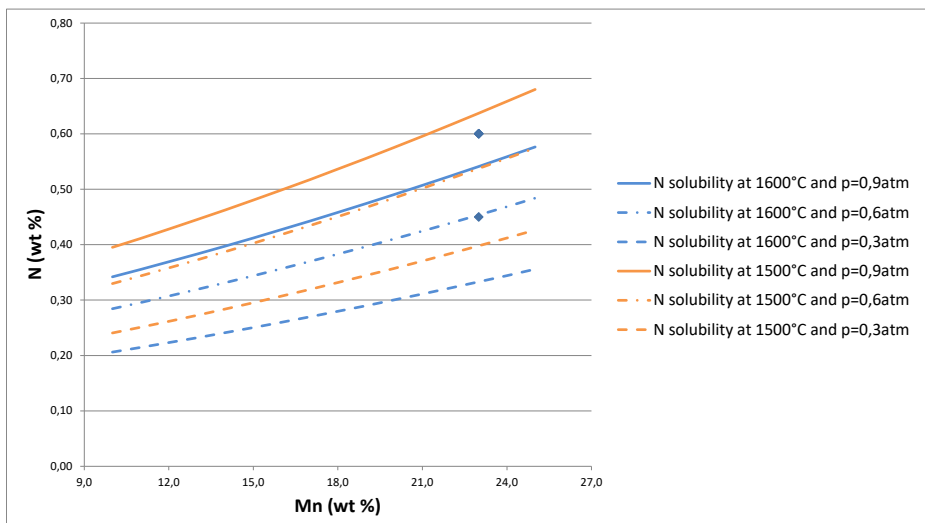


Figure 2.9. Estimation of Nitrogen solubility according to Thermo-Calc at pressure condition lower than p_{atm} (Mn=23%).

Further evaluations have been made for prediction of gas formation during solidification due to microsegregation phenomena. During solidification, Nitrogen and other solutes partition from growing solid phase towards residual liquid melt, thus resulting in an increase of solute content at the final stages of solidification range. A physical model developed by CSM [65] allows estimation risk for gas nucleation due to nitrogen microsegregation, taking into account different physical parameters involved in solidification. Size of gas bubble, in terms of its radius, can be related to local ferrostatic pressure ($p_{atm} + p_{ferr}$) and superficial tension for gas nucleation in the liquid melt according to Sievert law:

$$(f_N kN)^2 = \left(p_{atm} + p_{ferr} + \frac{2\sigma}{R} \right)$$

Previous relationship can be explicitated respect to R:

$$R = \left[\frac{2\sigma}{(f_N kN)^2 - p_{atm} - p_{ferr}} \right]$$

Where f_N and N vary during solidification due to composition evolution in the residual melt related to microsegregation and convection. Also p_{ferr} is a variable parameter varying with distance from meniscus in continuous casting or top of the ingot in casting process. Gas bubbles can nucleate in solidifying microstructure if following condition is satisfied:

$$R \leq \frac{SDAS}{2}$$

Where SDAS is secondary dendrite arm spacing, and can be expressed for different casting conditions as a function of cooling rate, depending on the distance from the mould and thickness of solidified shell. Estimations for gas nucleation were therefore made for compositions SW12 and SW15 at conditions lower than atmospheric pressure and $T=1500^\circ\text{C}$, which could be performed in standard VIM route. Condition for gas nucleation due to nitrogen segregation during solidification are not satisfied (Figure 2.10).

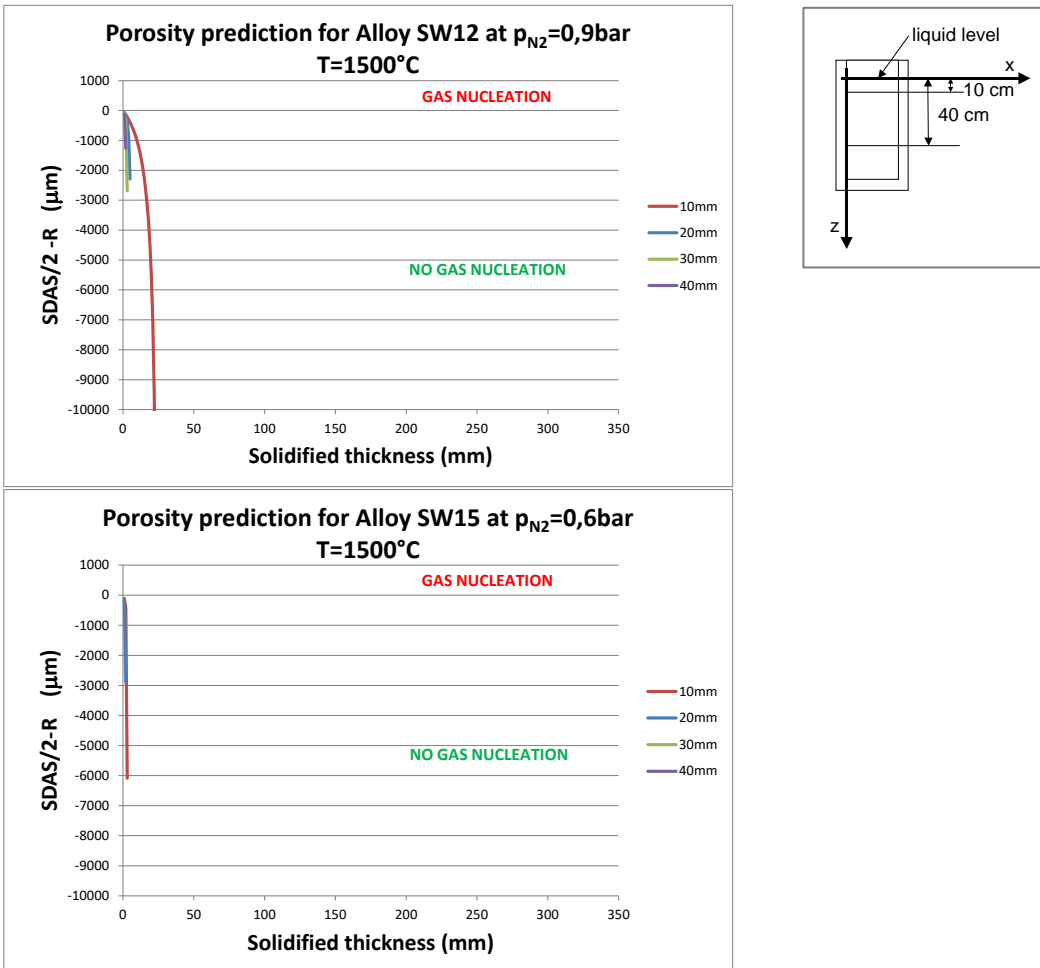


Figure 2.10. Estimation of gas nucleation during solidification at pressure condition lower than p_{atm} ($Mn=23\%$).

Summary of alloy design

Consideration expressed in previous sections can be resumed in the following Table 2.12.

Table 2.12. Summary of alloy design considerations.

Steel	Cu	Mn	Ni	N	Mechanical resistance in the annealed state	Work hardening related to SFE	Austenite stability	Manufacturing at atmospheric pressure
SW1	0.2	11.0	0.2	0.30	Low	High	Low	Feasible
SW2	0.2	11.0	0.2	0.60	Medium/High	Low (?)	High	Not feasible – PESR required
SW3	0.2	11.0	0.2	0.80	High	Low (?)	Very high	Not feasible – PESR required
SW4	0.2	15.0	0.2	0.30	Low	High	Low	Feasible
SW5	0.2	15.0	0.2	0.45	Medium/Low	Medium	Medium	Not feasible – PESR required (?)
SW6	0.2	15.0	0.2	0.60	Medium/High	Low (?)	High	Not feasible – PESR required
SW7	0.2	18.0	0.2	0.30	Low	High	Low	Feasible
SW8	0.2	18.0	0.2	0.60	Medium/High	Low (?)	High	Not feasible – PESR required
SW9	2.0	11.0	2.0	0.30	Low	Medium	Medium/Low	Feasible
SW10	2.0	15.0	2.0	0.30	Low	Medium	Medium/Low	Feasible
SW11	2.0	18.0	2.0	0.30	Low	Medium	Medium/Low	Feasible
SW12	0.2	23.0	0.2	0.60	Medium/High	Low (?)	High	Feasible (?)
SW13	1.0	23.0	1.0	0.60	Medium/High	Low (?)	High	Feasible (?)
SW14	2.0	23.0	2.0	0.60	Medium/High	Low (?)	Very high	Feasible (?)
SW15	1.0	23.0	1.0	0.45	Medium/Low	Medium	Medium	Feasible (?)

Compositions with N=0.3% are expected not to fulfill technical specifications, due to low mechanical resistance in the annealed state and poor stability of austenite respect to γ/δ trasformation at high temperature, even in case of alloying with Ni and Cu.

Compositions with N \geq 0.6% fall in the γ domain according to empirical models and show a limited stability of δ -ferrite which disappears for N=0.8%.

Compositions with N=0.45% shows an intermediate behaviour and fall near the boundary between γ and ($\gamma+\delta$) domains.

Mn stabilizes δ -ferrite and lowers temperature for Cr₂N precipitation, which is increased by N, Ni and Cu addition.

Compositions with N=0.6% can be manufactured via PESR route and, probably, at atmospheric pressure for 23wt% Mn content according to experiences reported in literature [66, 67].

Processing by VIM route of some alloys (i.e SW12, SW15) could be feasible if manufacturing conditions are adjusted respect to Nitrogen content:

- N=0.60% could be reached at 1500°C and pN₂=0,9bar
- N=0.45% could be reached at 1500°C and pN₂ \geq 0,6bar

According to preliminary assessment of porosity, dissolved nitrogen should not nucleate as bubbles during solidification.

Preliminary informations for tuning of SFE prediction models could be acquired by means of some trials on small ingots on the following compositions, starting from 0,3N% and 0,6%N compositions (SW6, SW8, SW9, SW10).

Experimental trials and selection of new HNAS compositions

The following considerations regard the selection of the high-N austenitic steel compositions, to be produced through the two manufacturing routes considered (route 1: VIM; route 2: VIM + PESR). They are based on the results of the alloy design as well as on further information, obtained by means of some experimental trials performed on small ingots (5 kg) with compositions ranging between N = 0.30 % and N = 0.60 % (see Table 2.13). The production process and the related sampling and testing are shown in Figure 2.11 . Casting has been performed by VIM at T = 1500 °C and pN₂ = 0.6 - 0.9 bar. The reference targets for mechanical properties are those already reported at the beginning of the alloy design.

Table 2.13. Compositions of experimental ingots (mass %).

Alloy	Cast	C	Cr	Cu	Mn	Ni	N	Si	Mo	V
SW6	BZ1167	0.07	18.6	0.11	12.2	0.12	0.45	0.32	0.21	0.11
SW8	BZ1168	0.07	17.8	0.10	17.8	0.12	0.58	0.23	0.19	0.09
SW9	BZ1165	0.07	17.8	2.04	10.0	2.04	0.27	0.27	0.20	0.06
SW10	BZ1166	0.06	18.2	2.13	13.7	2.11	0.29	0.27	0.19	0.08

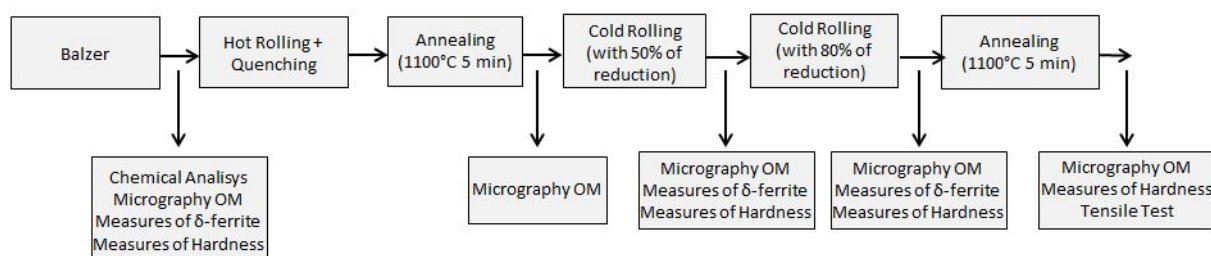


Figure 2.11. Production process, sampling and testing of 5 kg ingots.

The target for the mechanical properties in bulk is UTS = 1000 MPa. The tensile properties obtained in the annealed condition are reported in Figure 2.12. The correlation of YS and UTS with nitrogen content is following quite well the empirical relationship given by Speidel in [49], reported as lines for comparison.

The higher values for mechanical strength are reached by composition SW8 (BZ 1168) with N content close to 0.60 %. However UTS is still low, and a certain level of deformation is needed to achieve the level required. According to some analyses done on work hardening behaviour, even using the Mecking-Kocks model to study the evolution of dislocation density with plastic strain, a minimum true strain of 0.25 would be necessary. Otherwise, increasing the N level seems to be the only way to achieve the level of mechanical strength required for the bulk. The results summarized show that a N amount of at least 0.80 % is needed to achieve the mechanical strength required for the bulk (UTS = 1000 MPa). So, a composition with N = 0.90 % has been considered as a base. For such nitrogen level, the manufacturing route 2 (VIM + PESR) is required. The composition selected is reported in Table 2.14.

The effect of the other elements – in particular manganese – has been considered in terms of austenite stability, nitrogen solubility, mechanical strength, corrosion resistance. An increase in Mn tends to decrease the temperature precipitation of chromium nitride, extending the range of temperature suitable for heat treatments, and slightly increases the mechanical resistance by means of solid solution strengthening. On the other hand, it causes a reduction in the empirical corrosion indexes as MARC and PREN-Mn. The target selected represents a compromise among the different factors.

An addition of silicon up to 0.60 % has also been considered, because N addition in PESR is made by means of silicon nitride (Si₃N₄), resulting in silicon addition. From thermodynamic considerations, the effect of such silicon amount makes the precipitation temperature of chromium nitride increase, reducing the range of temperature suitable for heat treatments. Besides that, two different compositions have also been selected, to be obtained by means of Manufacturing Route 1 (VIM in nitrogen atmosphere), they are reported in Table 2.15.

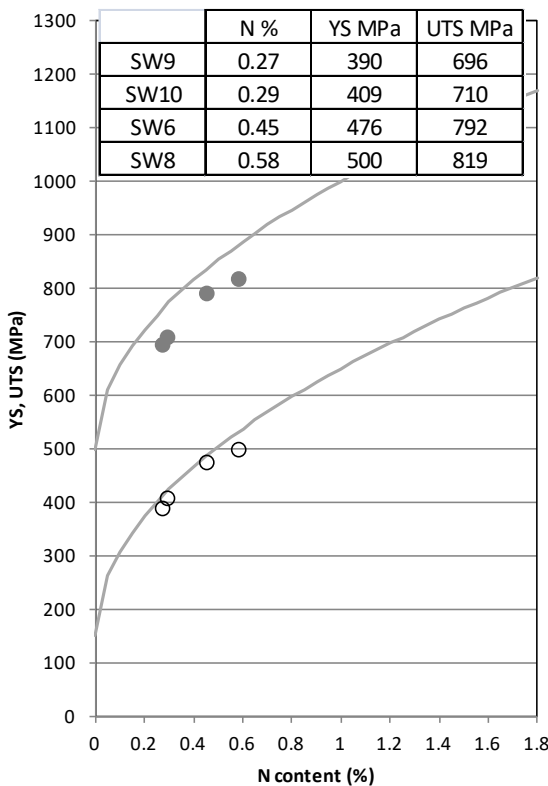


Figure 2.12. Tensile properties in the annealed state (YS: white circles, UTS: grey circles) and for comparison empirical relationships with N content given by Speidel (lines).

Table 2.14. Composition selected for Manufacturing Route 2 (VIM+PESR).

	C	N	Cr	Mn	Mo	Si	V	Cu	Ni
MR2	0.05	0.90	18.0	11.0	2.0	0.60	0.10	0.20	0.20

Table 2.15. Compositions selected for Manufacturing Route 1 (VIM, in N atmosphere).

	C	N	Cr	Mn	Mo	Si	V	Cu	Ni
MR1/1	0.40	0.60	18.0	19.0	1.0	0.30	0.10	0.20	0.20
MR1/2	0.05	0.60	18.0	18.0	2.0	0.30	0.10	0.20	0.20

The compositions MR1/1 is belonging to the so-called CARNIT alloys, based on the addition of carbon and nitrogen. According to the literature, UTS levels higher than 1000 MPa can be achieved with such composition [68]. The carbon amount (0.40 %) has been adjusted on the basis of thermodynamic calculations, which showed as an increase of this element brings to a higher temperature for $M_{23}C_6$ precipitation, so reducing the field of austenite stability (see Table 2.16).

Table 2.16. Austenite stability and carbon content in CARNIT composition.

Alloy CARNIT Mo = 1%	Temperature of precipitation $M_{23}C_6$ (°C) - JMatPro	δ -ferrite at 1300 °C (%)
C = 0.50	1130	0
C = 0.40	1080	0

Additions of Mo content have been found to increase the temperature of $M_{23}C_6$ precipitation: on that basis, the level of Mo has been limited to 1 % (see Table 2.17).

Table 2.17. Austenite stability and molybdenum content in CARNIT composition.

Alloy CARNIT Mo = 1 %	Temperature of precipitation $M_{23}C_6$ (°C) - JMatPro	δ -ferrite at 1300 °C (%)
Mo = 1 %	1080	0
Mo = 2 %	1090	0
Mo = 3 %	1100	0

2.2. Process design and HNAS lab manufacturing by production route 1 (casting by VIM) and production route 2 (casting by VIM followed by secondary remelting) (Task 2.2 - Task 2.3)

On the basis of the findings of the alloy design, as reported in detail in the section devoted to WP2, three specific alloys have been defined according to the requirements listed in Table 2.18.

Table 2.18. Summary of the selected alloys. VIM: Vacuum Induction Melting. PESR: Pressured Electro Slag Re-melting.

Alloy	Process route	Notes
MR1/1	VIM	CARNIT (C+N)
MR1/2	VIM	Medium N (N = 0.5-0.6 %)
MR2	VIM + PESR	High N (N = 0.9 %)

The chemical compositions assumed as a target are reported in Table 2.19.

Table 2.19. Target chemical compositions of the selected alloys. Mass %. (*) After PESR.

Alloy	C	N	Cr	Mn	Mo	Si	V	Cu	Ni
MR1/1	0.40	0.60	18.0	19.0	1.0	0.30	0.10	0.20	0.20
MR1/2	0.05	0.60	18.0	18.0	2.0	0.30	0.10	0.20	0.20
MR2	0.05	0.90	18.0	11.0	2.0	0.60 (*)	0.10	0.20	0.20

The Si amount of 0.6 % refers to the final compositions, after the process of re-melting, in which the achievement of the desired level of nitrogen requires the addition of silicon nitride (Si_3N_4).

For each selected alloy type two ingots have been cast. The compositions are reported in Table 2.20, Table 2.21 and Table 2.22 respectively, along with the related reference ranges.

Table 2.20. Composition of CARNIT alloy ingots (MR1/1). Mass %.

Range	C	N	Cr	Mn	Mo	Si	S	P	Cu	Ni
min	0.35	0.55	17.50	18.50	0.80	0.25	-	-	0.18	0.18
max	0.45	0.65	18.50	19.50	1.20	0.35	0.015	0.015	0.22	0.22
Ingots	C	N	Cr	Mn	Mo	Si	S	P	Cu	Ni
VM2947	0.38	0.59	17.85	18.70	0.88	0.25	0.007	<0.015	0.20	0.21
VM2950	0.40	0.60	17.75	18.71	0.96	0.30	0.006	<0.015	0.18	0.22

Table 2.21. Composition of medium N alloy ingots (MR1/2). Mass %.

Range	C	N	Cr	Mn	Mo	Si	S	P	Cu	Ni
min	0.040	0.55	17.50	17.50	1.80	0.25	-	-	0.18	0.18
max	0.060	0.65	18.50	18.50	2.20	0.35	0.015	0.015	0.22	0.22
Ingots	C	N	Cr	Mn	Mo	Si	S	P	Cu	Ni
VM2948	0.060	0.59	17.50	17.60	1.90	0.27	0.006	<0.015	0.19	0.21
VM2951	0.050	0.58	17.85	18.13	1.90	0.29	0.006	<0.015	0.19	0.21

Table 2.22. Composition of high N alloy ingots (MR2). Mass %.

Range	C	N	Cr	Mn	Mo	Si	S	P	Cu	Ni
min	0.040	0.85	17.50	10.50	1.80	-	-	-	0.18	0.18
max	0.060	0.95	18.50	11.50	2.20	0.65	0.015	0.015	0.22	0.22
Ingots	C	N	Cr	Mn	Mo	Si	S	P	Cu	Ni
PESR073	0.060	0.56	17.80	10.50	1.89	0.37	<0.015	<0.015	0.25	0.25
PESR074	0.050	0.83	18.00	10.90	1.93	0.33	<0.015	<0.015	0.22	0.20

The compositions of the ingots produced by means of the only VIM process (MR1/1, MR2) comply with the requirements. On the other hand, some problems have been encountered in PESR processing, due to that the required nitrogen level has not been achieved: in particular, the value obtained in PESR073

is far from the desired range, whilst that of PESR074 is very close to the minimum of the range. The casting process through VIM has been carried out according to the following process steps:

- Heating and melting. This operation is made under vacuum ($p = 0.1$ mbar).
- Alloy addition / adjustment of composition. Operation made at nitrogen pressure (900-950 mbar).
- Casting at temperature targeting $T_{\text{liquidus}} + 40$ °C. In the specific case, $T = 1450$ °C.

The PESR process occurs through the following procedure:

- Start phase (about 6-7 minutes).
- Melt phase, slag and Si_3N_4 addition, under nitrogen pressure of about 20 bar (about 30 minutes).
- Hot topping.

The ingots manufactured by means of VIM process (dimensions Ø142mm x 610mm) are shown in Figure 2.13.



Figure 2.13. Ingots manufactured via VIM. Size Ø142 mm x 610 mm).

Design of heat treatments

In order to obtain an austenitic microstructure, maintaining nitrogen in solid solution and avoiding nitride and carbide precipitation, the following criteria should be respected:

- Soaking temperatures must fall in the austenite stability range, avoiding formation of δ -phase.
- Soaking temperatures must be out of the range of carbide and nitride precipitation (solubilization).
- Cooling rate must be suitable to prevent precipitation of carbides and nitrides.

According to thermodynamics calculations (JMatPro) of the austenite stability at high temperatures, the heat treatment temperatures need to be fit to each specific composition. The range of austenite stability for CARNIT alloy (MR1/1) is quite wide (Figure 2.14: no δ -phase domain is found, the heat treatment temperature should be safely higher than the temperature of precipitation of carbides M_{23}C_6 . In the case of medium-N alloy with $N = 0.60$ % (MR1/2) a δ -phase domain is found starting from a temperature of 1220 °C, and the formation of precipitates start at temperatures lower than 930 °C (Figure 2.15). In the case of high-N alloy (MR2) with $N = 0.90$ %, no δ -phase domain is found and the formation of precipitates start at temperatures lower than 1070 °C (Figure 2.16).

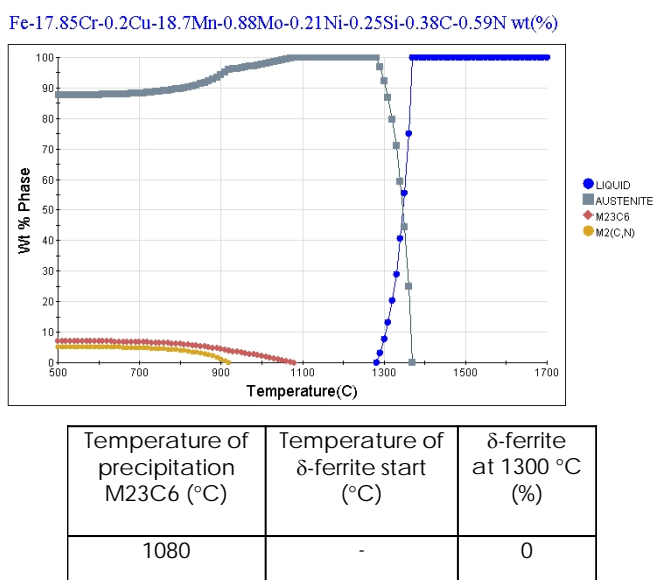


Figure 2.14. Thermodynamic calculation for CARNIT alloy (MR1/1).

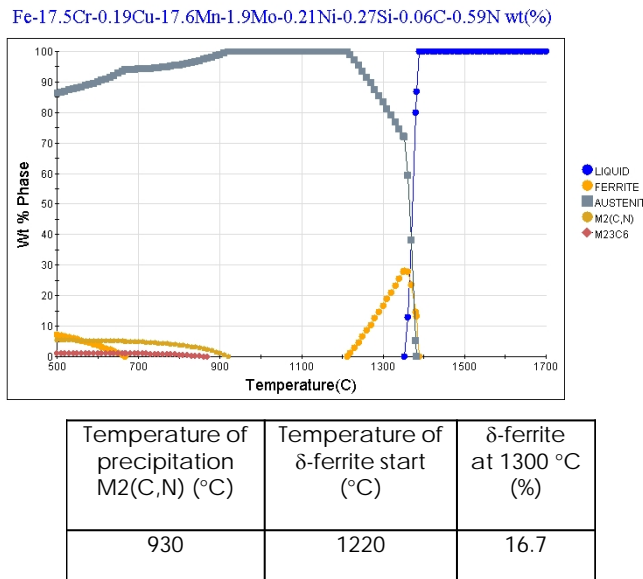


Figure 2.15. Thermodynamic calculation for medium-N alloy with N = 0.60 % (MR1/2).

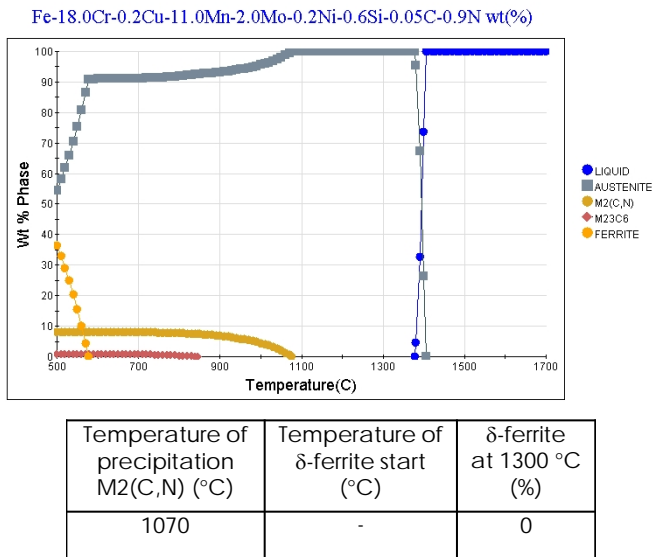


Figure 2.16. Thermodynamic calculation for high-N alloy with N = 0.90 % (MR2).

On the base of the previous considerations, a suitable set of solubilization temperature to be adopted in the heat treatment has been selected (Table 2.23). The time at the solubilization temperature should depend on the size of the sample or the component to be treated. For a thickness of 5 mm, it will be approximately 30 minutes. The cooling rate has to be set in order to avoid precipitation of nitrides, and carbides in CARNIT alloy. Water quenching can be considered a proper cooling at least for the sample treatment.

Table 2.23. Selection of solubilization temperatures.

Alloy	Composition	Solubilization temperature (°C)
MR1/1	CARNIT	1110
MR1/2	Medium N (0.60 %)	1030
MR2	High N (0.90 %)	1110

3. WP3. HNAS thermo-mechanical treatments

3.1. Hot workability tests and hot rolling/forging of test ingots (Task 3.1)

Hot workability tests

The hot workability of the High-Nitrogen Alloyed Steels produced in WP2 was assessed by Gleeble testing:

- MR1/1 - Carnit (C+N) - process: VIM - Ingot VM2947.
- MR1/2 - medium N (0.6 %) - process: VIM - Ingot VM2948.
- MR2 – high N (0.8 %) – process: VIM + PESR – Ingot PESR074.

As a reference, a 100Cr6 steel commonly used for the bearing manufacturing has also been characterised. The 100Cr6 heat was produced via Ingot Casting and then rolled to a bar of 62 mm diameter. The composition is the following: C = 0.96%; Cr = 1.44%.

Prior to perform the hot workability tests on the HNAS alloys, a preliminary forging has been carried out. This forging was necessary to create sufficient material properties for hot workability tests at Gerdau. Forging equipment was 16MN hammer. Forging start temperature was set to 1220°C, soaking time was 1.5h. The ingots VM2947 and VM2948 were forged in one forging heat to dia. 133 mm and then cooled by water immersion (Figure 3.1).



Figure 3.1. The bars after preliminary forging.

The ingot designated PESR074 (MR2, high-N) was also forged to a bar of 130-mm diameter. Following a first interruption due to surface cracks formation, the ingot was subjected to turning and grinding, and again forged. Massive cracks at both ends have been found: ultrasonic testing showed continuous cracks over the bar length.

Standard Gleeble specimens with a diameter of 10 mm and a Length of 150 mm were machined from the forged bars. In the case of the forged ingot PESR074 specimens free from defects were taken from the sound part of the bar (free from crack). The tests were carried out by a 3800 Gleeble equipment.

Two kinds of Gleeble tests, "On heating" and "On cooling tests", have been performed, following the recommendations of R.E. Bailey et al [69]. An initial series of "on heating" tests were performed to determine the optimum preheat temperature. Then, the specimens were tested "on Cooling" by being heated to the proposed furnace temperature, held at this preheat temperature for 5 minutes and cooled to various temperatures at intervals of 50°C below the preheat temperature, held for 5 seconds at the desired test temperature, and pulled in tension to fracture at the calculated strain rate.

"On heating" testing was performed in the temperature range between 850 °C and 1300 °C in 50 °C steps and at a strain rate of (0.1 s⁻¹). This strain rate was selected to closely simulate industrial forging processes. The specimens were heated to temperature with a heating rate of 5 °C/s, followed by a 5 min soaking time.

Reduction in area was utilized as a measure of hot ductility. As a rule, ductility curves display intervals of optimum deformation temperatures.

Figure 3.2 shows the reduction of area (RA) as a function of test temperature for HNAS MR1/1 and MR1/2 respectively. The most suitable temperature range to preheat the HNAS lies between the peak-ductility (PDT) and zero-ductility (ZDT) temperatures.

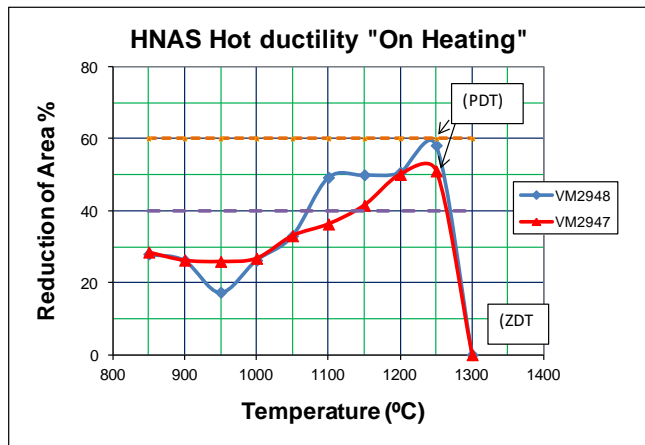


Figure 3.2. "On Heating" HNAS hot ductility curves (R.A. % versus deformation temperature).

Then, the specimens were tested "on-cooling" in the hot tensile unit by being heated to 1250°C (the proposed furnace temperature). Figure 3.3 shows the reduction of area (RA) obtained from "On cooling" tests as a function of test temperature for heats VM2947 and VM2948, respectively.

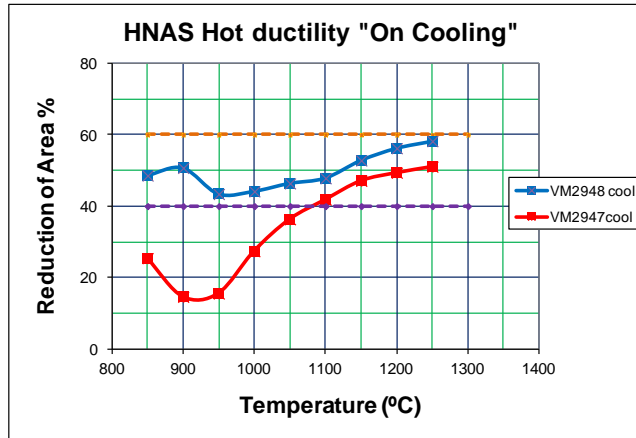


Figure 3.3. "On Cooling" HNAS hot ductility curves (R.A. % versus deformation temperature).

In general, according to Sidenor experience, the steel grades that exhibit a reduction of area higher than 60% have a good hot workability with absence of cracks. Below this value, the steel can still be forged but with moderate reductions and strain rates in order to avoid cracks.

Acceptable reductions may be applied to HNAS grades when reduction of area exceeds 60%, but lighter reductions are necessary when ductility falls below this level. Thus, in this rating system, the minimum hot working temperature is designated by the temperature at which the reduction of area falls to the 40% range. Values of less than 30 % in RA are generally considered very poor hot workability

Hot ductility curves recorded for VM2948 ("medium-N") show a progressive decrease of reduction of area with the temperature from the maximum preheat temperature. VM2948 on cooling tested specimens yielded reduction of area higher than 40% at all tested temperatures. Reduction of area values recorded for VM2947 ("Carnit C+N") on cooling specimen tests are lower than VM2948 ones. The remarkable drop in hot ductility from 1100°C, lower than 40% reduction of area, is apparent. VM2947 exhibits a trough or embrittlement ductility region at an intermediate temperature range, 850-950°C. Values of less than 20 % in RA are generally considered unacceptable for hot forming operations. An alloy whose hot tensile ductility is rated as marginal or poor; it may be hot worked, but smaller reductions and fewer passes per heating are required.

The changes in fracture behaviour for heats VM2947 and VM2948 are summarized in Figure 3.4 and Figure 3.5 respectively. It is possible to observe changes in fracture behaviour at different testing temperatures, from cup-cone fracture, semi-ductile, at 850°C, passing through a more ductile fracture at 1200-1250°C to zero-ductility fracture, brittle at 1300 °C. At lower temperatures, 850°C, microscopic fracture surface shows quasi-cleavage type with shallow dimple fracture indicative of poorer plasticity. Fracture morphology at 1250-1200°C consists of a large numbers of dimples than the one observed at lower temperature, indicative of a more ductile fracture. However, none of the tested samples show a completely dimple rupture. Heating to very high temperatures (1300°C) can cause partial melting of segregated zones at the grain boundaries, which results in brittle fracture (zero-ductility fracture).

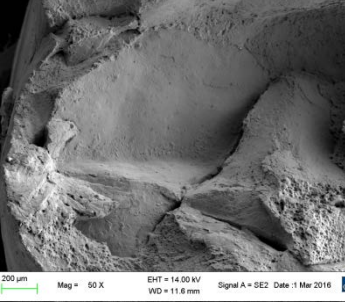
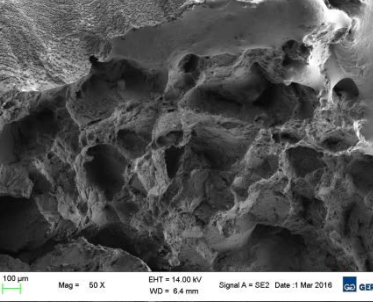
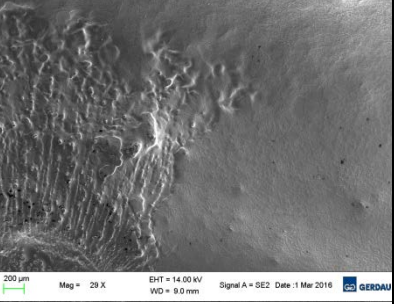
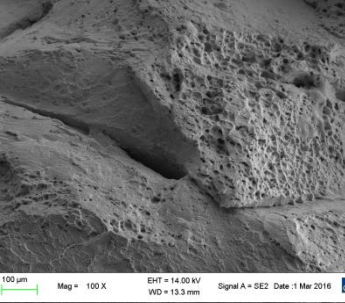
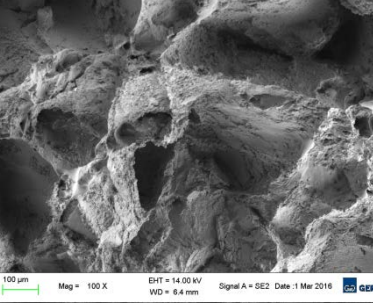
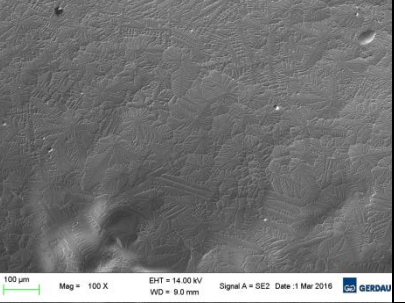
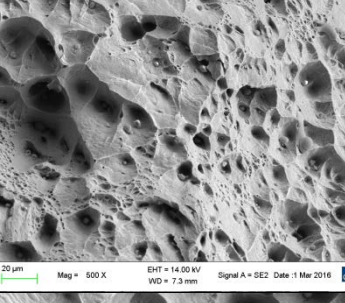
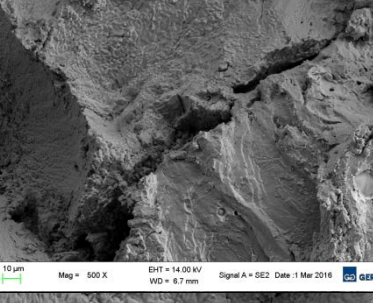
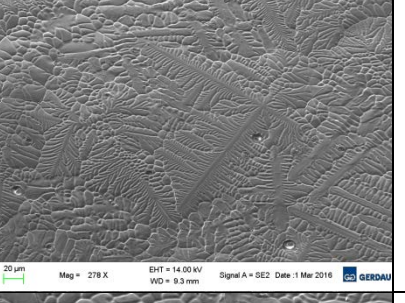
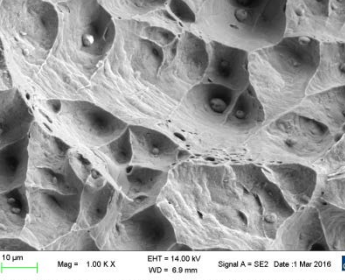
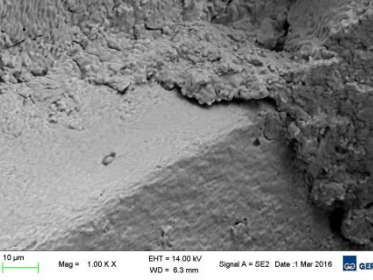
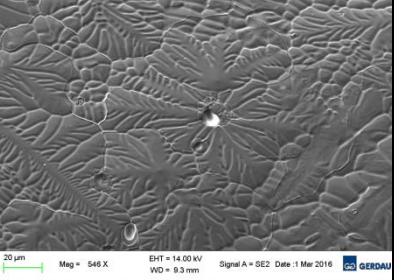
Cup-cone fracture	Semi-ductile fracture	z-d fracture	
			Broken sample
			Macroscopic fracture
			Microscopic fracture (X50)
			Microscopic fracture (X100)
			Microscopic fracture (X500)
			Microscopic fracture (X1.00K)

Figure 3.4. "Carnit C+N" VM2947 Gleble broken specimens after testing at 900°C (left,) 1250°C (centre) and 1300°C (right) temperatures.

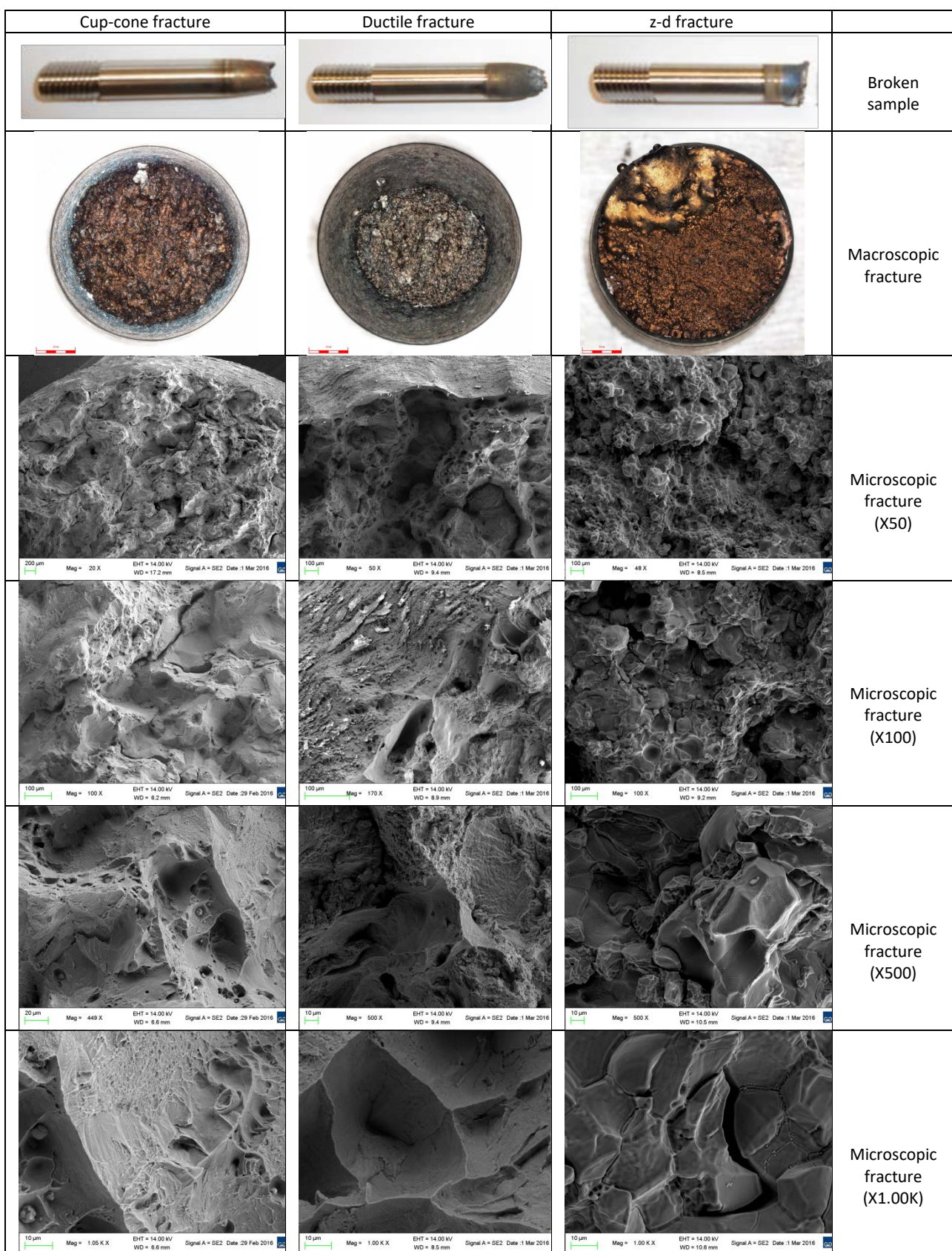


Figure 3.5. "Medium-N" VM2948 Gleeb broken specimens after testing at 900°C (left,) 1250°C (centre) and 1300°C (right) temperatures.

Figure 3.6 shows reduction of area (RA) as a function of test temperature for high-N steel. PESR074. Figure 3.7 shows some specimens after testing at different temperatures.

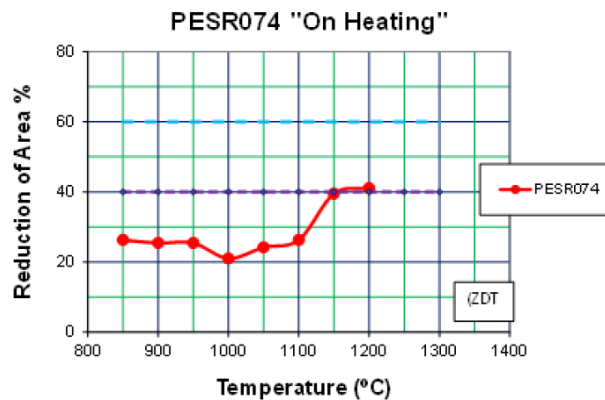


Figure 3.6. "High-N" (PESR074) steel results of Reduction of area as a function of tests temperature.



Figure 3.7. PESR074 specimens after testing at 1200 (Bottom) 1100°C (middle) and 950°C (Top) temperatures.

High-N steel PESR074 exhibits values of reduction of area in the range of 40% to 20%, meaning a very poor hot workability. This alloy when forged is very prone to the appearance of cracks and smaller reductions and fewer passes per heating are required. Gleeble tests confirm the difficulties found by ETE in forging this high-N steel grade.

The type of fracture present on High-N steel PESR074 is presented in Figure 3.8. Small areas with the presence of the typical voids responsible for the ductile fracture are observed. The rest of the surface fracture is brittle.

Two possible mechanisms of the brittle fracture are observed: transcrystalline (transgranular, cleavage) and intercrystalline (intergranular). Transgranular cracks pass along crystallographic planes through the grains. Intercrystalline fracture occurs through the grain boundaries, embrittled by segregated impurities, second phase inclusions and other defects.

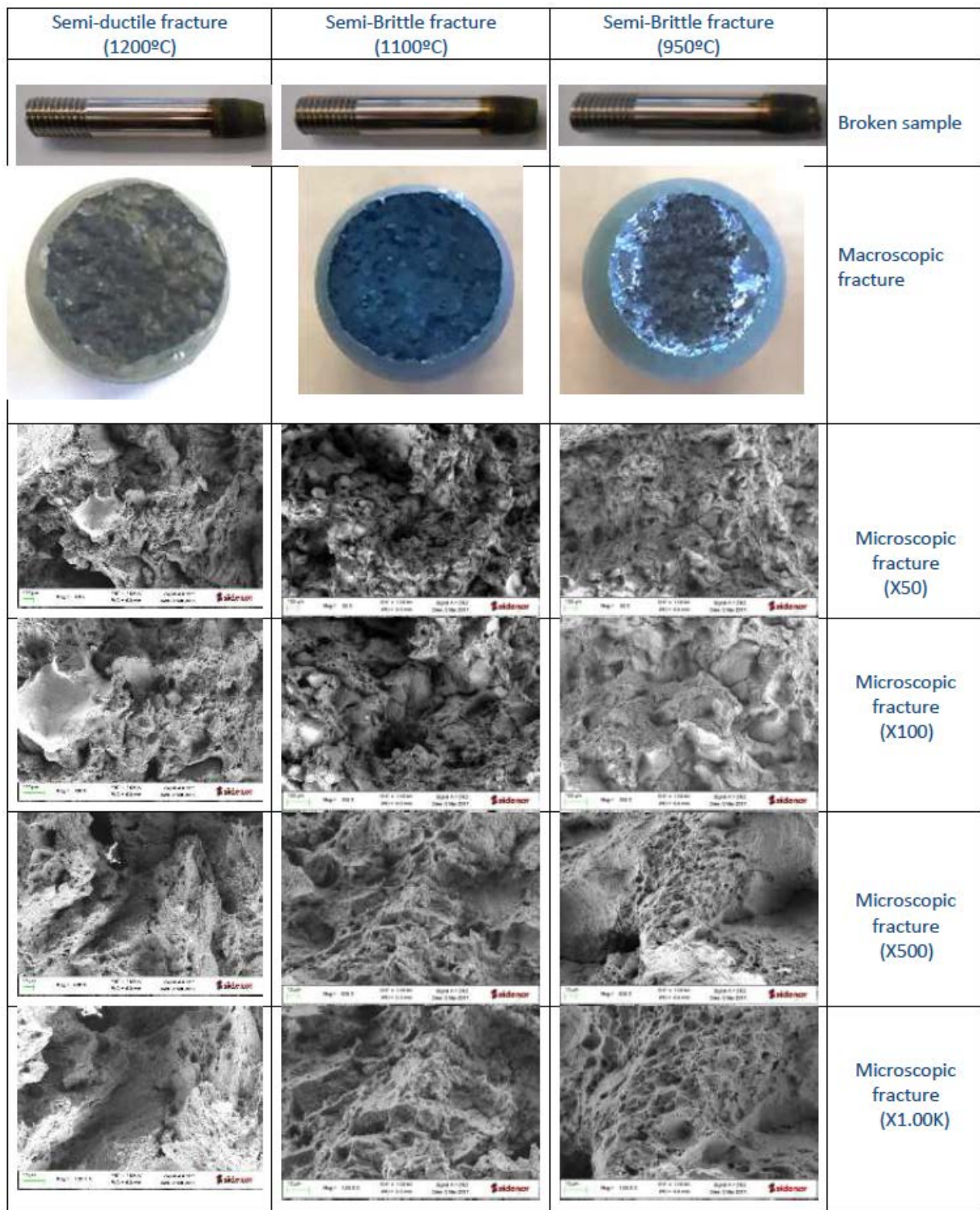


Figure 3.8. "High-N" PESR074 Gleeble broken specimens after testing at 1200°C (left) 1100°C (centre) and 950°C (right) temperatures.

The reduction of area (RA) as a function of test temperature for standard Gleeble testing conditions for the reference steel 100Cr6 is reported for comparison in Figure 3.9, while Figure 3.10 shows some specimens after testing at different temperatures. "On-heating" 100Cr6 data resulted in excellent hot ductility over a relatively wide temperature range (800-1200°C).

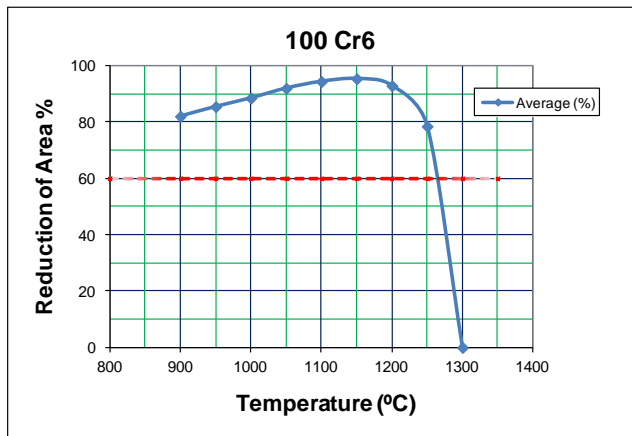


Figure 3.9. 100Cr6 Reduction of area as a function of tests temperature.



Figure 3.10. Specimens after testing at 1300 (Bottom) 1150°C (middle) and 900°C (Top) temperatures.

Hot forging of test ingots

The ingots in medium-N alloy and Carnit-type alloy have been forged at ETE on the basis of the results of the hot workability tests. In particular, two more ingots were forged with a diameter reduction of 10%:

- VM2950 - MR1/1: Carnit-type Ø143mm x 610mm
- VM2951 - MR1/2: medium N (0,6%) Ø143mm x 610mm.

Forging operation was performed at company Ossenberg GmbH in Alten (Germany). Forging equipment was 16MN hammer (Figure 3.11).



Figure 3.11. Forging and finished forged bar.

After cutting of test material at ETE for the tests devoted to the design of deep rolling tests, from bar VM2951 and VM 2950, chemical analysis and permeability check were performed.

3.2. Laboratory bulk heat treatments (Task 3.2)

The heat treatment of forged blanks is critical during the production of HN stainless steel grades to develop of a suitable microstructure to achieve the best condition and balance between mechanical characteristics, corrosion resistance and (surface) fatigue resistance of the prototype steel.

Laboratory heat treatments have been carried out in order to optimize the industrial heat treatments to get the desired structures and properties. Mainly attention has been paid to avoid the precipitation of carbides and nitrides.

In dependency to the carbon content and the tempering time, austenitic steels tend to precipitate $M_{23}C_6$ -Carbides at the grain boundaries. Through this the ductility and corrosion resistance of the material significantly declines. However, the strength properties have no mentionable change. The susceptibility for intercrystalline corrosion clearly increases. The precipitation behavior of this carbide can only be prevented through a quick quench in the critical temperature range.

In the case of the austenitic steels it should be considered, that in the temperature range of approx. 500- 900 °C and in connection with the alloy composition a precipitation of nitrides (Type Cr_2N) occurs. This nitrogen perlite identified microstructure raises significantly the susceptibility to cracking of the steel but can also support intergranular cracking. Depending on the alloy composition, the precipitation window for nitrogen perlite or other nitrides are adjusted to higher or lower temperatures.

For prevention of such brittle phases the precipitation area of the hot forming component must be followed through fairly quick quenching and/or heat treatment.

The purpose of this work is to investigate the effect of annealing heat treatment on the microstructure characteristics of the HNS.

VM2950 (MR1/1, CARNIT C+N) and VM2951 (MR1/2, medium-N N=0.60%) steel grades were used in the study. According to the thermodynamics calculations made by means of Thermocalc and JMatPro, VM2950 solubilization temperature should be in the range of 1110°C, and VM2951 solubilization temperature should be in the range of 1030°C.

The as received steel have been hot forged, direct quenched and machined to cubes of 20×20×20 mm³ section.

Five cube blanks of each steel composition numbered from 1 to 5 were subjected to laboratory heat treatment according to Table 3.1 and Table 3.2. One more cube blank were preserved to examine the as received condition.

Table 3.1. VM2950 (Carnit): heat treatment conditions.

VM2950 (MR1/1, Carnit C+N)	
Tested temperatures (°C)	1050 – 1080 – 1110 – 1120 - 1170
Heating time (hours)	2
Soaking time (hours)	2
Cooling	water

Table 3.2. VM2951 (Medium-N): heat treatment conditions.

VM2951 (MR1/2, medium-N, N = 0.60 %)	
Tested temperatures (°C)	930 – 970 – 1010 – 1050 - 1090
Heating time (hours)	2
Soaking time (hours)	2
Cooling	water

A second series of laboratory heat treatments were performed at 1180 °C and 1200 °C, heated for 2h and preserved for 2h, followed by water cooling, to check if a condition free from the second phases is achievable. Some analyses of the the microstructure have been performed just after heat treatment tests. A deeper metallurgical characterization has been carried out and presented in Task 4.1.

The VM2950 steel microstructure is reported in Figure 3.12 and Figure 3.13 in the state of as received sample – and after heat treatments. The steel as received contains porosity, likely related to N_2 formation and/or a low forging reduction. The major part of the formed precipitates have a morphology normally related to “nitrogen perlite”, Cr_2N as indicated in the rest of the micrographs. Cr_2N normally forms during cooling, however as these samples have been water quench it’s possible that they were formed during the heating process.

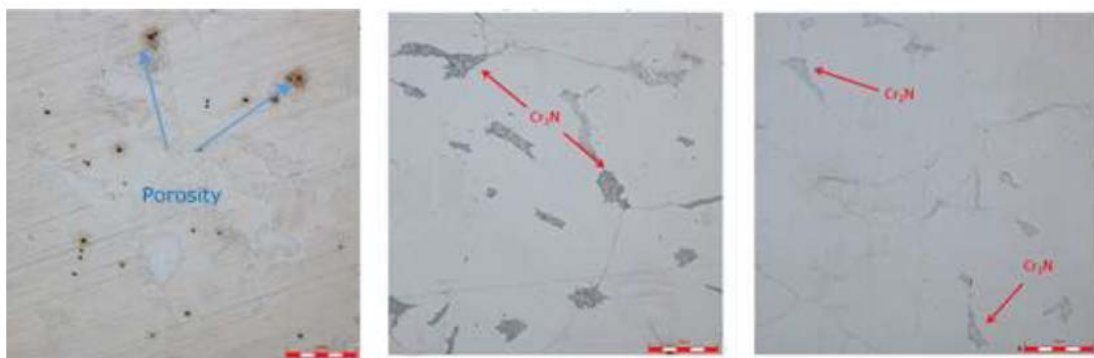


Figure 3.12. VM2950 Micrographs in the as received condition (left) and after being heated at 1050°C (centre) and 1080°C (right).



Figure 3.13. VM2950 Micrographs after being heated at 1110°C (left), 1120°C (centre) and 1040°C (right).

The VM2951 steel microstructure, as received sample and after heat treatments (Figure 3.14 and Figure 3.15) also contains porosity, likely related to N₂ formation and probably due to a low forging reduction.

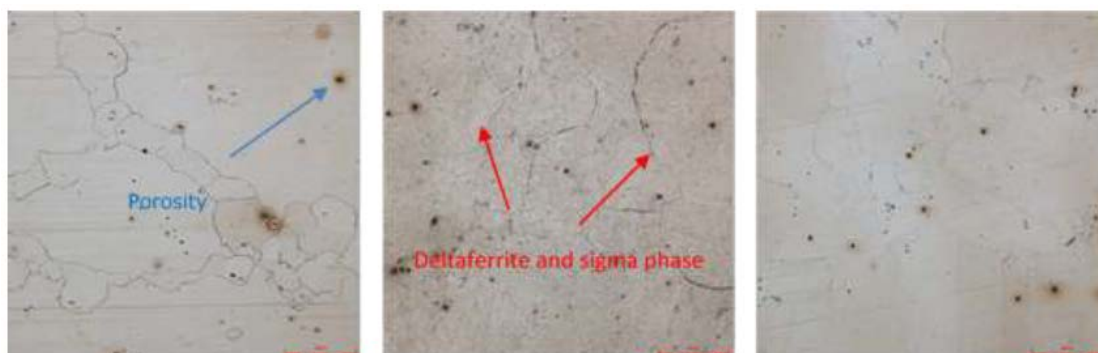


Figure 3.14. VM2951 Micrographs of the in the as received condition (left) and after being heated at 930°C (centre) and 970°C (right).



Figure 3.15. Micrographs after being heated at 1010°C (left), 1050°C (centre) and 1090°C (right).

Even the magnetic permeability measurements performed by a ferrite meter ($1.4 \mu\text{T}$) confirmed that VM2951 as cast samples have approximately a 15% of delta ferrite (Figure 3.16). This phase still remains after a solution annealing at 1030°C / 1 hour, (Figure 3.17).

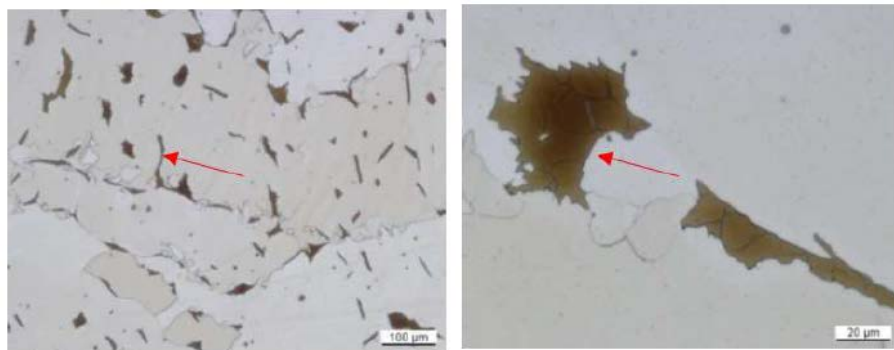


Figure 3.16. VM2951 micrographs showing the presence of delta ferrite.

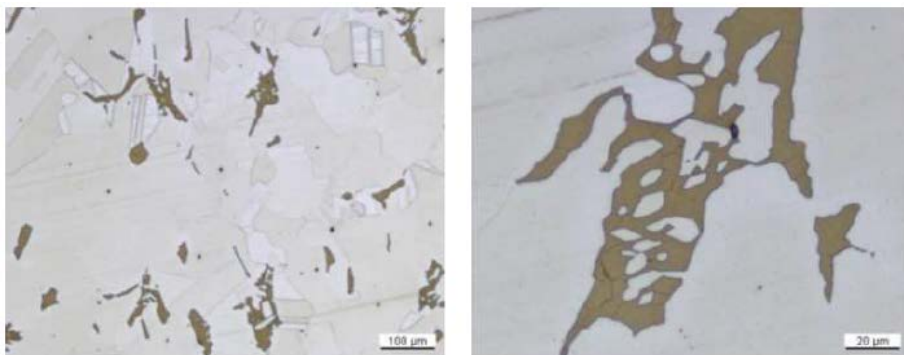


Figure 3.17. VM2951 after solution annealing at 1030°C for 1 hour showing the presence of δ ferrite.

3.3. Laboratory test rig construction (Task 3.3)

The test rig designed in the WP1 was realized. Some images are shown in Figure 3.18.



Figure 3.18. Test rig realized at ECOR.

4. WP4. HNAS prototype characterization

4.1. Metallurgical characterization of prototype (Task 4.1)

Materials, sample preparation and methods

The materials characterized in this task are those from the two heats: VM2950 (MR1/1, Carnit C+N) and VM2951 (MR1/2, Medium-N N=0.60%), heat treated according to what reported in Task 3.2. Samples for heat treatment were cubes of approximately 1.9x1.9x.1.9 cm. After heat treatment the samples were covered with surface oxide.

For cross section analysis a cut was performed at a depth of 0.5 cm from one of the oxidized cube-faces and the entire cross section was then embedded. Cross sections were prepared using standard metallographic procedures; the final polishing step was 1 μm diamond suspension. Etching was done using Kallings reagent. Cross sections were investigated with reflected light microscopy (RLM) using an Olympus CK40M equipped with a Leica DFC450C camera and SEM/EDX using a JEOL-5900 equipped with Oxford Instruments EDX. X-ray diffraction (XRD) was performed on a Bruker D8 Discover diffractometer applying a conventional symmetric Bragg-Brentano geometry.

Results – VM2951 (Medium-N) - X-Ray Diffraction

The measured diffractograms for all samples can be seen in Figure 4.1. The as-forged sample, contains δ -ferrite, see sample A marked with red line in Figure 4.1. For the heat treated samples, XRD revealed the presence of intermetallic σ -phase at low temperatures 930-1010°C while δ -ferrite (marked with α in Figure 4.1) is visible in the diffractograms at higher temperatures 1010-1090°C. At 1010°C, peaks from both σ -phase and δ -ferrite can be observed.

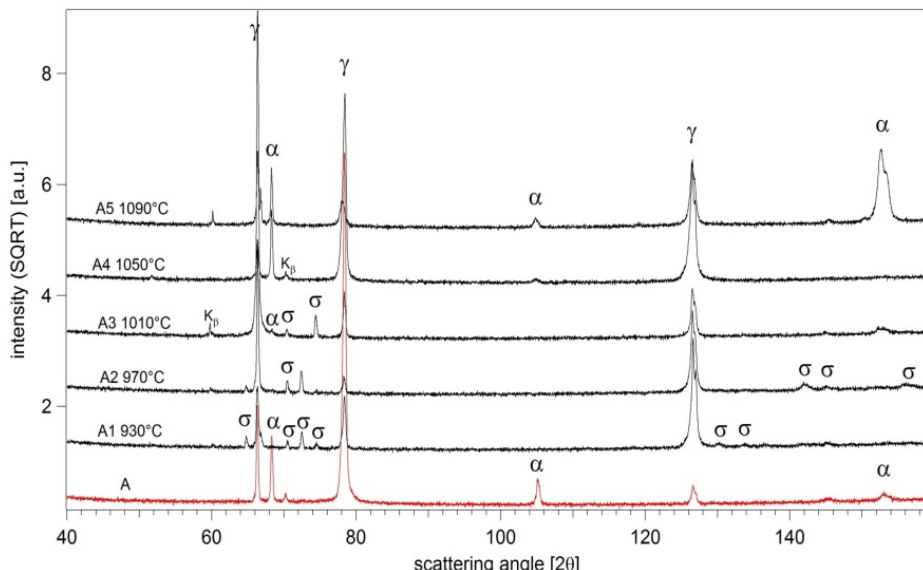


Figure 4.1. X-ray diffractograms for as-forged (red) and heat treated samples (black).

The XRD results indicate the presence of texture from the relative peak intensities with single reflections being very strong. It was not possible to align the samples in the same direction according to manufacturing and therefore it varies from sample to sample, which reflections are most pronounced.

Results – VM2951 (Medium-N) - RLM and SEM

RLM of the as forged sample in polished condition reveals the presence of a significant amount of inclusions/porosities as can be seen in Figure 4.2. The presence of δ -ferrite (as confirmed by XRD) is also visible in polished condition but becomes clearly visible after light etching, cf. Figure 4.3.

SEM/EDX composition measurements reveal that the δ -ferrite is enriched in Cr and Mo compared to the matrix, see Figure 4.4 and Table 4.1.

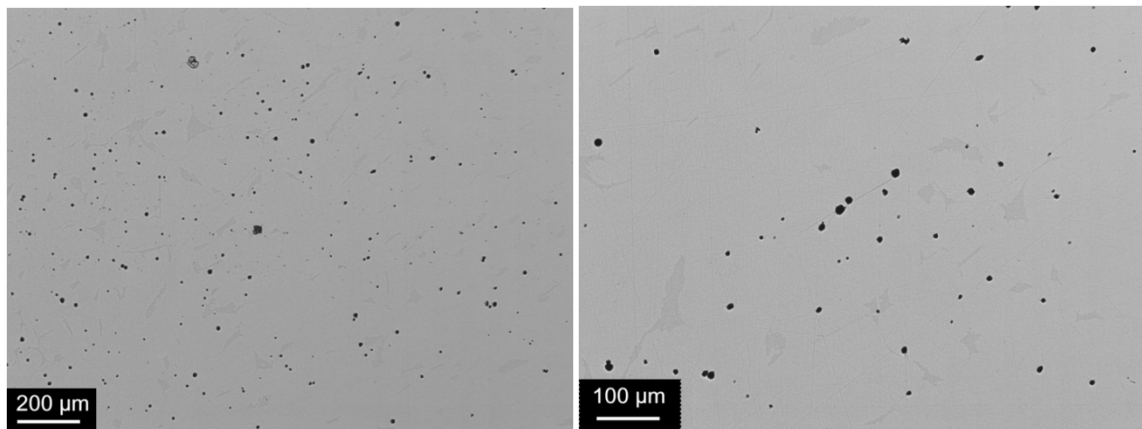


Figure 4.2. RLM of the reference sample in polished condition.

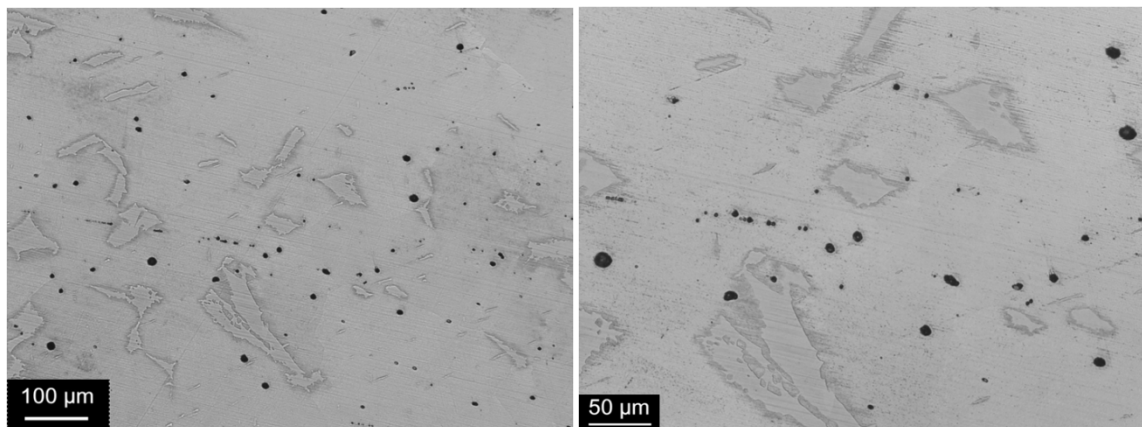


Figure 4.3. RLM of the reference sample in etched condition.

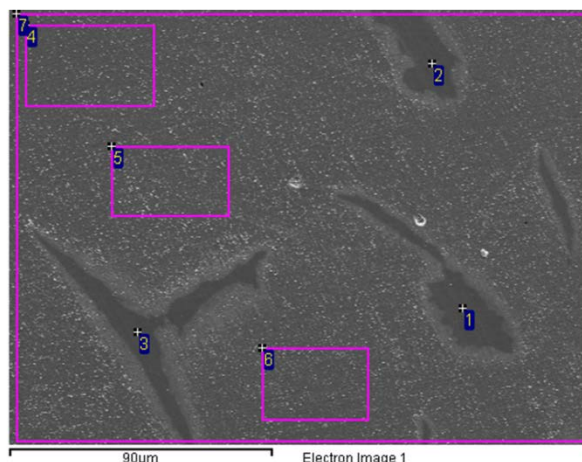


Figure 4.4. SEM/SE image of the as forged sample in etched condition. Positions of the EDX composition measurements reported in Table 4.1 are marked.

Table 4.1: SEM/EDX measurements from locations marked in Figure 4.4; all results in wt%.

Measurement	Si	Cr	Mn	Fe	Mo
1:δ-ferrite	0.6	20.8	15.7	58.7	4.3
2:δ-ferrite	0.6	21.0	15.7	58.3	4.5
3:δ-ferrite	0.5	20.9	15.7	58.2	4.7
4:Matrix	0.4	18.7	19.1	59.6	2.2
5:Matrix	0.5	18.6	18.8	59.9	2.1
6:Matrix	0.3	18.5	18.6	60.3	2.3
7:Area	0.5	18.9	18.6	59.6	2.5

In the samples heat treated at the lower temperatures, σ -phase (as confirmed by XRD) could be seen using RLM, cfr. Figure 4.5. In the SEM using backscatter contrast, σ -phase is clearly visible as bright regions due to larger average atomic number. The σ -phase seemed to form at positions where ferrite had been located prior to heat treatment. SEM/EDX revealed that the σ -phase is enriched in Cr and Mo, see Figure 4.7 and Table 4.2. In the intermetallic regions, two different composition sets could be found according to EDX measurements, see measurements 1-3 in Table 4.2 as well as from the backscatter images, where brighter regions inside the intermetallic regions can be identified corresponding to regions with higher Mo content.

Table 4.2: SEM/EDX measurements from locations marked in Figure 4.7; all results in wt%.

Measurement	Si	Cr	Mn	Fe	Mo
1: σ	0.7	25.2	14.2	53.3	6.6
2: σ	0.7	25.2	14.2	53.1	6.8
3: σ	0.6	21.3	15.2	50.0	12.9
4:Matrix	0.4	18.3	18.2	61.0	2.1
5:Matrix	0.4	18.2	18.2	61.0	2.3
6:Matrix	0.4	18.4	17.7	61.2	2.4

At the high end of the investigated temperature region the σ -phase no longer formed and only δ -ferrite could be found. SEM images of the sample heat treated at 1050 °C are shown in Figure 4.8. The positions where δ -ferrite is present is revealed in the SE image, whereas the BSE composition contrast is not large enough to clearly reveal the positions of the δ -ferrite. Composition measurements are similar to the results obtained for the as forged condition; see Figure 4.9 and Table 4.3.

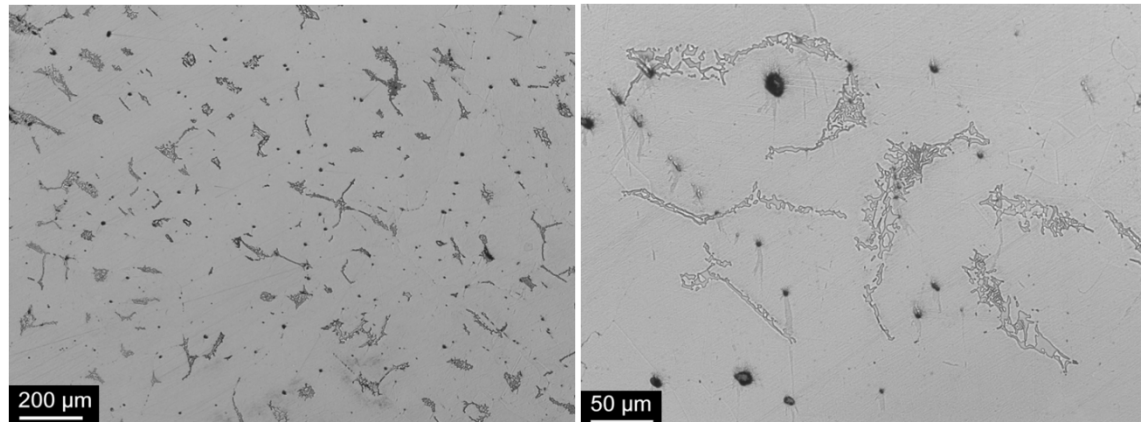


Figure 4.5. RLM of σ -phase in the sample heat treated at 930 °C; imaged in etched condition.

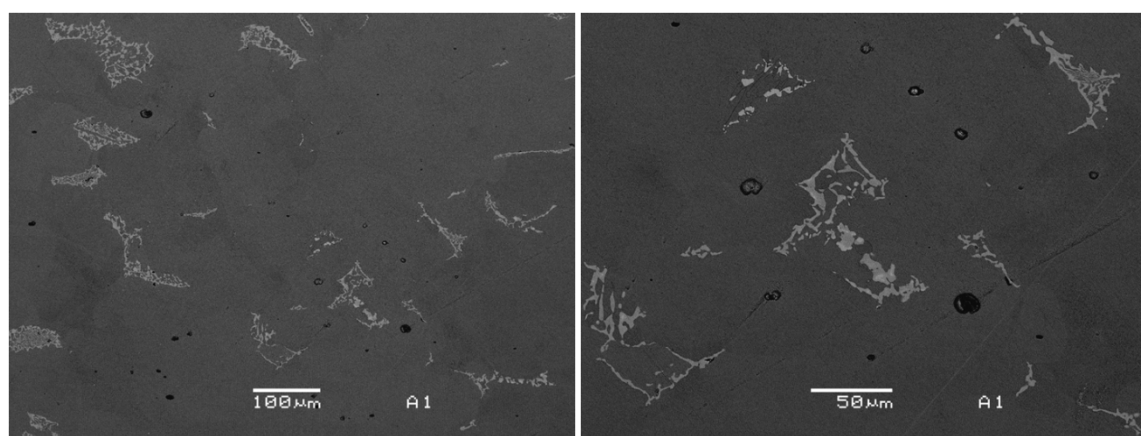


Figure 4.6. SEM/BSE of σ -phase in the sample heat treated at 930 °C; imaged in etched condition.

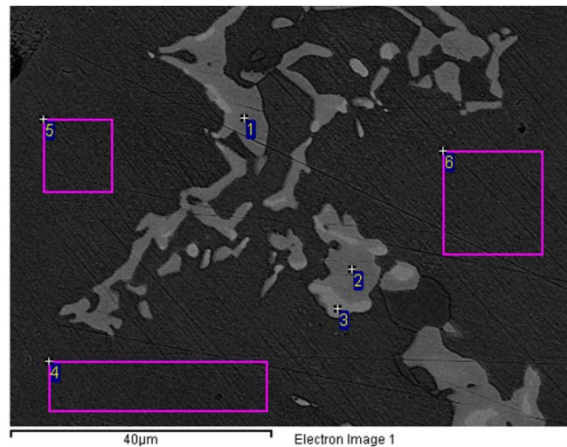


Figure 4.7. SEM/BSE image of the sample heat treated at 930°C. Positions of the EDX composition measurements reported in Table 4.2 are marked.

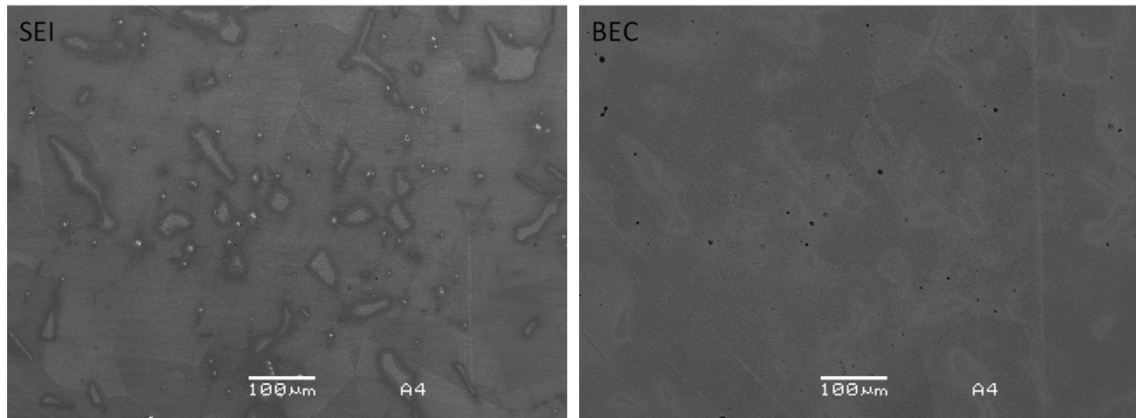


Figure 4.8. SEM images of δ-ferrite in the sample heat treated at 1050°C; imaged in etched condition.

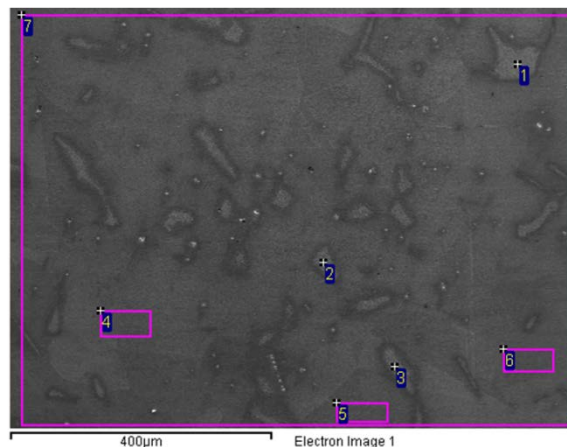


Figure 4.9 SEM/SE image of the sample heat treated at 1050°C in etched condition. Positions of the EDX composition measurements reported in Table 4.3 are marked.

Table 4.3: SEM/EDX measurements from locations marked in Figure 4.9 all results in wt%.

Measurement	Si	Cr	Mn	Fe	Mo
1:σ	0.5	21.1	15.5	58.4	4.5
2:σ	0.4	21.4	15.4	58.4	4.3
3:σ	0.5	21.4	15.3	58.3	4.6
4:Matrix	0.4	19.2	19.3	58.9	2.2
5:Matrix	0.3	18.3	18.8	60.5	2.1
6:Matrix	0.4	19.0	18.8	59.5	2.3
7:Area	0.4	18.9	18.8	59.7	2.2

Results – VM2950 (Carnit C+N) – X-Ray Diffraction

XRD revealed only presence of austenite; all observed minor peaks could be explained as K_β peaks resulting from very intense K_α peaks. Also here, the XRD results indicate the presence of strong texture from manufacturing. At the highest temperature (1140°C) there are clear indications of grain growth as it appears as though there are only one or very few grains diffracting (poor grain statistics). The measured diffractograms are presented in Figure 4.10.

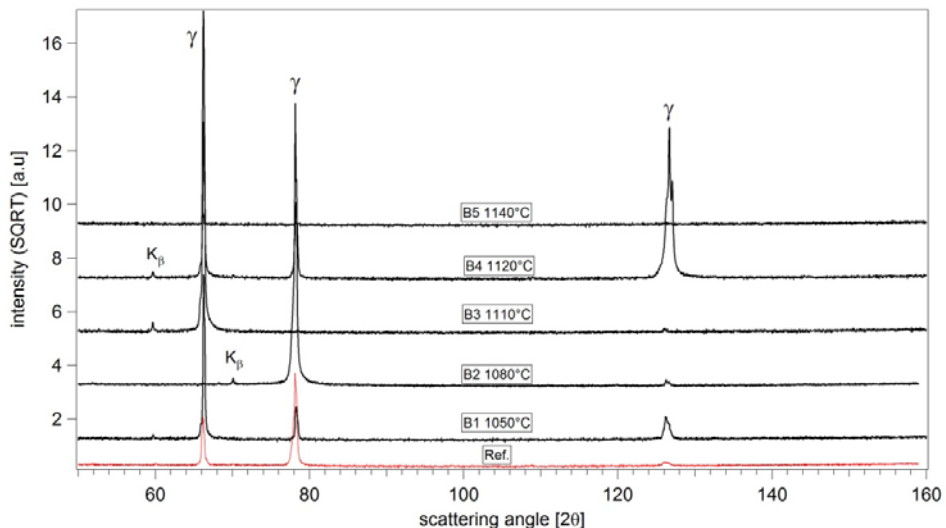


Figure 4.10. X-ray diffractograms for as-forged (red) and heat treated samples (black).

Results – VM2950 (Carnit C+N) – RLM and SEM

RLM of the as forged sample in polished condition revealed the presence of a number of inclusions and porosities present as dark areas. Their distribution indicates that their formation could be related to grain boundaries present during manufacturing, cfr. Figure 4.11. In lightly etched condition, chains of fine grains are revealed decorating the boundaries of the larger grains.

In Figure 4.13, RLM images at low magnification of the heat treated samples can be seen. Precipitation is occurring in and from the grain-boundaries of the fine grains. The precipitation seems to become coarser with temperature up until 1120°C , at higher temperatures the fine grains have disappeared, presumably due to growth of the larger grains. This is in agreement with the XRD measurements where significant grain growth was implied at 1140°C . At 1140°C there is still significant etching associated with grain boundaries, but at 1180°C it becomes much less pronounced and at 1200°C , there is no etching effect and no visible precipitation.

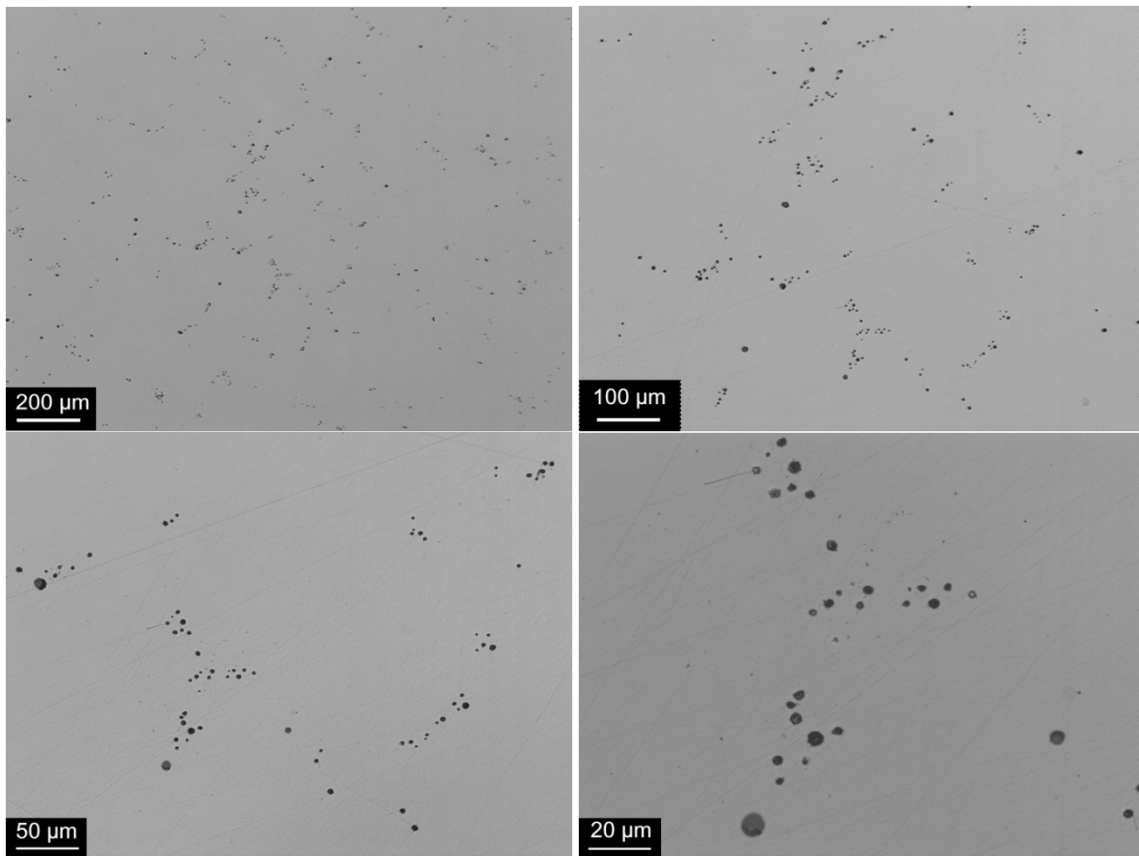


Figure 4.11. RLM of as forged polished sample at four different magnifications. Inclusions and porosities are visible.

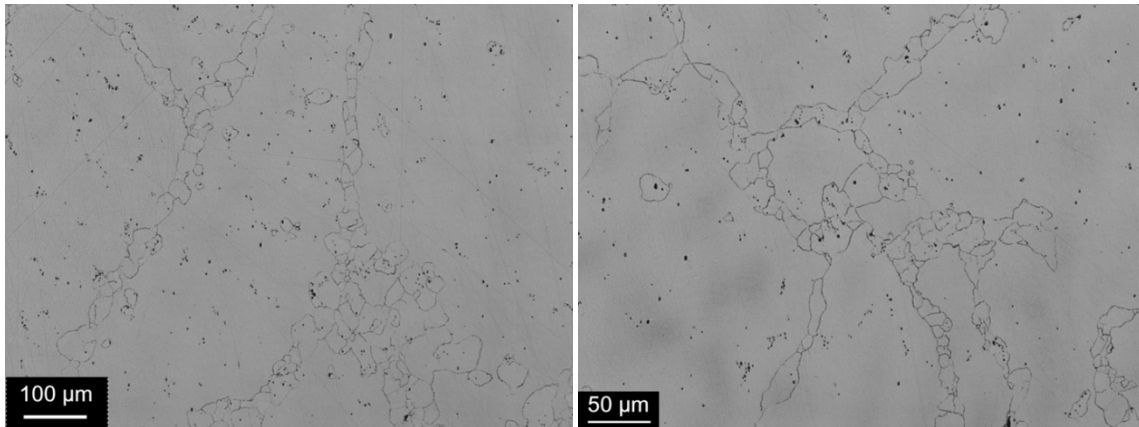


Figure 4.12. RLM of as forged, lightly etched sample. In lightly etched condition, revealing chains of fine grains decorating the boundaries of the larger grains.

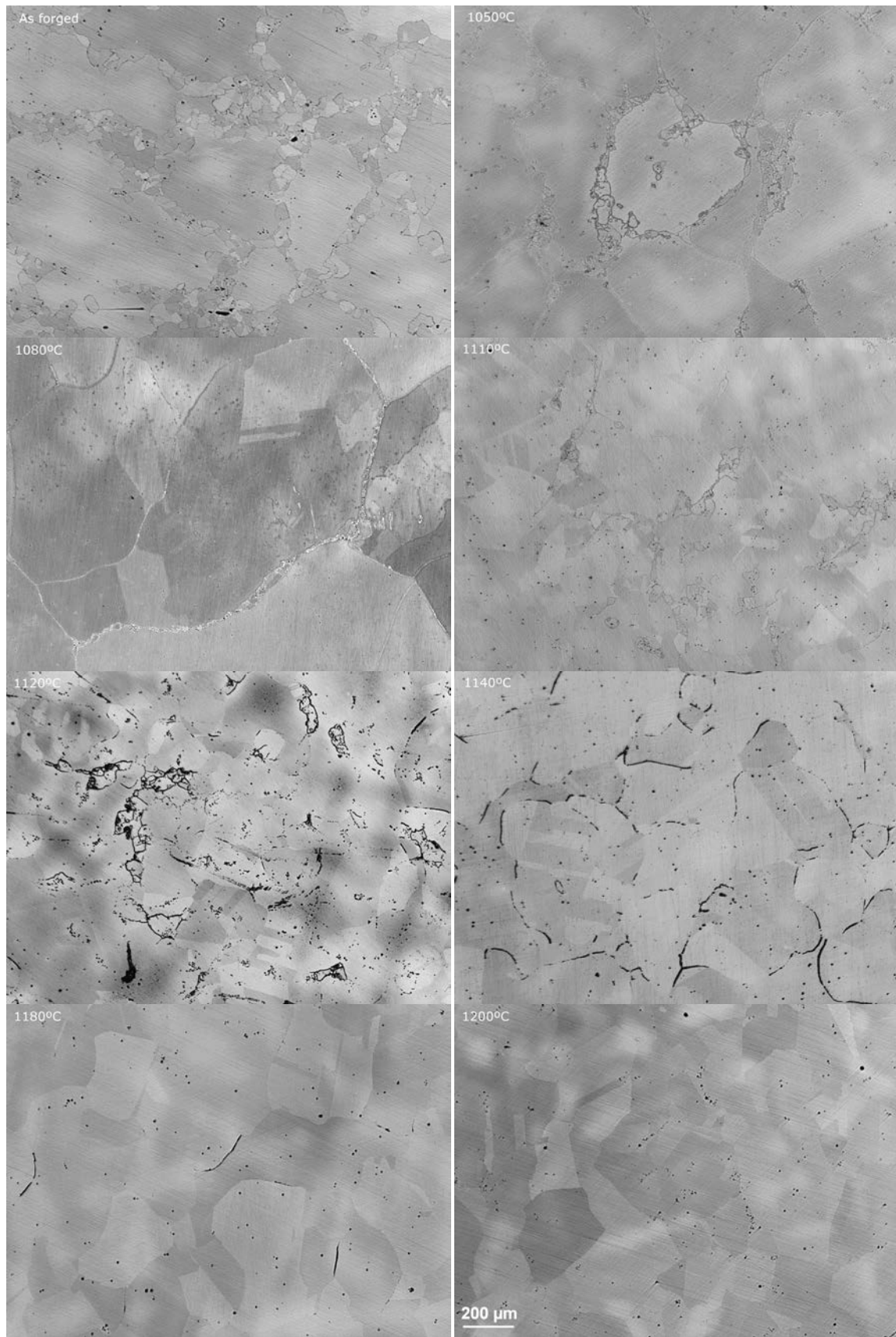


Figure 4.13. RLM of heat treated samples in etched condition.

Figure 4.14 and Figure 4.15 shows the precipitates at higher magnification and it is clear that the precipitation is taking place at grain boundaries and it is especially visible in the fine grained areas. The

precipitates are Cr-rich, but they are too small to get an exact composition measurement from SEM/EDX, see EDX mapping in Figure 4.16.

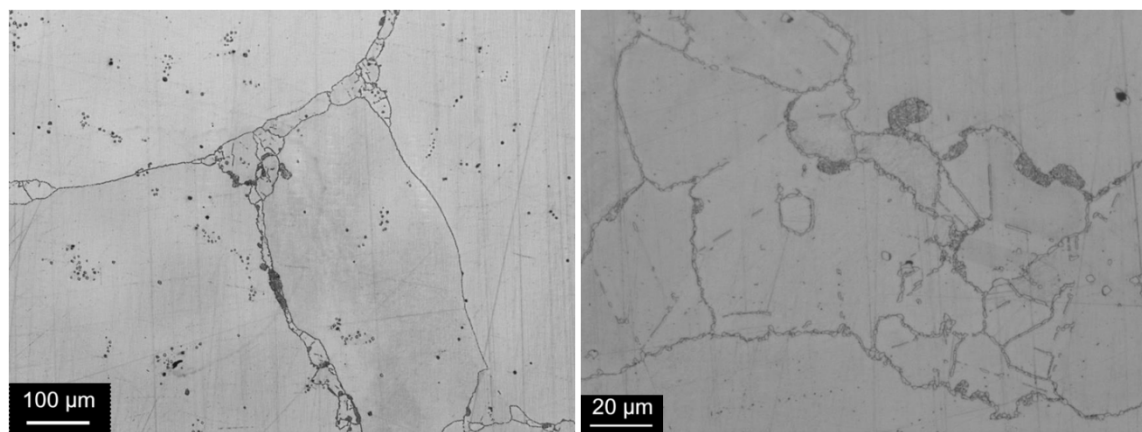


Figure 4.14: RLM of sample heat treated at 1050°C.

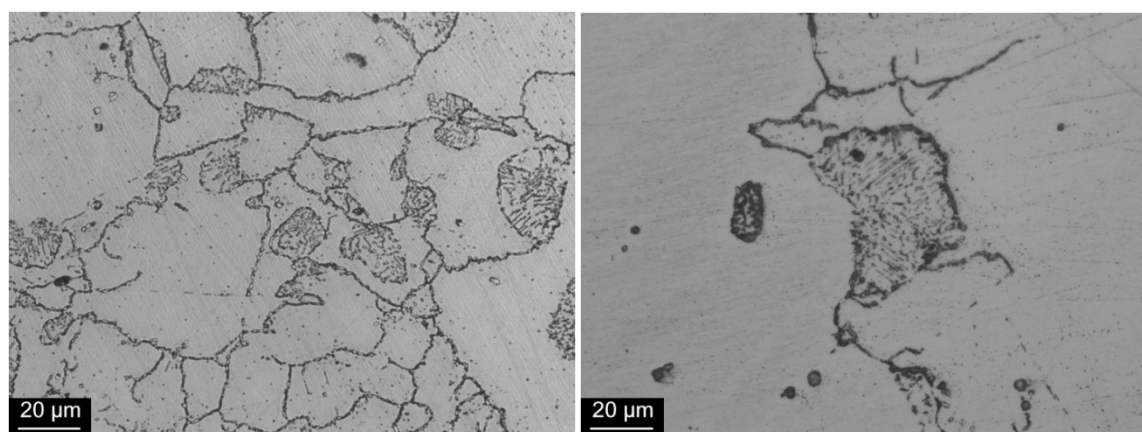


Figure 4.15 RLM of samples heat treated at: left) 1110°C, right) 1120°C.

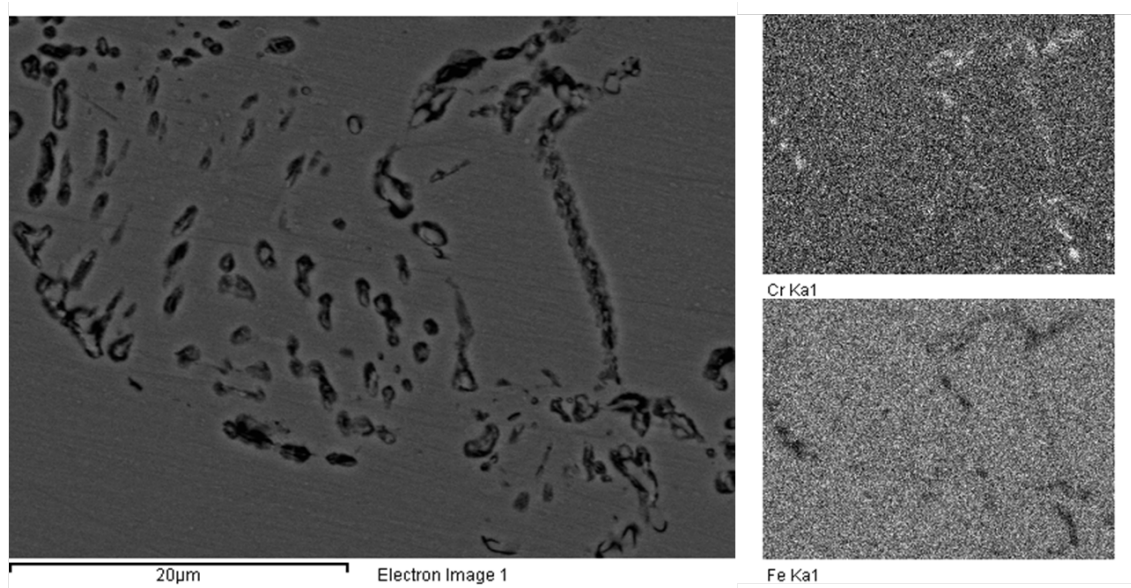


Figure 4.16: SEM/SE image and EDX elemental mapping showing the distribution of Cr and Fe from the sample heat treated at 1120°C.

Discussion – VM2951 (Medium-N)

The results show that there was no available heat treatment window where a complete FCC region could be obtained. This is despite that thermodynamic equilibrium calculations indicate that such a region should exist in the investigated temperature range; see Figure 4.17. Only at much lower nitrogen contents, i.e. below 0.4 wt% it is possible to find a region where σ -phase and δ -ferrite can coexist. Possible losses of nitrogen could be through the formation of gas-porosities as observed in Figure 4.2 or through surface loss during heat treatment, which was performed in an atmosphere that did not maintain high nitrogen pressure. Indeed loss of nitrogen/carbon at the surface could be observed through a changed microstructure, however it is also worth considering possible kinetic effects that can affect the heat treatment response.

In the as forged condition a rather large fraction of δ -ferrite is present, see Figure 4.3. The δ -ferrite is enriched in Cr and Mo; see Table 4.1. The same chemical elements partition into σ -phase, which could facilitate a quick transformation of δ -ferrite into σ -phase. Since Cr and Mo are already partitioned into the δ -ferrite and Mn (and likely also N and C) partition into the austenite, the transformation could be driven by the composition of the ferrite and not of the overall average composition. If this is the case, σ -phase formation is a result of the material being inhomogeneous prior to heat treatment and the chosen heat treatment times are not sufficiently long to achieve homogenization (re-dissolve the formed σ -phase).

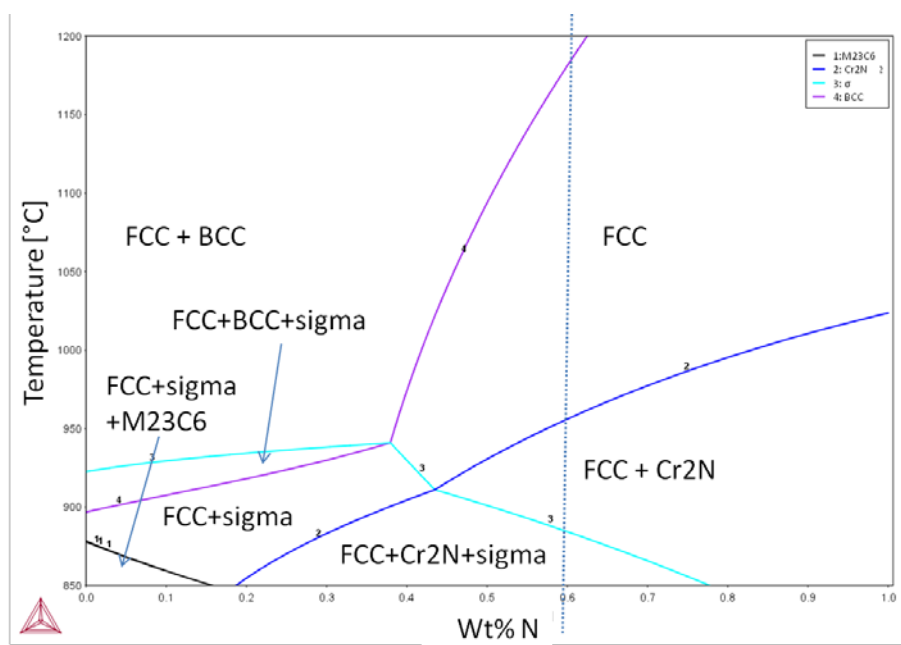


Figure 4.17. Thermo-calc diagram showing calculated phase stability areas for the VM2951 alloy. The intended nitrogen content of the alloy is marked with a blue dotted line.

Discussion – VM2950 (Carnit C+N)

The RLM images of the as forged sample revealed spherical porosities with a distribution that indicates that they are lying along boundaries that were present during a stage of the manufacturing. It is likely that at least some of these porosities are due to N_2 gas formation. Chains of fine grains could also be identified in the as forged sample, these fine grains are likely the result of dynamic recrystallization during the forging procedure.

During heat treatment precipitation would take place in and from the grain boundaries of the fine grains. The morphology of the precipitation is commensurate with that normally related to “nitrogen pearlite”; see e.g. [82-84]. Formation of nitrogen pearlite is usually considered as detrimental for the mechanical properties of high nitrogen steels [82]. The nitrogen pearlite consists of FCC+Cr₂N, which forms through a discontinuous precipitation reaction $FCC(N) \rightarrow FCC + Cr_2N$. Full confirmation that precipitates are indeed Cr₂N will require TEM, since the precipitate volume fraction is below the detection limit for XRD. Nitrogen pearlite normally forms during cooling when the cooling rate is below a critical rate allowing time for the precipitation to occur; the cooling rate is dependent on the steel composition. According to the studies reported in [83], the VM2950 heat should have a critical cooling time $t_{c10/7}$ (cooling time for 1000-700 °C) in the range of 5-20 seconds. For the present study, taking the small dimensions of test samples into

consideration, this critical cooling time should be reachable using water cooling; nevertheless precipitation was observed, especially related to the fine grained structure.

A thermodynamic equilibrium calculation done for the VM2950 composition shows that the predicted structure for all heat treatments are fully FCC with the 1050°C lying close to the phase line for M₂₃C₆ formation. For the sample heat treated at 1200°C no precipitation was observed and the structure appeared fully austenitic. With lower temperature, increased precipitation was observed affiliated with grain boundaries and at 1120°C and below especially at the grain boundaries of the fine grains.

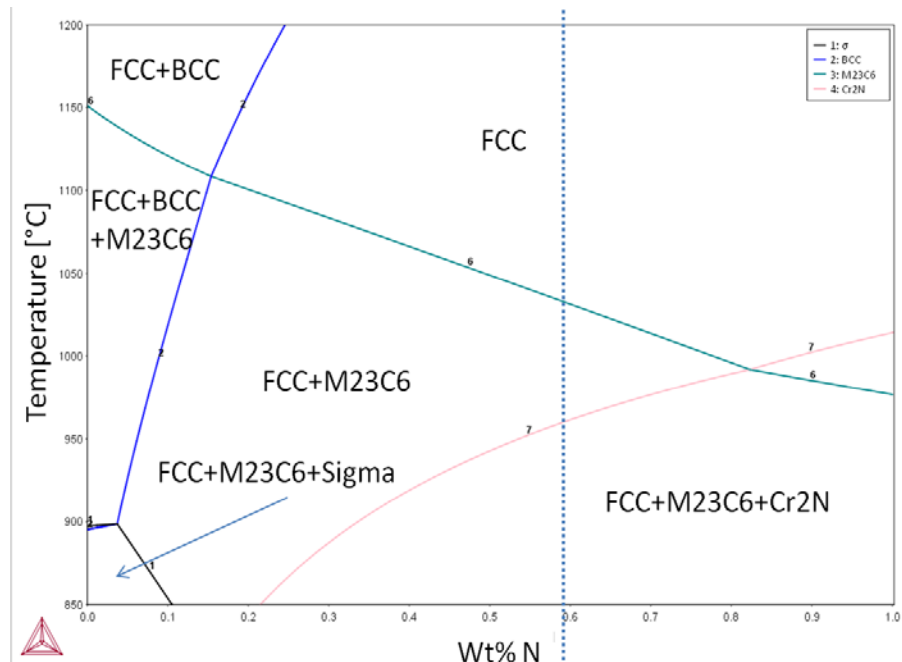


Figure 4.18. Thermo-calc diagram showing calculated phase stability areas for the VM2950 alloy. The intended nitrogen content of the alloy is marked with a blue dotted line.

Conclusions – VM2951 (Medium-N)

- The as forged sample contained porosity, likely related to N₂ formation
- The as forged sample contained δ-ferrite that is enriched in Cr and Mo
- For samples heat treated at 930°C and 970°C, the δ-ferrite decomposed and intermetallic σ-phase also rich in Cr and Mo formed instead
- For the sample heat treated at 1010°C both σ-phase and δ-ferrite is found
- For samples heat treated at 1050°C and 1090°C δ-ferrite was found, XRD indicates that the amount of δ-ferrite after heat treatment at 1090°C is increased in comparison to the as forged condition
- XRD indicates that the material has a clear texture

In conclusion, there was none of the heat treatments that resulted in a fully austenitic structure, in the low temperature region intermetallic was formed and at higher temperatures, δ-ferrite was present.

The behavior may be coupled to a too low nitrogen level and therefore not sufficient stabilizing effect of nitrogen on FCC but there may also be a kinetic factor influencing especially the σ-phase formation. σ-phase formation may be accelerated and (meta)stabilized through the presence of δ-ferrite at the beginning of the heat treatment.

Conclusions – VM2950 (Carnit C+N)

- The as forged sample contained porosity, likely related to N₂ formation
- The as forged sample has likely experienced dynamic recrystallization during forging resulting in variance in grain-size
- XRD indicates that the material VM2950 material also has a clear texture
- LOM and SEM show precipitation that is taking place in and from the grain-boundaries of the fine grains. No precipitation was revealed from XRD, likely due to low volume fraction.
- The major part of the formed precipitates have a morphology normally related to "nitrogen pearlite", FCC+Cr₂N, which forms through a discontinuous precipitation reaction FCC(N) -> FCC+Cr₂N

- Precipitation decreased at higher temperature commensurate with the disappearance of the fine grained zones due to grain growth.

4.2. Design of deep rolling process of prototype HNAS (Task 4.2)

Background

Deep rolling combines three main physical effects in cold work hardening of the surface. Through a hydraulically pumping system, a pressure is transferred to a rolling element, roller, which passes the pressure onto the component surface. The rolling element produces an elastic and plastic deformation of the surface layer, which is controlled by the rolling force and results in cold work hardening and residual compressive stresses. Furthermore, the treatment has a smoothing effect on the surface. This depends strongly on the previous surface quality of the component and the finishing quality of the rolling body.

All of the three effects: the cold work hardening of the surface, the introducing of residual compressive stresses and the reduction of the roughness, have a positive effect on the fatigue strength of components.

The main use of deep rolling lies on rotational symmetrical components (Figure 4.19).

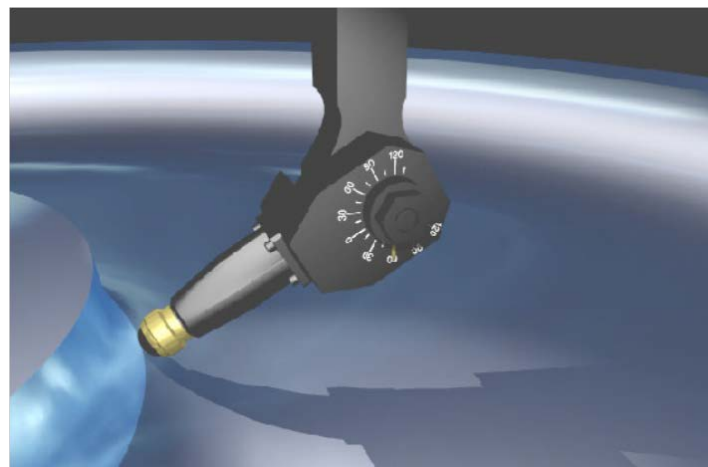


Figure 4.19. Deep rolling applied to a turbine wheel.

To obtain the best results in a component, is necessary to optimize the process variables: rolling force, ball diameter, rotational speed, feed rate, initial roughness, etc. The contact force is the main parameter, controlling the different residual compressive stresses induced through deep rolling. The pressure and the lining of the tooling control this force. To evaluate the effectiveness of the surface treatment is necessary to measure the stress distribution, and depth of the treated layer, the final roughness and the hardness increase. The Laboratory optimization trial should reproduce as much as possible the geometry and the steel properties of the component to be treated in order to get the best results on prototype when treated at industrial scale. Deep rolling is a proven process to enhance fatigue strength of dynamically loaded components, like turbine wheel, valves for engines, crank shafts, etc, see Figure 4.20 and Figure 4.21.



Figure 4.20 . Deep rolling of valves for diesel engines.

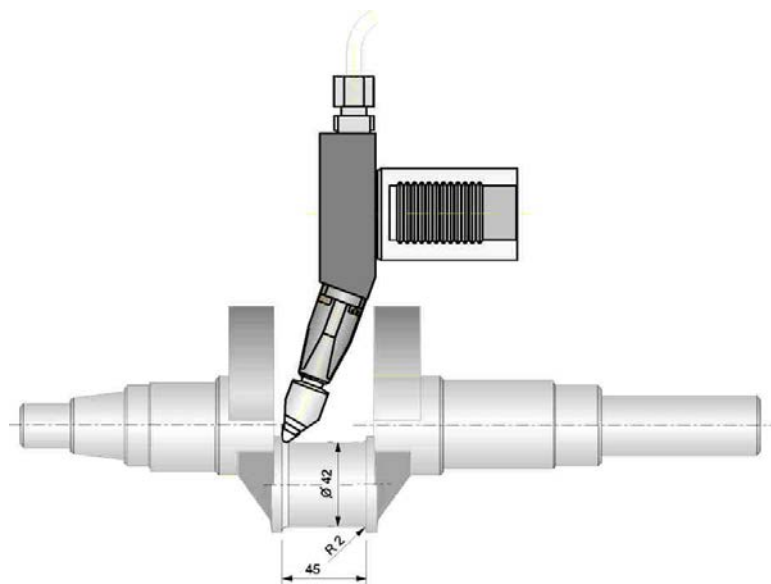


Figure 4.21. Crank Shaft deep rolling.

The main use of deep rolling lies on rotational symmetrical components. We don't have problem to apply the process to rotational external geometries. Deep rolling equipment is integrated into CNC-lathes with tool drive in the turret and to CNC milling centers.

The process limits are founded when a small radius has to be treated or when the geometry of the piece is too sharp to access to the internal areas with the tool, remember that smaller ball diameter is 6 mm. For instance, the force of the ball must be perpendicular to the workpiece, with a deviation of $\pm 30^\circ$, for a 6 mm ball, and $\pm 35^\circ$ for a 13 mm one.

For each application is necessary to know the geometry of the component to be treated to forecast operational problems and to perform some operational capacity trials.

Materials

The two High Nitrogen Steel grades: VM2950 (MR1/1, CARNIT C+N) and VM2951 (MR1/2, medium-N N=0.60%) were used in this tests. VM2950 (MR1/1, CARNIT C+N) samples shown in Figure 4.22 were machined to 130 mm diameter. Similarly, samples of VM2951 (MR1/2, medium-N N=0.60%) were machined to perform the second series of tests as shown in Figure 4.23.

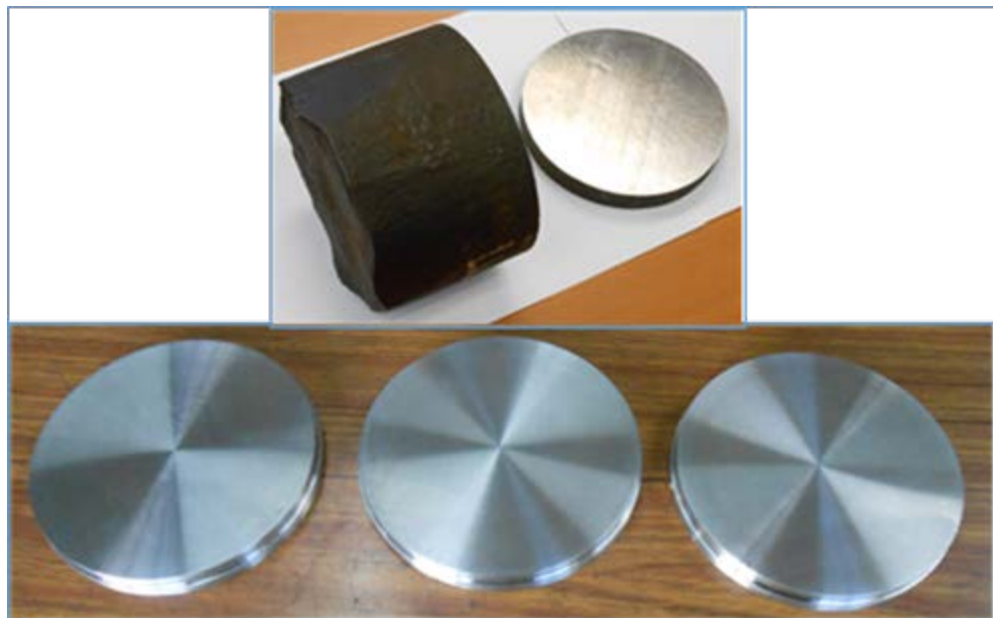


Figure 4.22. Machined samples (Bottom) from forged bar (top) VM2950 for deep rolling tests.

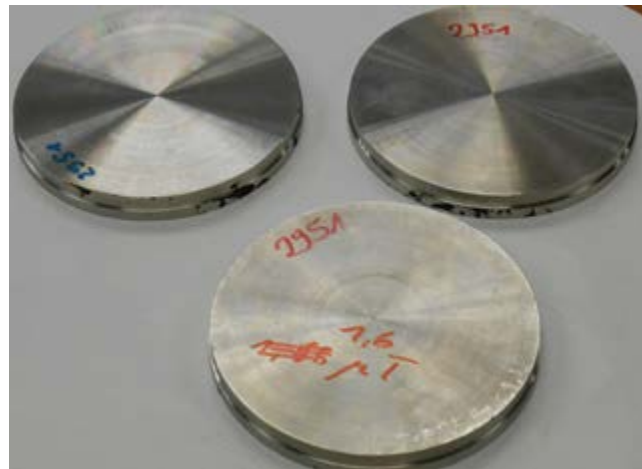


Figure 4.23. Machined samples from forged bar VM2951 employed for deep rolling tests.

All samples were mechanically grinded using SiC different grit sizes. Once polished the samples were tested to determine its initial hardness and roughness average values, see Table 4.4.

Table 4.4. Initial roughness and hardness average values of the samples.

	VM2950 (MR1/1, CARNIT C+N)	VM2951 (MR1/2, medium-N N=0.60%)
Initial Roughness	Ra 0.40-0.62 μm	Ra 0.32-0.44 μm
Initial Hardness	HRV 300-384	HRV 280-320

Lathe-Milling machine

An ECOROLL deep rolling equipment and tools with integrated sensors and a software for process monitoring were employed during trials.

DR tools are used on conventional lathe-milling machine tool. In this way, samples were directly deep rolled on this machine.

Due to the small size of the samples in comparison with the dimensions of the lathe chuck, a specific clamping device was made to support the samples during deep rolling process (Figure 4.24 and Figure 4.25).



Figure 4.24. Lathe-Milling Machine where the Deep Rolling trials were performed.



Figure 4.25. Lathe chuck used to support a wide variety of work pieces shapes with the four jaws and detail of the system employed to clamp the deep dolling samples.

Deep rolling trials

During the first DR trials, the influence of roll pressure (contact force) on the surface hardness was studied. In order to get the maximum pressure at the contact area, the maximum ball diameter available at SIDENOR at that moment was employed and the angle between the tool to the axis of rotation of the bearing samples was keep at 90 degrees. DR parameters employed during tests are presented in Table 4.5. The effect of these parameters on the residual stress state, surface roughness and hardness evolution were examined.

Table 4.5. Deep Rolling Process Parameters – first campaign.

Deep Rolling Process Parameters	
Pressure (bars)	200-400-600
Ball diameter (mm)	19
Speed (rpm)	60
Angle (°)	90

Deep rolling was applied to a circular portion of the disk enclosed by two diameters, from 10 to 80 mm, as shown in Figure 4.26.



Figure 4.26. Area of the samples where DR is applied.

The second DR trials were carried out during first semester of 2017. These second series of deep rolling (DR) tests were performed on VM2951(MR1/2, medium-N N=0.60%), to determine the effect of DR pressure and tool angle on the surface hardness.

Three different contact pressures (200, 400 and 600 bars) and two different tool angles (90 and 110°) were employed during tests. DR parameters employed during the second trials are presented in Table 4.6.

Table 4.6. Deep Rolling Process Parameters – second campaign.

Pressure (bars)	200-400-600
Ball diameter (mm)	19
Speed (rpm)	60
Angle (°)	90 and 110

Three different sectors can be observed in the samples after testing, see Figure 4.27. The first sector, was deep rolled with a 90° tool angle, comprises the portion of the disk enclosed by 5 mm and 45 mm diameters and an arc of 360°. The second sector, was deep rolled with a 110° tool angle, comprises the portion of the disk enclosed by 50 mm and 100 mm diameters. The outer sector of the sample was kept in the as polished condition without applying DR. The diameter of the samples is 130 mm.

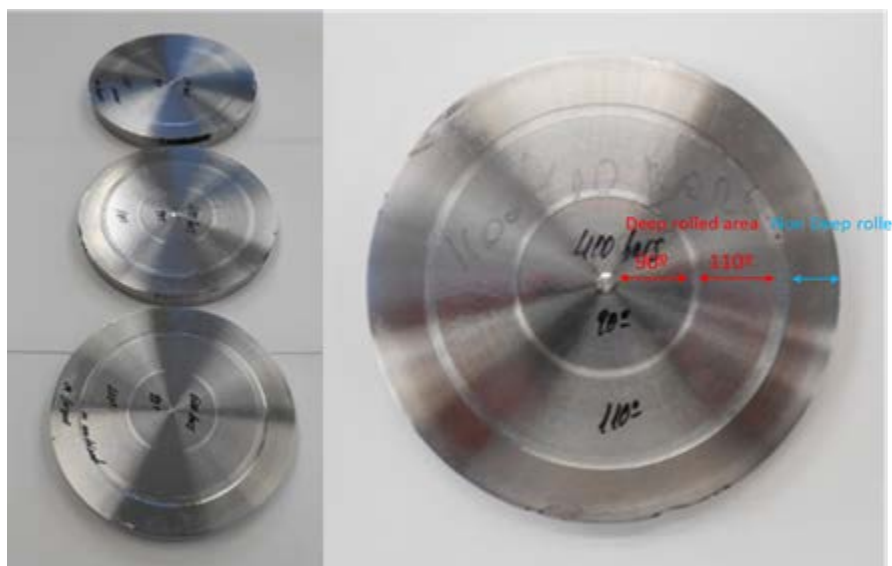


Figure 4.27. Visual aspect of the samples after DR with different tool angles and pressures.

Surface roughness

The arithmetic mean roughness (R_a) and the average maximum height of the profile (R_z) were used to represent the surface roughness. An average of five roughness measurements was taken for each sample.

Important surface smoothening is observed on VM2950 (MR1/1, CARNIT C+N) samples after DR, see Table 4.7. Initial roughness ranges from 0.40 to 0.62 R_a . Final roughness ranges from 0.12 to 0.16 R_a . Deep Rolled areas are 3-5 times smoother than non-treated ones.

Table 4.7. Roughness measurements (μm) before (left) and after (right) deep rolling. First campaign.

Pressure	R _a	R _z
200 bars	0,40	2,74
400 bars	0,54	3,32
600 bars	0,62	3,86
Average	0,52	3,31

Pressure	R _a	R _z
200 bars	0,14	0,66
400 bars	0,16	0,86
600 bars	0,12	0,60
Average	0,14	0,71

In the second campaign of trials (VM 2951, MR1/2, medium-N N=0.60%), roughness was ranging from 0.32 to 0.44 Ra in non-deep rolled areas. Again, an important surface smoothening is observed after deep rolling: final roughness after DR ranges from 0.10 to 0.14 Ra. Deep Rolled areas are 3-4 times smoother than non-treated ones (Table 4.8). The DR tool angle and the pressure do not have a significant effect on the surface smoothening.

Table 4.8. Roughness measurements (μm) before (left) and after (right) deep rolling. Second campaign.

reF VM2951			VM2951 After Deep Rolling					
Pressure	R _a	R _z	Tool Angle	90°		110°		
Pressure	R _a	R _z	Pressure	R _a	R _z	Pressure	R _a	R _z
200 bars	0,44	3,35	200 bars	0,10	0,76	0,12	1,02	
400 bars	0,32	2,90	400 bars	0,14	0,84	0,12	0,78	
600 bars	0,38	3,10	600 bars	0,10	0,80	0,10	0,84	
Average	0,38	3,12	Average	0,11	0,80	0,11	0,88	

Surface hardness

The surface hardness evolution in the zones deep rolled at different pressures – for steel VM 2950 / Carnit - are shown in Figure 4.28. Deep rolling has led to an important surface hardness increase. The maximum average hardness was obtained with a pressure of 600 bar. Hardness increased from 384 to 495 HV10. The average hardness increment changes from 25 to 40 % depending on its initial value. In general, the higher the initial hardness of the steel the smaller seems to be the influence of the deep rolling on the hardness surface increment.

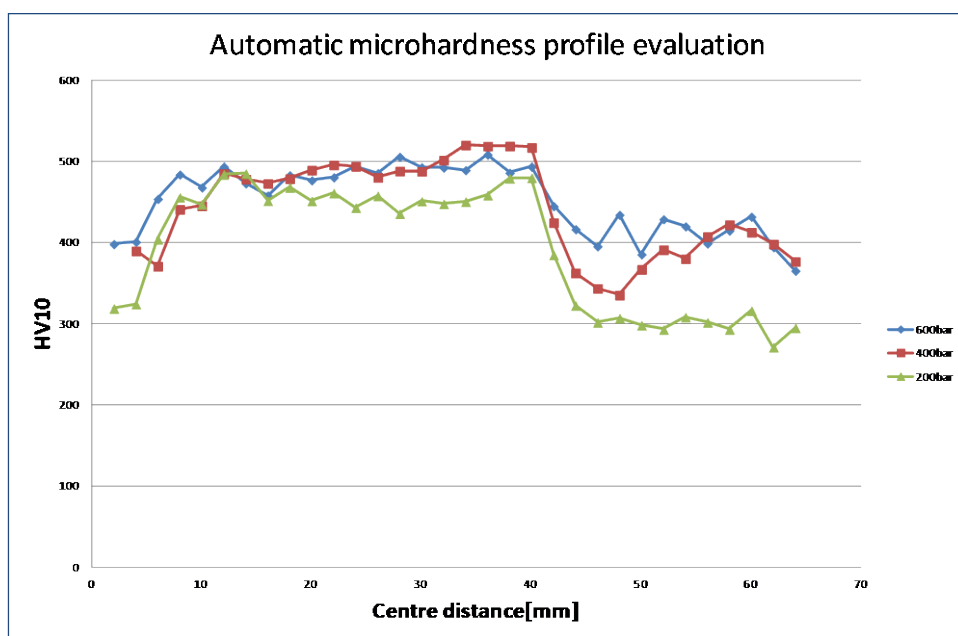


Figure 4.28. Surface hardness evaluation for Carnit steel. Green: 200 bar, red: 400 bar, blue: 600 bar.

The influence of the DR tool angle on the hardness increment – investigated on the samples VM2951 / medium N steel - is shown in Figure 4.29. Three different contact pressures (200, 400 and 600 bars) and two different tool angles (90 and 110°) were employed during tests. Each line (color) corresponds to a different pressure. DR produces an important increase in hardness with regard to their initial hardness values.

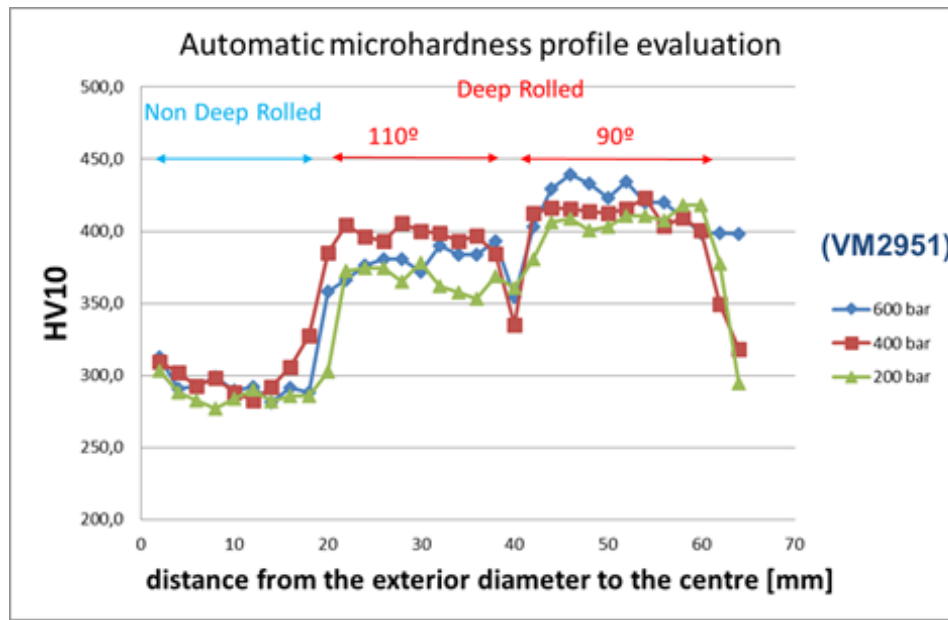


Figure 4.29. Surface hardness evaluation after DR with different tool angles.

The results presented in Figure 4.29 are summarized in Table 4.9. This table shows the average hardness values and the hardness increase measured on the high nitrogen steel grade sample surface after deep rolling. The edge and core points have not been taken into account.

With a tool angle of 90°, the average hardness values of the deep rolled area for 600, 400 and 200 bars are 419, 406 and 403 HV10, which represent increments of 43 %, 36.5 and 40 % respectively with regard to its initial values.

With a 110° toll angle, the average hardness values of the deep rolled area for 600, 400 and 200 bars are considerably lower: 378, 395 and 360 HV10 which represent increments of 29%, 32 and 25% respectively with regard to its initial values.

Table 4.9. Influence of deep rolling parameters on the surface hardness and hardness increase of VM2951(MR1/2, medium-N N=0.60%).

	Tool angle			
	90°		110°	
Pressure (bar)	Average hardness (HV10)	Hardness increase (%)	Average hardness (HV10)	Hardness increase (%)
600	419	43.0%	378	29.0%
400	406	36.5%	395	32.8%
200	403	39.9%	360	25.3%

With a proper selection of DR parameters a maximum of 43% hardness increase have been obtained for VM2951 high nitrogen stainless steel, from 293 to 419 HV10. The tool angle of 90° gave the highest surface hardness in comparison to the other angle. The maximum hardness value is obtained with a pressure of 600 bars. The maximum average hardness increment varies from 25 to 43% after DR for VM2951 high nitrogen stainless steel, depending on its initial hardness value. The higher the initial hardness of the steel grade the smaller the influence of the DR on the hardness surface increment after deep rolling.

Hardness profiles and Residual stress

Some hardness profile (HV) have been performed on some of the samples, in order to understand the depth affected by the deep rolling operation.

The hardness evolution for the Carnit sample subjected to deep rolling (first campaign) with a tool angle of 90° and pressure 200 bar is reported in Figure 4.30. A reduction up to about 2/3 of the surface hardness is occurring in the first 250 µm of depth.

On the same samples, an evaluation of the residual stresses has been attempted by means of XRD technique. To that purpose, the following conditions has been applied:

- Diffractometer in Bragg-Brentano geometry.
- Cu K_α radiation.
- (311) reflection.
- Measurements performed on surfaces parallel to the disc surface.
- In-depth analysis has been carried out by serial sectioning at 90, 235 and 390 µm.
- The method of $\sin^2\psi$ has been used with $-30^\circ \leq \psi \leq +30^\circ$ step 15°.

The reference lattice spacing of the (311) reflection, d_0 , has been measured on a specimen of the same material subjected to an annealing treatment to fully relax the internal stresses. For any depth level the lattice spacing associated to the angle ψ , d_ψ , has been determined. From the plot of $\Delta d/d_0$ versus $\sin^2\psi$ the slope m is calculated:

$$\frac{d_\psi - d_0}{d_0} = a + m \cdot \sin^2 \psi$$

Finally, it is converted into stress:

$$\sigma = \frac{E}{1+\nu} \cdot m$$

where E is the Young modulus and ν the Poisson ratio.

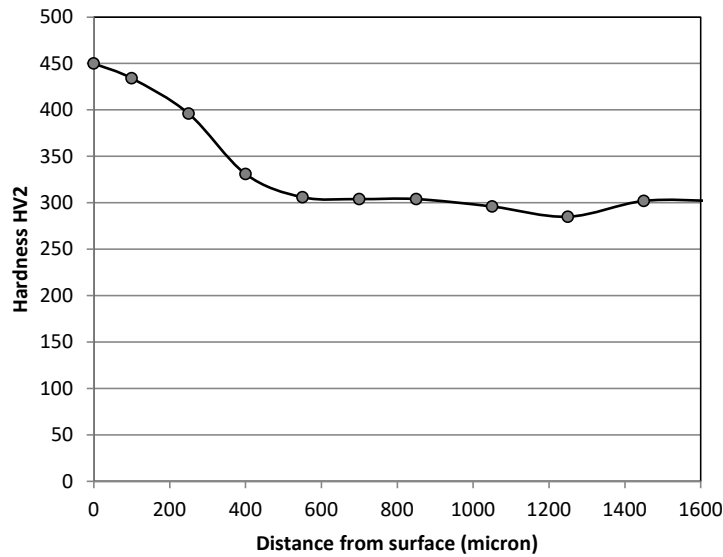


Figure 4.30. Hardness profile, Carnit steel, Tool angle 90°, p = 200 bar.

The average residual stress measured on the specimen as a function of the distance from surface is shown in Figure 4.31. The evolution of the residual stress in the region investigated is quite consistent with that of the hardness.

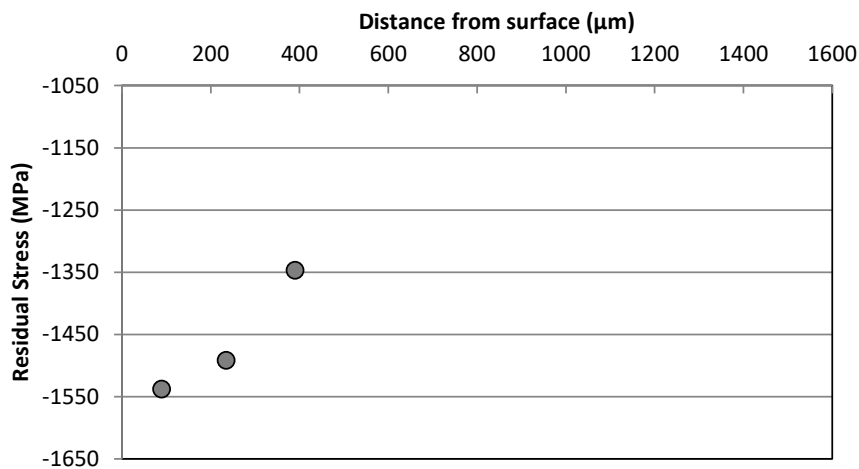


Figure 4.31. Evolution of residual stress.

Annealing tests on deep rolled samples

A number of new tests have been carried out to evaluate the effect of a “tempering” at temperatures up to 600 °C to VM2951 samples (medium-N steel) subject to different deep rolling surface treatments. The interest in that investigation was motivated by the consideration that an intermediate tempering after the Deep Rolling, could produce a hardness gain, due to blocking of dislocations by nitrogen that diffuses to the dislocations.

As-Deep Rolled samples were annealed at four different temperatures, 300, 400, 500 and 600 °C. The heating time and the soaking time employed were one hour respectively. After soaking, the samples were cooled in air. After each heat treatment the surface hardness profiles of the specimens were evaluated. Figure 4.32 and Figure 4.33 show the hardness profile evaluation after DR and annealing at different temperatures ranging from 300°C to 600°C. Tempering from 300°C up to 500°C on Deep Rolled samples have a small influence on hardness on deep rolled samples. The hardness only slightly increase at 500° annealing, with an average increment lower than 8 HV10. Afterwards, at 600°C a reduction in hardness is observed.

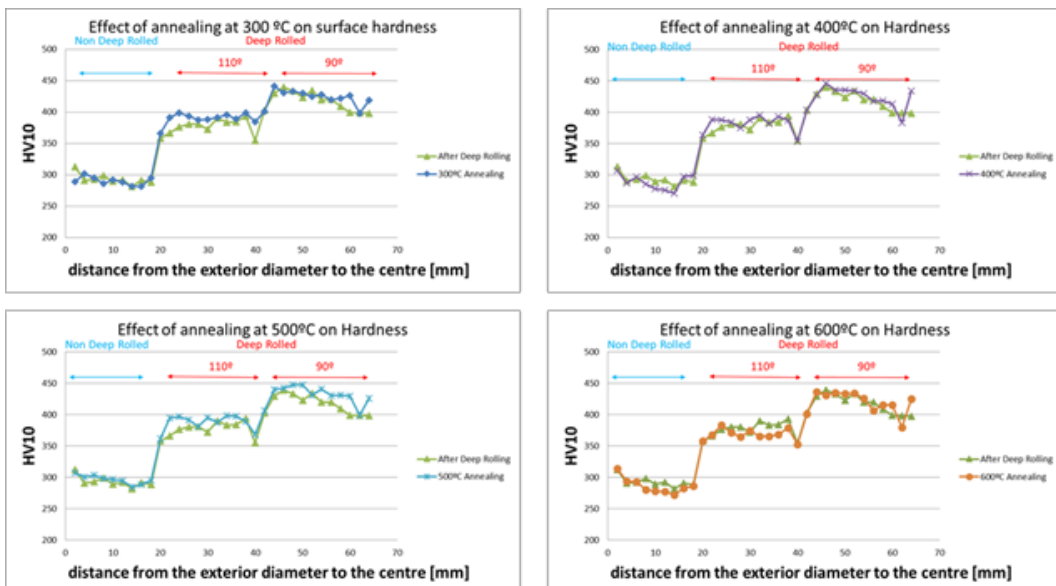


Figure 4.32. Hardness profile evaluation after Deep Rolling and annealing at different temperatures.

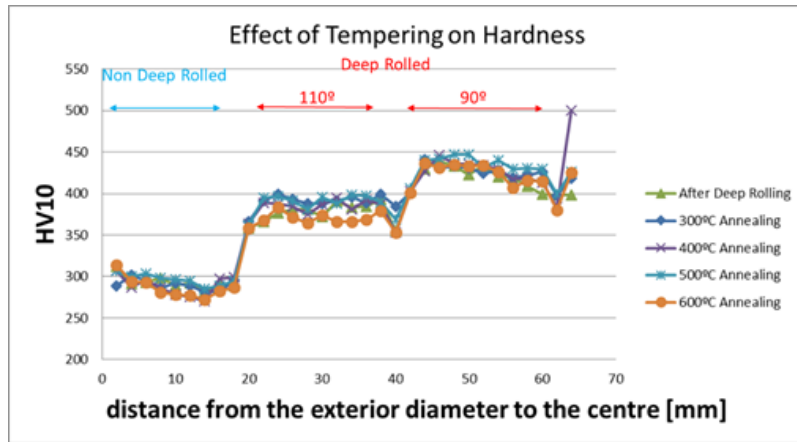


Figure 4.33. Hardness profile evaluation after Deep Rolling with different tool angles and annealing at different tempering temperatures.

Summary - conclusions

- The best conditions found are a tool angle of 90° and a pressure of 600 bar.
- In such conditions, a surface hardness increase of 30-40 % is found.
- Some evaluations of hardness profile through the thickness and residual stresses measurement (XRD) are in substantial agreement. A reduction up to about 2/3 of the surface hardness is occurring in the first 250 µm of depth.
- Tempering from 300 °C up to 500 °C on Deep Rolled samples have a very small influence on hardness on deep rolled samples.

4.3. Test rig set up and FE8 tests (Task 4.3)

Test rig (ECOR) - Preliminary considerations

The activities focused on the setup of the test rig developed for the laboratory characterisation and simulation of White Etching Cracks damage of the bearings. The main test rig characteristics have been defined taking in account the following boundary conditions:

- Failure modes
- Mechanical working conditions
- Environment
- Input data from SCHAEFFLER.

A specific bearing type has been identified in collaboration with SCH, the code NU207-E-MP1A in martensitic steel 100Cr6. These bearings are subject to failure characterised by the so called "White Etched Cracks". The failure causes are not well understood and they are still under investigation from the scientific world. Furthermore, a set of tailored characteristics have been discussed with SCH in order to introduce innovative capabilities of the tribometer for the laboratory testing of the components.

A test campaign has been carried out varying test parameters according to the evidence of the results on tested bearings. The modification of test parameters and the actions to improve the working way of the system were agreed with the support of SCH researchers.

In fact, periodic meetings have been carried out among ECOR and SCH researchers in order to discuss the achieved results and to find the most suitable procedures to modify in the most proper the testing parameters and the actions to be performed.

The test rig main structure and the position of testing bearing are reported in Figure 4.34. The test rig has been equipped with a vibration analysis system supplied by QASS GmbH (Figure 4.35) specifically adapted by the supplier with a tailor design to the ECOR test rig.

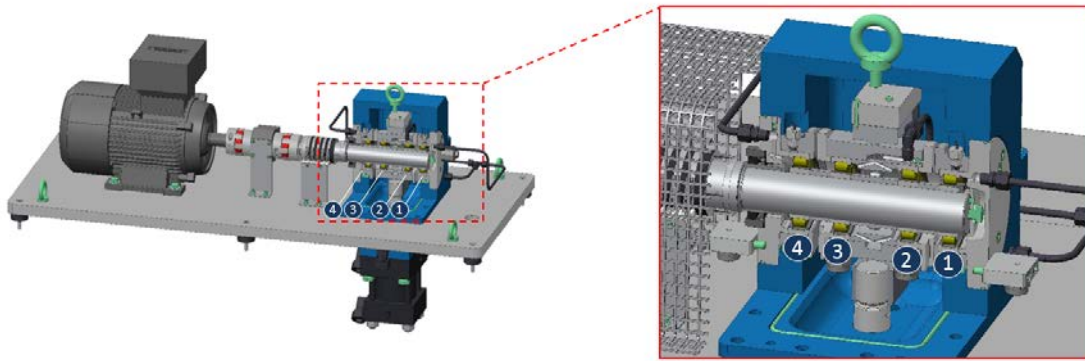


Figure 4.34. Test rig structure and the position (station) of testing bearings.

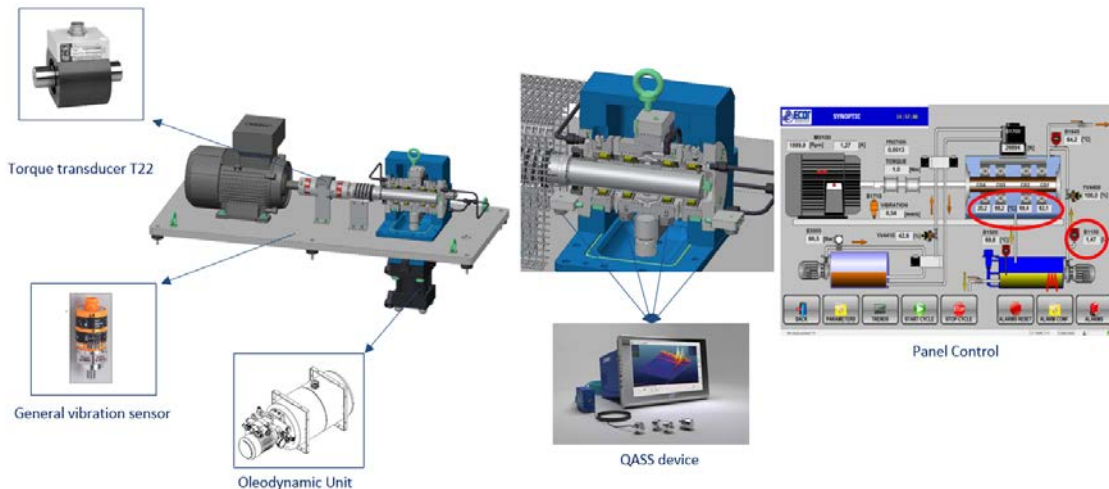


Figure 4.35. Noise signals acquisition from the testing bearing positions.

The built-in sensors of the testing stations are for analysing the bearing surface or strong noise generation when rolling the rolling body. The generated frequencies during motion are scarcely audible but mostly inaudible to the human ear. Especially the inaudible signals are interesting for evaluating the bearings. Specific frequency areas ≥ 50 kHz describe friction noise, unstable bearing races, and the development of early damages. The common acceleration sensors have a high inertia and do not allow to detect these kinds of highly frequent signals, especially since they can occur in short intervals of a few milliseconds. Acceleration sensors detect the smallest movements, which can be started by impulses, which mostly come from damages on the bearing surface, which, however, have already been there for a long time. The QASS system uses vibration sensors to detect the inaudible frequencies. The sensor allows listening to the whole frequency spectrum, which is then sampled highly frequent with 100 MHz.

The simultaneous data acquisition leads to every change in the bearings becoming visible. The vibration sensors convert the inaudible sounds into electrical currents, which simultaneously are depicted on a three dimensional diagram on the axis for time, frequency and the energy associated to the amplitude of the vibration (Figure 4.36).

The energy associated to the amplitude of the vibration depends on the vibration from the bearing motion, then the energy is only another way representing the same physical variable of vibration and of the same phenomenon under observation.

The signal is directly transformed using a mathematical formula (Fast-Fourier-Transformation), so that additional information becomes available. The signal is depicted in such a way that the assignment of frequencies to their corresponding amplitudes in the corresponding point of time is possible.

Through this adapted system, friction noise and the smallest roughness on the surface of bearings can be detected.

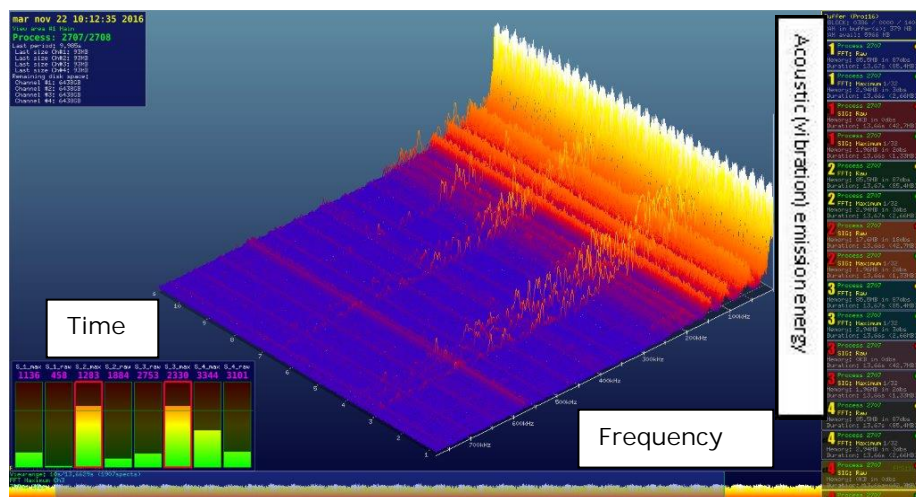


Figure 4.36. Example of a recorded image of acoustic emission by QASS System.

In practice, in order to evaluate the behaviour of the testing bearings, the whole spectrum is recorded after a brief running in period (representing the working conditions in the suitable way because the bearings are new) and another one is observed when something changes in the vibration spectrum in order to stop the test in the proper time. The recording of noise is imposed at a frequency of 20 seconds every 20 minutes during the test. The signals are recorded (Figure 4.37) for a starting period in which the proper working conditions are ensured (no damage).

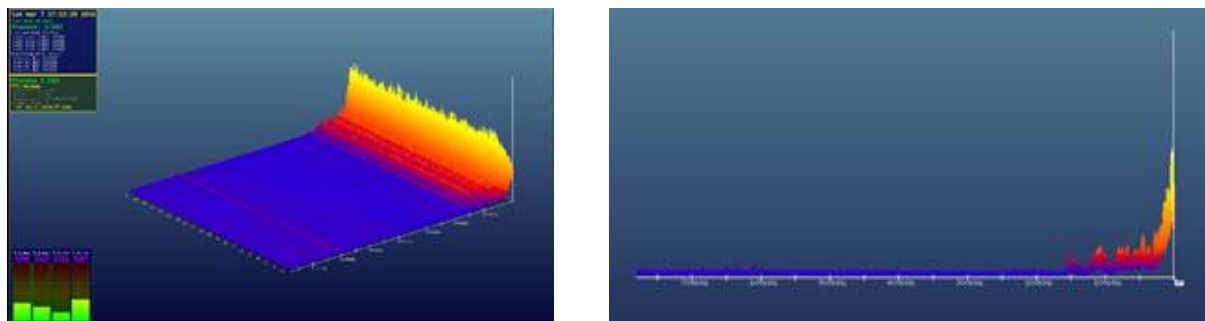


Figure 4.37. Example of recorded data by QASS System (starting reference conditions).

When a change in the emission spectrum is detected (Figure 4.38), the system stops the test because it exceeds an energetic index associated with the spectrum itself. This means a damage has been developed in the testing bearing reflecting this condition in the spectrum.

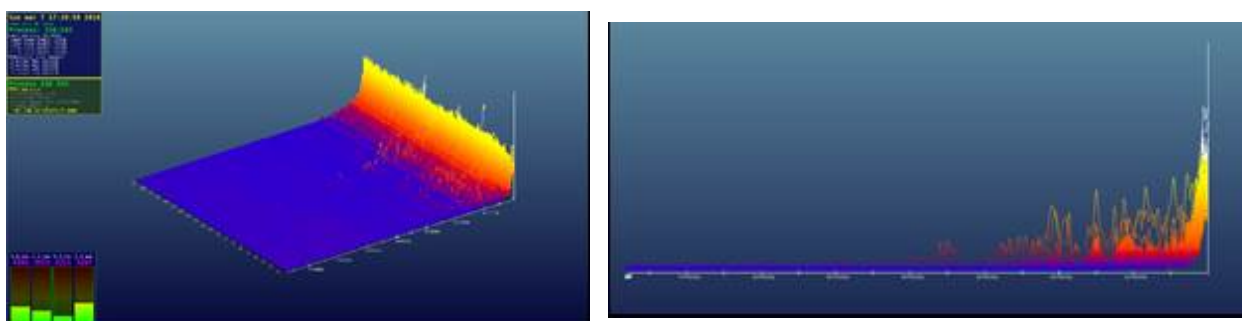


Figure 4.38. Example of recorded data by QASS System (end of test).

At present, a specific spectrum depending on WEC development can not be wholly described because it depends on some parameters like crack density, entity and some specific constructive characteristics of each test rig. Anyway, being a phenomenon inducing really a small volume increment under surface, the associated frequencies should be at high values on the corresponding axis.

Testing activities

The bearing typology is NU207-E-MP1A made in 100Cr6 martensitic steel (Q&T), used as reference material. Before every single test, a cleaning process is carried out.

The tests carried out during the project are listed in Table 4.10. Some samples were not delivered to SCH limiting the forwarding to those bearings with relevant pitting or axial cracks. Secondly, when the duration of the test was short (less than 100 hours), the samples have not been usually dispatched to SCH because the time required to produce the under investigation defects is generally highest. Some of the samples not delivered to SCH were analyzed in ECOR laboratory.

Table 4.10. List of the tests carried out since the beginning of the project.

Year	Test	Bearings tested	Delivered to SCH
2016 - 2017	From RUN#1 to RUN #8	34	YES (RUN #1 - #5) NO (RUN #6 - #8)
2017	From RUN #9 To RUN 12	16	YES RUN 11 – RUN 12
2018	From RUN #13.1 To RUN 15	24	YES RUN 13.2 – RUN 14 – RUN 15
Total	18 tests (~2360 hours)	74 bearings	-

Test rig (ECOR) – Setup (RUN 1-6)

A preliminary test campaign has been planned for the set up phase. The test parameters are reported in Table 4.11 and Table 4.12.

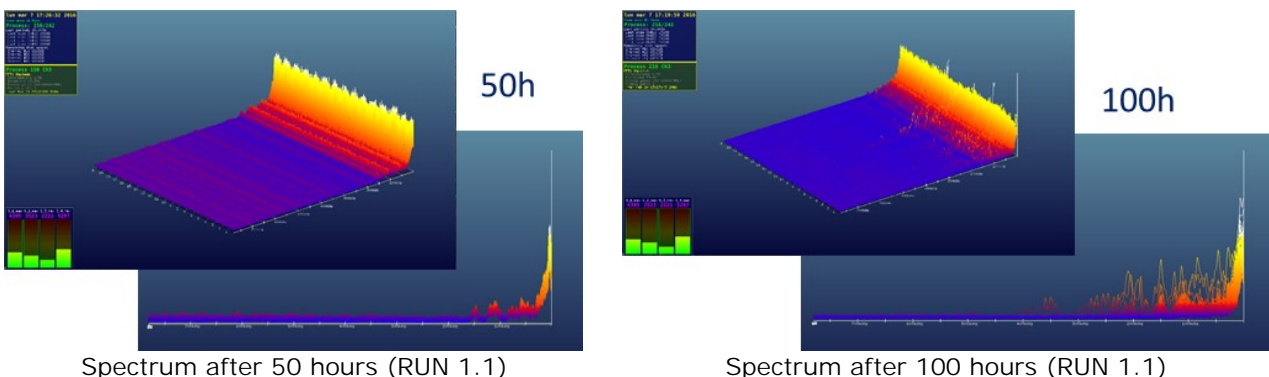
Table 4.11. Testing parameters of bearings tested at ECOR for the setup phase.

RUN 1.1	Hours	Bearing	Load (kN)	Speed (rpm)	Efield (V)	T(°C)	Lubricant
Station 1	100	SW-B11	6	2500	0	70	Total Ti
Station 2	100	SW-B22	6	2500	0	70	Total Ti
Station 3	100	SW-B33	6	2500	-5	70	Total Ti
Station 4	100	SW-B44	6	2500	-5	70	Total Ti

Table 4.12. Testing parameters of bearings tested at ECOR for the setup phase.

RUN 1.2	Hours	Bearing	Load (kN)	Speed (rpm)	Efield (V)	T(°C)	Lubricant
Station 1	80	SW-B11	15	2000	0	70	Total Ti
Station 2	80	SW-B25	15	2000	0	70	Total Ti
Station 3	80	SW-B36	15	2000	-5	70	Total Ti
Station 4	80	SW-B44	15	2000	-5	70	Total Ti

The total test time was 180 hours. The data from the vibration detection system are reported in Figure 4.39 for the bearing SW-B11 on which a surface crack has been detected. An increment in vibration can be observed in the picture after 100 hours test.



Spectrum after 50 hours (RUN 1.1)

Spectrum after 100 hours (RUN 1.1)

Figure 4.39. Spectrum RUN 1.1.

The failed bearing has been analysed at Schaeffler to evaluate the failure causes. The results are reported in the following SCH report.

Table 4.13 shows the test parameters adopted for the first test.

Table 4.13. Testing parameters of bearings tested at ECOR and supplied by SCH.

RUN 1	Hours	Bearing	Load (kN)	Speed (rpm)	Efield (V)	T(°C)	Lubricant
Station 1	100	SW-102	6	2500	0	70	Total Ti
Station 2		SW-202		2500	0	70	Total Ti
Station 3		SW-302		2500	-5	70	Total Ti
Station 4		SW-402		2500	-5	70	Total Ti

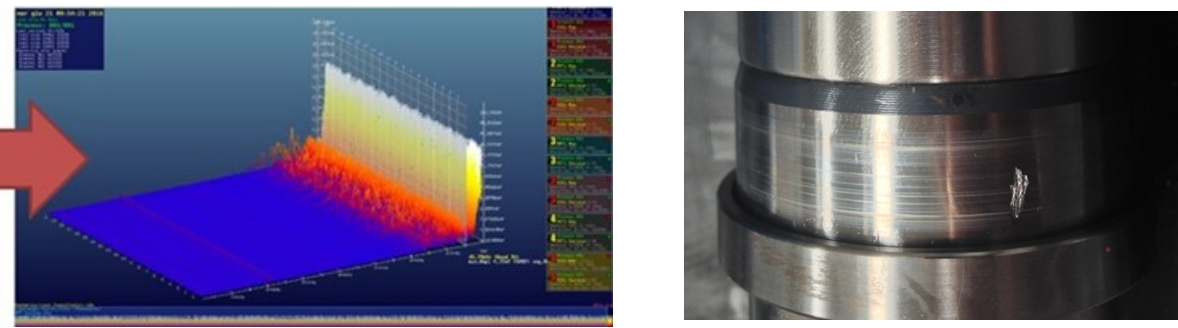
Other two tests were performed in the same conditions to validate the repeatability, and the same results have been achieved.

A second and more intensive campaign was performed in order to check the suitability of the system in the simulation of the bearing damage. Table 4.14 shows the test parameters used.

Table 4.14. Testing parameters of bearings tested at ECOR and supplied by SCH.

RUN 2	Hours	Bearing	Load (kN)	Speed (rpm)	Efield (V)	T(°C)	Lubricant
Station 1	130	SW-102	13	3000	5	70	Total Ti
Station 2	130	SW-202	13	3000	0	70	Total Ti
Station 3	130	SW-302	13	3000	0	70	Total Ti
Station 4	130	SW-402	13	3000	5	70	Total Ti

The vibration spectrum (Figure 4.40) is shown for the bearing SW-402. This bearing has failed during the test.



QASS recorded data after 130 h

Figure 4.40. RUN 2: SW-402.

SW-402 damaged bearing

After the surface analysis, supported by SCH, the damages were attributed to mixed friction, then a cleaning phase of the lubricant circuit has been performed. After that, RUN 3, RUN4, RUN 5 and RUN 6 were carried out with similar test parameters. Similar increment in acoustic emission were observed and also in these cases the damages were not induced by WEC.

Test rig (ECOR) set up – alumina contamination problem (RUN 7)

The test parameters of RUN 7 are reported in Table 4.15.

Table 4.15. Testing parameters of bearings tested at ECOR (RUN 7).

RUN 7	Hours	Bearing	Load (kN)	Speed (rpm)	Efield (V)	Lubricant	T (°C)	Lubricant flow rate (L/min)
	55	SW-107 SW-207 SW-307 SW-407	13	3000	5	Total Ti	70	0.4

After 55 h an increment in acoustic emission has been observed for the SW-307 bearing on which a surface crack has been detected.

The failed bearings have been analyzed by SCH in order to evaluate the failure causes. No WEC were detected and SEM analyses identified some particles of alumina in the bearing inner ring (Figure 4.41).

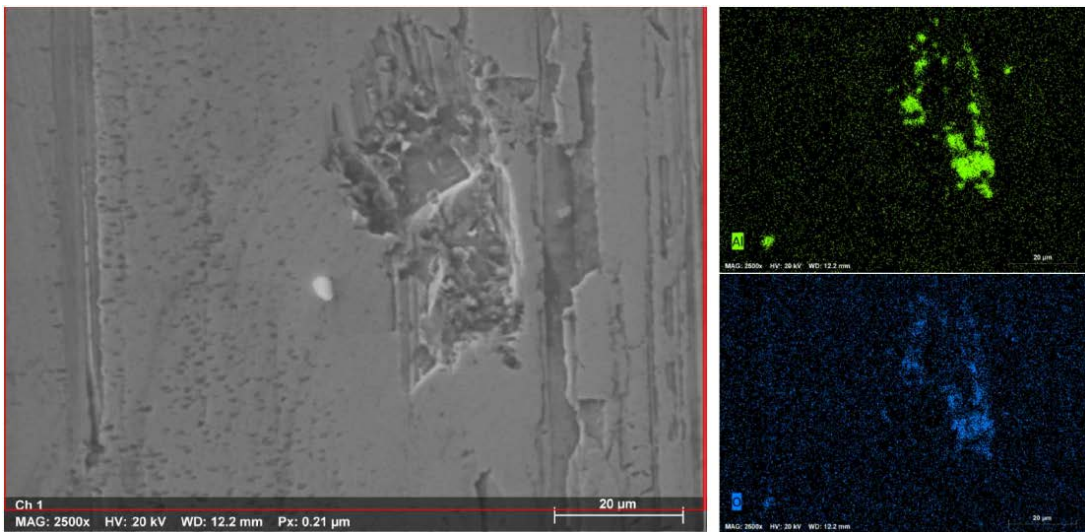


Figure 4.41. Capture from SEM analysis of inner bearing ring with tracks of Aluminium and Oxygen.

The coating of the flanges is made of this material, and this contamination damages the bearing irremediably. The presence of these particles is detected by QASS system that gives notice of this anomaly. For this reason, it happens that we stop the test because of a high energy value read in the system, believing that the excess of the defined threshold is due to WEC appearance. In addition, the degradation of the coating might entail leakage in the electric insulation system. Therefore, the current flow is uncontrollable.

Test rig (ECOR) set up – new electrical insulating coating

The system detected failure always reducing the test time. In spite of the cleaning procedures, no suitable results have been achieved in terms of debris elimination. Also the failure analyses by SCH reached the same conclusions. This means the insulating coating induces a pollution having the effect to anticipate failure by other effects. To solve these problems, new countermeasures were studied and adopted. A new insulating coating has been found and analyzed: the ceramic coating, which has highly cohesive metal-ceramic structure (Figure 4.42) that results in bond strengths exceeding 10,000 psi (69 MPa). Internal surfaces can be coated. The coating trade name is RPC-EI (electrically insulating Reaction Processed Ceramic) supplied by REFMET.

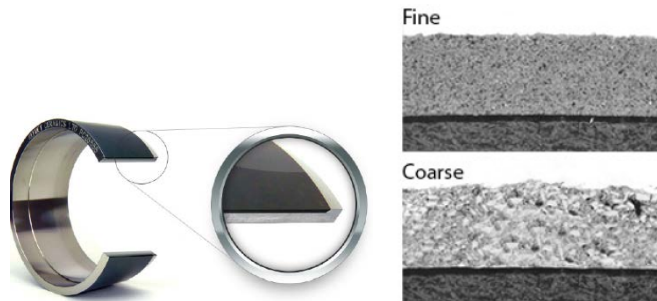


Figure 4.42. Refmet coating for the insulation of test rig component.

The fine microstructure and its thickness allows a suitable insulating coating as demonstrated by the measurements carried out at ECOR. However, due the production time of the flanges was excessive, the tests with the new items started only from RUN 13.

Test rig (ECOR) set up – Improvement of the test parameters - RUN 8-12

During the following tests, a study on the parameter set of the test rig started in order to promote WEC formation:

- 1) to increase the electric field in the bearing by increasing the voltage feeding so that the voltage across the bearing raise. When the current is in the range of 150-200 μA, the crossing voltage is in the range of 1-1.5 V.
- 2) to increase the bearing temperature by increasing lubricant temperature setting our test rig maximum value (73°C). Doing so, the maximum bearing temperature is approximately 80°C,

which is not that much. Therefore, we improved the heating of lubricant by a heat exchanger, in order to reach 100°C of bearing temperature for the tests beginning in 2018.

- 3) to decrease the lubricant flow rate, previously set at 1.5 l/min (which means approximately 0.4 l/min per bearing), and we set 1.2 l/min (0.3 l/min per bearing). For the tests beginning in 2018 we want to reduce it up to 1 l/min, thus 0.25 l/min per bearing.

RUN 10 was the first run with these improvements (Table 4.16), but it finished early due to an alarm of the general vibration sensor. It was found that the main shaft was very ruined, maybe for a bad lubricant distribution. RUN 11 was set like the previous one, but it lasted 280 hours. The energy threshold was exceeded by bearing SW-211 (Figure 4.43).

Table 4.16. Testing parameters of bearings tested at ECOR (RUN 10).

RUN 10	Hours	Bearing	Load (kN)	Speed (rpm)	Efield (V)	Lubricant	T (°C)	Lubricant flow rate (L/min)
	55	SW-110 SW-210 SW-310 SW-410	13	3000	6	Total Ti	73	0.3

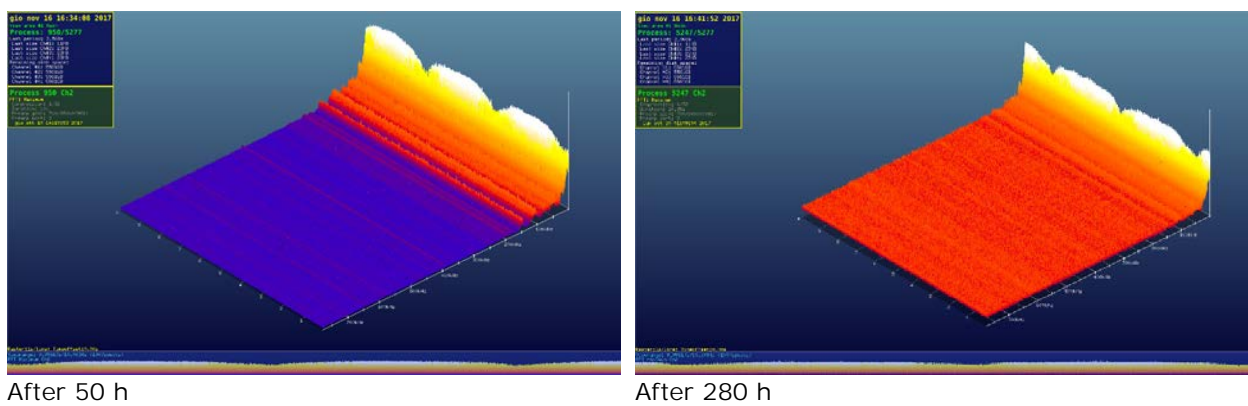


Figure 4.43. Process landscape for bearing 2 (RUN 11).

Test rig (ECOR) set up – New REFMET flanges - RUN 13-15

The RUN 13.1 is the first test of the 2018 and also the first of the campaigns with the new flanges provided by REFMET. This supplier was able to produce a new insulation ceramic coating with better adhesion to the flanges.

The test parameters are reported in Table 4.17. In this test, there are two parameters quite different from the last test of 2017: the voltage feeding "Efield (V)" and the lubricant temperature "T (°C)". The modification of the voltage feeding was agreed with SCH, while the increase of the lubricant temperature was obtained through the introduction of the heat exchanger.

Table 4.17. Testing parameters of bearings tested at ECOR (RUN 13.1).

RUN 13.1	Hours	Bearing	Load (kN)	Speed (rpm)	Efield (V)	Lubricant	T (°C)	Lubricant flow rate (L/min)
	80	SW-113.1 SW-213.1 SW-313.1 SW-413.1	13	3000	-5	Total Ti	82	0.3

The energy threshold was exceeded precisely by bearing SW-313.1 on which a surface crack has been detected. The failed bearing has been analysed by ECOR researchers in order to evaluate the failure causes.

Repeating the same conditions of the test RUN 13.1 (RUN 13.2), the failure has been observed at 277 hours on bearings SW-413.2 in which micropitting formation was found (Figure 4.44). Bearing SW-413.2 has been analysed by SCH researchers in order to evaluate the failure causes.

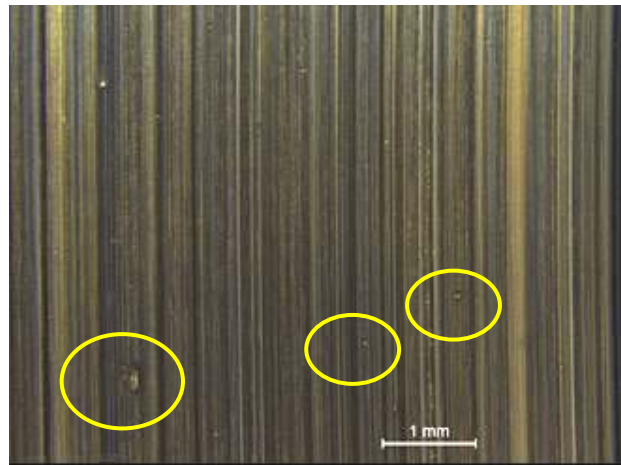


Figure 4.44. Micropitting formation on bearing SW-413.2.

The RUN 13.3 was made in the same condition was made. The energy threshold was exceeded by bearing SW-313.3 after 92 h. The failed bearings have been analysed by ECOR researchers in order to evaluate the failure causes.

During this test, ECOR found spurious lack of insulation on the bearings SW-213.3 and SW-313.3. The insulation of the two central bearings is ensured by the flange E9003116, so it was decided to dismount the flange and check if it was working properly.

It was found that, across the surface in contact with the outer ring of the bearings, the coating was thinner on one side than the other (Figure 4.45). So the component was sent to the supplier, the coating was completely removed and the flange recoated.

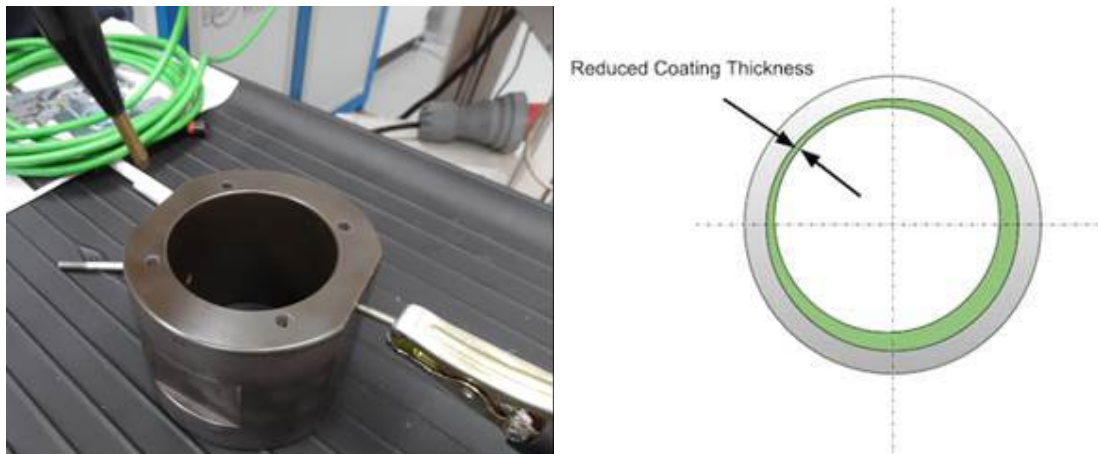


Figure 4.45. Control of the insulation of the flange and sketch of the issue.

RUN 14 started, using the same parameters RUN 13, as the flange came back to ECOR and ended when 2 macro-pittings on bearing SW-414 occurred (Figure 4.46) after 45 h. The failure of the bearing was not detected by the QASS detection system but it was noticed from a huge value of the general vibration sensor. Bearing SW-414 has been analysed by SCH researchers in order to evaluate the failure causes.

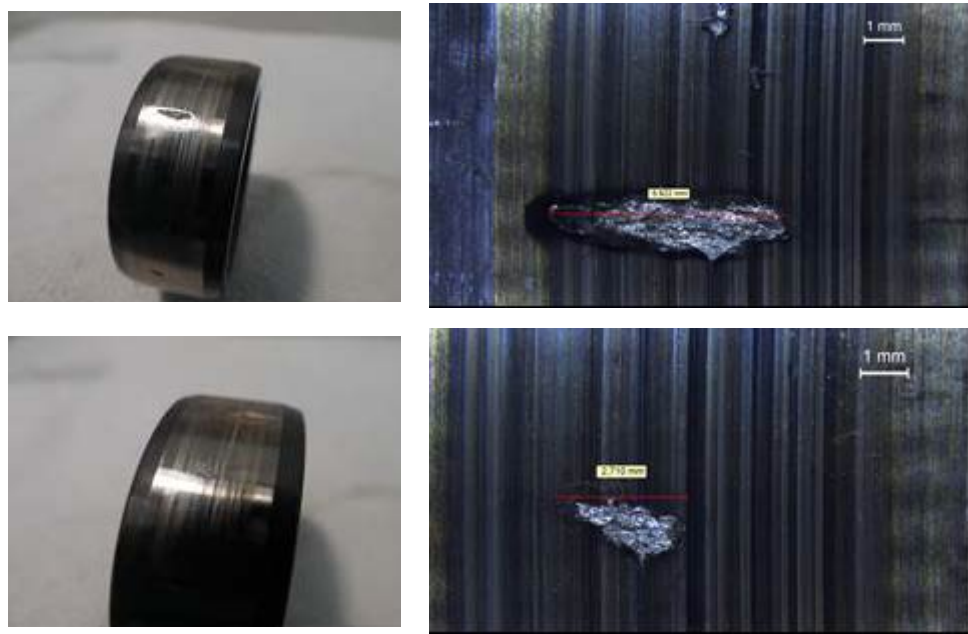


Figure 4.46. Details of the 2 macro-pittings on bearing SW-414.

RUN 14.2, performed in the same condition RUN 14 ended after 66 hours, in a similar way to the previous run in terms of duration of the test and surface damages (Figure 4.47).



Acoustic emissions after 66 test hours

Detail of the macro-pitting

Figure 4.47. Bearing SW-414.2.

The failed bearings have been analysed by ECOR researchers in order to evaluate the failure causes.

RUN 15 (Table 4.18) ended after 360 hours. In this test, the lubricant flow rate was slightly increased. The failure has been observed in bearing SW-415. The failed bearings have been analysed by SCH in order to evaluate the failure causes.

Table 4.18. Testing parameters of bearings tested at ECOR (RUN 15).

RUN 15	Hours	Bearing	Load (kN)	Speed (rpm)	Efield (V)	Lubricant	T (°C)	Lubricant flow rate (L/min)
	360	SW-115 SW-215 SW-315 SW-415	13	3000	-5	Total Ti	82	0.35

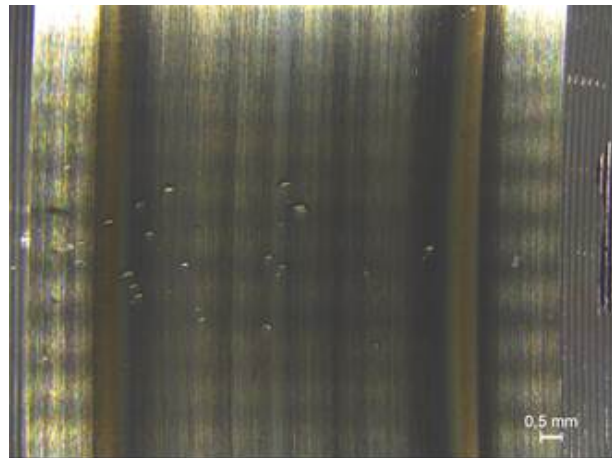


Figure 4.48. Micropitting formation on bearing SW-415.

The bearings NU207 from different test setups were delivered to Schaeffler. The sample names and corresponding testing data are listed in Table 4.19 for the latest two setups, No. 14 and 15. All the tests were performed at kappa values above 1 (nominal fully separated bearing components).

Table 4.19. Bearings from test setup No. 14 and No. 15.

RUN	HOURS	BEARING	VISIBLE DAMAGE
14	45 h	SW-414	2 macro-pittings on IR
15	360 h	SW-415	IR: several pits; OR: pitting

Results on test No. 14 - bearing 4-1-4

This bearing was affected by several pittings on the IR. By means of light optical microscopy (LOM) and scanning electron microscopy (SEM) it was figured out, that all the pittings originated from the surface and caused by mixed friction. In circumferential microcut through the area in which the pittings were found, no signs for WEC could be observed.

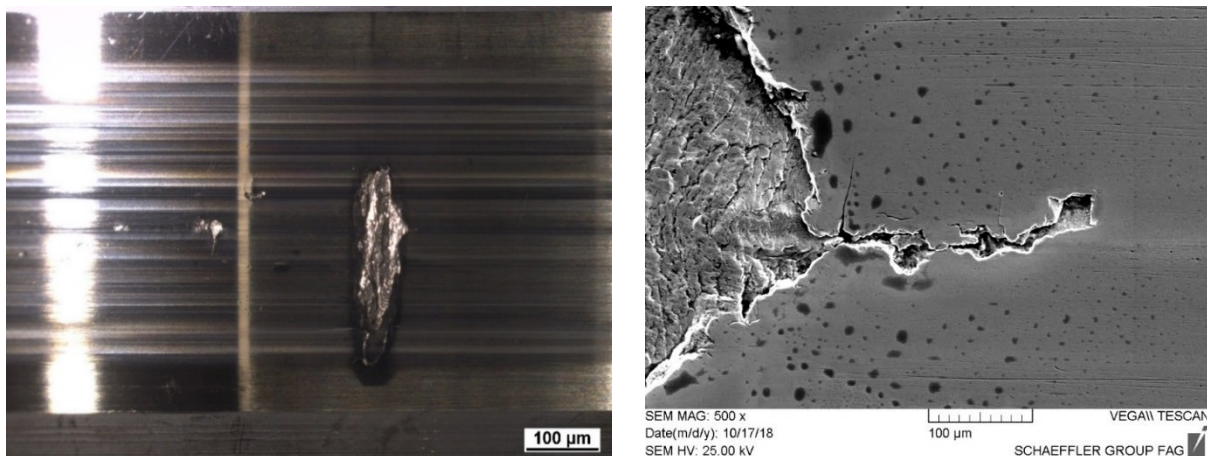


Figure 4.49. SW-414 IR left) LOM overview. right) SEM detail of the surface initiation.

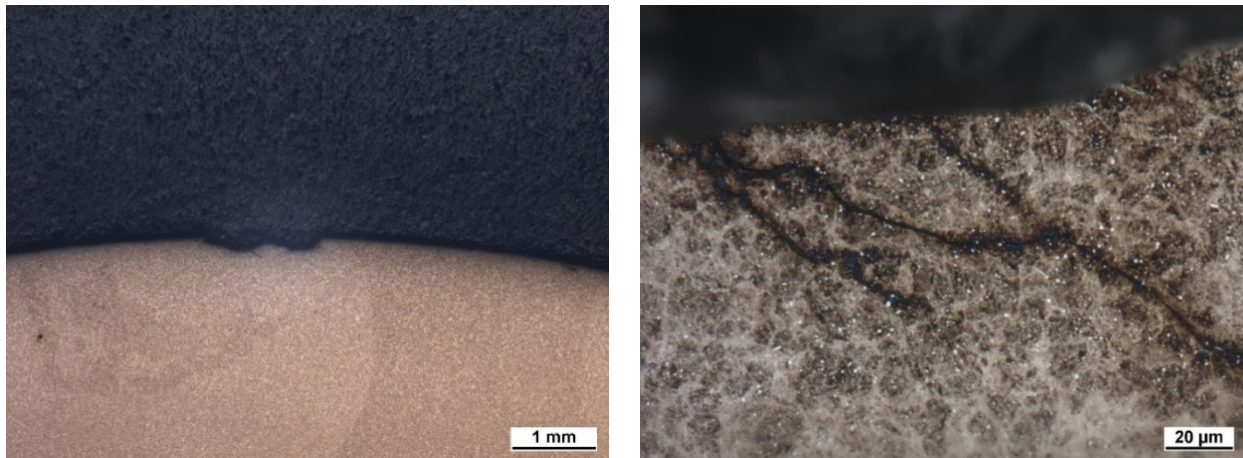


Figure 4.50. SW-414 left) Circumferential microcut through the bigger pitting. Right) Detail of circumferential microcut.

Results on test No. 15 - bearing 4-1-5

This bearing showed several dents on the IR, as well as a bigger pitting on the OR. By means of light optical microscopy (LOM) and scanning electron microscopy (SEM) it was figured out, that the dents on the IR were not pittings, but scratches. The pitting on the OR originated from the surface.

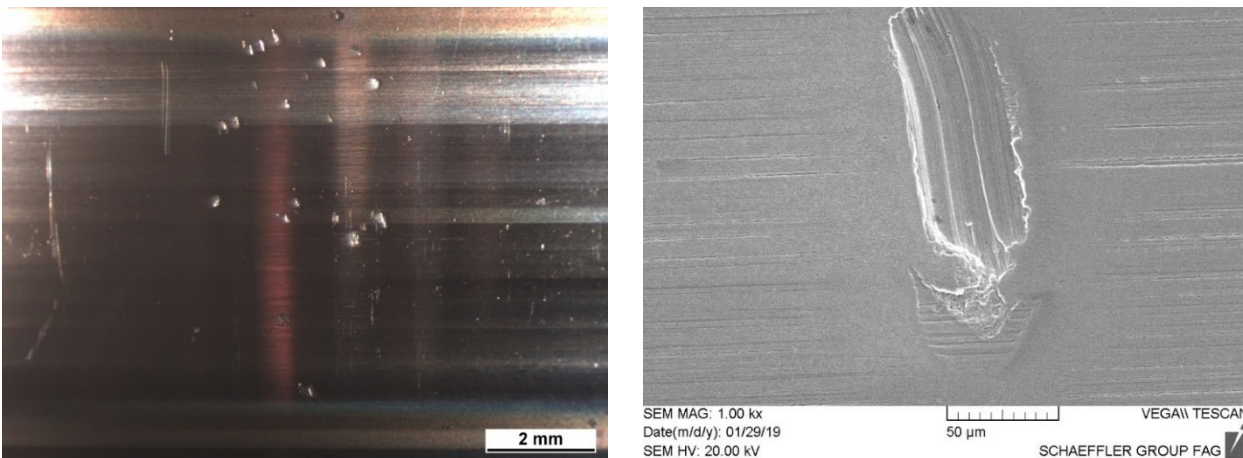


Figure 4.51. SW-415 IR left) LOM overview. Right) SEM detail.

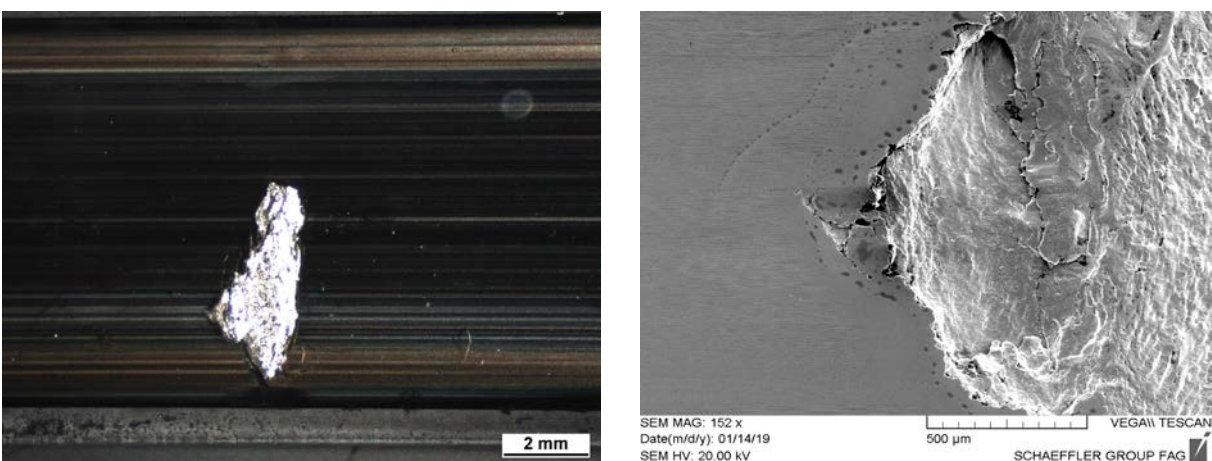


Figure 4.52. SW-415 OR left) LOM overview. Right) SEM detail.

In the microcuts, performed in circumferential direction, no WEC structures were identified. However some butterflies were seen. An example is reported in Figure 4.53 left, showing butterflies wings detected at a depth of approximately 300 μm.

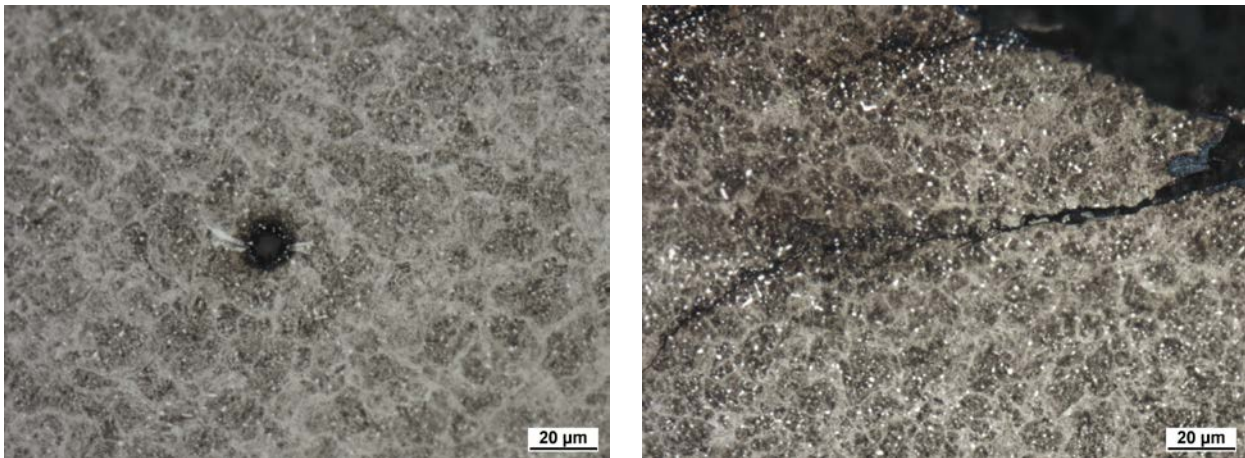


Figure 4.53 - SW-415 left) Circumferential microcut through IR showing one butterfly, right) Circumferential microcut through the pitting of OR having no evidences for WEC.

The following findings can be summarized:

- The investigation, performed at Schaeffler obtained, that no White Etching Cracks were generated in the bearings, tested at ECOR.
- All the rings, affected with damages after test showed surface initiated fatigue due to mixed friction conditions and/or contaminated environment. The amount of contamination significantly decreased from test to test. Nevertheless, there were some contaminations with hard particles, even in the latest two test runs.
- Via SEM analysis, the occurrence of electrical current flow (as the applied additional load, which should provoke the WEC-formation) could at least be proven on samples of the test No. 15.
- The prototype testing system is able to induce the development of butterfly defect, which is often found in WEC damage.
- Suitable test parameters for developing butterfly defects have been established.
- Once established suitable parameters, the butterfly density seems to depend on test duration.

The concurrence between Alumina induced damage and butterflies' development has been unfortunately favourable to the first one. This condition has reduced the possibility of further test duration as required to obtain WECs.

Test rigs at Schaeffler

At Schaeffler, several test concepts are established, so as the belt tensioner tests, the FE8-test and the larger bearing test R4G [70, 71]. The latter two are chosen to test the HNAS steels regarding their properties in comparison to standard bearing steel 100Cr6 martensitic hardened.

Test rig FE8 according to DIN 51819

The tribology test rig FE8 test allows short tests to be performed to investigate the wear protection behavior of oils acc. to DIN 51819-3 as well as performing different tribological tests. By using a special setup, with regards to speed, pressure and special so called Low Reference Oil, this test is capable of repeatedly creating White Etching Cracks in axial cylindrical roller bearings within a reasonable time. Therefore, different materials can be tested for their WEC susceptibility, as described in [72]. For the comparison of materials, the axial cylindrical roller bearing FAG 81212 is used, whereas the washers are the test pieces. To avoid early failures of the rollers, these parts are made out of Si_3N_4 ceramics.

The test rig itself has a simple structure: the force is applied by a cup spring, and the rotational speed is generated by an electric motor. The oil circulates within a closed system, which allows the lubricant temperature to be controlled. During the test run, the torque and temperature, as well as the noise and acceleration are recorded. The last two are the main parameters which are used for early failure detection.

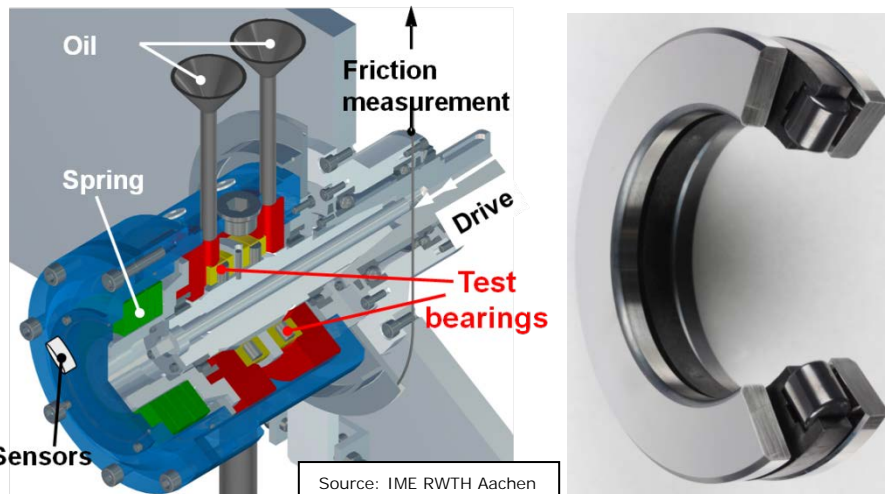


Figure 4.54. Schematic drawing of the FE8 test rig and bearing type (FAG 81212) used. The parameters for the two different FE8 tests can be found in the following table:

Test parameters	FE8-03 wear test	FE8-25 WEC-risk-assessment
Bearing type	FAG 81212	FAG 81212-TV
Oil	Wear Reference Oil	WEC-Low-Reference Oil
Rotation speed [rpm]	7,5	750
Load [kN]	80	60
Hertzian Pressure [N/mm ²]	2150 *	2075 **
Temperature [°C]	80	100
Kappa value	< 0,1	0,4 – 0,5
Running time [hrs]	80	1000
Measurement	Wear [mg], frictional moment [Nm], temperature [°C]	Frictional moment [Nm], temperature [°C], noise [arb.unit], solid borne noise [arb.unit]
Assessment	Wear of bearing parts [mg]	WEC y/n, time to failure [hrs]

*) Steel rollers **) Si₃N₄ rollers

To exclude classical damages and core crushing, the axial washers of the bearing 81212 must have an appropriate hardness distribution. Using the Schaeffler program BEARINX®, the required hardness pattern can be calculated out of the van Mises equivalent stress distribution. In the pattern is drawn, considering a maximum test load of 80 kN.



Figure 4.55. BEARINX® calculation of the required hardness of the FE8 - shaft washers, if testing with an axial force of $F = 80$ kN (Hertzian pressure of ≈ 2150 MPa).

Test rig R4G

The R4G test rig uses cylindrical roller bearings up to an outer diameter of 250 mm. Four bearings are tested in parallel with pure radial loading. With the current test setup, Hertzian pressures up to 2400 MPa can be achieved on the higher stressed IR.

The rotational speed is applied by an electrical motor, an insulating coupling avoids electrical currents running through the bearing system. The force is applied by a hydraulic cylinder into the two inner bearings. By the shaft, the load distribution is resulting constantly into the four bearings. For the WEC test, cylindrical roller bearings NU222 with an outer diameter of 200 mm are used. The IR is chosen to be the testing part, because this mirrors somehow the field experience, where also the IR are mostly affected of (WEC) failures.

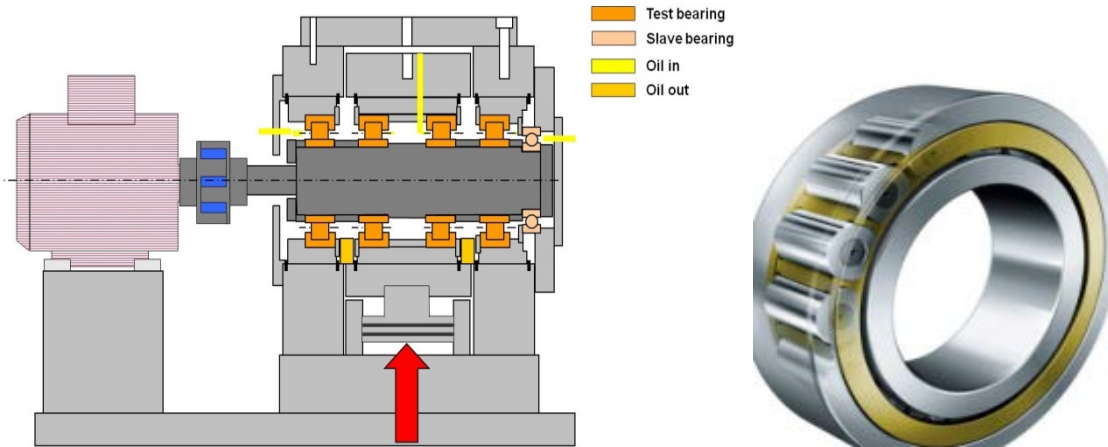


Figure 4.56. Schematic drawing of the R4G test rig and bearing type (NU222) used.

The test parameters used are described in the following chart:

Test parameters	R4G
Bearing type	NU 222
Oil	ISO VG 320
Rotation speed[rpm]	1000 - 4500
Load [kN]	max. 100
Hertzian Pressure OR [N/mm²]	max. 1900

Hertzian Pressure IR [N/mm²]	max. 2400
Temperature [°C]	80 - 100
Kappa value	> 5
Running time [hrs]	> 1000
Measurement	Temperature [°C], frictional moment [Nm]
Assessment	WEC y/n, time to failure [hrs]

To avoid classical damages on R4G the rings have to be manufactured to guarantee the following hardness pattern. Therefore the final cold deformation process is from outstanding interest.

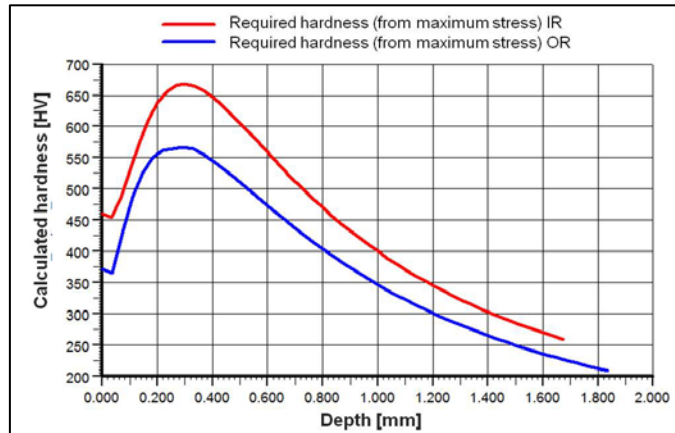


Figure 4.57. BEARINX® calculation of the required hardness of IR and OR, if testing with a radial force of 100 kN.

Summary

Two test benches are chosen out of Schaefflers test portfolio to exam the performance of new HNAS variant in comparison to the performance of standard bearing steel 100Cr6. Using the FE8 test informations are gathered about the wear behavior and the WEC-performance of the bearing parts.

The large scale test R4G is used to exam the lifetime of wind turbine – like bearing of type NU222. This test not only investigates the bearings in terms of WEC, but also in terms of classical fatigue resistance, because applied pressures (IR are above 2000 MPa) which corresponds to max. peak loads applied in wind turbine gearbox applications.

The hardness distribution in the bearing parts were calculated, respectively and show that hardness of about 600 HV has to be obtained during cold deformation of HNAs considering the washers for axial bearings, tested on FE8. Looking in particular on the IR for NU222, this hardness has to be above 670 HV.

5. WP5. Design and set up of functional laboratory tests

5.1. Preliminary considerations (Task 5.4. Selection of the steel grade)

At the end of the previous WPs, it was possible to identify the best temperature ranges for the heat treatments (solubilization) of the medium-N and Carnit C+N alloy. In particular, it was found that only Carnit alloy possessed a range of austenite stability, even though a further optimization is required in order to face the issues related to the presence of second phases (precipitates). Accordingly, a C+N austenitic steel (Carnit) alloyed with chromium and manganese (Carnit) has been selected as the alloy to produce some industrial material, complete the experimental activities (in particular, mechanical testing, corrosion and tribological testing) planned in WP5, and then manufacture the prototypes and perform full-scale / functional testing planned in the WP6.

The choice of Carnit steel has been based on the need to withstand both dynamic loads – achieving high levels of strength - and corrosion attack of water, especially sea water when used in offshore applications. The development of the Carnit composition was based on the investigation results of earlier projects [85]. Despite the results of the thermodynamic calculations, it was found that larger parts would not be able to manufacture without unwanted precipitations like N-perlite.

To improve the microstructure it has been necessary to further change the composition of the alloy, substantially in the balance of C and N, and in the content of added elements as Mo. The recent investigations suggest that the change of the composition not only improves the microstructure after solution annealing but also improves the fatigue strength and the resistance against surface breakdown [86, 87], which are important properties for bearing steels. The grade selected has been the Carnit 90.

Bars in different diameters – according to the needs of experimental activities and prototype manufacturing – have been forged from an industrial heat of Carnit 90 steel (actual composition: C = 0.33 %, Mn = 18.6 %, Cr = 18.2 %, N = 0.44 %) and made available for the completion of experimental testing planned in WP5 and for the activities planned in WP6 (prototype manufacturing and full-scale tests). A campaign of laboratory heat treatments, followed by a basic characterization (evaluation of microstructure and steel cleanliness), has been preliminary performed on the bars:

- The material is characterized by a good quality in terms of absence of porosity.
- The steel cleanliness (non-metallic inclusions) is good according to the usual specifications given for bearing steel bars.
- A temperature of 1120 °C can be selected as the condition for the industrial heat treatment (solubilization annealing): at that temperature, a complete recrystallization and absence of undesired precipitates are found.
- The hardness level is 300-320 HV. According to a first estimation, the hardness target of 500 HV for bearing parts (which enables to perform scale test on FE8 with a Hertzian pressure of 2000 MPa) can be achieved by means of the operations included in the component manufacturing process: cold deformation (to be adjusted even on the basis of some preliminary tests) and deep rolling.

More details about the manufacturing of the industrial bars and the related characterization are reported in Task 6.1.

5.2. Design of the test plan (Task 5.1)

A specific test bench has been designed in order to get available a test on a laboratory involving different damage variables, with the aim of simulating the conditions in field of the bearings by means of a tribological test.

Literature based on continuum mechanics and numerical modelling they show that the single contact areas can be characterized by zones which have, at the same time, both adhesive stick and slip (Figure 5.1, from Appendix D1.1 – Dynamic and kinetic analysis).

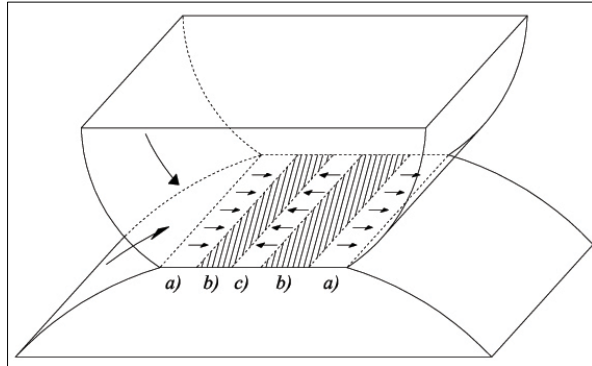


Figure 5.1. Slip and stick regions in the roller-ring cylindrical contact: a) slip with the same sense of the entering velocity; b) stick regions; c) slip with sense opposite to the entering velocity. From Appendix D1.1 - Dynamic and kinetic analyses.

The Universal Micro Tribometer CETR UMT-3 (Figure 5.2) can be useful, with the due modifications, to reproduce conditions that are more realistic with respect to the simple pin-on-disk or roll-on-disk devices, where the sliding and traction directions never change their sense of motion. The fretting mode, in fact, can be modified in order to apply asymmetrical alternative tangential loads, together with the normal load. This idea conveys the concept that the test is able to reproduce not only sliding between the non-conformal contact surfaces but also a portion of rolling. As described in Appendix D1.1 we notice that, within the contact region of elastic deformation, some area stick together while other may present sliding. However, the relative motion can be directed both forward and backward with respect to the macroscale relative motion of the roller with respect to the ring. For this reason, an alternative motion may have a chance to reproduce such situation better than a simple one-directional sliding test rig. As far as rolling simulation is concerned, it is worth noticing that our test system has been designed in such a way to allow the sample holder to admit small rotations around an axis which is orthogonal to the plane defined by motion direction and the load application line. Such choice will allow the system to simulate also rolling, although in the simulation sliding will be more accelerated than rolling.

Although the main possible applications are the characterization of lubricants and the determination of friction coefficients, our modification made the stand able to detect the damage on a sample with both *alternative sliding and rolling*.

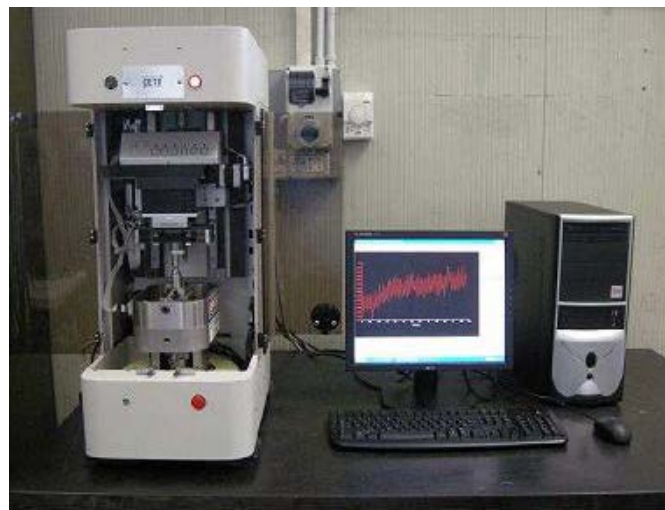


Figure 5.2. The Universal Micro Tribometer CETR UMT-3 at CSM.

The upgrading of the Micro Tribometer configuration is shown in Figure 5.3, while a functional diagram of the assembled device is reported in Figure 5.4. An alternately moving bowl contains a soft material plate "B" which can be used to create a cylindrical surface which is conjugate with a rotating cylinder "C". Such element is rigidly connected with the sample holder "A" on which two sample can be positioned. The two position are characterized by two different ratio of sliding-to-rolling. The softer material is actually acting in the system as a spring, allowing the rotation around the axis and aiming at obtaining a certain degree of rolling.

All the parts have been built and assembled in the device, getting the test bench available for the set-up of the parameters of the test (Load, Run, Frequency). The lubricated contact will be also considered.

The equipment has been also equipped with an electric circuit that allows a current to flow through the contact. Such current can be adjusted in a range up to 12 A Furthermore, galvanic insulation is provided to guarantee safety in operation. The current flow allows us to simulate the eddy currents in the bearing, which are mounted in epicycles gearbox. This current arises in the bearing elements during motion. As known, currents are due to the flux created by the large electrical generator. In planetary gear trains, bearing are also floating. They move within a strong electromagnetic field (near to the generator) which is also not constant. Hence, in any case currents are induced.

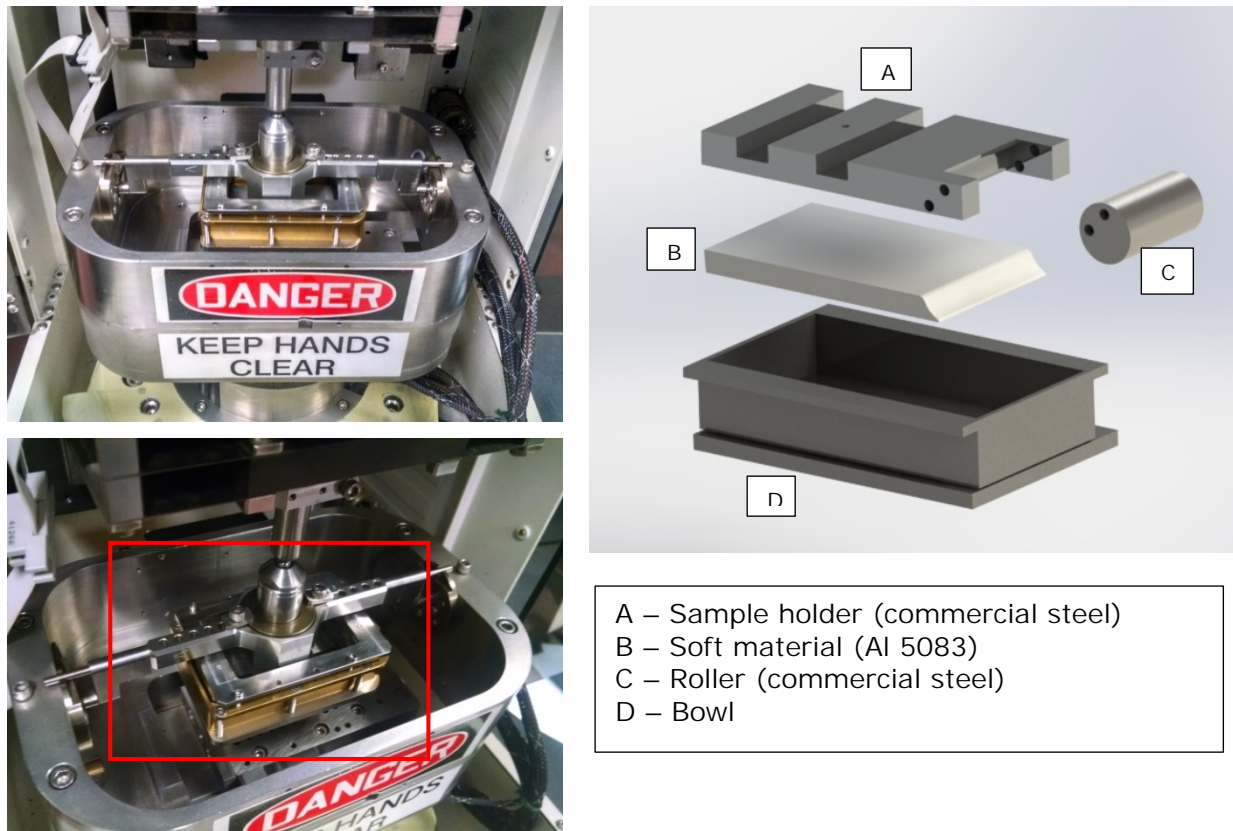


Figure 5.3. Details of the upgraded configuration of CETR UMT-3.

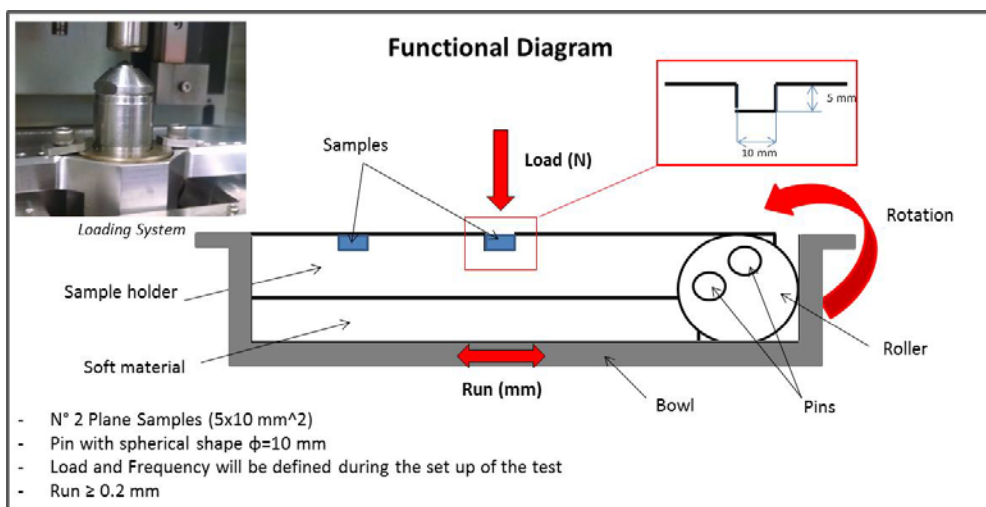


Figure 5.4. Functional diagram of the assembled device.

Offshore wind turbines are characterized by the presence of a large generator which induces a electromagnetic field which is crossed by the bearings. Some of them belong to an epicyclic gear-drive

and therefore are mounted on floating shaft. The situation appears as in Figure 1, where some short circuits may appear. For example, currents around the inner i_I and outer i_O rings, and also between two rollers.

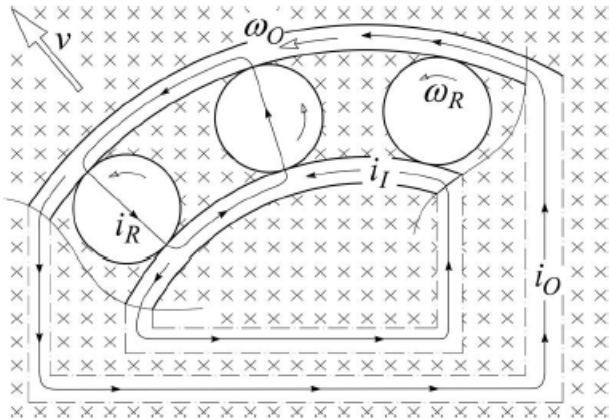


Figure 5.5. Schematic representation of the induced currents.

A first set of tests have been carried out on a reference material, a high-C Cr-added steel (100Cr6 QT), with current flowing through the sliding contact. In this set of experiments the applied load has been set using the Hertz formulae to adjust the acceleration degree of the test due to pressure, taking into account the spherical pin radius of the test stand and the real roller principal radii. A load of 8 N was applied, with a 3 Hz alternating cycling, for a time of 2.5 h. A second set of tests have been performed on Carnit 90 steel. The main attention has been paid to the effect of the electric current.

The wear tracks have been evaluated in terms of width and depth, by means of optical microscope (example in Figure 5.6) and optical profilometer (example in Figure 5.7)

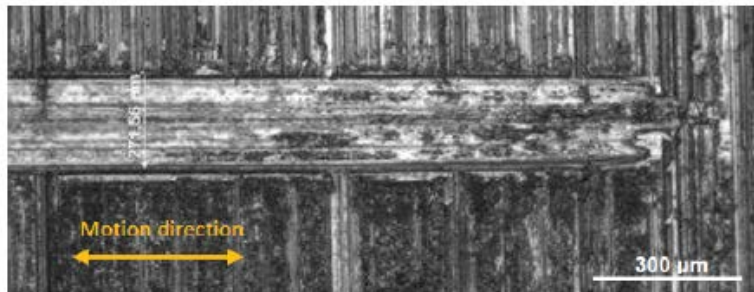


Figure 5.6. Macro image of the wear track (steel 100Cr6, $I = 2 \text{ A}$).

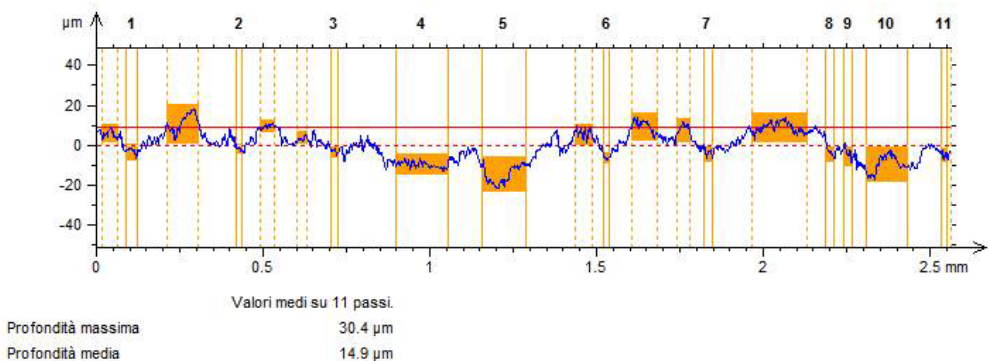


Figure 5.7. Profile of the wear track (steel Carnit 90, $I = 4 \text{ A}$).

A summary of these first attempts is reported in Table 5.1. The interpretation of these results is not easy and not completely clear, and further tests will be needed on the experimental equipment to understand the effect of the different variables on the system. In any case, the effect of the current seems to affect

mainly the width of the wear tracks, while the depth tends to remain quite constant. The lower wear track width observed on the reference material (almost negligible in absence of current, up to 600 µm with 10 A) with respect to Carnit 90 (210-320 µm without current, 640-650 µm with 4 A) may be attributed to the higher surface hardness of the former (650 HV). It should be noted that the samples taken from Carnit 90 had a surface hardness equal to that of the bulk (about 300 HV) as in the given condition it has not been possible to subject them to the operations designed to enhance surface hardness, as deep rolling. In the future tests with such equipment, it will be necessary to take into account this issue and find a way to obtain experimentally the required surface hardness of the samples.

Table 5.1. Summary of the first sets of tests.

Test condition		Wear track	
Steel	Current (A)	Width (µm)	Depth (µm)
100Cr6	0	practically negligible	15-30
	2	260-300	
	4	350-390	
	10	600-620	
Carnit 90	0	210-320	15-30
	2	345-400	
	4	640-650	

5.3. Mechanical characterization of prototype HNAS (Task 5.2)

As previously explained, the following testing activities have been carried out on the material (Carnit 90) industrially produced at ETE. The details of manufacturing and a basic characterization are described in Task 6.1. The material for testing was delivered in the form of round bars about one meter long, the reference material (100Cr6) bars had a 60 mm diameter, while the new grade was supplied in two diameters, 60 and 160 mm, according to the needs of prototype construction. For the conventional material test were performed in the as produced condition and after a heat treatment of quenching and tempering – according to the usual procedure normally applied to the components. Since machining of specimens from hardened material would be extremely difficult, the heat treatments were performed on the specimens already machined.

Vickers hardness (HV10) profiles were performed on metallographic cross sections along one diameter of the bar. The reference grade "as-rolled" has a hardness of around 200 HV, after Quench and Tempering according to Schaeffler specifications the hardness increases to 650-700 HV. The bars of Carnit 90 show hardness values fairly consistent around 300 HV across the whole section with an increase to about 400 Hv10 very close to the periphery.

Tensile tests were performed according to ISO 6892-1 for room temperature testing and ISO 6892-2 for high temperature testing. The specimen geometry is shown in Figure 5.8.

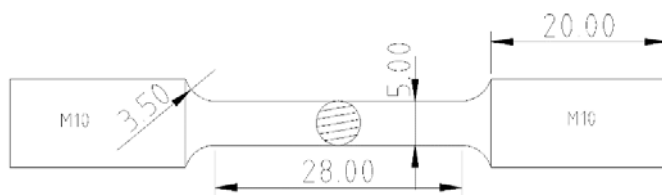


Figure 5.8. Tensile test specimen geometry.

Table 5.2 summarizes the tensile data obtained for all materials. Although not achieving the strength of the reference material in the QT condition, as expected, the new grade Carnit 90 has tensile strength of 950-1000 MPa at room temperature, matching with the target for the bulk, and still around 700 MPa at 400 °C.

Table 5.2. Summary of tensile properties for all materials and HT condition.

Steel	Test temperature (°C)	Yield Strength (MPa)	Tensile Strength (MPa)
Reference 100Cr6 QT	23	n.d.	1479
	400	839	1198
Carnit 90 D60	23	558	954
	400	328	715
Carnit 90 D160	23	635	1007
	200	336	807
	400	347	701

The results of **impact toughness** evaluation, performed on Charpy-V specimens taken in the longitudinal direction, at temperatures in the range -35 – 22 °C, are summarized in Figure 5.9. It is worth noting the excellent behaviour of the new grade Carnit 90, when compared to the reference material. A significantly different behaviour can also be observed between the smaller (D60) and larger (D160) diameter bar. The former was in practice insensitive to temperature changes in the range detected and exhibited much higher values of impact energy, whereas the latter shows a clear decrease at temperature lower than 0°C. Such behaviour can be related to the different reduction rate of the bars in forging, and to a higher rate of micro-defects acting as initiation points, which can still be present in the D160 bars.

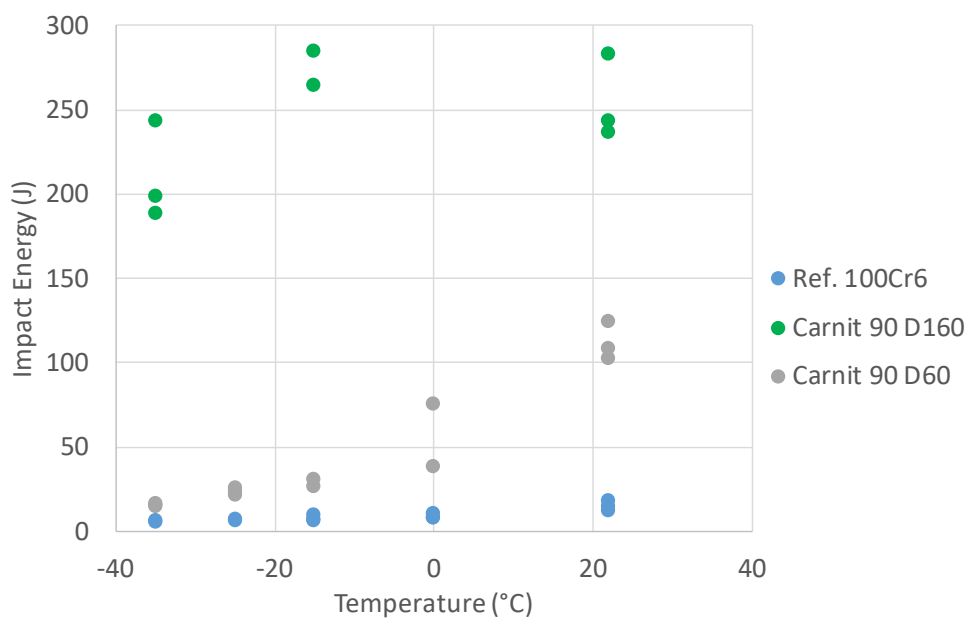


Figure 5.9. Impact toughness results.

Fatigue tests were performed according to ASTM E466, the specimen geometry is presented in Figure 5.10. All tests were performed on a servo hydraulic testing machine, Instron 8502, under load control. According to the specimen geometry above the tests were carried out in uniaxial tensile conditions with $R=0.1$, a sinusoidal wave and a frequency between 15 and 30 Hz. Tests run up to failure or until an arbitrary runout limit of 2×10^6 cycles limit was reached upon which the test was discontinued. A summary of all fatigue tests is presented in Table 5.3.

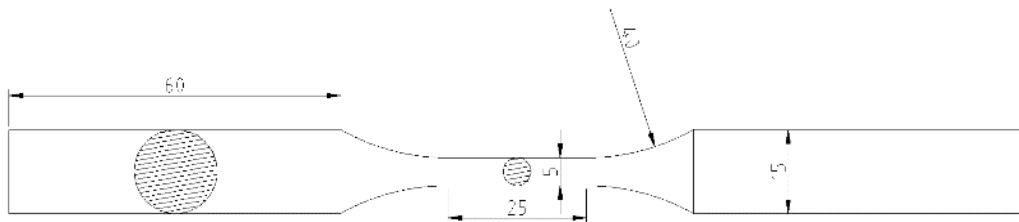


Figure 5.10. Fatigue specimen geometry.

Table 5.3. Summary of fatigue test results for materials and conditions.

MATERIAL	Stress (MPa)				f	Nf	Fracture
	Min	Med	Max	Range			
Reference With TT	133	732	1331	1198	15	4300	Y
	118	651	1183	1065	15	3487	y
	104	569	1035	932	15	11247	Y
	89	488	887	799	15	23777	Y
	59	325	592	532	15	2000581	N
	118	651	1183	1065	15	4924	Y
	89	488	887	799	15	11693	Y
	104	569	1035	932	15	8354	Y
	133	732	1331	1198	15	2949	Y
	74	407	740	666	25	67800	Y
Reference Without TT	35	190	346	311	25	2000001	N
	36	201	365	328	25	2000001	N
	38	209	380	342	25	2000001	N
New grade D60 periphery	52	285	519	467	30	2068535	N
	55	300	546	491	30	875944	Y
	57	315	573	516	30	255090	Y
	53	293	532	479	30	262144	Y
New grade D60 center	52	285	519	467	30	947073	Y
	54	294	535	482	30	1330734	Y
New grade D160 center	57	315	573	516	30	167270	Y
	52	285	519	467	30	655742	Y
	49	270	491	442	30	993295	Y
	46	255	464	418	30	2000000	N
New grade D160 periphery	57	315	573	516	30	454253	Y
	52	285	519	467	30	1999091	N
	60	330	601	541	30	191631	Y
	53	293	532	479	30	680181	Y
	55	300	546	491	30	1994537	Y
	53	293	532	479	30	2000000	N
	60	330	601	541	30	244308	Y
	55	300	546	491	30	313621	Y
	57	315	573	516	30	266739	Y
	55	300	546	491	30	968515	Y

The test results for the reference material (100Cr6 with and without HT) and for the new grade (Carnit) are summarized in Figure 5.11. Hardened material was tested between 50% and 95% of the failure stress whereas some limited tests were also performed in the softened material at stresses between 90% and the yield stress itself.

The new grade steel prove to be extremely hard to machine, some specimens were damaged during production and could not be tested. Particularly for the small diameter bar the number of specimens that could be obtained was very limited, therefore most testing was focused on the larger diameter bar. For the fatigue testing of the new grade steel an average value of 546 MPa was considered as the yield stress for all conditions and the stress levels for the fatigue tests set-up on this basis. Figure 5.11 presents the results obtained for the new grade steel. Although the limited number of tests does not allow a clear conclusion, the center of the D160 bar seems to have a behavior similar to the reference material without HT whereas the periphery exhibited a considerably higher fatigue resistance. In all conditions there were some results that look like outliers compared with the general material trend. If these results are ignored than the smaller diameter bar seem to have a behavior similar to the larger one periphery regardless of the location (center or periphery).

Because of its higher yield stress, the QT reference material endures fatigue cycling at elastic stresses much higher than the Carnit grade, however that difference does not seem so large when compared at similar stresses, where the reference material seem to be just slightly above the Carnit grade.

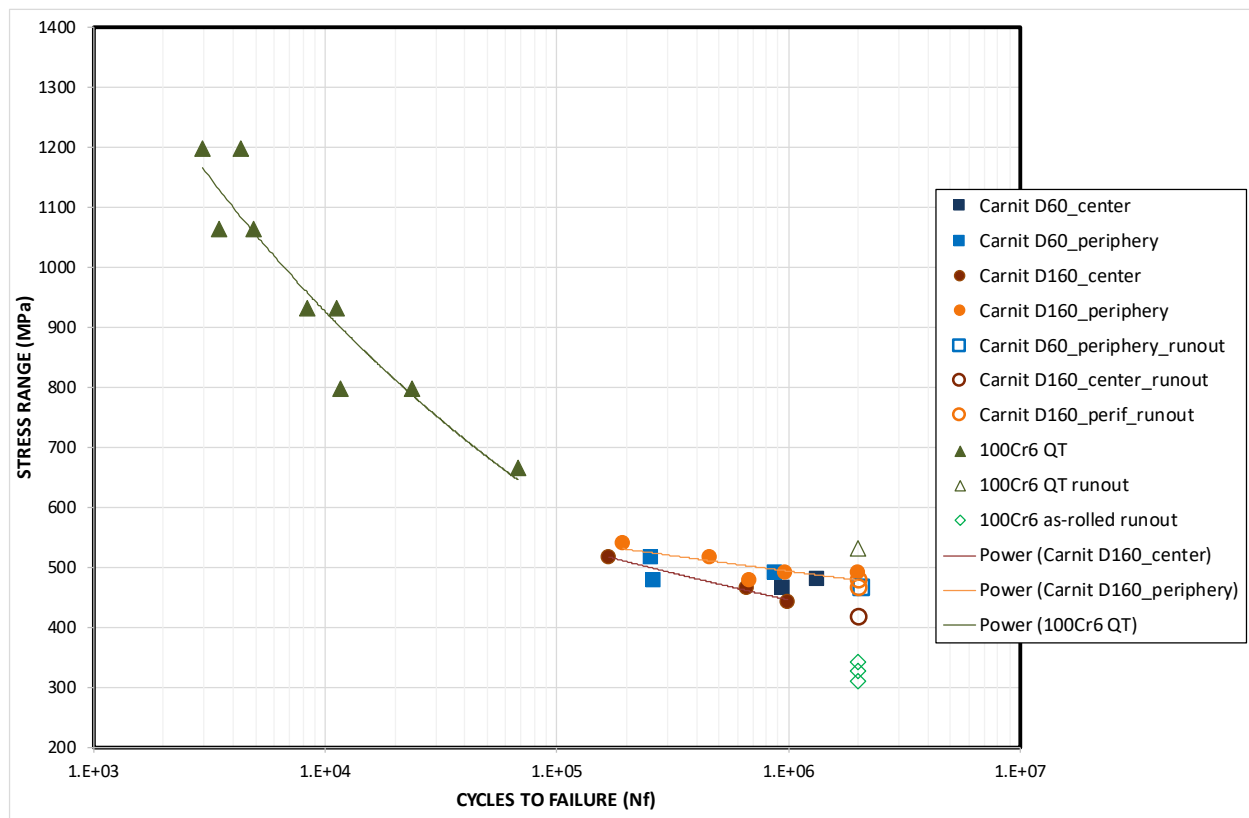


Figure 5.11 – Summary of the results of fatigue tests.

Fracture surface analysis of tensile specimens of the new grade steel reveals what seems to be a general grain boundary weakness translated in general de-bonding of the grains more noticeable in the center of the specimen than close to the edges, Figure 5.12, where the material exhibited a predominantly dimpled structure with sporadic de-cohesion of boundaries. Similar behavior was observed on a run out fatigue specimen tensile tested afterwards, Figure 5.13. This seems to be an inherent characteristic of the material under high stresses (or strains) not associated with a particular dynamic or monotonic loading mode.

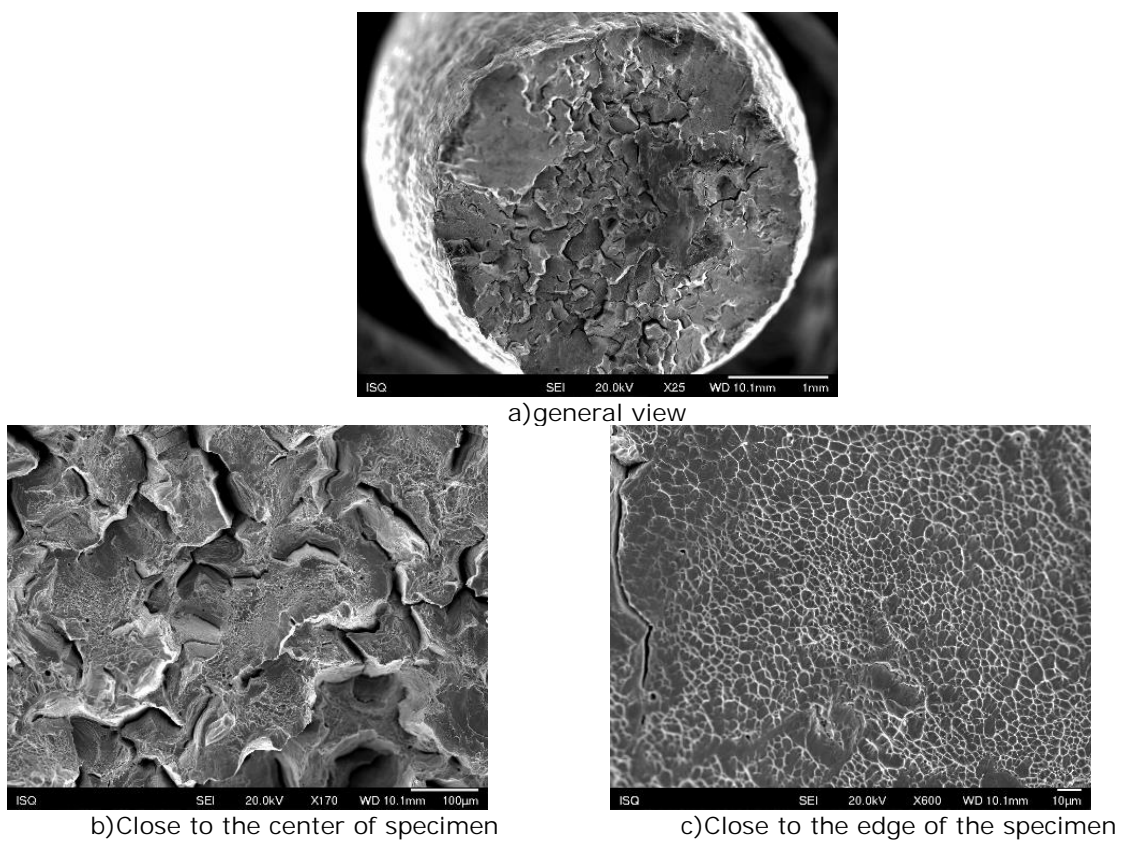


Figure 5.12. Typical fracture surface of a tensile specimen from new grade steel (D160).

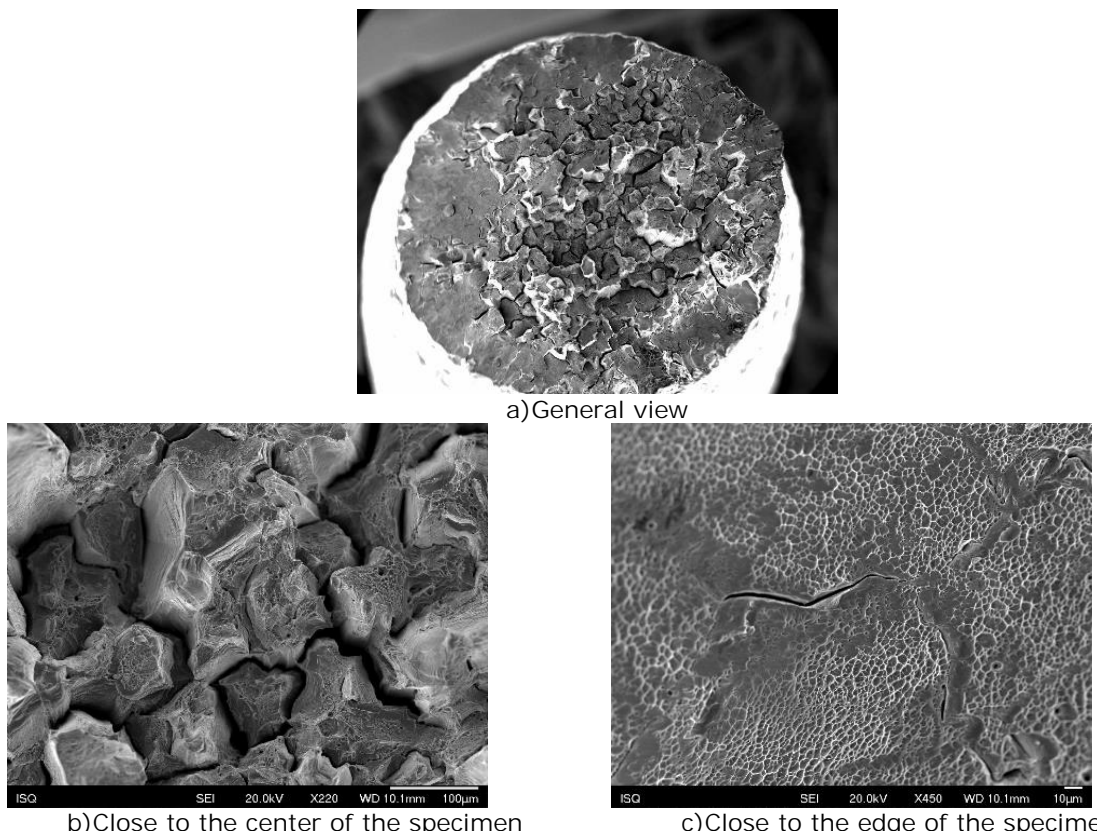
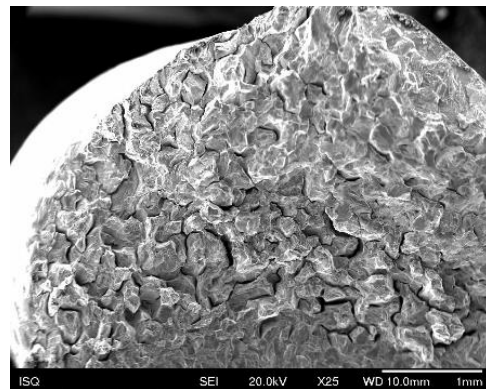


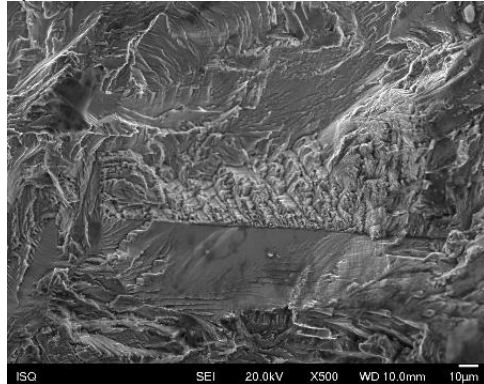
Figure 5.13. Typical fracture surface of run out fatigue specimen (2×10^6 cycles) then tested in tensile.

Similar analysis of fatigue specimens showed that this weakness could be, at least in part, associated with the processing route of the material. Specimens from the larger bar (D160 mm) showed a similar

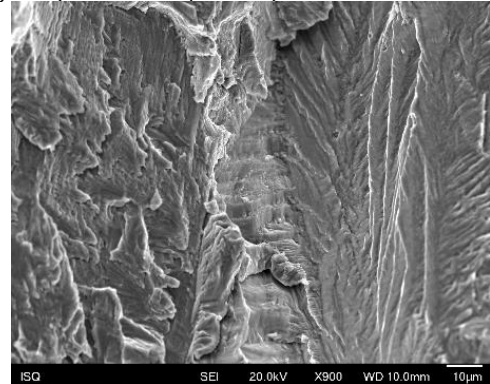
behaviour in the final unstable fracture propagation, Figure 5.14, this behaviour being associated with specimens from both the center and the periphery of the bar. No material or machining defects could be associated with the fatigue initiation in neither specimen analyzed. Although some large grains were often visible near the initiation site, Figure 5.14 b), a clear correlation between this and the fatigue life could not be established. The initial stage of stable propagation was generally associated with a complex failure mode resembling grain cleavage, sporadic striation could also be observed, Figure 5.14 c). The transition from stable to unstable fracture was quite sharp, Figure 5.14 d), the latter being predominantly by grain de-cohesion with some evidence of plasticity, Figure 5.14 e), similar to what was observed in tensile specimens.



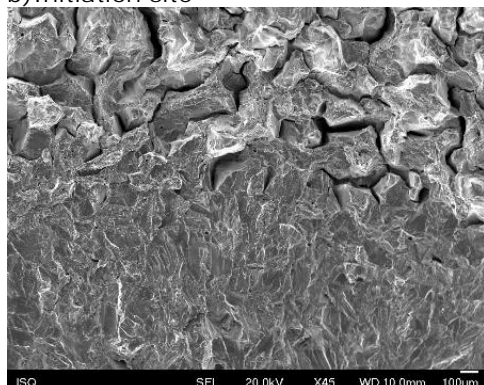
a) General view of final fracture and transition region (bottom of picture)



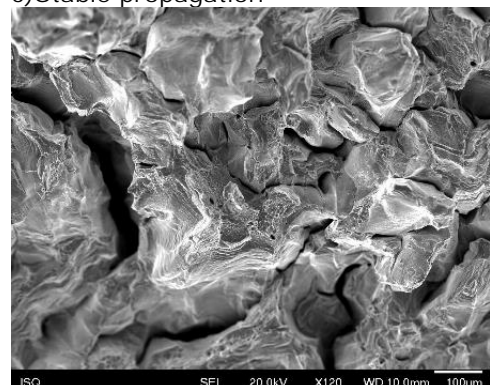
b) Initiation site



c) Stable propagation



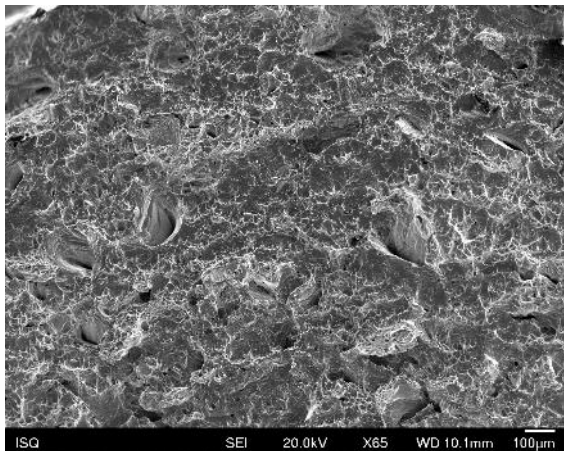
d) Transition region detail



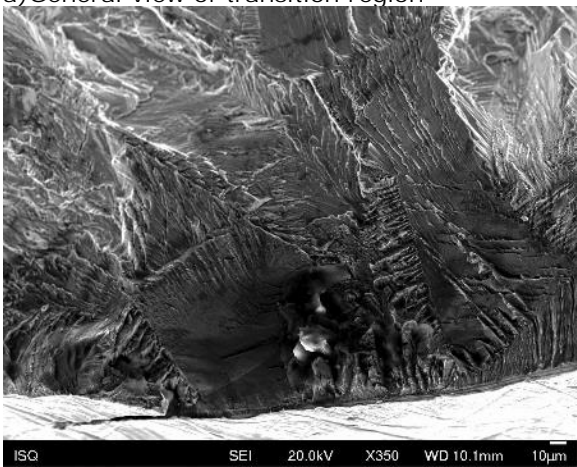
e) Fast unstable fracture

Figure 5.14. Fractographic analysis of a fatigue specimen from D160 periphery. Stress range 516 Mpa, fatigue life 266739 cycles.

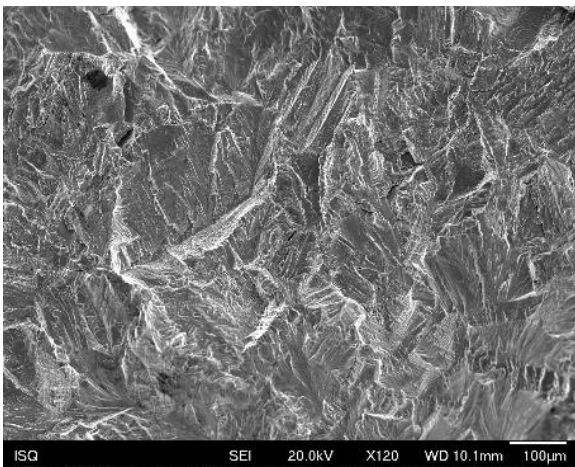
Specimens from the smaller diameter bar, D60, though exhibited a slightly different behavior, again identical regardless the position of the specimen within the bar, center or periphery. Although the failure mode had some similarities the transition from the stable to the unstable mode was not so sharp and well defined and there was much less grain de-bonding in the final unstable fracture surface, Figure 5.15. Ductility in this final stage was also higher. These conclusions were also valid for both center and periphery of the D60 bar and independent of the stress range.



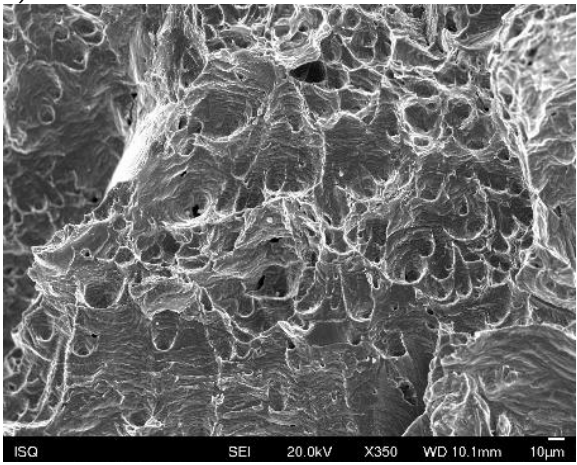
a) General view of transition region



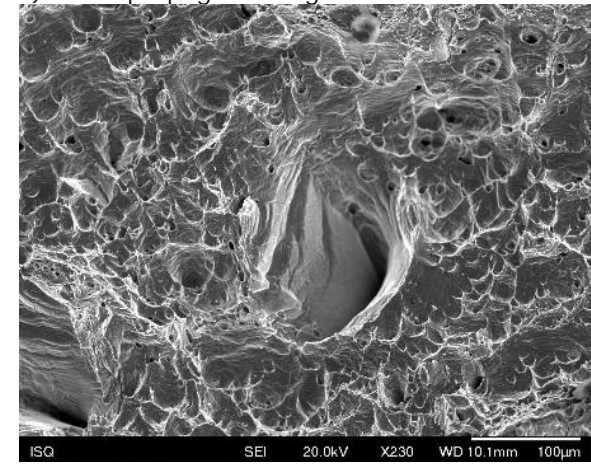
b) initiation site



c) Stable propagation region



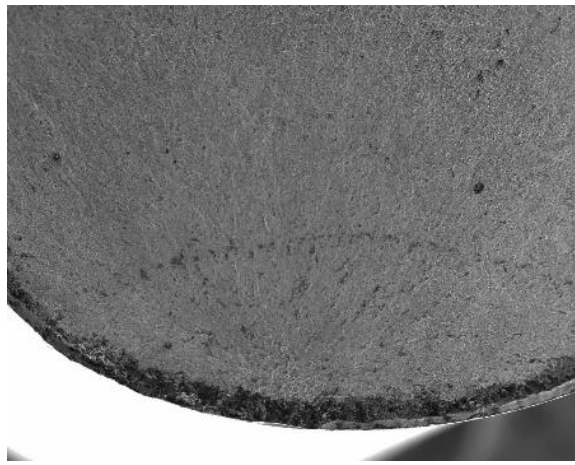
d) Unstable propagation region



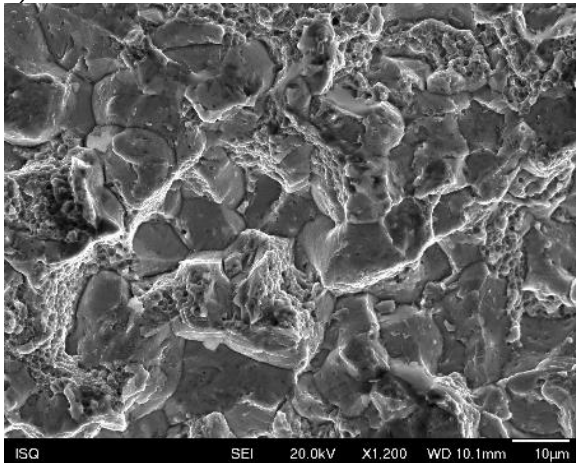
e) Final failure

Figure 5.15. Fractographic analysis of a fatigue specimen from D60 periphery. Stress range 516 Mpa, fatigue life 222090 cycles.

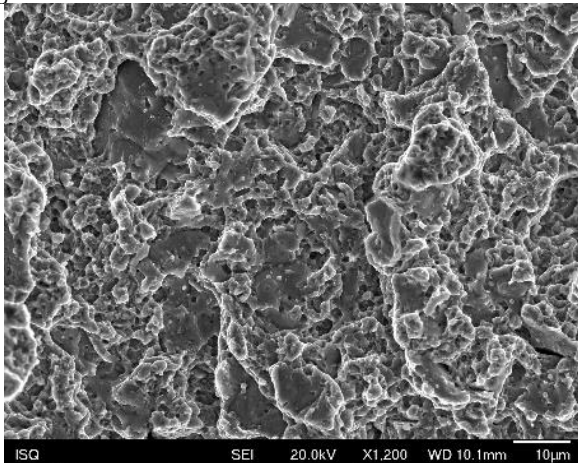
Notably the reference material presented a completely different behavior all along. Figure 5.16, presents the analysis of a fracture surface of this material. Initiation seems to be associated with some intergranular failure, Figure 5.16 b), and there is no clear distinction between the stable growth region and the final unstable one, Figure 5.16 d) and e).



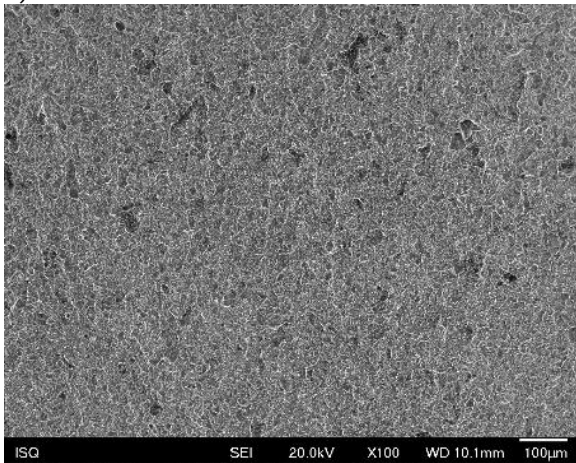
a) General view of the initiation and transitions region.



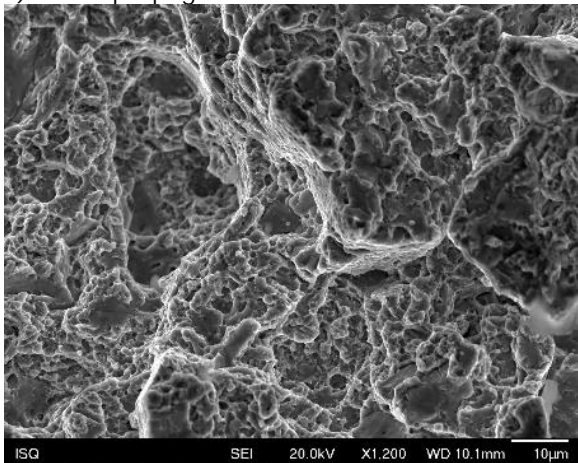
b) Initiation site



c) Stable propagation



d) Unstable propagation



e) Final failure

Figure 5.16. Fractographic analysis of a fatigue specimen from reference material. Stress range 932 MPa, fatigue life 8354 cycles.

Rolling Contact Fatigue (RCF) tests could be performed on a set of reference material, while due to the significant delay and difficulties encountered in the production of experimental materials, could not be carried out on the new grade steel.

Rolling contact fatigue tests on 100Cr6 steel produced via ingot have been carried out using MAYES UNISTEEL MARK IV. Samples for Rolling contact fatigue tests were machined according to the standard test requirements ($R_a < 0.05 \mu\text{m}$).

The usual test procedure involves performing the rolling contact fatigue tests at a constant load applied on a number of rollers. The load is shared between the rollers and generates a stress field in the surface of the material which is higher in points slightly below the surface. The presence of inclusions in the

vicinity of these points produces local stress riser leading to the generation of microcracks and in medium term, leads to the failure of the component. Due to the high dispersion of test results during rolling contact fatigue tests, even under strict conditions, it is necessary to perform a large number of tests and then take a statistical analysis of the data obtained. The most accurate method, called the full trial, consist of running the entire population to the end of life. In reality, since there is a non-null probability that some specimens survive a number of cycles nearly infinite, life test is limited and a limit number of cycles is chosen above which it is considered that the sample don't breaks and the test specimen is stopped.

A large population (typically 50 specimens) is researched and all samples were tested at the same load (50.5 Kg of weight, equivalent to a contact pressure of 4200 MPa, as recommended by the manufacturer home team MAYES-UNISTEEL). Each specimen was tested to failure or to a sufficiently high number of cycles (typically $50 \cdot 10^6$ revolutions). The usual loading system consists of a support on which the weights by a lever arm presses against the assembly, cage and rollers are located lower the sample ring. The cage contains sixteen balls ($\Phi 7.15$ mm) (eight of these are extracted from alternate positions in order to double the ball load and reduce by half the frequency). Currently ten balls are maintained, thus reducing the test time in half, but to retain the ball load is necessary to increase the number of weights. Pitting is detected by vibration sensor which automatically stops the machine. The results should be treated statistically and adjusted to a Weibull distribution, which corresponds to the case of component failure probability which varies with time (aging cumulative damage), which is typical in bearings.

Figure 5.17 represents the Weibull distribution of rolling contact fatigue life of 100Cr6 produced via ingot.

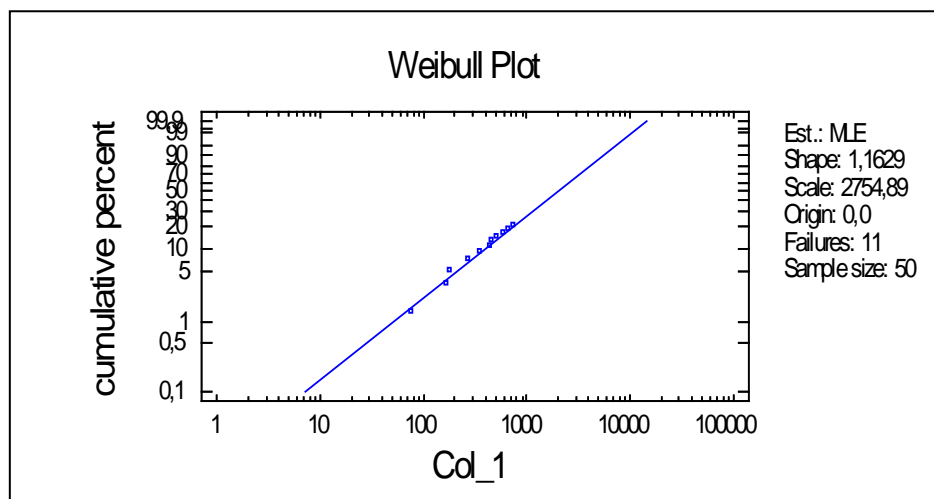


Figure 5.17. Cumulative percentage vs time to failure for 100Cr6.

The estimated cumulative percentage failed versus the time to pitting is plotted in Figure 5.18, fitting a straight line to the points. From this figure we can read out the L10, L50, and L90 lives prediction.

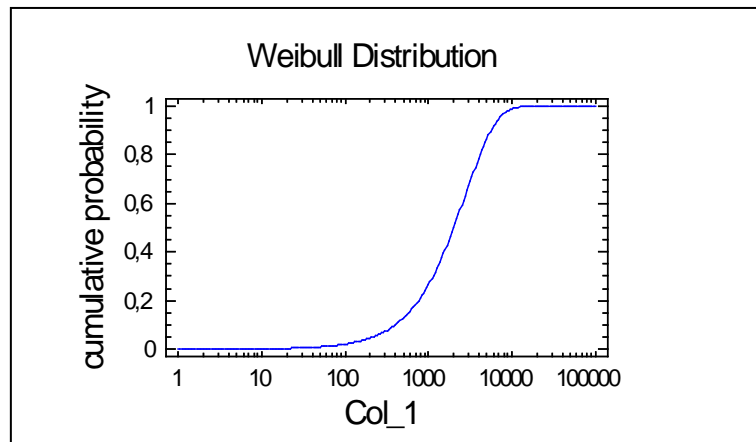


Figure 5.18. Weibull distribution of rolling contact fatigue life of 100Cr6.

5.4. Corrosion and tribological characterization (Task 5.3)

Introduction

Wear and corrosion of materials are among the most important failure mechanisms in industry [73]. An important problem in tribology concerns the interaction between friction and surface chemical reactions (corrosion) occurring in reactive environments such as aqueous media or hot aggressive gases. Corrosion is the degradation and removal of a material surface into its constituent atoms due to chemical reactions (e.g., oxidation, sulphidation, chlorides/salts), and is essentially an electrochemical process in reaction with an oxidant (such as oxygen). The severity of corrosion depends on chemical kinetics, which can have a strong dependence on temperature. According to Wood, the corrosion control is a growing concern in wind turbines [74].

Tribocorrosion describes material degradation due to the simultaneous action of chemical and mechanical effects in a tribological contact. It may occur in a variety of conditions – sliding, fretting, rolling, impingement – in a corrosive medium and in many engineering applications: power generation, marine and offshore industries to biomedical implant. The term *tribocorrosion* was defined by Landolt in 1993. As corrosion and wear can also behave synergistically to further degrade performance and reduce the lifetime of the metal surface component or part [74, 75], it is worth noting that material loss can be larger than the sum of the losses due to wear and corrosion acting separately. In tribocorrosion, then, the consideration of the individual mechanism – wear and corrosion – is not sufficient to explain the overall phenomenon. Although tribocorrosion has achieved significant momentum among many tribology and corrosion researchers, the topic is less recognized in industry field. This reflects in the guidelines, standard test methods, literature publications and papers, where the lack of tribocorrosion studies related to marine and offshore applications is obvious.

Experimental

A tribo-electrochemical test apparatus has been realized at CSM laboratory modifying a pin-on-disc tribometer (RTM, Italy) by installing a 3 electrode electrochemical cell (Figure 5.19) [76]. To ensure the electric insulation the electrochemical cell was made of a polymeric corrosion resistant material and the counterpart, namely a 10 mm diameter Al_2O_3 sphere (1120 HV), was lodged in a polymeric ball-holder (Figure 5.20).



Figure 5.19 The modified RTM ball-on-disk tribometer with the electrochemical cell during a test.

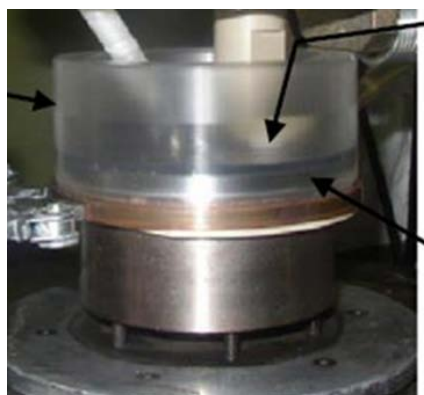


Figure 5.20. A detail of the electrochemical cell. Clockwise arrows indicate: the polymeric cell containing the electrolyte, the Al_2O_3 ball in its ball holder and finally the AISI 52100 disk.

Inside the electrochemical cell the sample (disk) serves as working electrode (WE) and a platinum wire as counter electrode (CE). To complete the electrochemical set-up a reference electrode, namely a saturated calomel electrode (SCE), is placed close to the WE in a fixed reproducible position in order to minimize ohmic drop and shielding effects (see Figure 5.21).



Figure 5.21. Detail of electrodes inserted in the electrochemical cell: reference calomel electrode is the one with green upper part, while the counter electrode -a Pt wire- has a rubber insulating collar (red).

The material to be tested is installed as the bottom base of the cell, facing the solution at one side and screwed to a disc shaped copper support at the opposite side. A sliding contact on a copper disc allows the electrical signal to reach the potentiostat measurement system. Unidirectional sliding test (ball-on-disk) schematic representation is shown in Figure 5.22.

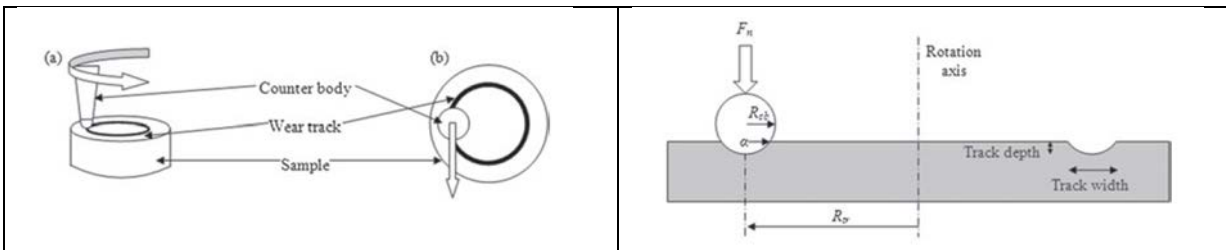


Figure 5.22. Scheme of the experimental setup for unidirectional sliding test. Left: (a) front view (b) top view. Right: zoom-in.

In continuous unidirectional sliding test the relative motion between pin and disk is constant throughout the test duration and the pin describes circles of a given radius on the disk surface. When sliding is applied wear occurs and the real contact area (ball/surface of disk) increases (while the contact pressure decreases) [77]. During a tribocorrosion experiment, the cell rotates at specified speed and the alumina ball rubs against the specimen surface immersed in 3.5 wt. % NaCl natural aerated solution. The electrolytic solution was prepared starting from analytical grade NaCl salt (Carlo Erba) and D.I. water. Sliding wear test were conducted at a contact load of 150 N applied by means of a loading cell. A preliminary campaign of test was carried out aimed at selecting suitable load/sliding speed coupling. The value of normal force F_n should be selected to avoid plastic deformation of the bulk material. Electrochemical characteristic parameters, current, potential and their changes were measured by a potentiostat / galvanostat Autolab PGStat 30 S/N instrumentation with Nova software to analyse polarization data. All potential values in the experiments are given with respect to SCE reference electrode.

Samples for ball-on-disk tribometer used as test specimens were discs of 7.3 mm diameter and 6.5 mm in height (Figure 5.23), made in AISI 52100 (Q&T) martensitic steel (100Cr6). The disks were machined from original piece, than heat-treated (Q&T) and finally mirror-like polished. All test were carried out at R.T. In the event of temperature increase due to rubbing, an air cooling system was adopted. To compare

results in each corrosion/tribocorrosion couple of tests, the area of the disk exposed to corrosion and rubbing experiments need to be the same. For this reason, disks were protected to avoid the contact of the whole surface with the electrolyte. Disks were painted by a varnish, forming a film after drying. Then part of the film was removed and only let defined area of the sample exposed to the solution. Figure 5.23 shows drawings and disk samples. Down left-right images shows 100Cr6 martensitic steel (Q&T) disk after mirror-like polishing and a samples after tribotests painted with protective varnish with a defined area exposed (to the solution). The last image show a cleaned sample after the painting removal. Two tracks are visible: a wear track and a corrosion test zone. Each area was exposed to the solution in two separate experiments.

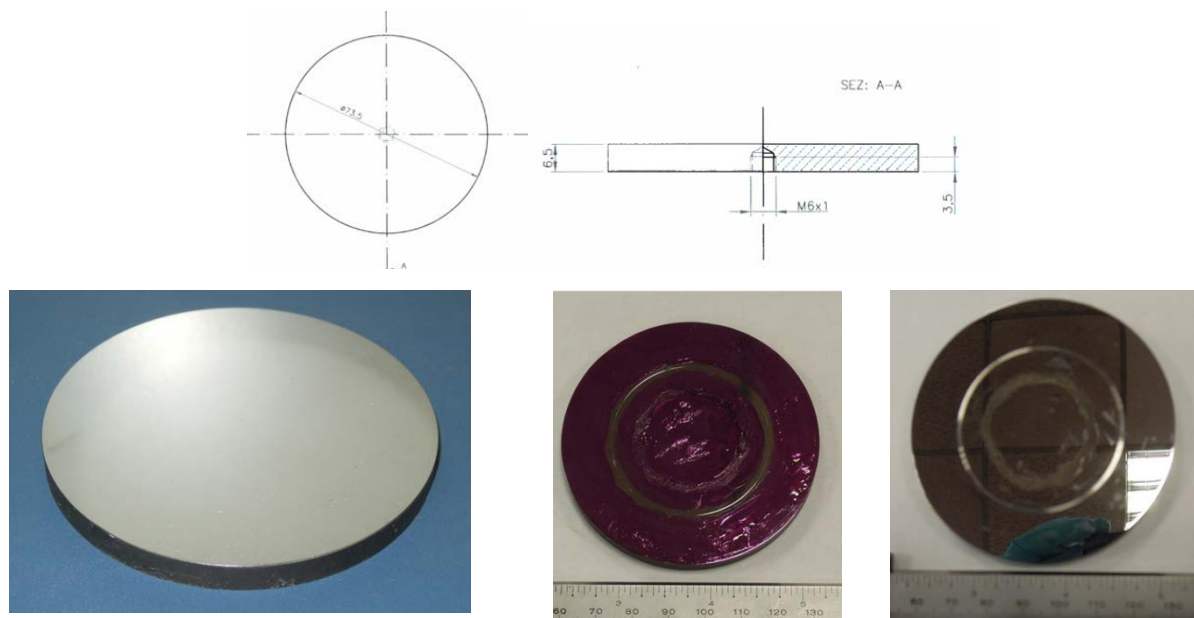


Figure 5.23. Disk drawings and 100Cr6 steel samples before and after tests.

Preliminary study of the tribocorrosion behaviour of 100Cr6 martensitic steel, that will be adopted as 'reference material' for comparative analysis, aimed at establishing a baseline and testing the experimental setup. In fact, in future activities involving tribocorrosion behaviour of new HNAS alloys and of 100Cr6 will be compared. Several series of experiments were carried out to study corrosion-wear behaviour [78, 79]. They are summarized hereinafter:

- ✓ Open Circuit Potential measurements. A control if a stable equilibrium condition is reached.
- ✓ Potentiodynamic tests following OCP, involving measuring polarization curves. A potential sweep at $1 \text{ mV}\cdot\text{s}^{-1}$ speed was applied.

The experiments repeated during sliding, with a normal load of 150 N applied were:

- ✓ Open Circuit Potential measurements
- ✓ Potentiodynamic tests following OCP.
- ✓ Wear test at protection potential (Potentiostatic)
- ✓ Wear test at OCP.

After the corrosion-wear tests the specimens were ultrasonically cleaned in acetone to remove debris. The normal load was checked and varied from lower to higher values in preliminary experiments until a detectable wear track originated. All wear test in this activity were carried out with 150 N load. When a fixed normal load is applied to the sample a wear track originates and material coefficient of friction in the experimental condition (CoF) can be measured. Ring shaped wear track diameter was measured to obtain the exposed area. The wear scars depth were estimated measuring track profile by means of the Carl Zeiss Axio Imager M2m optical system.

Results

The results of two experiments on 100Cr6 martensitic disks are reported in Figure 5.24. Evolution of OCP vs time shows that potential decreases with time toward less noble values. The two PD curves are

superimposed showing a good repeatability. The anodic branch in both curves evidences that the current increases as the potential increases and no passivity takes place.

OCP measurements enables to gather electrochemical information but is powerless for assessing corrosion kinetics. The latter can be extracted from PD curves.

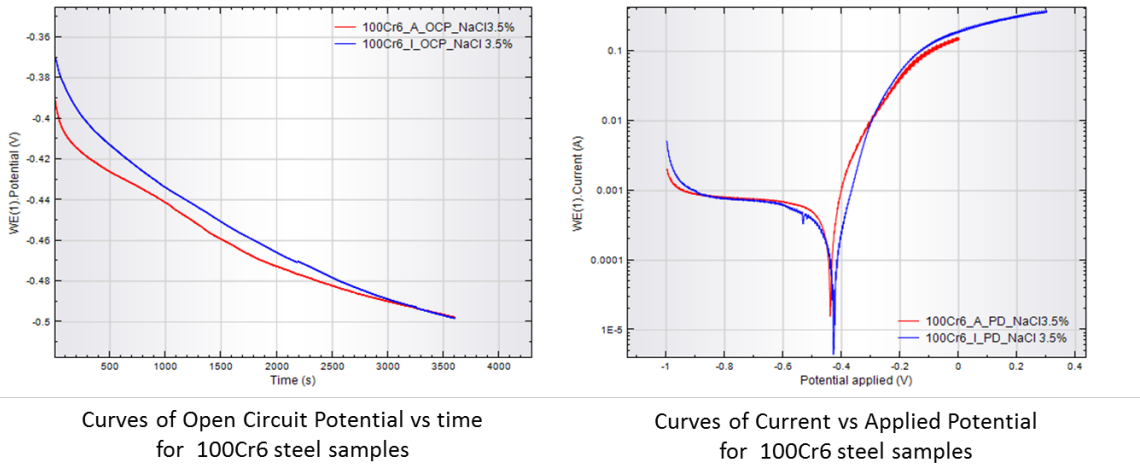


Figure 5.24. Curves of OCP vs time (left) and potentiodynamic Current vs applied potential (right) for two 100Cr6 samples (NaCl 3.5 wt.% solution, Potential sweep rate: 1 mV·s⁻¹).

When load is applied in a tribocorrosion experiment, the polarization curve reflects the corrosion behaviour with a shift toward active values of potential (Figure 5.25). The OCP curve shifts abruptly toward lower potential values (red curve, left). The PD curve moves slightly leftward and up in the Current/Potential plane. This means that the material is suffering for a tribocorrosion phenomenon the extent of which has to be evaluated. In these experiments OCP after PD was not recorded. Oscillations that are visible in tribocorrosion curves are an expected phenomenon and originates by contact positions of friction couples that change continuously.

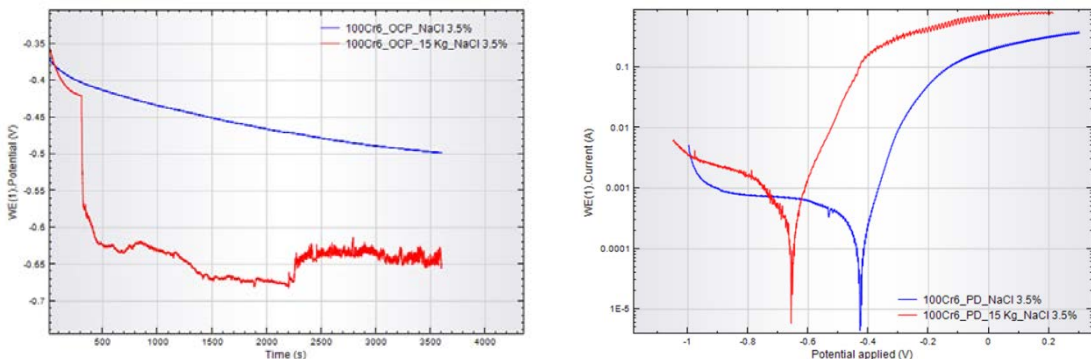


Figure 5.25. Comparison curves of OCP and potentiodynamic for two 100Cr6 samples with (150 N) and without applied load. Left: applied potential vs time; right: current vs applied potential. (NaCl 3.5 wt.% solution, Potential sweep rate: 1 mV·s⁻¹)

Table 5.5 reports characteristic E_{corr} and I_{corr} and J_{corr} parameters values for corrosion and tribocorrosion of 100Cr6 steel evaluated from PD curves (Tafel extrapolation method). Current densities are normalized values with respect to the sample area exposed to the solution. The current density values J_{corr} are of the same order of magnitude in both corrosion and tribocorrosion, while E_{corr} shift is more than 200 mV cathodic for tribocorrosion with respect to corrosion.

Table 5.4. Characteristic E_{corr} and I_{corr} and J_{corr} parameters for 100Cr6 martensitic steel in corrosion and tribocorrosion (150 N load) experiments.

Sample	E_{corr} V	I_{corr} A	J_{corr} A/cm ²
100Cr6			
100Cr6_A	0.422	2.09x10-4	6.97x10-5
100Cr6_I	0.422	1.20x10-4	4.0x10-5
100Cr6_L_150N	0.657	2.04x10-4	6.8x10-5

Wear test were conducted at OCP to evidence the total loss of material due to both wear and corrosion were carried out for a duration of three hours (rotation speed and total path length fixed). The same conditions were selected for experiments at cathodic protection (1V cathodic vs E_{corr}) to evaluate the material loss due to wear only. Coefficient of friction (CoF) was recorded. After tests and ultrasonic cleaning samples tracks shape and depth were evaluated. In Figure 5.26 and Figure 5.27 CoF curve for 150 N load experiments at OCP and in cathodic protection condition are reported. The CoF average value at OCP and in cathodic protection (-1V vs E_{corr}) are 0.39 and 0.42 respectively. Plots of track cross sectional profile shown in Figure 5.27 evidenced a possible limit of the optical system of detection: track cross sections seem to be flat with the result that no wear volume can be extracted from these data.

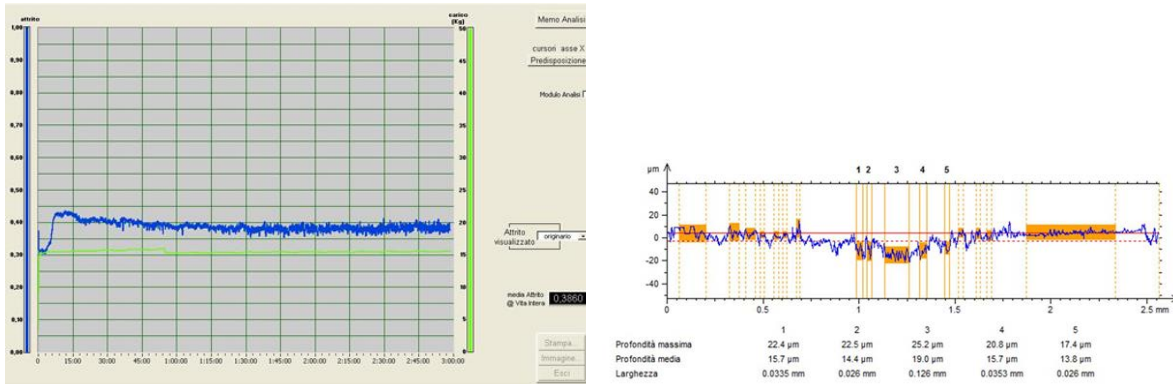


Figure 5.26. 100Cr6 CoF curve (vs test time) at OCP and 150 N load in a 3 h test and the wear track cross sectional profile detected by means of the optical system: Carl Zeiss Axio Imager M2m. plot. 3 hours tests in NaCl 3.5 wt.% solution.

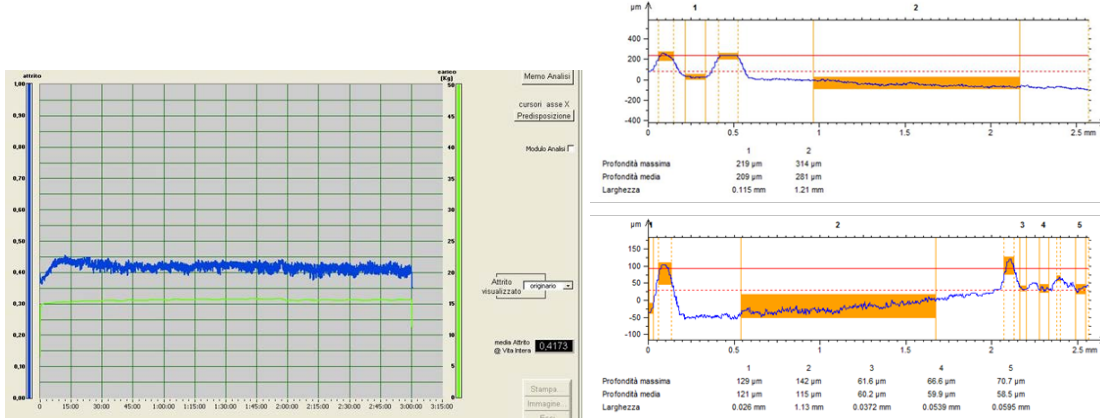


Figure 5.27. CoF curve (vs test time) in potentiostatic control; 3 hours test and 150 N load. Wear track cross sectional profile detected by means of the optical system: Carl Zeiss Axio Imager M2m. Potentiostatic conditions (-1 V vs E_{corr}), NaCl 3.5 wt.% solution.

A set of corrosion/ tribocorrosion experiments was carried out on 100Cr6 just before the campaign on the developed and produced CARNIT steel. The 100Cr6 OCP and PD curves (new set) without load and in 150N load condition, the samples after experiments and the CoF profile curve are reported in the following Figure 5.28, Figure 5.29, Figure 5.30.

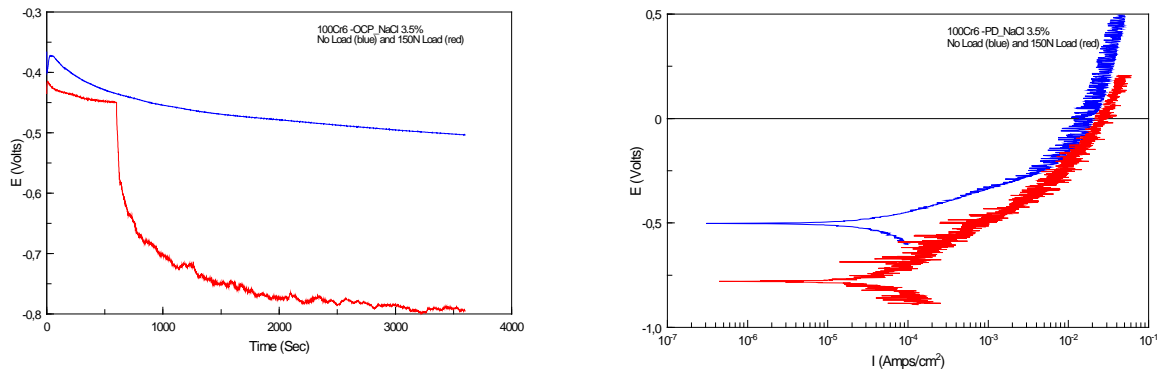


Figure 5.28. Comparison between curves for OCP and potentiodynamic polarization for 100Cr6 with 150 N load and with no applied load. Left: applied potential vs time; right: applied potential vs log of current (NaCl 3.5 wt.% solution, Potential sweep rate: 1 mV·s⁻¹).



Wear-corrosion track after a PD test, with 150 N Load in a 100Cr6 specimen. NaCl 3.5% solution.



Corrosion track (outer circle) after a PD test, with no Load applied in a 100Cr6 specimen.

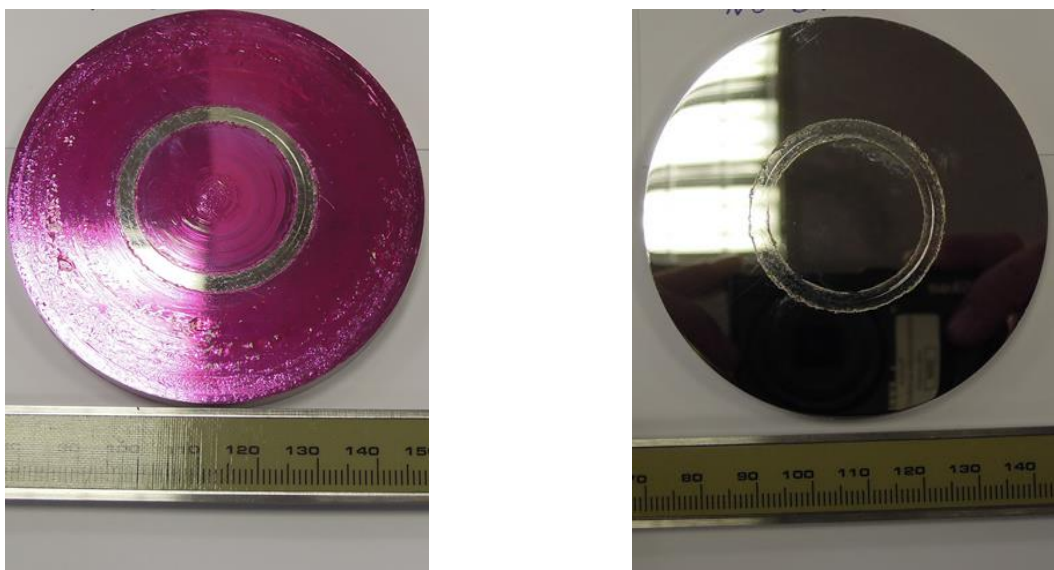
Figure 5.29. A 100Cr6 tribocorrosion specimen with the two tracks developed after a tribocorrosion and a corrosion experiment. Left: a wear track due to potentiodynamic test carried out at 150 N load; right: the outer corrosion track is from a potentiodynamic test.



Figure 5.30. CoF recorded during PD test with 150 N Load for 100Cr6 specimen. NaCl solution 3.5%.

When the potential is scanned and then changed a modification of the surface exposed to the electrolyte is expected. At the same time the exposed surface is modified due to interaction with the pin under the applied load. A complex synergism takes place and fluctuations in the CoF values and trends are expected. The average value of CoF is 0.23.

For tests on CARNIT samples were protected following the already described procedure. After PD testing in NaCl solution only the exposed area has been modified by corrosion phenomena while the protected zone of the sample are unaffected, as shown in Figure 5.31.



Corrosion area on a CARNIT specimen after a PD test in 3.5% NaCl solution

The corrosion track on the same CARNIT specimen after the removing of the protective varnish

Figure 5.31. CARNIT specimen after a PD corrosion test in 3.5% NaCl solution.

The potentiodynamic test carried out after 60 minutes of stabilization at OCP in the NaCl solution, with a load of 150 N gave the results shown in Figure 5.32. In the E vs t graph the steep decreasing of OCP corresponds to the load application. The wear – corrosion track and the profile of the coefficient of friction during the test are reported in Figure 5.33; the average value for the CoF is 0.42. After the PD test at 150 N load the wear-corrosion track for CARNIT immediately appeared wider than the 100Cr6 one to the naked eye (compare Figure 5.31 with Figure 5.29).

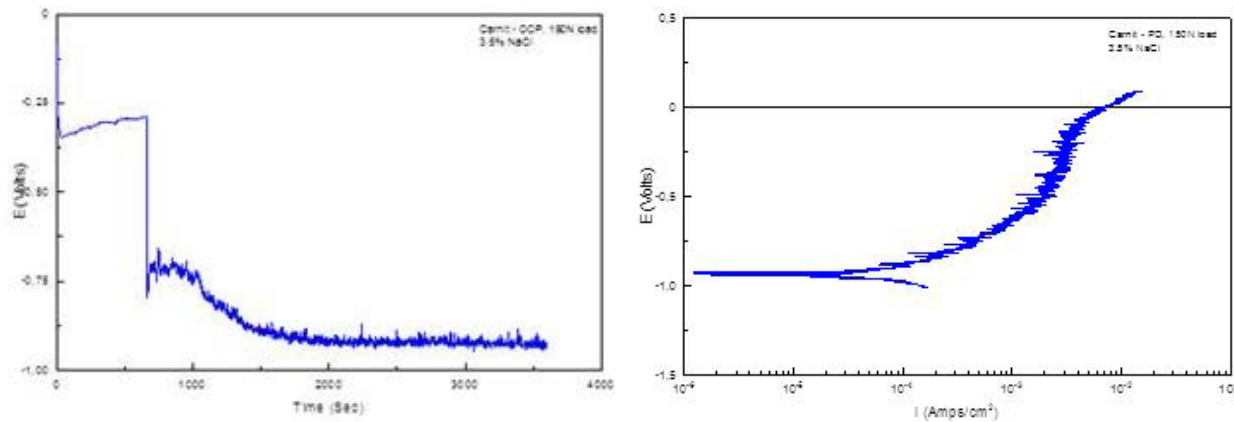
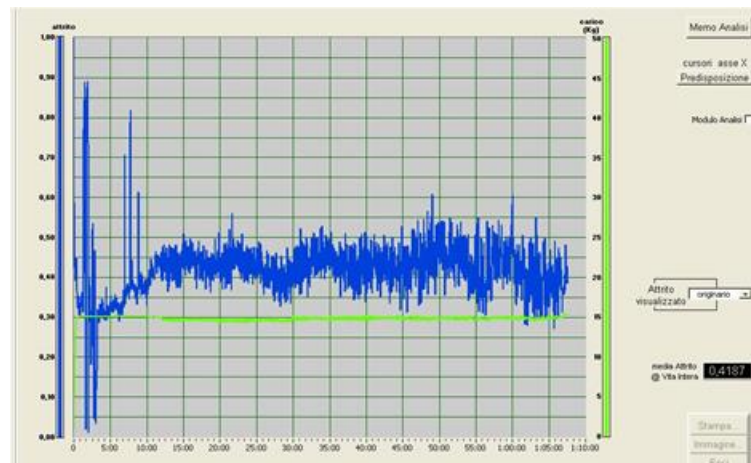


Figure 5.32. OCP and potentiodynamic polarization curves for CARNIT at 150 N load. Left: applied potential vs time; right: applied potential vs log of current density. (NaCl 3.5 wt.% solution, Potential sweep rate: $1 \text{ mV} \cdot \text{s}^{-1}$).



Wear-corrosion track after a PD test, with 150 N Load in a Carnit specimen. NaCl 3.5% solution



CoF recorded during the PD test with 150 N Load for the Carnit specimen. NaCl solution 3.5%

Figure 5.33. A track on Carnit tribocorrosion specimen after a potentiodynamic tribocorrosion experiment carried out at 150 N load.

The average value of CoF for Carnit is higher (double) than 100Cr6 and the corresponding curve less stable being very noisy.

According to the friction and wear signals the shape of the curves is the response to the contact between pin and disk and it is the combination of an instant decrease in roughness caused by the application of the load and its successive increase caused by the debris formation. For Carnit the increase in CoF and the related phenomena are more evident.

In the following Figure 5.34, OCP and PD curves are referred to experiments carried out without any load and 150N load and compared, for 100Cr6 and Carnit.

In the in the E vs t plot the curves for the two materials exchange their trend showing an opposite behaviour according to the experimental conditions (corrosion or tribocorrosion).

Carnit curve lies at higher potential values (more positive, better corrosion resistance) in the upper pair but the material potential drops below the one for 100Cr6 in tribocorrosion condition, evidencing a lower capacity to resist corrosion under load.

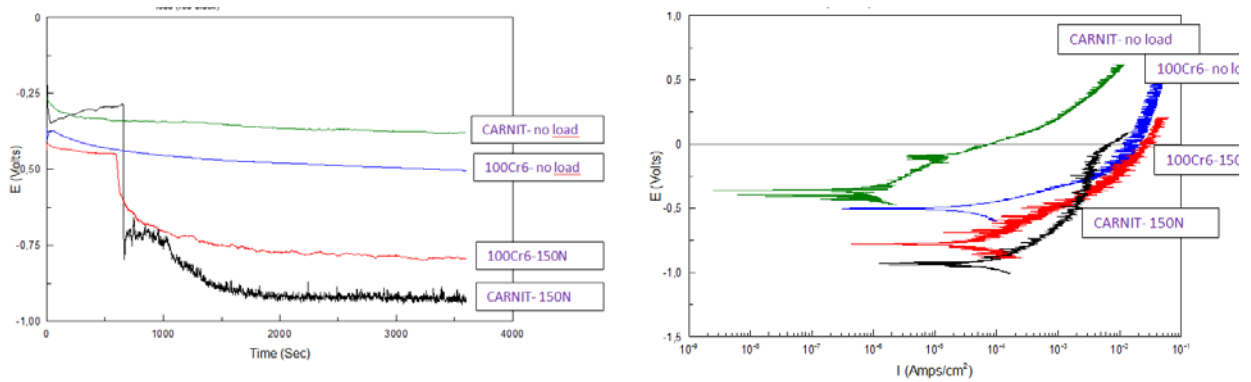


Figure 5.34. Comparison between Carnit and 100C6 OCP curves (left) and PD curves (right) in corrosion and tribocorrosion tests. Tests carried without any load and at 150 N load. NaCl 3.5% solution. Potential sweep rate: $1 \text{ mV}\cdot\text{s}^{-1}$.

In Table 5.6. Characteristic E_{corr} and I_{corr} and J_{corr} parameters for Carnit and 100Cr6 martensitic steel in corrosion and tribocorrosion (150 N load) experiments are summarized the characteristic E_{corr} , I_{corr} and J_{corr} parameters values for corrosion and tribocorrosion of Carnit and 100Cr6 steels. E_{corr} calculated and observed values mainly reflect the behaviour already described. A slightly high dispersion was evidenced between new and previous results for 100Cr6.

Table 5.5. Characteristic E_{corr} and I_{corr} and J_{corr} parameters for Carnit and 100Cr6 martensitic steel in corrosion and tribocorrosion (150 N load) experiments.

E_{corr} Obs, V	E_{corr} Calc, V	J_{corr} A/cm ²	Load N
CARNIT			
-0.858	-0.852	8.89×10^{-5}	150
-0.815	-0.806	2.49×10^{-4}	150
-0.310	-0.306	1.04×10^{-6}	-
-0.388	-0.403	1.82×10^{-6}	-
-0.354	-0.356	1.94×10^{-6}	-
100Cr6			
-0.504	-0.502	9.43×10^{-5}	-
-0.794	-0.779	1.19×10^{-4}	150

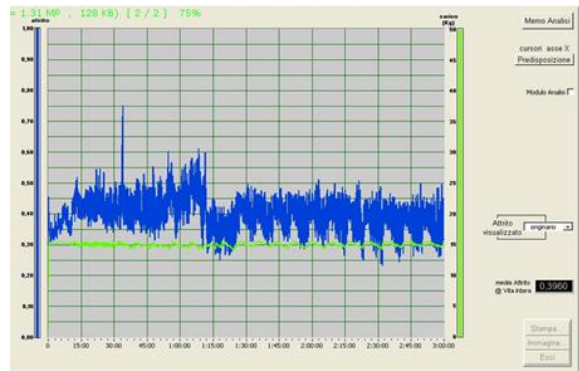
In tribocorrosion tests Carnit current densities, that are normalized values with respect to the sample area exposed to the solution, resulted two order of magnitude higher (and equal to those for 100Cr6) than the values recorded in corrosion tests. Current densities for 100Cr6 are of the same order of magnitude in both corrosion and tribocorrosion experiments.

Potentiostatic (PS) and OCP tests aimed at evaluating the loss of material due to tribocorrosion under protection and tribocorrosion in a free corrosion conditions (no applied voltage).

Test were carried out for three hours at 150N load in 3.5% NaCl solution, the same experimental condition set for 100Cr6 (TQ). Wear scars were evaluated by a profilometer and roughness Tester, Mitutoyo SV 3200 H4.



Wear track after a PS test, with 3h at 150 N Load for a Carnit specimen. 1V cathodic vs Ecorr. NaCl 3.5% solution



CoF recorded during the PS test, with 3h at 150 N Load for the Carnit specimen. NaCl solution 3.5%

Figure 5.35. The track on Carnit tribocorrosion specimen after a PS tribocorrosion experiment carried out at 150 N load for 3 hours and -1V cathodic vs Ecorr. Average CoF value resulted 0.40.

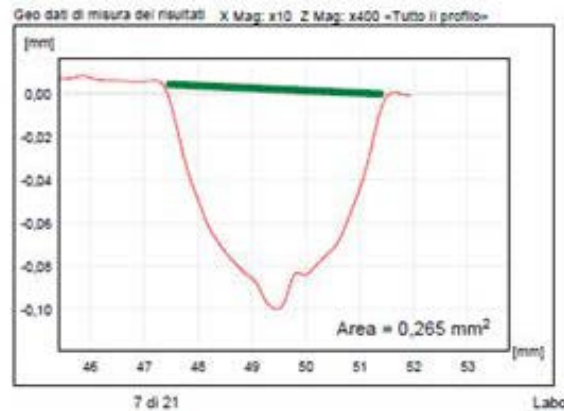
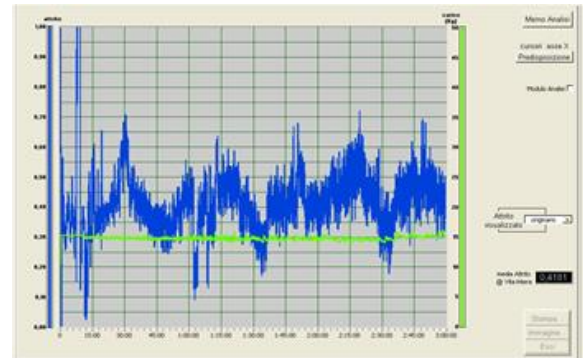


Figure 5.36 The method adopted for track profile measurements and a cross sections of the track with area evaluation for Carnit specimen after a PS experiment carried out at 150 N load for 3 hours and 1V cathodic vs Ecorr.



Wear track after at OCP test, with 3h at 150 N Load for a Carnit specimen. NaCl 3.5% solution.



CoF recorded during the OCP test, with 3h at 150 N Load for the Carnit specimen. NaCl solution 3.5%.

Figure 5.37. The track on Carnit specimen after a OCP experiment carried out at 150 N load for 3 hours, and the recorded CoF curve. Average CoF value resulted 0.42.

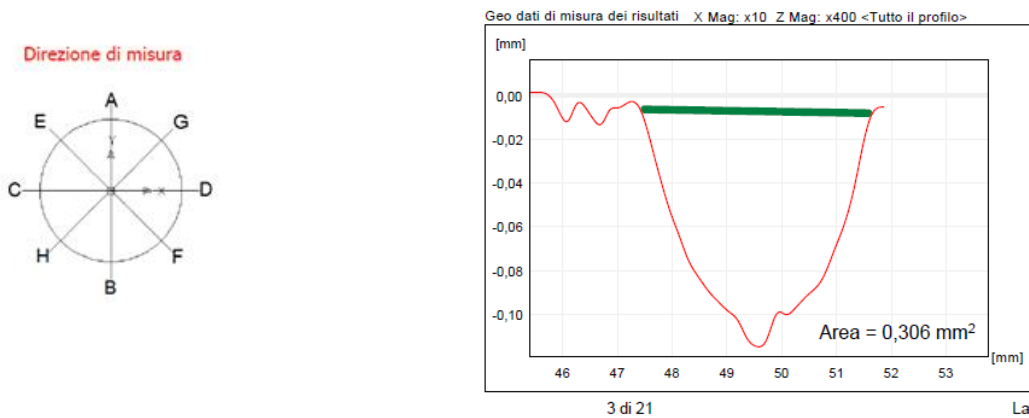


Figure 5.38. The method adopted for track profile measurements and a cross section of the track with area evaluation for Carnit specimen after a OCP experiment carried out at 150 N load for 3 hours.

However for Carnit the wear track was easily measurable by evaluation of the cross section area and the weight loss as well, but values of the volume loss or the difference in weight were very close in the two PS experiments, this indicating that a possible instrumental or experimental issue affected the results.

Summary

To assess tribocorrosion behaviour of 100Cr6 (Q&T) martensitic steel in marine environment, corrosion/tribological first tests were carried by means of a modified tribometer. The activity also aimed at testing the experimental setup.

100Cr6 steel in Q&T state was used as reference system in activities involving tribocorrosion of new HNAS alloys (comparative analysis).

A series of experiments in potentiodynamic or potentiostatic mode, namely electrochemical without sliding, 'tribo-electrochemical' with sliding and sliding wear, were carried out.

For sliding tests under controlled load (contact load: 150 N) and speed conditions, an insulating holder carrying a Al_2O_3 ball slider was used.

The results of first experiments on 100Cr6 steel (in the described experimental conditions) seemed to evidence that sliding in saline electrolyte modifies the corrosion potential of the material but does not change its corrosion rate significantly.

This result was further confirmed, evidencing that at 150 N load 100Cr6 the corrosion potential is lowered without any substantial variation in the current density. The 100Cr6 steel showed a high resistance to wear under sliding, developing shallow and scarcely detectable tracks.

The experimental activity highlighted a possible limit of the first adopted optical system of detection for the evaluation of track cross section. No wear volume (related to wear mass loss) was extracted from the data acquired in the potentiostatic mode for 100Cr6. This was confirmed by additional investigations with the new CSM Instrument (Roughness Tester Mitutoyo S-3000).

Comparative characterizations carried out on Carnit evidenced a better corrosion behavior. The situation is reversed in sliding or in corrosion-sliding tests, when a load is applied (tribometer). The wear-corrosion tracks for Carnit are wider and deeper compared to 100Cr6, a confirmation of the fact that Carnit is less wear resistant with respect to 100Cr6 in the adopted conditions. In all the typologies of tribological testing (sliding) the track cross section area was detectable and in some cases the material loss evaluable by weighing, unlike 100Cr6.

However, the variation in weight or track cross sections, were very close for the two PS experiments and this prevented deeper interpretation of results. A possible interpretation could be related to instrumental or experimental issues.

6. WP6. Bearing prototyping and Full-Scale Tests, Life Cycle Assessment (LCA), cost analysis

6.1. Manufacturing of final HNAS electrodes/ingots (Task 6.1)

The Carnit 90 electrode (electrode ID S83725, Figure 6.1) had to be subjected to pressure electro slag re-melting (PESR), to obtain the re-melted heat (ID D37130, see Figure 6.2). The final chemical composition of the heat is reported in Table 6.1. The sum of C+N is actually 0.77 %, lower than that planned for Carnit 90 (C+N = 0.90 %).

The ingot (\varnothing 630 mm) was hot rolled to a 230 mm x 230 mm square shaped bar (Figure 6.3). The final hot deformation was induced by means of forging, up to the final dimensions of the forged bars of \varnothing 60 mm, \varnothing 120 mm and \varnothing 160 mm (Figure 6.4).



Figure 6.1. Electrode S83725 prepared for PESR operation.



Figure 6.2. PESR ingot D37130 (\varnothing 630 mm).

Table 6.1. Chemical composition of D37130 PESR ingot (mass %).

C	Mn	Si	P	S	Cr	Ni	Mo	V	Cu	Al	N
0.33	18.6	0.87	0.016	0.001	18.0	0.08	0.03	0.025	0.04	0.006	0.44



Figure 6.3. Hot rolled bars (square 230 mm x 230 mm).



Figure 6.4. Bars forged to the final sizes (\varnothing 60 mm, \varnothing 120 mm and \varnothing 160 mm).

Solution annealing and basic characterization

In principle, the materials for some specific bearing parts may require a hardness up to 58 HRC (650 HV) in the maximum depth of von Mises equivalent stress to get the highest lifetime. With lower hardness values, a material factor has to be implemented in the lifetime calculation according to ISO 281 (for examples this factor is set to be 0.65 if the hardness level is at 50 HRC (equal to 512 HV)). Practically, a hardness of around 500 HV for bearing parts made of Carnit 90 enables for full scale test on FE8 with a Hertzian pressure of 2000 MPa, which corresponds to max pressure in wind turbine gearbox applications). Based on experiences on steel of composition similar to that selected, a reasonable level for the bulk hardness is around 300 HV [88]. The surface hardness can be increased to the required level by means of the operations introduced in the manufacturing cycle (cold deformation + deep rolling). As a rough estimation, a surface hardness of 500-530 HV is expected to be reached by means of a cold deformation operation of about 10 %. Some compression tests can be performed in order to better determine the proper deformation level required. The following operation of deep rolling – as shown in the following sections – can further enhance the surface hardness approximately of 30-40 %.

In terms of microstructure, the requirements are: absence of porosity and good homogeneity. In terms of steel cleanliness, the usual requirements are in terms of non-metallic microscopic inclusions, according to ASTM E45 method A. The reference levels given in Table 6.2 are those of the common requirements for bearing steel. Most of the specifications for bearings used in wind turbine applications do not require higher cleanliness levels. Only in some specific cases, specifications give stricter requirements for macro-inclusions, evaluated by Immersion Ultrasonic Testing.

Table 6.2. Requirements for steel cleanliness (maximum limits).

A (Sulfide type)		B (Alumina type)		C (Silicate type)		D (Globular Oxide)	
Thin	Heavy	Thin	Heavy	Thin	Heavy	Thin	Heavy
2-4 µm	4-12 µm	2-9 µm	9-15 µm	2-5 µm	5-12 µm	2-8 µm	8-13 µm
2.0	1.0	1.5	0.5	0.0	0.0	1.0	0.5

The Ø 60 mm bars were chosen to perform laboratory heat treatments and experimentally determine the more suitable solution annealing temperature, to be adopted in the bar heat treatment. To that purpose, disc-shaped samples with dimensions Ø 60 mm x 25 mm were cut from the bar. The samples were annealed at the temperatures given in Table 4, with a soaking time of 50 minutes. The temperature range for the solution annealing has been chosen according to the results of preliminary thermodynamic estimations by means of JmatPro. After soaking, the samples were oil quenched to room temperature. Heat treatment was followed by standard metallographic sample preparation for light optical microscopy as well as hardness investigation. Hardness was measured by means of the Vickers (HV30) method according to DIN EN ISO 6507-1. The steel cleanliness was determined for sample according to ASTM E45 Method A.

The measured hardness values are given in Table 6.3. Hardness decreases with increasing solution annealing temperature from an average value of approx. 370 HV30 at 1070 °C to approx. 312 HV30 at 1090 °C. It does not increase higher than 320 HV30 up to 1140 °C. A slight increase occurs after quenching from a solution annealing temperature of 1170 °C as shown in Figure 6.5.

Table 6.3. Annealing temperatures and related hardness values.

Sample #	Annealing Temperature (°C)	Hardness (HV30)
1	1070	369 ± 14
2	1090	313 ± 9
3	1120	319 ± 12
4	1140	315 ± 6
5	1170	330 ± 6

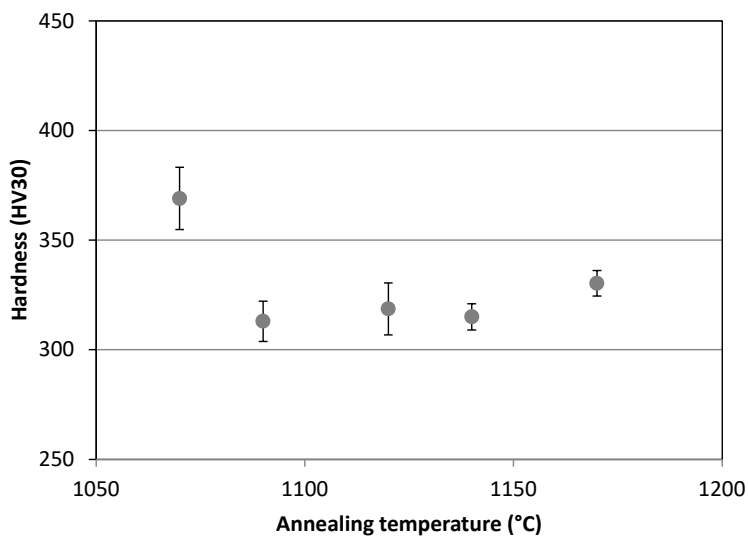


Figure 6.5. Hardness (HV30) as a function of solution annealing temperature (soaking time 50 min).

The microstructures are reported in Figure 6.6 - Figure 6.10. The microstructure after annealing at 1070 °C is hardly recrystallized and the grain size is non homogenous. Undissolved precipitations appear to be located mainly at the grain boundaries. The degree of recrystallization and the grain size increase with increasing solution annealing temperature (grain size is in the range 3-4 ASTM), while the amount of spherically shaped precipitations decreases. Reoccurring line shaped traces of not recrystallized grains with spherically shaped boundary precipitations are apparent after quenching from 1090 °C. Plate like shaped grain boundary precipitations are visible after quenching from temperatures > 1120 °C. After quenching from 1170 °C additional plate like shaped structures are visible within the grains. These plate like shaped structures appear to be oriented along the close-packed crystallographic planes and are the probable reason for the measured hardness increase.

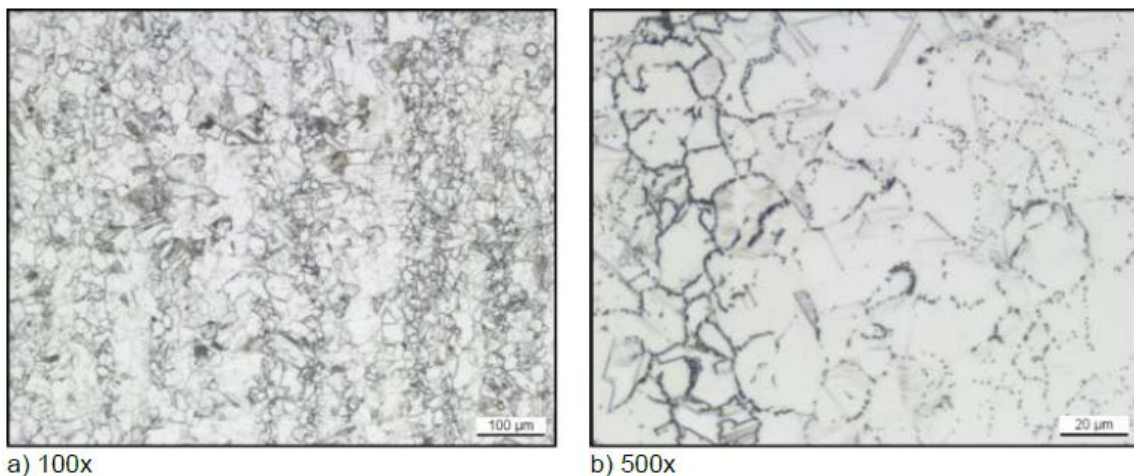


Figure 6.6. Microstructure, annealing temperature 1070 °C.

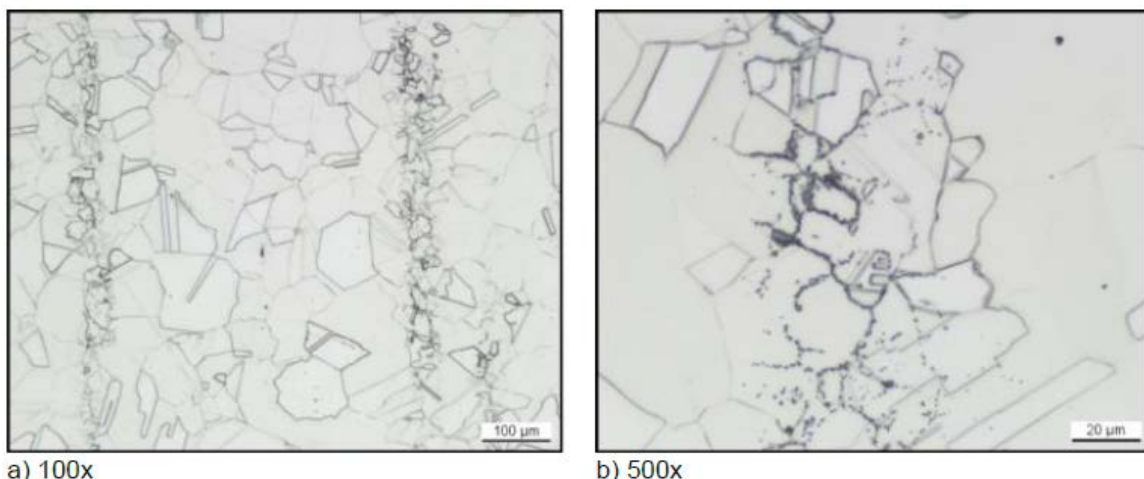


Figure 6.7. Microstructure, annealing temperature 1090 °C.

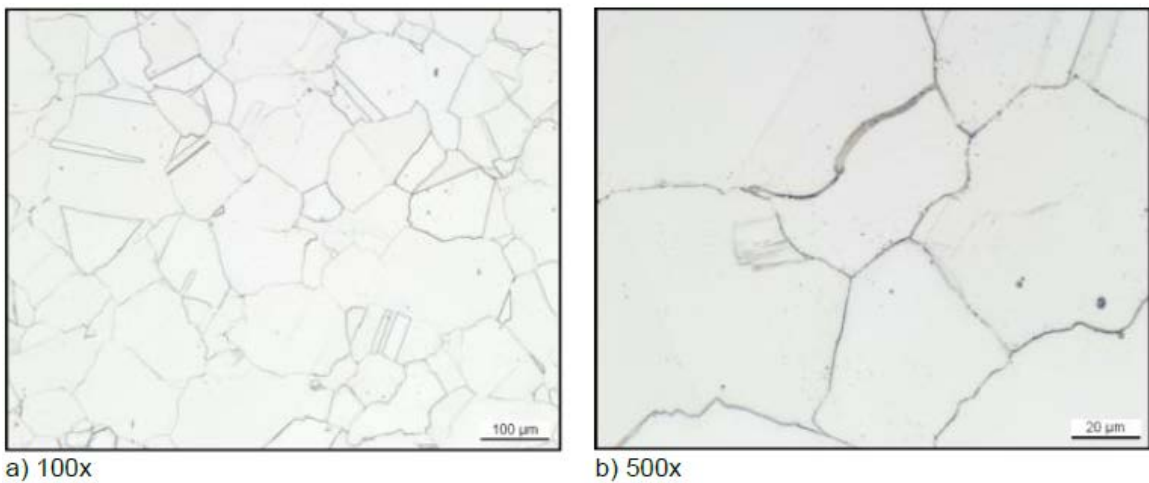


Figure 6.8. Microstructure, annealing temperature 1120 °C.

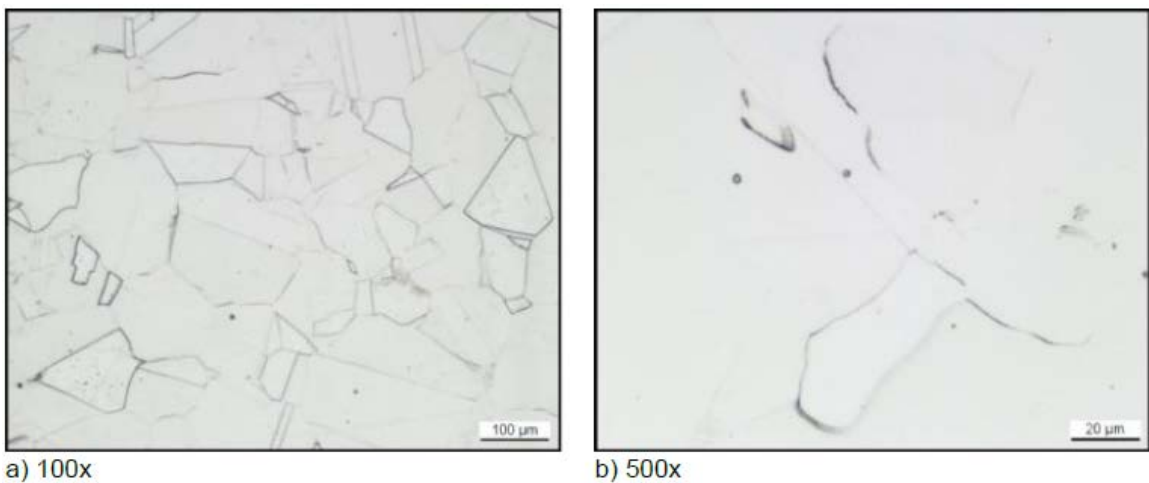


Figure 6.9. Microstructure, annealing temperature 1140 °C.

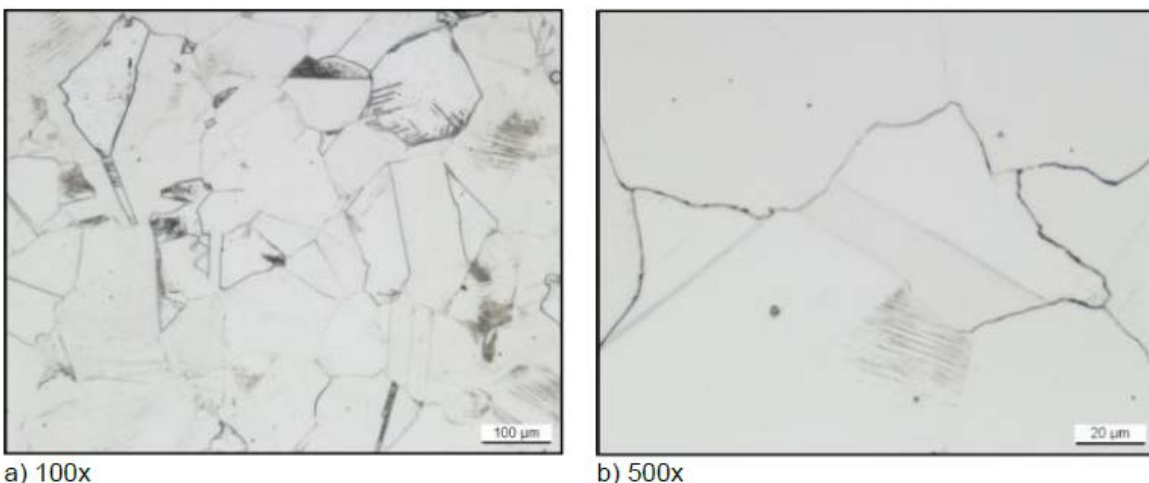


Figure 6.10. Microstructure, annealing temperature 1170 °C.

On the basis of the results reported, it is possible to state that the steel industrially cast and forged exhibits a microstructure quite homogeneous and free from porosity. The target in terms of surface hardness level, necessary for producing test bearings for the full scale test, can potentially be achieved

taking into account the considerations made about the increases produced by means of the operations included in the manufacturing process (cold deformation + deep rolling).

A temperature of 1120 °C has been selected for the following industrial heat treatment (solubilization annealing. The quite grain size obtained at that annealing temperature is quite large. The effect in terms of toughness has been partially evaluated in the next section, and the level of impact toughness seems quite good at room temperature. In terms of fatigue properties, they need to be evaluated as a completion of mechanical properties assessment.

The steel cleanliness according to ASTM E45 method A is given in Table 6.4. It is clear that the steel cleanliness in terms of non-metallic inclusions achieves the level which is typically required for bearing steel.

Table 6.4. Steel cleanliness according to ASTM E45 method A.

A (Sulfide type)		B (Alumina type)		C (Silicate type)		D (Globular Oxide)	
Thin	Heavy	Thin	Heavy	Thin	Heavy	Thin	Heavy
2-4 µm	4-12 µm	2-9 µm	9-15 µm	2-5 µm	5-12 µm	2-8 µm	8-13 µm
1.0	0.5	1.0	0.0	0.0	0.0	1.0	0.0

A deeper investigation has been made to check that the material produced to build the prototype components is free from the issues detected in the experimental material. Samples heat treated at 1120 °C for 90 (sample 1.4.2) and 160 min (sample 4.4.2) and subsequently quenched were investigated.

Figure 6.11 shows a micrograph of one of the heat treated samples, compared to the earlier VM2950 CARNIT material only slight etching of the grain boundaries could be observed and there were no indications of large scale precipitation of CrN taking place in either of the two investigated heat treatment conditions.

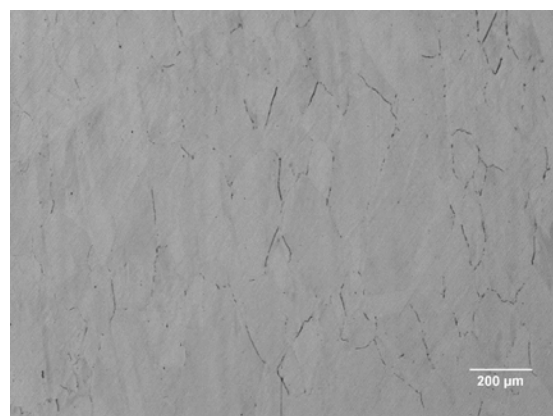


Figure 6.11 RLM image of the sample heat treated at 1120°C for 160 min after etching.

This was confirmed by the SEM investigation, where images of the heat treated samples are shown in Figure 6.12. Again, compared to the findings for VM2950, no precipitation could be observed and no areas with deviating grain size could be observed. Some porosities could be found (appearing dark in the SEM images) but not at all in the same amount as observed for the VM2950 batch.

EBSD revealed a structure consisting of only FCC with average grain sizes of 79 µm and 87 µm for the 90 min and 160 min treatments respectively, see Figure 6.13.

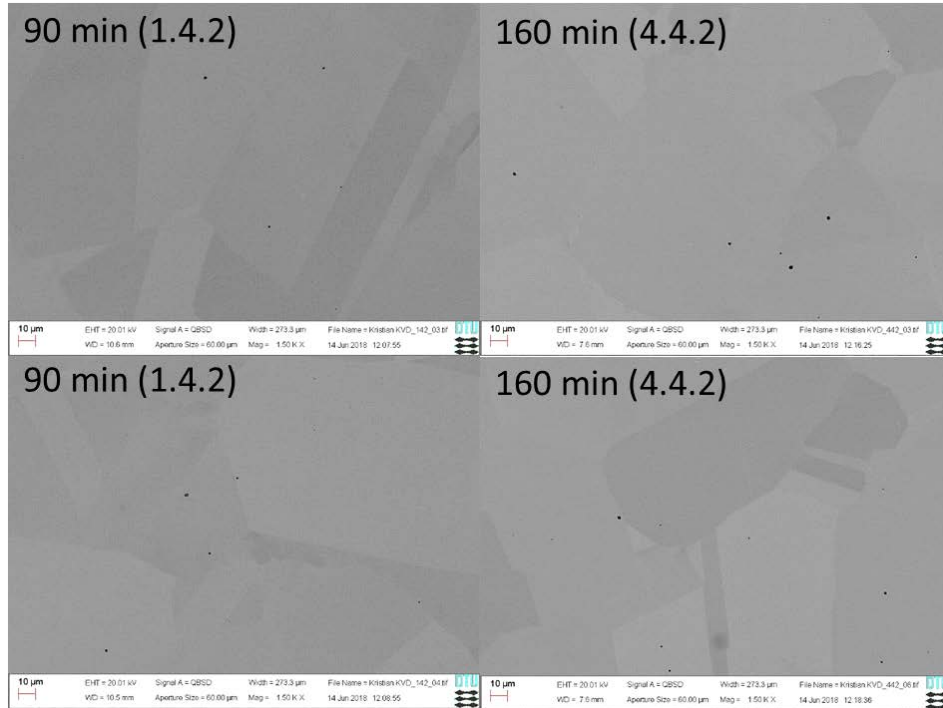


Figure 6.12. SEM BSE images of the two heat treated samples.

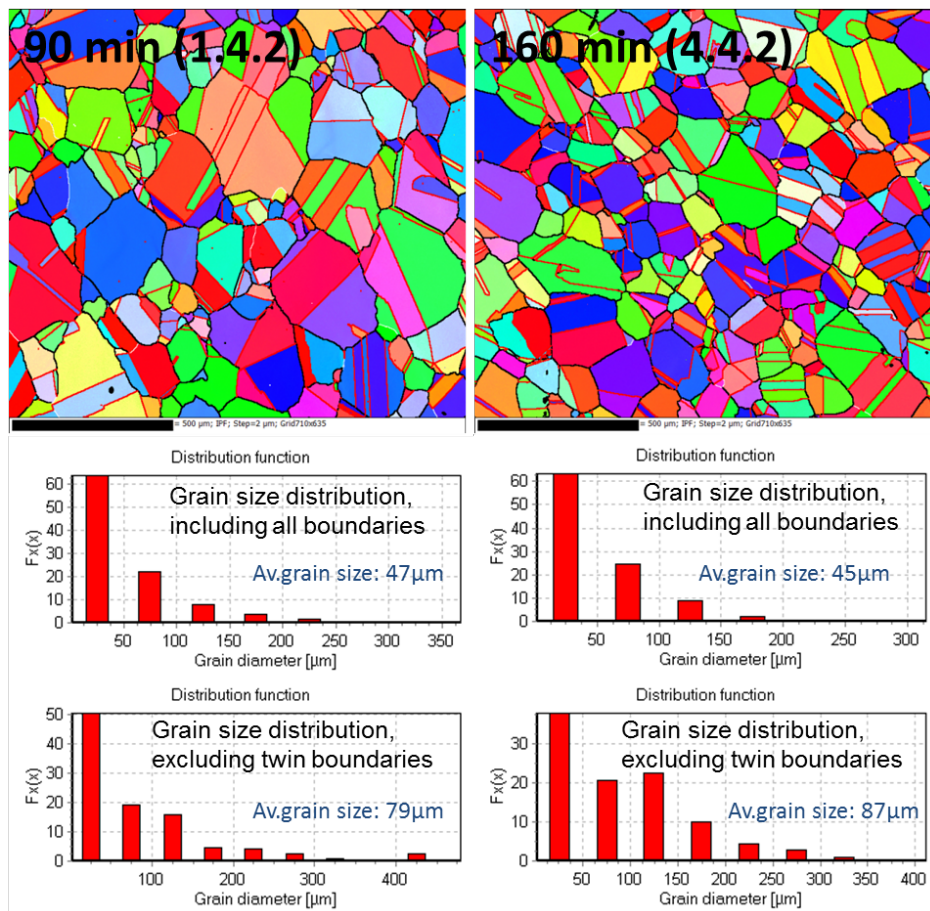


Figure 6.13. SEM EBSD results for the two heat treated samples.

Microhardness measurements were performed for the directly heat treated materials as well as for tensile test samples that had experienced deformation hardening during the tensile testing. The results are listed in Table 6.5.

Table 6.5. Microhardness results (50 g load, average of 5 measurements).

	90 min	+-	160 min	+-
ST 1120C	272	6	273	5
Tensile sample near fracture	555	16	559	14
Tensile sample >12 mm from fracture	480	12	470	19

Very close to the fracture point, the hardness had increased to above 550 HV, however in this region also significant voiding and damage for the tensile testing could be observed. In larger distance from the fracture, where the material appeared intact, hardness values of 480 and 470 HV were obtained for the two materials.

Both heat treatments has resulted in material with FCC structure and without the problems identified for the VM2950 batch material. The hardness vlaues measured in fractured tensile test samples reached a maximum of 559 HV close tot he fracture where the material was damaged, further away from the fracture hardness values just below 500 HV were measured.

6.2. Production of full scale prototype HNAS (Task 6.2)

Production route according to project plan

The full-scale production includes, according to the project plan, the following steps: casting of the alloy and forging to final dimension, solution heat treatment (these steps have been described in section 6.1), turning in a soft condition, surface hardening via cold deformation and hard machining to final geometry (Figure 6.14).



Figure 6.14: Route for HNAS full scale production according to the project plan.

The full-scale production of bearings was performed on axial cylindrical roller bearings type FAG81212, whereas the washers were made of the Carnit material, cage made of polymer and rollers made from ceramic Si₃N₄. The soft annealing of the material was already performed at ETE. So, a set of 20 housing washers and 20 shaft washers were produces out of 120 mm raw material bars. Those bearings parts (washers) were cold deformed at Sidenor via deep rolling to achieve an appropriate hardness level, enabling the parts to withstand the loads applied in the assigned FE8 test. The "cold forming" process was applied using deep rolling with the parameters given in Table 1.1Table 6.6.

Table 6.6: Parameters applied via deep rolling @Sidenor.

Pressure	Ball diameter	Speed	Angle
600 bars	19 mm	60 rpm	90°

The visual aspect of the prototypes before and after deep rolling are presented in Figure 6.15 and Figure 6.16 respectively.



Figure 6.15. Visual aspect of the prototypes before deep rolling.



Figure 6.16. Visual aspect of the prototypes after deep rolling.

The reported data on the hardness were the average values measured in three diagonals performed in each type of prototype in the as received condition and after deep rolling. The measurements of the indents were performed on three different diagonals for each samples.

The effect of the deep rolling on the surface hardness are presented in Table 6.7. Deep rolling has led to an important surface hardness increase. For F-562831-0023-000 prototype, the hardness increase varies from 320.9 to 465.5 HV10. For F-562831-0013-000 prototype, the hardness increase varies from 340.1 to 476.3 HV10. The average hardness increment varies from 40.9 to 45.1 % depending on its initial value. The higher the initial hardness of the steel the smaller the influence of the deep rolling on the hardness surface increment.

Table 6.7. Effect of deep rolling on surface hardness.

Roll Hardness Evolution						
Ref	Condition	Pos	HV10 Hardness	Avg HV10	Hardness Increment	
F-562831-0023-000	As received	#1	323.7	320.9	45.1%	
		#2	321.4			
		#3	317.7			
	After deep rolling	#1	463.8	465.5		
		#2	467.2			
		#3	465.4			
F-562831-0013-000	As received	#1	339.5	340.1	40.9%	
		#2	340.7			
		#3	340.0			
	After deep rolling	#1	488.4	476.3		
		#2	473.0			
		#3	467.4			

The resulting hardness pattern can be seen in Figure 6.17. The hardness values, measured in a depth of 0.1 mm are about 450 HV1, so extrapolating this value towards the surface a hardness of 500 HV1 can be expected. This means that in comparison with the core hardness (about 250 HV1) an increase of about 100 % was reached. But nevertheless, this value was somewhat lower, than desired.

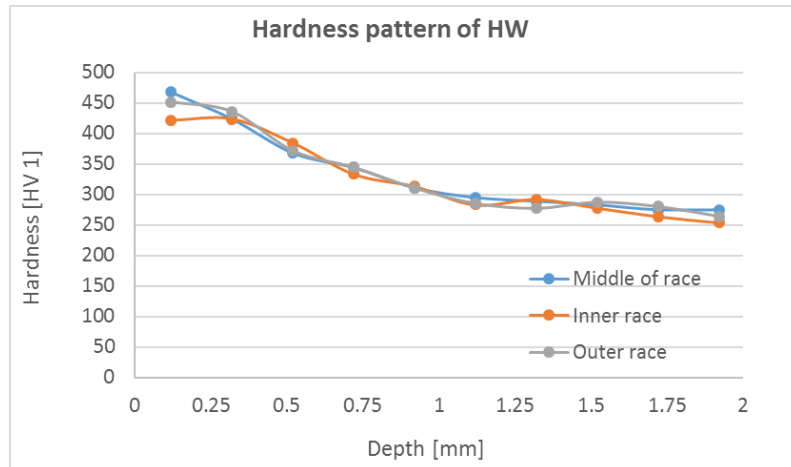


Figure 6.17. Hardness patterns on an example of housing washer after deep rolling process.

The results of the geometrical measurement can be seen in Figure 6.18 and Figure 6.19. In these figures, the deviation in the geometry from the required dimension can be seen. There was a plastic deformation of the washers up to 0.23 mm measurable. Therefore, it was not meaningful to apply the last step of production (hard machining), since it was impossible to reach the geometry, required to fit in the full-scale test FE8 without removing the cold deformed surface area.

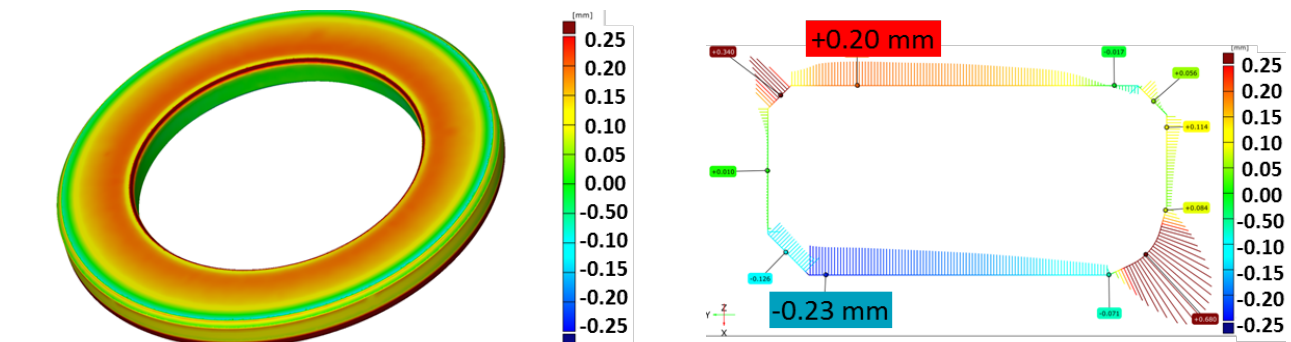


Figure 6.18: 3D - geometrical measurement of one washer after deep rolling process. Red and blue colors indicate deviation from desired geometry

Figure 6.19: Geometrical measurement of one washer after deep rolling process. Deviation in dimensions up to 0.23 mm

Alternative production route: "in situ" cold deformation on FE8

Another production route was designed and attempted, aiming to apply the cold deformation in the FE8 test rig. Basically, that production route required a soft machining (after the casting and solution treatment of the alloy) which lead to geometrical values and roughness values, which were normally achieved via hard machining (grinding).

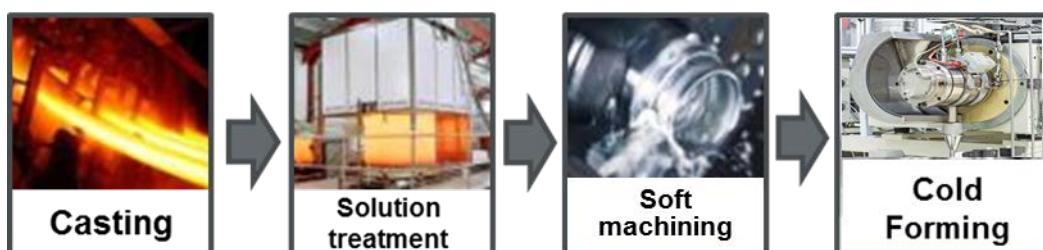


Figure 6.20. Route for HNAS full scale production using FE8 test rig for cold deformation (schematic)

The plastic deformation was then applied using the test rig FE8. This way to produce the test bearings should reach two goals: elimination of one production step and avoiding of macroscopic deformations, since the washers were clamped in the bearings seats during the deformation steps. The FE8 test rig (Figure 6.21) applies a pure axial load onto two bearings in parallel, whereas the structure of the rig is quite simple: the force is applied by a spring, and the rotational speed is generated by a direct drive. The rotation is transmitted by an insulated coupling disc to avoid any electrical influence on the bearings. The lubricant is supplied by a closed loop system with temperature control and regulation. During the action / test, different signals are monitored: torque and temperature, as well as the noise to detect failures of the bearings.

Originally, the FE8 is assigned for several bearing tests (see also Table 6.8) – but it was chosen later also for the “in situ” cold deformation since all required features are included in this test rig.

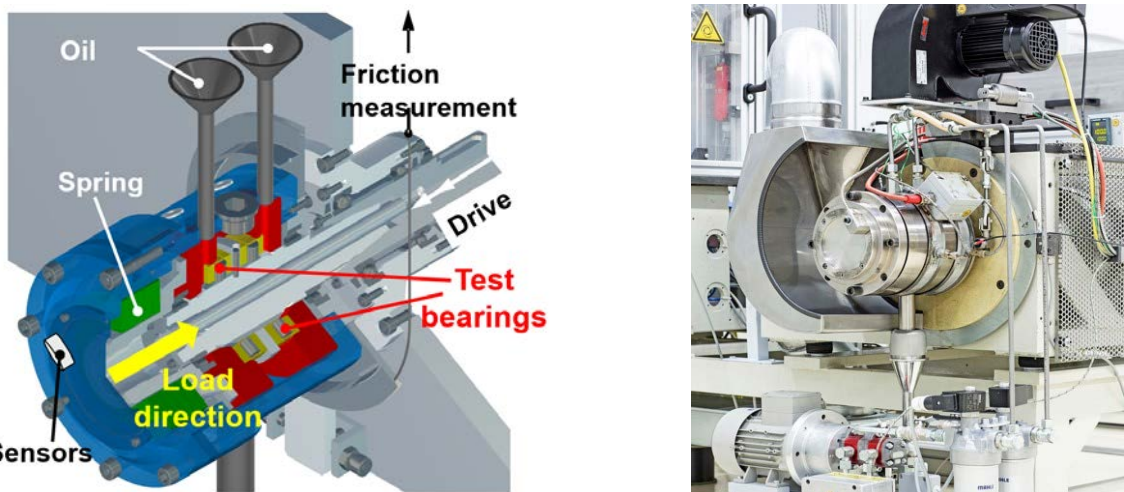


Figure 6.21. FE8 test rig. (left) schematic drawing of the FE8 test rig; (right) photo of the FE8 test rig

Numerical simulation of “in situ” cold deformation process

A washer (FAG 81212 = F-562831-0021) with 15 rollers (ZRB11X11-LP/111K01) evenly distributed on its raceway was modelled (by the commercial Finite Element software system Simufact.forming v15) to investigate the plastic deformation near the surface of the raceway numerically. The FE model utilizes the symmetrical property thus considers one single roller in simulations. The model size is sufficiently large and the evaluation of the deformation was performed in the middle section of the washer so that any possible influence of the fixed boundary condition defined at both sides of the washer is minimized. The roller rolls over the raceway several times, aiming to reach a steady state of deformation on the surface. During the rolling process, the roller rotates simultaneously with respect to its own axis and the axis of the washer. The multiple rolling process was studied at different loading forces of 5, 6.67, 10 and 20 kN per roller. The preliminary results show that the plastic deformation on the outer race way is slightly higher than that on the inner race way (Figure 6.22 b and c). The reason is that the linear velocity of the roller is smaller than the linear velocity of the washer on the outer race way so that the material piles up in front of the roller, causing higher deformation upon over-rolling. The plastic deformation obtained at 10 and 20 kN was further evaluated in depths up to 1 mm (Figure 6.22 d). It is seen that for both loading cases the deformation is strongly localized near the surface that the plastic deformation decays quickly into the depth. Further, the difference of the plastic deformation between the inner and outer race way disappears almost immediately below the surface. While a steady state of plastic deformation at the load of 5 and 6.67 kN was nearly reached after 15 rolling passes, at 10 and 20 kN, the material shows a continuous work hardening behavior after 25 rolling passes (Figure 6.22 e).

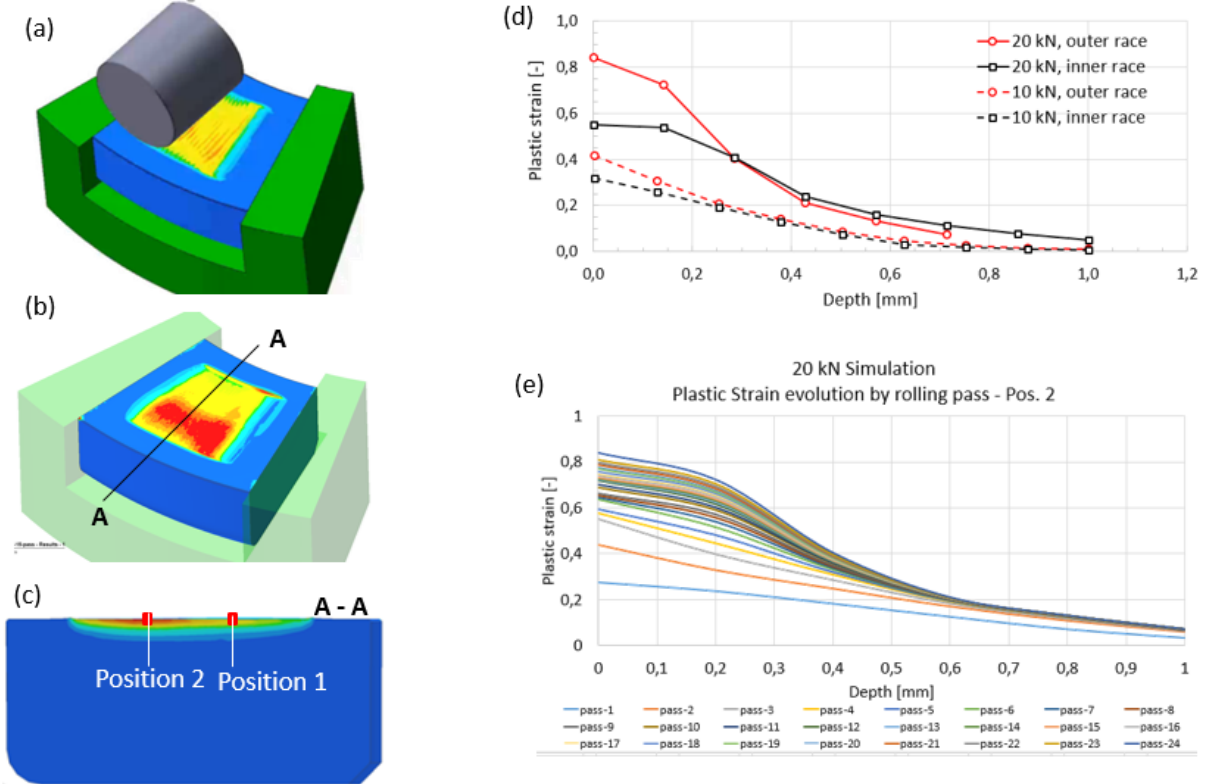


Figure 6.22. Simulation model and chosen results. (a) simulation model (24° piece) containing one roller; (b) inhomogeneous deformation at the inner and outer race; (c) Cross section in the middle of the modelled washer and the two positions at which the plastic deformation was evaluated in depth; (d) plastic deformation in depth at 10 and 20 kN after 25 rolling passes; (e) Evolution of the plastic strain with rolling passes and depth

Practical implementation

Two different setups were performed, treating two bearings in parallel. The bearings themselves were assembled with 5 ceramic rollers, only. These decrease in number of rollers should increase the force (pressure) per roller, since the max. applicable axial load of the test rig is limited to 100 kN. Two different parameter settings were applied during the “in situ” cold deformation. The applied pressures are given as some nominal values. While each of the values exceeds the elastic limit, the resulting plastic deformation practically decreases these values (significantly).

Table 6.8. Parameters for “in situ” cold deformation on FE8.

Test no	Applied force	Applied pressure (nominal)	Revolutions
production I	10 kN / roller	≈ 5 GPa	30
production II	20 kN / roller	≈ 10 GPa	30

After the in situ cold deformation, the washers were gauged. It was figured out, that some plastic deformation occurred in both the productions. Within the 10 kN / roller productions, this pileup was about 15 μm , only developed on the outer diameter of the racetrack. The production applying 20 kN / roller resulted in pileups up to 40 μm on the outer and on the inner diameter of the racetrack. The washers did show a clearly distinguishable cold-deformed raceway having also some indentations of the rollers (standstill after cold deformation), see Figure 6.23 and Figure 6.25.



Figure 6.23. washer after "in situ" cold deformation on FE8 with 10 kN / roller

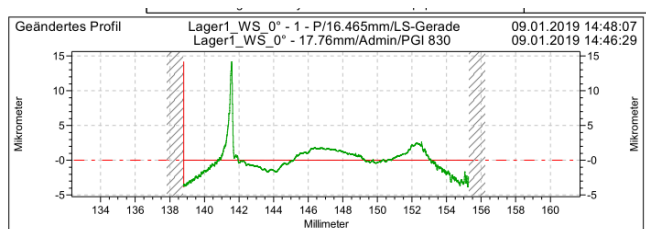


Figure 6.24. Geometrical measurement of the washer in radial direction



Figure 6.25. washer after "in situ" cold deformation on FE8 with 20 kN / roller

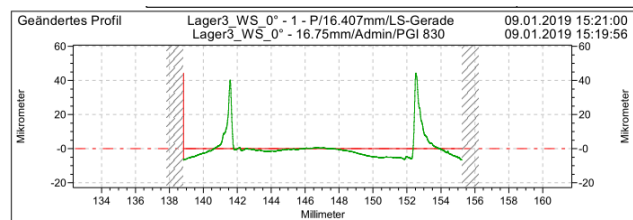


Figure 6.26. Geometrical measurement of the washer in radial direction

The hardness pattern of one washer, deformed with 10 kN / roller and one deformed with 20 kN / roller can be seen in Figure 6.27. The hardness in 0.1 mm was measured to be about 420 HV1, so a hardness of 450 HV1 can be extrapolated with both the variants. A differentiation in between the two variants can be seen in the hardness at higher depth, e.g. 0.5 mm. Here is the influence of cold deformation more effective using the higher force (higher pressure) level.

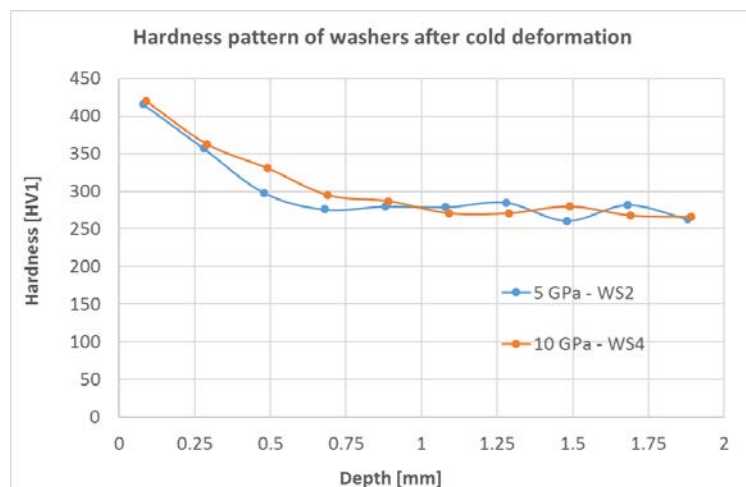


Figure 6.27. Hardness measurement on washers after "in situ" cold deformation on FE8 using 10 kN / roller (≈ 5 GPa) and 20 kN / roller (≈ 10 GPa)

6.3. Full scale tests, Lab analysis and Life Cycle Assessment (Task 6.4-6.6)

Full-scale test on FE8 rig

Initially it was aimed to test the HNAS steel under two different setups: the FE8_03, which is basically a wear test which applies boundary mixed friction, and the WEC test FE8_25, aiming to generate WECs in the washers at mixed friction and high sliding velocities. The required hardness to withstand the applied pressures of 2150 MPa (FE8_03) or 1900 MPa (FE8_25) were calculated to be 610 HV and 540 HV, respectively. Since these hardness values could not be achieved during the production process, neither with deep rolling nor with "in situ" cold deformation on FE8, another setup was chosen to test the bearings. This FE8_25* had a decreased axial force, resulting in Hertzian pressure of roughly 1660 MPa. So, the minimum hardness of the washers to run this test procedure was calculated to be 450 HV according to Schaeffler guideline PA1.002.

Table 6.9. test conditions for wear test FE8_03, WEC test FE8_25 and adapted WEC test FE8_25*.

	FE8_03	FE8_25	FE8_25*
Rolling elements	steel	steel	ceramic
Rotational Speed [rpm]	7.5	750	750
Applied Load [kN]	80	60	40
Hertzian Pressure [MPa]	≈2150	≈1900	≈1660
Lubrication Viscosity Class	ISO VG 68	ISO VG 68	ISO VG 68
Kappa Ratio	<0.1	0.46	0.46
Min hardness of washers [HV]	610	540	450

Unfortunately both the tests did not reach a running time of more than 10 hrs. For comparison: bearings with washers, made of 100Cr6 failed after 110 hrs with WEC. The test of those bearings produced in production I failed after 4 hrs. The bearings, manufactured in production II did fail after 8 hrs.

Table 6.10. Results of the full-scale tests, performed according FE8_25*.

Test	Bearings	Running time	Damage
A	A1 & A2 (production I)	4 hrs	pittings on all 4 washers
B	B3 & B4 (production II)	8hrs	pittings on all 4 washers

Laboratory analysis of the failed components

After the tests, a laboratory analysis of the failed components has been performed. All the washers showed several pittings in the raceway. The pittings were rather shallow. Some of them showed a typical V-shape in the origin, which underlies that the failures were surface initiated in each case.



Figure 6.28. LOM of washer from bearing A2 after test on FE8_25* showing several pittings, mainly in the radial middle of the racetrack

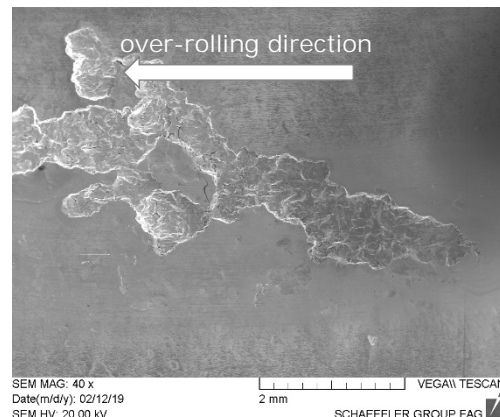


Figure 6.29. SEM detail of a pitting in a washer from bearing A2 after test on FE8_25*, which shows an origin from the surface



Figure 6.30. LOM of washer from bearing B42 after test on FE8_25* showing several pittings, mainly in the radial middle of the racetrack

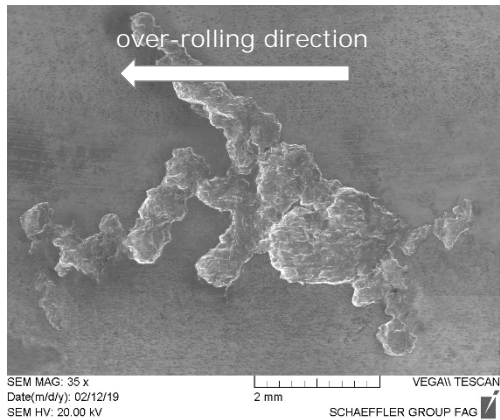


Figure 6.31. SEM detail of a pitting in a washer from bearing B4 after test on FE8_25*, which shows an origin from the surface

Summary of full-scale test on FE8 rig

The alloy Carnit 90 produced (actually, with a C+N amount equal to 0.77 %) as reported in Task 6.1 had an initial hardness of not more 330 HV10. Due to some preliminary basic compression and tension tests, a maximum hardness increase up to 590 HV10 was expected.

The full scale production (following the route according to Technical Annex) with a cold deformation applied via deep rolling process was performed without success in obtaining proper samples with the required surface hardness values. In fact, this process resulted in a noticeable hardness increase, up to about 480 HV1 at the surface, but also in massive geometrical deformation of the whole bearing parts (washers).

An alternative production route was attempted (in-situ deformation), accompanied by numerical simulation. During this production route, the cold deformation was deployed in the same FE8 device, in which the later full-scale tests were completed. This production lead to a max. hardness of about 450 HV1. This lower hardness required an adapted test procedure on FE8. So, the tests were performed at 1600 MPa only. Nevertheless, even this relatively low pressure resulted in early failures of the washers made of Carnit steel. The failure mode was surface initiated fatigue in each test. This leads to the assumption that the hardness level was not high enough, even for this low Hertzian pressures. The influence of other features of the alloy, e.g. the large grain size can also not be excluded.

Life Cycle Assessment

The ISO 14040: Environmental Management — Life cycle Assessment —Principles and Framework [ISO, 2006] has defined the four major components of an LCA as: (1) goal and scope; (2) inventory analysis; (3) impact assessment; and (4) interpretation of results.

An LCA starts with an explicit statement of the goal and scope of the study, which shall include a clearly description of the product system, the functional unit, the system boundaries, the assumptions and limitations, the data requirements and the allocation procedures to be used, and the types of impact and methodology of impact assessment.

The working procedure of LCA is iterative, meaning that information gathered in a later stage can cause effects of a former stage. When this occurs, the former stage and the following stages have to be reworked considering the new information. Accordingly, from a general perspective, LCA evaluates the environmental performance of products, processes or services throughout its entire life cycle, from its "cradle" all the way to the "grave". The life cycle model of a product, process or service usually starts with the acquisition of raw materials and energy that is needed for the production of the studied object, the "cradle". The model follows the stages of processing, transportation, manufacturing, use phase and, finally, waste management, which is considered as the "grave". The assessment is accomplished by identifying quantitatively and qualitatively the studied object stages requirements for energy and materials, and the emissions and waste materials released to the environment.

Goal of the study

For this project, the main goal was to create a scientific basis for a better understanding of the environmental impact of the bearings production. The purpose of this assessment is three-fold: (1) establish a scientific baseline evaluating the potential life-cycle environmental impacts of Steelwind and standard bearings; (2) generate key performance indicators (KPI) to understand benefits and disadvantages of Steelwind Bearings in comparison with standard bearings; and (3) identify data gaps or other potential areas of analysis for future investigation. The evaluation considers impacts related to the 'cradle to gate' life cycle stages, including material consumption, energy, air and water resources, residues generation, sub-products and air, soil and water emissions.

Functional unit

In LCA, product systems are evaluated on a functionally equivalent basis. The functional unit normalizes data based on equivalent use to provide a reference for relating process inputs and outputs to the inventory and impact assessment across alternatives. For this project, the functional unit is 1000 bearings ready for sale. This signifies one complete bearings, packed in their packaging material.

System description

In a "cradle-to-grave" analysis, the product system includes three life-cycle stages. Table 6.11 shows the three stages modelled in this study and the activities and processes partitioned among each stage.

Table 6.11. Major stages of the Bearings LCA.

Stage		Activities included
1.	Raw materials extraction and/or acquisition	Activities related to the extraction and acquisition of natural resources, including mining non-renewable material required to produce the different system components and transporting these materials to processing facilities.
2.	Materials Processing	Processing natural resources in preparation for the manufacturing stage; and transporting processed materials to product manufacturing facilities.
3.	Product manufacture	Manufacture and assembly of system components, and transportation for use or application stage.

The assessment boundaries determine, from the entire product's life cycle, which unit processes shall be included within the LCA. The following sections explain the data categories, the physical and geographic limitations, and general exclusions to the LCA, all of which combine to determine the project boundaries. The life cycle consists in unit processes connected by flows of intermediate products, performing one or more defined functions. This is called the product system. As explained above, in a "cradle-to-gate" product analysis, the product system starts with the extraction and/or acquisition of materials, fuel and energy sources. The second stage includes the operations that transforms these materials from a raw-material state into industrial usable materials (Materials Processing). The next stage represents the manufacture of the components to be used on the NU bearing assembly. This includes the different components used in the NU bearing, as the outer ring, inner ring, rollers and cage. Once all parts have

been produced they are assembled and the bearing is ready for shipment to its client. Geographic and temporal boundaries are used in a LCA to show where and when impacts are likely to occur for each life cycle stage. This is important for assessing the impact of such activities as transportation of materials between life cycle stages. Regarding the temporal boundaries, the reference year for the assessment was set on 2017. However, each data entry reference period is dependent from collected data quality and specifications, which can only be clearly assessed during the collection process. Nevertheless, it is possible to determine expected framing timelines for some of the stages, as shown in Table 6.12. Concerning the geographical boundaries, the main aim of the assessment is to give an overall picture of the bearings production. In order to generate more reliable results, some specific geographical data of the project should be used on certain life cycle stages. This includes the stages and activities where primary data is expected to be used, namely, those in which the project consortium partners have an active participation.

Table 6.12. Data temporal and geographical boundaries by life cycle stage.

Life Cycle Stage	Period/Time frame	Geographical Coverage of data
Extraction and Acquisition of Raw Materials, Fuel and Energy	n.a.	World
Materials Processing	n.a.	Europe
Bearings Components Manufacturing	2017	SCHAEFFLER
Bearings Assembly	2017	SCHAEFFLER

Table 6.13 describes the data categories for which inventory data should be collected, including material and resource flows (inputs), and emission, waste, and product flows (outputs). In general, inventory data is normalized to either (1) the mass of an input or output per functional unit, or (2) energy input (i.e., joules, [J]) per functional unit. As mentioned, the functional unit is 1000 Bearings. For that purpose, data that reflect production for one year of continuous processes should be scaled to distribute over time the excessive material or energy consumption. Consequently, any modelling associated with the impact assessment reflects continuous emissions when equilibrium concentrations may be assumed. If data were reported over a period of less than one year for any inventory item, the analysis should be adjusted as appropriate to the functional unit.

Table 6.13. LCI Data Categories.

Data Category	Unit	Description
Materials and Resources flows (input)		
Material flows	kilograms [kg] per functional unit	Actual materials that make up the final product for a particular process (primary materials) and materials that are used in the processing of a product for a particular process. Materials may be non-renewable (i.e., materials extracted from nature that are non-renewable or stock resources such as coal), renewable, or flow resources such as water.
Energy flows	J per functional unit	Process energy and pre-combustion energy (i.e., energy expended to extract, process, refine, and deliver a usable fuel for combustion) consumed by any process in the life-cycle.
Emissions, wastes, and product flows (outputs)		
Emissions to Air	kilograms [kg] per functional unit	Air outputs represent the releases to the environment of gaseous or particulates from a point or diffuse source of any stage of life cycle, after passing through emission control devices, if applicable.
Emissions to water	kilograms [kg] per functional unit	Water outputs represent liquid surface and groundwater discharges to from point or diffuse sources of any stage of life cycle, after passing through any water treatment devices.
Emissions to soil	kilograms [kg] per functional unit	Soil emissions represent discharges of masses of chemical constituents that are considered pollutants to soil from point or diffuse sources of any stage of life cycle.
Wastes	kilograms [kg] per functional unit	Represents the mass of a product or material, either solids or liquids, that are deposited as hazardous or non-hazardous waste, either before or after treatment (e.g., incineration, composting), recovery, or recycling processes.
Primary Products	kg of material or substance, or MJ per functional unit	Material or substance outputs from a process that are received as input by a subsequent unit process within the components life cycle.
Co-Products	kilograms [kg] per functional unit	Material outputs from a process that can be used, either with or without further processing that are not used as part of the final functional unit product.

Decision rules are usually applied in LCA in order to make manageable the collection process of the enormous amount of data involved in inventorying all the flows for a product system. Decision rules are a set of criteria established by project participants used to determine if a given process or material flow is to be evaluated in the LCA. For example, in materials extraction and processing stage, the decision rules were based on the materials used on system manufacture and consequently, the processes to be included on this stage, and for which data will be necessary, are related to the extraction and processing

of these materials. Therefore, and due to enormous amount of data involved in this particular LCA, the decision rules presented below will be taken into account.

1. The quantitative contribution of material or energy source to the product system.

Decision rule: Materials or energy sources used in large quantities have the potential to be associated with even more materials and resources on their manufacture, and thus should be included, due to their higher potential for having a significant environmental impact.

2. Materials that are of known or suspected environmental significance.

Decision Rule: In an environmental LCA, materials or components that are known or suspected to exhibit an environmental hazard or significant impact should be included to the extent feasible.

3. Materials that are known or suspected to have a large energy contribution to the systems energy requirements.

Decision Rule: Significant environmental impacts are associated with the production of energy, therefore, materials or processes that are known or suspected to consume large amounts of energy should be included.

4. Materials that are physically unique to one component over another.

Decision Rule: The physical uniqueness of a material or component has the potential to accentuate the environmental differences among components and, thus, should be included in the study.

5. Materials that are functionally significant to the components.

Decision Rule: "Functionally significant" is defined as important to the technically successful use of the product and its functions, and therefore should be included.

The LCI is the identification and quantification of the material, resource, emission, waste, and product flows from the unit processes in the life cycle of a product system (Figure 6.34). For this assessment, LCI inputs should include materials used in the NU bearings, ancillary materials used in the components processing and manufacturing, and energy and other resources consumed in the manufacturing. LCI process output flows include primary and co-products, as well as emission releases to air, water, and land.

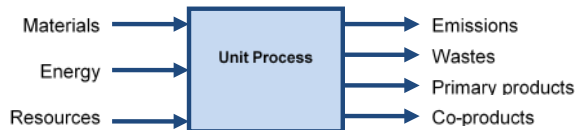


Figure 6.32. Unit process inventory conceptual diagram.

LCI data should be collected both from primary and secondary sources. Prevalence should be given to primary data collected from project partners, in order to better associate the obtained results with the particular system under study. Whenever it is not possible to obtain primary data, secondary data should be used. Secondary data comes from literature sources or other LCA, being specific to either a product, material, or process in question. For those processes that both secondary data were lacking, modelled data or assumptions may serve as defaults. Table 6.14 presents the different types of data expected to be used in each life cycle stage, as well as their sources and partners who will be involved in the collection process.

Table 6.14. Type and source of data for each life cycle stage.

Life Cycle Stage	Type of data	Data Source
Extraction and Acquisition of Raw Materials, Fuel and Energy	Secondary	Ecoinvent
Materials Processing	Secondary	Ecoinvent
NU Bearings Components Manufacture	Primary and Secondary	Schaeffler and Ecoinvent
NU Bearings Assembly	Primary and Secondary	Schaeffler and Ecoinvent

Materials input for bearings production was supplied by Schaeffler. However only the amount of steel and copper used in the components were reported. To be able to elaborate the study, remaining materials input were sourced from the literature when possible.

Inventory analysis

This LCA study follows an attributional approach, which focuses on quantifying the relevant environmental flows related to the production of the NU bearings. The life cycle inventories compiled for each product are compiled from the inputs and outputs of the component processes. All relevant flows of energy and materials crossing the system boundaries have been accounted for (e.g. energy, material resources, wastes and emissions). The Umberto LCA+ software and ecoinvent databases have been used to model the scenarios and to generate the life cycle inventories and impact assessments on which the study conclusions are based.

Material breakdown

For this study we considered the production of bearings having the following parts and material.

Table 6.15. Material breakdown of NU Bearing.

Material classification	Unit	Turbines
Steel (total)	Kg	4.37
Outer ring	Kg	1.86
Inner ring	Kg	1.23
Rollers (16)	Kg	1.28
Copper (total)	Kg	0.7
Cage	Kg	0.7
Total mass	Kg	5.07

Figure 6.35 below shows the unit operations included in the production of the standard bearings components: Outer Ring, Inner Ring, Rollers and Cage. The difference to the Steelwind bearings production bears in the absence of the thermal treatment for the later.

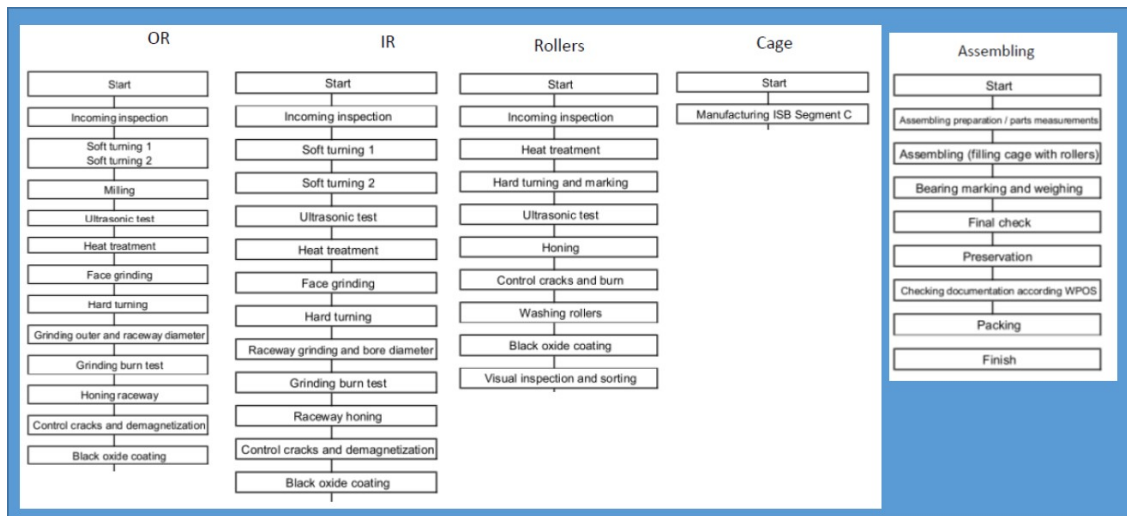


Figure 6.33. Process steps of Standard bearings at Schaeffler.

Impact assessment

The results of this assessment are presented taking into the perspective of determining the environmental performance of the Steelwind and standard bearings production steps. The objective is to understand and analyse the environmental performance of the bearings production.

As can be seen in Table 6.16 and Table 6.17, there are not significant differences in the environmental impact of the two processes.

Table 6.16. Whole-life environmental impacts of the Steelwind bearings production.

Environmental impact categories	Unit	Quantity
terrestrial acidification, TAP500	kg SO ₂ -Eq	130.55
climate change, GWP500	kg CO ₂ -Eq	11531.82
freshwater ecotoxicity, FETPinf	kg 1,4-DCB-Eq	1486.43
marine ecotoxicity, METPinf	kg 1,4-DCB-Eq	1876191.20
terrestrial ecotoxicity, TETPinf	kg 1,4-DCB-Eq	214.64
human toxicity, HTPinf	kg 1,4-DCB-Eq	1679538.13
Ionising radiation , IRP_HE	kg U235-Eq	865.61
water depletion, WDP	m ³	181.32
Fossil depletion, FDP	kg oil-Eq	3189.71
Metal depletion, MDP	kg Fe-Eq	21655.21
photochemical oxidant formation, POFP	kg NMVOC	58.93
freshwater eutrophication, FEP	kg P-Eq	22.68
marine eutrophication, MEP	kg N-Eq	24.57
particulate matter formation, PMFP	kg PM10-Eq	71.70

Table 6.17. Whole-life environmental impacts of the standard bearings production.

Environmental impact categories	Unit	Quantity
terrestrial acidification, TAP500	kg SO ₂ -Eq	132.26
climate change, GWP500	kg CO ₂ -Eq	11779.51
freshwater ecotoxicity, FETPinf	kg 1,4-DCB-Eq	1488.90
marine ecotoxicity, METPinf	kg 1,4-DCB-Eq	1878990.53
terrestrial ecotoxicity, TETPinf	kg 1,4-DCB-Eq	214.88
human toxicity, HTPinf	kg 1,4-DCB-Eq	1683514.73
Ionising radiation , IRP_HE	kg U235-Eq	874.70
water depletion, WDP	m ³	181.82
Fossil depletion, FDP	kg oil-Eq	3246.05
Metal depletion, MDP	kg Fe-Eq	21686.11
photochemical oxidant formation, POFP	kg NMVOC	59.76
freshwater eutrophication, FEP	kg P-Eq	22.74
marine eutrophication, MEP	kg N-Eq	24.89
particulate matter formation, PMFP	kg PM10-Eq	72.14

Analysis of results: impact categories

The results for each impact category are described in further detail in the following sections, identifying the potential impacts of each process step, Table 6.18 and Table 6.19 show the results for each impact category, for each bearing manufacturing step. Because there are not much differences in the environmental impacts of the production of the types of bearings, only the impacts of the Steelwind bearings are shown in the following figures.

Table 6.18. Environmental impacts of Steelwind bearings by process step.

Environmental impact categories	Unit	Rollers	IR	OR	Cage
terrestrial acidification, TAP500	kg SO ₂ -Eq	9.46	17.53	28.04	75.52
climate change, GWP500	kg CO ₂ -Eq	1707.77	3166.46	5063.62	1593.98
freshwater ecotoxicity, FETPinf	kg 1,4-DCB-Eq	143.76	266.26	425.99	650.42
marine ecotoxicity, METPinf	kg 1,4-DCB-Eq	177929.97	329563.15	527257.24	841440.84
terrestrial ecotoxicity, TETPinf	kg 1,4-DCB-Eq	22.70	42.03	67.25	82.67
human toxicity, HTPinf	kg 1,4-DCB-Eq	32492.74	60246.68	96342.82	1490455.89
Ionising radiation , IRP_HE	kg U235-Eq	128.57	238.73	381.53	116.78
water depletion, WDP	m ³	23.01	42.63	68.20	47.48
Fossil depletion, FDP	kg oil-Eq	473.62	878.24	1404.40	433.45
Metal depletion, MDP	kg Fe-Eq	2455.54	4547.32	7275.69	7376.66
photochemical oxidant formation, POFP	kg NMVOC	6.87	12.73	20.36	18.97
freshwater eutrophication, FEP	kg P-Eq	0.79	1.46	2.34	18.10
marine eutrophication, MEP	kg N-Eq	2.66	4.93	7.89	9.08
particulate matter formation, PMFP	kg PM10-Eq	8.28	15.35	24.56	23.51

Table 6.19. Environmental impacts of Standard bearings by process step.

Environmental impact categories	Unit	Rollers	IR	OR	Cage
terrestrial acidification, TAP500	kg SO ₂ -Eq	9.47	19.20	28.07	75.52
climate change, GWP500	kg CO ₂ -Eq	1710.82	3405.86	5068.85	1593.98
freshwater ecotoxicity, FETPinf	kg 1,4-DCB-Eq	143.79	268.64	426.05	650.42
marine ecotoxicity, METPinf	kg 1,4-DCB-Eq	177978.94	332229.63	527341.11	841440.84
terrestrial ecotoxicity, TETPinf	kg 1,4-DCB-Eq	22.70	42.27	67.25	82.67
human toxicity, HTPinf	kg 1,4-DCB-Eq	32851.01	64065.22	96442.61	1490455.89
Ionising radiation , IRP_HE	kg U235-Eq	129.06	246.48	382.37	116.78
water depletion, WDP	m ³	23.03	43.09	68.22	47.48
Fossil depletion, FDP	kg oil-Eq	474.55	932.07	1405.99	433.45
Metal depletion, MDP	kg Fe-Eq	2455.56	4578.15	7275.74	7376.66
photochemical oxidant formation, POFP	kg NMVOC	6.88	13.54	20.38	18.97
freshwater eutrophication, FEP	kg P-Eq	0.79	1.52	2.34	18.10
marine eutrophication, MEP	kg N-Eq	2.67	5.25	7.90	9.08
particulate matter formation, PMFP	kg PM10-Eq	8.29	15.77	24.57	23.51

Atmospheric deposition of inorganic substances, such as sulphates, nitrates, and phosphates, cause a change in acidity in the soil. For almost all plant species there is a clearly defined optimum of acidity. A serious deviation from this optimum is harmful for that specific kind of species and is referred to as acidification. Figure 6.36 shows the potential impacts of terrestrial acidification per production of 1000 bearings. The production of the cage dominates this impact category, followed by the production of the OR, IR and rollers. Climate change impacts result in a warming effect of the earth's surface due to the release of greenhouse gases into the atmosphere and is measured in mass of carbon dioxide equivalents. Figure 6.37 shows the potential impacts of climate change per 1000 bearings produced. Here the OR production is the major contributor.

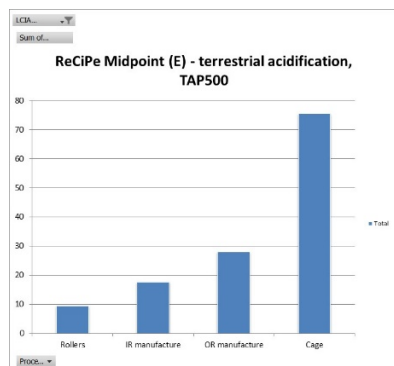


Figure 6.34. Contribution by process step to Terrestrial acidification (kg SO₂-Eq).

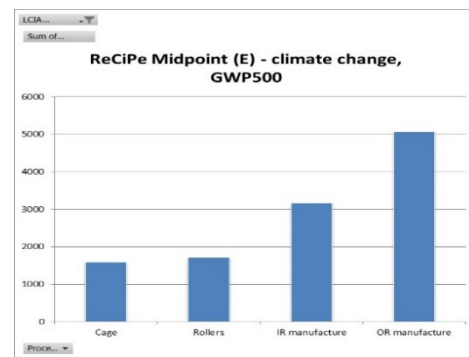


Figure 6.35. Contribution by process step to Climate change (kg CO₂ Eq).

Freshwater ecotoxicity, in general terms, refers to the impact on fresh water ecosystems, as a result of emissions of toxic substances to air, water and soil, and is measured in mass of dichlorobenzene equivalents. Figure 6.38 shows the potential impacts of freshwater ecotoxicity per 1000 bearings produced. Here the Cage production is the major contributor.

Marine ecotoxicity refers to the impact on marine water ecosystems, as a result of emissions of toxic substances to air, water and soil, and is measured in mass of dichlorobenzene equivalents. Figure 6.39 shows the potential impacts of marine ecotoxicity per 1000 bearings produced. Here the Cage production is the major contributor.

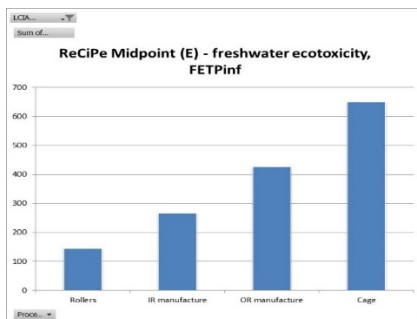


Figure 6.36. Contribution by process step to Freshwater ecotoxicity (kg 1,4-DCB-Eq)

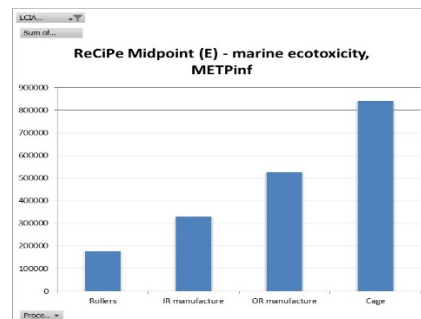


Figure 6.37. Contribution by process step to Marine ecotoxicity (kg 1,4-DCB-Eq).

Terrestrial ecotoxicity refers to the impact on terrestrial ecosystems, as a result of emissions of toxic substances to air, water and soil, and is measured in mass of dichlorobenzene equivalents. Figure 6.40 shows the potential impacts of terrestrial ecotoxicity per 1000 bearings produced. Here the Cage production is the major contributor. Human toxicity refers to the impact on humans, as a result of emissions of toxic substances to air, water and soil, and is measured in mass of dichlorobenzene equivalents. Figure 6.41 shows the potential impacts of human toxicity per 1000 bearings produced. Here the Cage production is the major contributor. It accounts for 89% of the impacts.

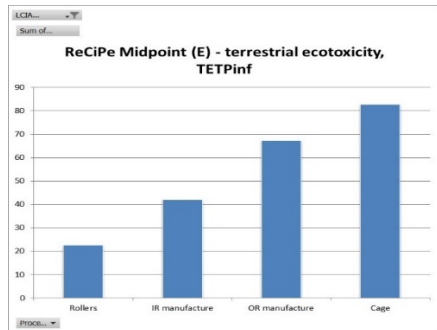


Figure 6.38. Contribution by process step to Terrestrial ecotoxicity (kg 1,4-DCB-Eq).

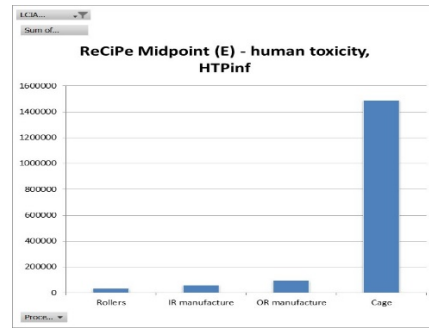


Figure 6.39. Contribution by process step to Human toxicity (kg 1,4-DCB-Eq) per kWh.

Ionising radiation refers to the impact on humans, as a result of the routine releases of radioactive material to the environment. Figure 6.42 shows the potential impacts of ionising radiation per 1000 bearings produced. Here the OR manufacturing is the major contributor.

Water is a scarce resource in many parts of the world, but also a very abundant resource in other parts of the world. Unlike other resources there is no global market that ensures a global distribution. Extracting water in a dry area can cause very significant damages to ecosystems and human health, but so far no models are available to express the damage on the endpoint level. This midpoint indicator simply expresses the total amount of water used. Figure 6.43 shows the potential impacts of water depletion per 1000 bearings produced. Here the OR manufacturing is the major contributor.

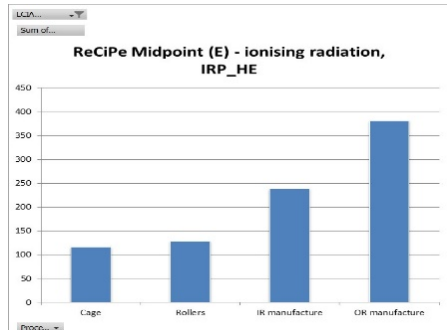


Figure 6.40. Contribution by process step to Ionising radiation (kg U235-Eq).

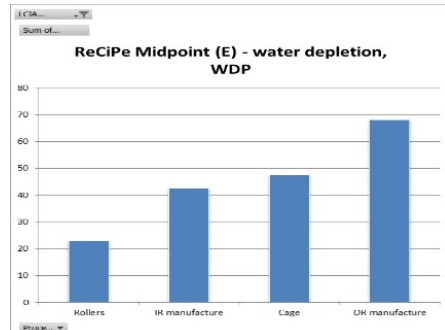


Figure 6.41 – Contribution by process step to Water depletion (m³).

The term fossil fuel refers to a group of resources that contain hydrocarbons. The group ranges from volatile materials like methane, to liquid petrol, to non-volatile materials like anthracite coal. The characterization factor of fossil depletion is the amount of extracted fossil fuel extracted, based on the lower heating value. The unit is kg oil equivalent (1 kg of oil equivalent has a lower heating value of 42 MJ). Figure 6.44 shows the potential impacts of Fossil depletion per 1000 bearings produced. Here the OR manufacturing is the major contributor.

The proposed methodology focuses on the depletion of deposits, instead of individual commodities. The characterization factor for metal depletion is the decrease in grade. The unit is kg Iron (Fe) equivalents. Figure 6.45 shows the potential impacts of Metal depletion per 1000 bearings produced. Here the cage manufacturing is the major contributor followed closely by the OR manufacturing.

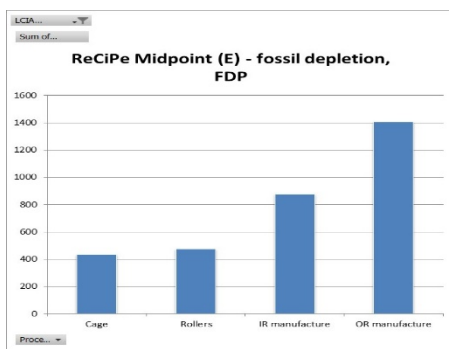


Figure 6.42. Contribution by process step to Fossil depletion (kg oil-Eq).

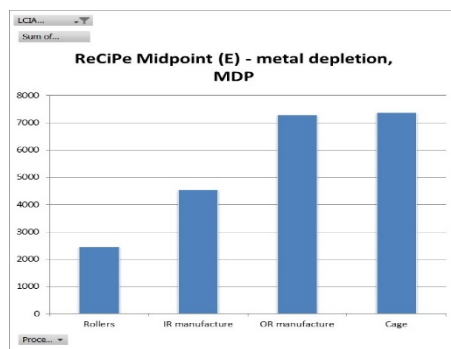


Figure 6.43. Contribution by process step to Metal depletion (kg Fe-Eq).

The characterization factor of photochemical oxidant formation is defined as the marginal change in the 24h-average European concentration of ozone ($d\text{CO}_3$ in $\text{kg}\cdot\text{m}^{-3}$) due to a marginal change in emission of substance x (dM_x in $\text{kg}\cdot\text{year}^{-1}$). The unit is kg NMVOC. Figure 6.46 shows the potential impacts of photochemical oxidant formation per 1000 bearings produced. Here the OR manufacturing is the major contributor followed closely by the cage manufacturing.

In general terms, freshwater eutrophication provides a measure of nutrient enrichment in aquatic environment, which leads to ecosystem damage to those locations from over-enrichment, and is measured in mass of phosphate equivalents. Figure 6.47 shows the potential impacts of eutrophication per 1000 bearings produced. Here the cage manufacturing is the major contributor accounting for 80% of the impact.

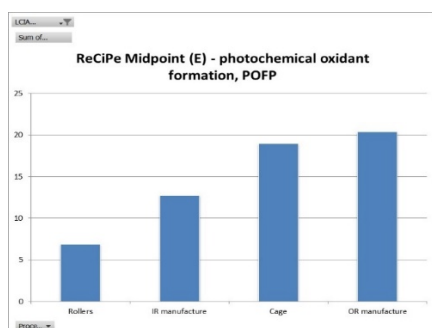


Figure 6.44. Contribution by process step to Photochemical oxidant formation (kg NMVOC).

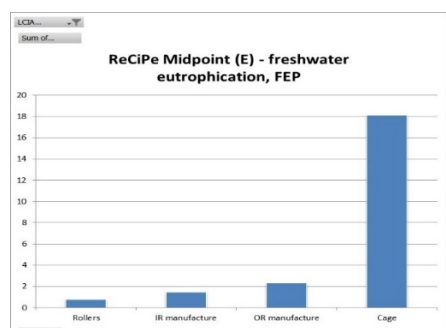


Figure 6.45. Contribution by process step to Freshwater eutrophication (kg P-Eq).

The characterization factor of marine eutrophication accounts for the environmental persistence (fate) of the emission of N containing nutrients. The unit is yr/kg N to freshwater equivalents. Figure 6.48 shows the potential impacts of Marine eutrophication per 1000 bearings produced. Here the cage manufacturing is the major contributor.

Fine Particulate Matter with a diameter of less than 10 μm (PM10) represents a complex mixture of organic and inorganic substances. PM10 causes health problems as it reaches the upper part of the airways and lungs when inhaled. The characterization factor of particulate matter formation is the intake fraction of PM10. The unit is yr/kg PM10 equivalents. Figure 6.49 shows the potential impacts of Particulate matter per 1000 bearings produced. Here the OR manufacturing is the major contributor, followed closely by the cage manufacturing.

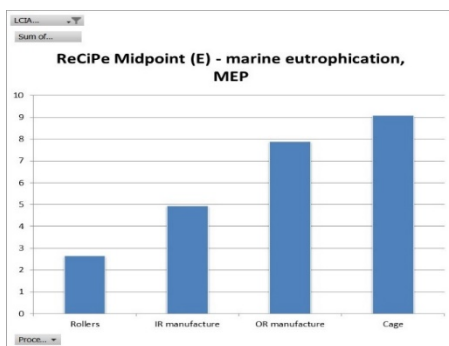


Figure 6.46. Contribution by process step to Marine eutrophication (kg N-Eq).

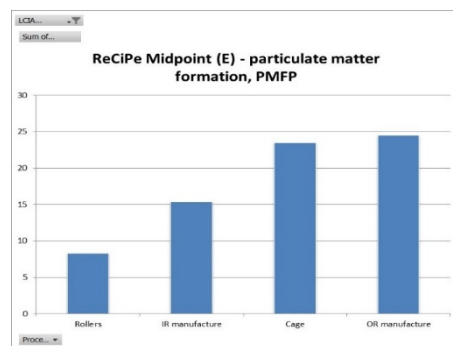


Figure 6.47. Contribution by process step to Particulate matter formation (kg PM10-Eq).

Interpretation

The interpretation stage of the LCA has been carried out in accordance with the main steps defined in ISO (2006a) for life cycle assessment, which includes an assessment of the significant environmental flows and environmental impacts based upon the results of the life cycle inventory (LCI) and life cycle impact assessment (LCIA). The most significant life cycle stages and inventory flows (substance extraction and emissions to/from the environment) are identified and assessed.

The results presented in this report show the environmental profile for the production two types of bearings, one produced with the new steel developed in Steelwind and another produced with the standard steel used by Schaeffler.

The life cycle impact assessment shows that the manufacturing of both types of bearings do not show significant differences in terms of environmental impact. The main difference between the two processes is the absence of the thermal treatment step in the bearings produced with the new steel.

In general, the manufacturing stage impacts could be better assessed if more data was made available. As referred before, most data had to be sourced from the literature and the ecoinvent database. The actual production of the bearings using the new steel grade did not occur so many assumptions and extrapolations had to be made, which implies that the results have large uncertainties. Nevertheless, this study provides some results that can be useful for Schaeffler.

Conclusions and recommendations

The study represents a first approach of the potential environmental impacts of the production of the bearings using the new steel grade. The LCA is based upon current best-practice in the field of life cycle assessment both in the methodologies applied and datasets used to account for environmental impacts, as well as the LCA tools and software applied.

The life cycle assessment could further benefit from considering the following:

- include detailed specific data regarding the production and assembly of the bearings;
- include detailed data concerning the materials used in the process;
- include specific data for the transport of incoming materials

The new steel grade offers the promise of longer life cycle and thus the greater advantage of using such steel will be on extending the working time of the turbines where the bearings will be used. The potential environmental benefits will thus most probably be on the use stage of the bearing.

Conclusions

In this project, a High Nitrogen Austenitic Steel has been developed aimed at the application in bearings in wind turbines. Such applications require particular properties in terms of strength, surface hardness, fatigue, wear, and corrosion resistance. An alloy design based on the updated literature and the application of different models allowed to select a small number of steel grades, variable in particular for the amounts of interstitial (carbon and nitrogen).

After the experimental phase, the C+N Carnit 90 steel has been selected. This is a steel at high content of interstitial, which showed a good hot workability, and is capable to be forged without cracks and porosity, and after a suitable heat treatment possesses a completely austenitic microstructure, free from precipitates (as N-pearlite). Such properties were not obtained with the other steel grades initially selected, which suffer for the great difficulties in hot working (forging) and – in case of the steel with medium-N (N = 0.60 %) – was affected by the presence of delta ferrite.

The mechanical properties of the Carnit 90 steel comply with the requirements established for the bulk (300 HV, 900-1000 MPa), with an excellent level of toughness in comparison with the reference materials (i.e. high-C Cr-added as 100Cr6/AISI 52100). In terms of corrosion, the developed steel represents an improvement. Unfortunately, it has not been possible to evaluate properly the possible improvements in terms of tribocorrosion, due to the lower strength / hardness. To be correctly compared to the reference material, the Carnit 90 would need to be tested in surface hardened conditions (e.g. by deep rolling), further modifications in the test methodology would be needed.

Another result of the project was the optimization of the deep rolling process – aiming at increasing the surface hardness up to the level required for the application – through a number of experimental trials. This process seems to be very promising in that it allows to obtain a surface hardness increase of more than 40 % with respect to the bulk, and its effect extends up to 200-300 µm from the surface. A problem identified with the deep rolling operation, detected in the phase of manufacturing prototype, which will have to be evaluated in the employment of this technique in such applications, is that it induces some plastic deformation in the component. In the case of the experimental prototypes, the geometry of the components was significantly modified, no hard machining was possible, and an alternative method had to be used (cold deformation in-situ).

A number of prototypes (axial washer) have been manufactured from the developed Carnit steel. As specified, in situ cold deformation was needed to obtain components with a proper geometry and suitable to be tested on the full-scale test rig FE8 (Schaeffler). However, the operations of surface strengthening – included an in-situ cold deformation applied on the test rig – were not able to achieve the required hardness levels. This resulted in early failures of the prototypes in the full-scale tests. On the basis of the results found, it is clear that many problems still need to be solved in order to employ the steel grade in this kind of applications.

A result of the project involved the deep investigations about the failure mechanisms of the current bearings. After an extensive failure analysis of typical case, along with a theoretical study of the dynamic and kinetic work conditions of the bearing, specific functional test rigs – and related test methodologies – have been developed for the simultaneous evaluation of steel surface fatigue and corrosion properties. One of the primary scopes of these methodologies is to simulate damage of steel bearings in service conditions. It has been found that the testing system developed to work on components (bearings) is able to induce the development of typical butterfly defect, which are often found coupled to WEC damage.

A test equipment on smaller scale, working with material specimens and aimed at performing accelerated tests, has also been designed and a setup has been attempted. The characteristic of such tests is the chance to simulate induced currents typical of the generators, by means of a device which makes the current flow through the sample during a tribological test.

Exploitation and impact of the research results

The project allowed to propose and produce industrially an austenitic steel grade alternative to the conventional high carbon steels, with good properties in terms of hot workability (forging), mechanical properties and impact toughness. Many problems related with the real applicability of this steel raised and have been pointed out, which will have to be taken into account in the possible future research. It can be mentioned, for example, the difficulty in obtaining a high increase in surface hardness, having to guarantee at the same time a proper geometry and precision of the components.

Finally, the test methodologies developed in the project (functional test rig, accelerated tests on small scale) can be useful tools to investigate the local work conditions of bearing in future projects.

List of figures

Figure 1.1. Gust Wind speed according to IEC 61400-1 [27]	16
Figure 1.2. Rotor load schematic (left); Measurements of rotor load and moment (right)[28]	17
Figure 1.3. Loads on a turbine (DFVLR)	17
Figure 1.4. Low-speed shaft torque during normal shut-down [27]	17
Figure 1.5. Global and local turbine loads [30]	18
Figure 1.6. Oil samples from wind turbines gearboxes in the as received condition.....	19
Figure 1.7. EDS spectrum of the particle side identified with	20
Figure 1.8. Drawings of FAG81212 and NU222 type bearings, and shaft (SW)	21
Figure 1.9. Top left: <i>New</i> SW from axial cylindrical roller bearing FAG 81212. Top right: SW from cylindrical roller bearing FAG 81212 <i>no-failed</i> tested for 461h. Bottom left: SW from <i>failed</i> cylindrical roller bearing FAG 81212. Bottom right: OR from <i>failed</i> cylindrical roller bearing NU222.	21
Figure 1.10. Samples labelled NU222_14 A (right) and NU222_14 B (left).	22
Figure 1.11. NU222_14A: SEM 'collage' of images of the damaged zone of a part of the OR pointed up in the green circle in Figure 1.10.	22
Figure 1.12. NU222_14A: SEM images of the enlarged areas of zones depicted in the previous images: left image corresponds to zone labelled 1 and right image to zone labelled 2.....	22
Figure 1.13. Sample NU222_14B. Left side: SEM image of edge areas evidenced by red circle in Figure 1.10 (90° rotated). On the right enlarged image of damaged zones.....	23
Figure 1.14. NU222_14A. SEM images with MnS (red arrow) and WECs (blue arrow). EDS spectra: Mn sulphide and steel matrix area with no visible inclusions.	23
Figure 1.15. NU222_14 B: SEM BSE image and details at higher magnification (SE mode) of WECs... .	24
Figure 1.16. SEM (SE) images of WECs area with presence of pitting in FAG81218_14 A section sample (Circumferential - no etched sample). The third image is a detail of the second one.	24
Figure 1.17. MnS inclusion (confirmed by EDS microanalysis) close to crack tip	25
Figure 1.18. New FAG 81212-12 (Transversal section): OM images after 3% Nital etching.	25
Figure 1.19. OM images for NU222_14 B after 3% Nital etching.	25
Figure 1.20. FAG 81212_14 A:OM images of WECs after 3% Nital etching.	26
Figure 1.21. FAG 81212-12 no failed-461 hrs: OM images after 3% Nital etching.....	26
Figure 1.22. FAG 81212-14: indentations for micro-hardness and hardness measurements.....	27
Figure 1.23. New FAG 81212-12: SEM images of 100Cr6 steel microstructure after Nital 2% etching. .	27
Figure 1.24. FAG 81212-14: SEM image showing a crack and a WEA.	27
Figure 1.25. FAG 81212-14: EDS analysis on selected areas; spectrum 5 refers to a WEA; spectrum 6 to a chromium carbide.....	28
Figure 1.26. EDS analysis on selected areas: spectra 1 and 3 refer to MnS while spectrum 4 to a chromium carbide particle. Spectrum 2 to the steel matrix.	28
Figure 1.27. FAG 81212-14: SEM image (SE) of WEA/steel matrix sharp boundary. Inclusion, cracks and chromium carbides in steel matrix and in WEA (red circle) are highlighted.	28
Figure 1.28. NU222-14 A sez sample after etching. SEM images. Inclusion with a crack (left); a WEA with crossing cracks and signs of pitting (right).	29
Figure 1.29. Subsurface branched cracks with distance from surface of NU222-14 A sez sample.	29
Figure 1.30. SEM-BSE image of WEC below the raceway surface.	29
Figure 1.31. SEM-BSE images of staircase crack and local positions with different WEA morphologies.30	30
Figure 1.32. SEM-BSE image of line like features aligned with the main crack within a fine-grained homogeneous appearing WEA.	30
Figure 1.33. SEM-BSE image of inhomogeneous WEA with local coarser-grained homogeneous areas along the small cracks and a varied grain size in the central area with grain sizes up to approximately 0.2 µm.).	31
Figure 1.34. SEM-BSE image of local microstructure alterations around cracks. Indications of local plastic deformation are visible in the form of dark parallel line-like features.....	31
Figure 1.35. Butterflies images with SEM-BSE (left) and SEM-SE mode (right). Cracks in and next to the inclusions are visible.....	32
Figure 1.36. SEM-BSE image of a butterfly and local microstructure changes (WEA) at one end of the inclusion.	32
Figure 1.37. SEM-BSE images of interaction between crack network and inclusions; inclusion marked with arrow in the right image.	32
Figure 1.38. Design process flow [80].	34
Figure 1.39. Dynamic simulation of servomotor.	35
Figure 1.40. Load and boundary conditions for the structural analysis of the shaft.	35
Figure 1.41. haft model with "beam" elements.	36

Figure 1.42. Scheme of the test rig	36
Figure 1.43. Servomotor and Drive performance summary	38
Figure 1.44. Von Mises Stresses of the main shaft	39
Figure 1.45. Maximum combined stresses	39
Figure 1.46. Total deformation	39
Figure 1.47. Deformation in the Y direction (between the two central bearings)	40
Figure 1.48. Notched fatigue strength of AISI 431 stainless steel [81]	40
Figure 1.49. 3D model of the test rig	41
Figure 1.50. Detail of the section for the testing area	41
Figure 2.1. Effect of cold deformation on the yield strength of various austenitic steels [45]	43
Figure 2.2. Effect of temperature and stacking fault energy on the deformation microstructures of austenite Fe-Mn-Cr-C alloys [49]	45
Figure 2.3. Effect of Nitrogen content temperature and stacking fault energy on the deformation microstructures of austenite Fe-Mn-Cr-C alloys [55]	45
Figure 2.4. Prediction of SFE according to Olson-Cohen equation	45
Figure 2.5. Modified Schaeffler diagram according to Rechsteiner/Speidel [43]	46
Figure 2.6. Diagrams of phase stability according to JMatPro code	47
Figure 2.7. Estimation of Nitrogen solubility according to Thermo-Calc (Mn=11-18%)	51
Figure 2.8. Estimation of Nitrogen solubility according to Thermo-Calc (Mn=23%)	51
Figure 2.9. Estimation of Nitrogen solubility according to Thermo-Calc at pressure condition lower than p_{atm} (Mn=23%)	51
Figure 2.10. Estimation of gas nucleation during solidification at pressure condition lower than p_{atm} (Mn=23%)	52
Figure 2.11. Production process, sampling and testing of 5 kg ingots	54
Figure 2.12. Tensile properties in the annealed state (YS: white circles, UTS: grey circles) and for comparison empirical relationships with N content given by Speidel (lines)	55
Figure 2.13. Ingots manufactured via VIM. Size Ø142 mm x 610 mm)	57
Figure 2.14. Thermodynamic calculation for CARNIT alloy (MR1/1)	57
Figure 2.15. Thermodynamic calculation for medium-N alloy with N = 0.60 % (MR1/2)	58
Figure 2.16. Thermodynamic calculation for high-N alloy with N = 0.90 % (MR2)	58
Figure 3.1. The bars after preliminary forging	60
Figure 3.2. "On Heating" HNAS hot ductility curves (R.A. % versus deformation temperature)	61
Figure 3.3. "On Cooling" HNAS hot ductility curves (R.A. % versus deformation temperature)	61
Figure 3.4. "Carnit C+N" VM2947 Gleeble broken specimens after testing at 900°C (left,)	62
Figure 3.5. "Medium-N" VM2948 Gleeble broken specimens after testing at 900°C (left,) 1250°C (centre) and 1300°C (right) temperatures	63
Figure 3.6. "High-N" (PESR074) steel results of Reduction of area as a function of tests temperature	64
Figure 3.7. PESR074 specimens after testing at 1200 (Bottom) 1100°C (middle) and 950°C (Top) temperatures	64
Figure 3.8. "High-N" PESR074 Gleeble broken specimens after testing at 1200°C (left) 1100°C (centre) and 950°C (right) temperatures	65
Figure 3.9. 100Cr6 Reduction of area as a function of tests temperature	66
Figure 3.10. Specimens after testing at 1300 (Bottom) 1150°C (middle) and 900°C (Top) temperatures	66
Figure 3.11. Forging and finished forged bar	66
Figure 3.12. VM2950 Micrographs in the as received condition (left) and after being heated at 1050°C (centre) and 1080°C (right)	68
Figure 3.13. VM2950 Micrographs after being heated at 1110°C (left), 1120°C (centre) and 1040°C (right)	68
Figure 3.14. VM2951 Micrographs of the in the as received condition (left) and after being heated at 930°C (centre) and 970°C (right)	68
Figure 3.15. Micrographs after being heated at 1010°C (left), 1050°C (centre) and 1090°C (right)	68
Figure 3.16. VM2951 micrographs showing the presence of delta ferrite	69
Figure 3.17. VM2951 after solution annealing at 1030°C for 1 hour showing the presence of delta ferrite	69
Figure 3.18. Test rig realized at ECOR	69
Figure 4.1. X-ray diffractograms for as-forged (red) and heat treated samples (black)	70
Figure 4.2. RLM of the reference sample in polished condition	71
Figure 4.3. RLM of the reference sample in etched condition	71
Figure 4.4. SEM/SE image of the as forged sample in etched condition. Positions of the EDX composition measurements reported in Table 4.1 are marked	71
Figure 4.5. RLM of σ -phase in the sample heat treated at 930°C; imaged in etched condition	72
Figure 4.6. SEM/BSE of σ -phase in the sample heat treated at 930°C; imaged in etched condition ...	72

Figure 4.7. SEM/BSE image of the sample heat treated at 930 °C. Positions of the EDX composition measurements reported in Table 4.2 are marked.	73
Figure 4.8. SEM images of δ-ferrite in the sample heat treated at 1050 °C; imaged in etched condition.	73
Figure 4.9 SEM/SE image of the sample heat treated at 1050 °C in etched condition. Positions of the EDX composition measurements reported in Table 4.3 are marked.	73
Figure 4.10. X-ray diffractograms for as-forged (red) and heat treated samples (black).	74
Figure 4.11. RLM of as forged polished sample at four different magnifications. Inclusions and porosities are visible.	75
Figure 4.12. RLM of as forged, lightly etched sample, In lightly etched condition, revealing chains of fine grains decorating the boundaries of the larger grains.	75
Figure 4.13. RLM of heat treated samples in etched condition.	76
Figure 4.14: RLM of sample heat treated at 1050°C.	77
Figure 4.15 RLM of samples heat treated at: left) 1110°C, right) 1120°C.	77
Figure 4.16: SEM/SE image and EDX elemental mapping showing the distribution of Cr and Fe from the sample heat treated at 1120°C.	77
Figure 4.17. Thermo-calc diagram showing calculated phase stability areas for the VM2951 alloy. The intended nitrogen content of the alloy is marked with a blue dotted line.	78
Figure 4.18. Thermo-calc diagram showing calculated phase stability areas for the VM2950 alloy. The intended nitrogen content of the alloy is marked with a blue dotted line.	79
Figure 4.19. Deep rolling applied to a turbine wheel.	80
Figure 4.20 . Deep rolling of valves for diesel engines.	80
Figure 4.21. Crank Shaft deep rolling.	81
Figure 4.22. Machined samples (Bottom) from forged bar (top) VM2950 for deep rolling tests.	81
Figure 4.23. Machined samples from forged bar VM2951 employed for deep rolling tests.	82
Figure 4.24. Lathe-Milling Machine where the Deep Rolling trials were performed.	82
Figure 4.25. Lathe chuck used to support a wide variety of work pieces shapes with the four jaws and detail of the system employed to clamp the deep dolling samples.	83
Figure 4.26. Area of the samples where DR is applied.	83
Figure 4.27. Visual aspect of the samples after DR with different tool angles and pressures.	84
Figure 4.28. Surface hardness evaluation for Carnit steel. Green: 200 bar, red: 400 bar, blue: 600 bar.	85
Figure 4.29. Surface hardness evaluation after DR with different tool angles.	86
Figure 4.30. Hardness profile, Carnit steel, Tool angle 90°, p = 200 bar.	87
Figure 4.31. Evolution of residual stress.	88
Figure 4.32. Hardness profile evaluation after Deep Rolling and annealing at different temperatures.	88
Figure 4.33. Hardness profile evaluation after Deep Rolling with different tool angles and annealing at different tempering temperatures.	89
Figure 4.34. Test rig structure and the position (station) of testing bearings.	90
Figure 4.35. Noise signals acquisition from the testing bearing positions.	90
Figure 4.36. Example of a recorded image of acoustic emission by QASS System.	91
Figure 4.37. Example of recorded data by QASS System (starting reference conditions).	91
Figure 4.38. Example of recorded data by QASS System (end of test).	91
Figure 4.39. Spectrum RUN 1.1.	92
Figure 4.40. RUN 2: SW-402.	93
Figure 4.41. Capture from SEM analysis of inner bearing ring with tracks of Aluminium and Oxygen.	94
Figure 4.42. Refmet coating for the insulation of test rig component.	94
Figure 4.43. Process landscape for bearing 2 (RUN 11).	95
Figure 4.44. Micropitting formation on bearing SW-413.2.	96
Figure 4.45. Control of the insulation of the flange and sketch of the issue.	96
Figure 4.46. Details of the 2 macro-pittings on bearing SW-414.	97
Figure 4.47. Bearing SW-414.2.	97
Figure 4.48. Micropitting formation on bearing SW-415.	98
Figure 4.49. SW-414 IR left) LOM overview. right) SEM detail of the surface initiation.	98
Figure 4.50. SW-414 left) Circumferential microcut through the bigger pitting. Right) Detail of circumferential microcut.	99
Figure 4.51. SW-415 IR left) LOM overview. Right) SEM detail.	99
Figure 4.52. SW-415 OR left) LOM overview. Right) SEM detail.	99
Figure 4.53 - SW-415 left) Circumferential microcut through IR showing one butterfly, right) Circumferential microcut through the pitting of OR having no evidences for WEC.	100
Figure 4.54. Schematic drawing of the FE8 test rig and bearing type (FAG 81212) used.	101
Figure 4.55. BEARINX® calculation of the required hardness of the FE8 - shaft washers, if testing with an axial force of F = 80 kN (Hertzian pressure of ≈ 2150 MPa).	102

Figure 4.56. Schematic drawing of the R4G test rig and bearing type (NU222) used.....	102
Figure 4.57. BEARINX® calculation of the required hardness of IR and OR, if testing with a radial force of 100 kN.	103
Figure 5.1. Slip and stick regions in the roller-ring cylindrical contact: a) slip with the same sense of the entering velocity; b) stick regions; c) slip with sense opposite to the entering velocity. From Appendix D1.1 - Dynamic and kinetic analyses.....	105
Figure 5.2. The Universal Micro Tribometer CETR UMT-3 at CSM.....	105
Figure 5.3. Details of the upgraded configuration of CETR UMT-3.	106
Figure 5.4. Functional diagram of the assembled device.....	106
Figure 5.5. Schematic representation of the induced currents.	107
Figure 5.6. Macro image of the wear track (steel 100Cr6, I = 2 A).....	107
Figure 5.7. Profile of the wear track (steel Carnit 90, I = 4 A).....	107
Figure 5.8. Tensile test specimen geometry.....	108
Figure 5.9. Impact toughness results.	109
Figure 5.10. Fatigue specimen geometry.	110
Figure 5.11 – Summary of the results of fatigue tests.	111
Figure 5.12. Typical fracture surface of a tensile specimen from new grade steel (D160).	112
Figure 5.13. Typical fracture surface of run out fatigue specimen (2×10^6 cycles) then tested in tensile.	112
Figure 5.14. Fractographic analysis of a fatigue specimen from D160 periphery. Stress range 516 Mpa, fatigue life 266739 cycles.	113
Figure 5.15. Fractographic analysis of a fatigue specimen from D60 periphery. Stress range 516 Mpa, fatigue life 222090 cycles.	114
Figure 5.16. Fractographic analysis of a fatigue specimen from reference material. Stress range 932 MPa, fatigue life 8354 cycles.	115
Figure 5.17. Cumulative percentage vs time to failure for 100Cr6.	116
Figure 5.18. Weibull distribution of rolling contact fatigue life of 100Cr6.	116
Figure 5.19 The modified RTM ball-on-disk tribometer with the electrochemical cell during a test.	117
Figure 5.20. A detail of the electrochemical cell. Clockwise arrows indicate: the polymeric cell containing the electrolyte, the Al ₂ O ₃ ball in its ball holder and finally the AISI 52100 disk.	117
Figure 5.21. Detail of electrodes inserted in the electrochemical cell: reference calomel electrode is the one with green upper part, while the counter electrode -a Pt wire- has a rubber insulating collar (red).	118
Figure 5.22. Scheme of the experimental setup for unidirectional sliding test. Left: (a) front view (b) top view. Right: zoom-in.....	118
Figure 5.23. Disk drawings and 100Cr6 steel samples before and after tests.	119
Figure 5.24. Curves of OCP vs time (left) and potentiodynamic Current vs applied potential (right) for two 100Cr6 samples (NaCl 3.5 wt.% solution, Potential sweep rate: 1 mV·s ⁻¹).	120
Figure 5.25. Comparison curves of OCP and potentiodynamic for two 100Cr6 samples with (150 N) and without applied load. Left: applied potential vs time; right: current vs applied potential. (NaCl 3.5 wt.% solution, Potential sweep rate: 1 mV·s ⁻¹)	120
Figure 5.26. 100Cr6 CoF curve (vs test time) at OCP and 150 N load in a 3 h test and the wear track cross sectional profile detected by means of the optical system: Carl Zeiss Axio Imager M2m. plot. 3 hours tests in NaCl 3.5 wt.% solution.	121
Figure 5.27. CoF curve (vs test time) in potentiostatic control; 3 hours test and 150 N load. Wear track cross sectional profile detected by means of the optical system: Carl Zeiss Axio Imager M2m. Potentiostatic conditions (-1 V vs E _{corr}), NaCl 3.5 wt.% solution.	122
Figure 5.28. Comparison between curves for OCP and potentiodynamic polarization for 100Cr6 with 150 N load and with no applied load. Left: applied potential vs time; right: applied potential vs log of current (NaCl 3.5 wt.% solution, Potential sweep rate: 1 mV·s ⁻¹).	122
Figure 5.29. A 100Cr6 tribocorrosion specimen with the two tracks developed after a tribocorrosion and a corrosion experiment. Left: a wear track due to potentiodynamic test carried out at 150 N load; right: the outer corrosion track is from a potentiodynamic test.	122
Figure 5.30. CoF recorded during PD test with 150 N Load for 100Cr6 specimen. NaCl solution 3.5%.	123
Figure 5.31. CARNIT specimen after a PD corrosion test in 3.5% NaCl solution.	123
Figure 5.32. OCP and potentiodynamic polarization curves for CARNIT at 150 N load. Left: applied potential vs time; right: applied potential vs log of current density. (NaCl 3.5 wt.% solution, Potential sweep rate: 1 mV·s ⁻¹).	124
Figure 5.33. A track on Carnit tribocorrosion specimen after a potentiodynamic tribocorrosion experiment carried out at 150 N load.	124

Figure 5.34. Comparison between Carnit and 100C6 OCP curves (left) and PD curves (right) in corrosion and tribocorrosion tests. Tests carried without any load and at 150 N load. NaCl 3.5% solution. Potential sweep rate: $1 \text{ mV} \cdot \text{s}^{-1}$	125
Figure 5.35. The track on Carnit tribocorrosion specimen after a PS tribocorrosion experiment carried out at 150 N load for 3 hours and -1V cathodic vs Ecorr. Average CoF value resulted 0.40.	126
Figure 5.36 The method adopted for track profile measurements and a cross sections of the track with area evaluation for Carnit specimen after a PS experiment carried out at 150 N load for 3 hours and 1V cathodic vs Ecorr.....	126
Figure 5.37. The track on Carnit specimen after a OCP experiment carried out at 150 N load for 3 hours, and the recorded CoF curve. Average CoF value resulted 0.42.	126
Figure 5.38. The method adopted for track profile measurements and a cross section of the track with area evaluation for Carnit specimen after a OCP experiment carried out at 150 N load for 3 hours. .	127
Figure 6.1. Electrode S83725 prepared for PESR operation.	128
Figure 6.2. PESR ingot D37130 (\varnothing 630 mm).....	128
Figure 6.3. Hot rolled bars (square 230 mm x 230 mm).....	129
Figure 6.4. Bars forged to the final sizes (\varnothing 60 mm, \varnothing 120 mm and \varnothing 160 mm).....	129
Figure 6.5. Hardness (HV30) as a function of solution annealing temperature (soaking time 50 min).	130
Figure 6.6. Microstructure, annealing temperature 1070 °C.	131
Figure 6.7. Microstructure, annealing temperature 1090 °C.	131
Figure 6.8. Microstructure, annealing temperature 1120 °C.	132
Figure 6.9. Microstructure, annealing temperature 1140 °C.	132
Figure 6.10. Microstructure, annealing temperature 1170 °C.	132
Figure 6.11 RLM image of the sample heat treated at 1120°C for 160 min after etching.	133
Figure 6.12. SEM BSE images of the two heat treated samples.....	134
Figure 6.13. SEM EBSD results for the two heat treated samples.	134
Figure 6.14: Route for HNAS full scale production according to the project plan.	135
Figure 6.15. Visual aspect of the prototypes before deep rolling.	136
Figure 6.16. Visual aspect of the prototypes after deep rolling.	136
Figure 6.17. Hardness patterns on an example of housing washer after deep rolling process.	138
Figure 6.18: 3D - geometrical measurement of one washer after deep rolling process. Red and blue colors indicate deviation from desired geometry.....	138
Figure 6.19: Geometrical measurement of one washer after deep rolling process. Deviation in dimensions up to 0.23 mm.....	138
Figure 6.20. Route for HNAS full scale production using FE8 test rig for cold deformation (schematic)	138
Figure 6.21. FE8 test rig. (left) schematic drawing of the FE8 test rig; (right) photo of the FE8 test rig	139
Figure 6.22. Simulation model and chosen results. (a) simulation model (24° piece) containing one roller; (b) inhomogeneous deformation at the inner and outer race; (c) Cross section in the middle of the modelled washer and the two positions at which the plastic deformation was evaluated in depth; (d) plastic deformation in depth at 10 and 20 kN after 25 rolling passes; (e) Evolution of the plastic strain with rolling passes and depth	140
Figure 6.23. washer after "in situ" cold deformation on FE8 with 10 KN / roller	141
Figure 6.24. Geometrical measurement of the washer in radial direction.....	141
Figure 6.25. washer after "in situ" cold deformation on FE8 with 20 KN / roller	141
Figure 6.26. Geometrical measurement of the washer in radial direction.....	141
Figure 6.27. Hardness measurement on washers after "in situ" cold deformation on FE8 using 10 KN / roller (\approx 5 GPa) and 20 kN / roller (\approx 10 GPa)	141
Figure 6.28. LOM of washer from bearing A2 after test on FE8_25* showing several pittings, mainly in the radial middle of the racetrack	142
Figure 6.29. SEM detail of a pitting in a washer from bearing A2 after test on FE8_25*, which shows an origin from the surface.....	142
Figure 6.30. LOM of washer from bearing B42 after test on FE8_25* showing several pittings, mainly in the radial middle of the racetrack	143
Figure 6.31. SEM detail of a pitting in a washer from bearing B4 after test on FE8_25*, which shows an origin from the surface.....	143
Figure 6.32. Unit process inventory conceptual diagram.....	146
Figure 6.33. Process steps of Standard bearings at Schaeffler.	147
Figure 6.34. Contribution by process step to Terrestrial acidification (kg SO ₂ -Eq).....	149
Figure 6.35. Contribution by process step to Climate change (kg CO ₂ Eq).	149
Figure 6.36. Contribution by process step to Freshwater ecotoxicity (kg 1.4-DCB-Eq).....	149
Figure 6.37. Contribution by process step to Marine ecotoxicity (kg 1.4-DCB-Eq).....	149

Figure 6.38. Contribution by process step to Terrestrial ecotoxicity (kg 1,4-DCB-Eq)	150
Figure 6.39. Contribution by process step to Human toxicity (kg 1,4-DCB-Eq) per kWh	150
Figure 6.40. Contribution by process step to Ionising radiation (kg U235-Eq)	150
Figure 6.41– Contribution by process step to Water depletion (m ³)	150
Figure 6.42. Contribution by process step to Fossil depletion (kg oil-Eq)	151
Figure 6.43. Contribution by process step to Metal depletion (kg Fe-Eq)	151
Figure 6.44. Contribution by process step to Photochemical oxidant (kg NMVOC)	151
Figure 6.45. Contribution by process step to Freshwater eutrophication (kg P-Eq)	151
Figure 6.46. Contribution by process step to Marine eutrophication (kg N-Eq)	152
Figure 6.47. Contribution by process step to Particulate matter formation (kg PM10-Eq)	152

List of tables

Table 1.1 – Oil chemical composition, provided from the customer Castrol BBX A320.	20
Table 1.2. Schaeffler's analysed samples	21
Table 1.3. FAG 81212-12 new bearing hardness measurements results	25
Table 1.4. FAG 81212-14 microhardness and hardness measurements results	26
Table 1.5. Accessory components for control and measure.	37
Table 1.6. Results of the dynamic simulation	38
Table 2.1. Chemical compositions of reference solutions for bearings.	42
Table 2.2. Mechanical properties of reference solutions for bearings	42
Table 2.3. Target mechanical properties of new HNAS steel (source Schaeffler)	42
Table 2.4. First set of considered alloys	43
Table 2.5. Empirical relationships for prediction of mechanical properties	44
Table 2.6. Predicted mechanical properties	44
Table 2.7. Considered modified Schaeffler diagrams	46
Table 2.8. Estimations of austenite stability according to Thermo-Calc	47
Table 2.9. Empirical models for determination of N solubility based on interaction parameters for f_N	48
Table 2.10 Empirical models for determination of nitrogen solubility based on C_{eq} and C_{eq}	49
Table 2.11. Predictions of nitrogen solubility according to considered empirical models	50
Table 2.12. Summary of alloy design considerations	53
Table 2.13. Compositions of experimental ingots (mass %)	54
Table 2.14. Composition selected for Manufacturing Route 2 (VIM+PESR)	55
Table 2.15. Compositions selected for Manufacturing Route 1 (VIM, in N atmosphere)	55
Table 2.16. Austenite stability and carbon content in CARNIT composition	55
Table 2.17. Austenite stability and molybdenum content in CARNIT composition	55
Table 2.18. Summary of the selected alloys. VIM: Vacuum Induction Melting. PESR: Pressured Electro Slag Re-melting	56
Table 2.19. Target chemical compositions of the selected alloys. Mass %. (*) After PESR	56
Table 2.20. Composition of CARNIT alloy ingots (MR1/1). Mass %	56
Table 2.21. Composition of medium N alloy ingots (MR1/2). Mass %	56
Table 2.22. Composition of high N alloy ingots (MR2). Mass %	56
Table 2.23. Selection of solubilization temperatures	58
Table 3.1. VM2950 (Carnit): heat treatment conditions	67
Table 3.2. VM2951 (Medium-N): heat treatment conditions	67
Table 4.1: SEM/EDX measurements from locations marked in Figure 4.4; all results in wt%	71
Table 4.2: SEM/EDX measurements from locations marked in Figure 4.7; all results in wt%	72
Table 4.3: SEM/EDX measurements from locations marked in Figure 4.9 all results in wt%	73
Table 4.4. Initial roughness and hardness average values of the samples	82
Table 4.5. Deep Rolling Process Parameters – first campaign	83
Table 4.6. Deep Rolling Process Parameters – second campaign	84
Table 4.7. Roughness measurements (μm) before (left) and after (right) deep rolling. First campaign	84
Table 4.8. Roughness measurements (μm) before (left) and after (right) deep rolling. Second campaign	85
Table 4.9. Influence of deep rolling parameters on the surface hardness and hardness increase of VM2951(MR1/2, medium-N N=0.60%)	86
Table 4.10. List of the tests carried out since the beginning of the project	92
Table 4.11. Testing parameters of bearings tested at ECOR for the setup phase	92
Table 4.12. Testing parameters of bearings tested at ECOR for the setup phase	92
Table 4.13. Testing parameters of bearings tested at ECOR and supplied by SCH	93
Table 4.14. Testing parameters of bearings tested at ECOR and supplied by SCH	93
Table 4.15. Testing parameters of bearings tested at ECOR (RUN 7)	93
Table 4.16. Testing parameters of bearings tested at ECOR (RUN 10)	95
Table 4.17. Testing parameters of bearings tested at ECOR (RUN 13.1)	95
Table 4.18. Testing parameters of bearings tested at ECOR (RUN 15)	97
Table 4.19. Bearings from test setup No. 14 and No.15	98
Table 5.1. Summary of the first sets of tests	108
Table 5.2. Summary of tensile properties for all materials and HT condition	109
Table 5.3. Summary of fatigue test results for materials and conditions	110
Table 5.4. Characteristic E_{corr} and I_{corr} and J_{corr} parameters for 100Cr6 martensitic steel in corrosion and tribocorrosion (150 N load) experiments	121

Table 5.5. Characteristic E_{corr} and I_{corr} and J_{corr} parameters for Carnit and 100Cr6 martensitic steel in corrosion and tribocorrosion (150 N load) experiments	125
Table 6.1. Chemical composition of D37130 PESR ingot (mass %).....	128
Table 6.2. Requirements for steel cleanliness (maximum limits).....	130
Table 6.3. Annealing temperatures and related hardness values.....	130
Table 6.4. Steel cleanliness according to ASTM E45 method A.....	133
Table 6.5. Microhardness results (50 g load, average of 5 measurements).....	135
Table 6.6: Parameters applied via deep rolling @Sidenor.	135
Table 6.7. Effect of deep rolling on surface hardness.	137
Table 6.8. Parameters for "in situ" cold deformation on FE8.....	140
Table 6.9. test conditions for wear test FE8_03, WEC test FE8_25 and adapted WEC test FE8_25*..	142
Table 6.10. Results of the full-scale tests, performed according FE8_25*.....	142
Table 6.11. Major stages of the Bearings LCA.	144
Table 6.12. Data temporal and geographical boundaries by life cycle stage.	145
Table 6.13. LCI Data Categories.	145
Table 6.14. Type and source of data for each life cycle stage.	146
Table 6.15. Material breakdown of NU Bearing.....	147
Table 6.16. Whole-life environmental impacts of the Steelwind bearings production.	148
Table 6.17. Whole-life environmental impacts of the standard bearings production.	148
Table 6.18. Environmental impacts of Steelwind bearings by process step.	148
Table 6.19. Environmental impacts of Standard bearings by process step.	149

List of acronyms and abbreviations

4PCVBB	Four point contact ball bearing
BB	Deep groove ball bearing
BF	Butterfly
BSE	Back Scattered Electrons
CAD	Computer-Aided Design
CRB	Cylindrical Roller Bearings
CSM	Centro Sviluppo Materiali
DEZ	Dark Etching Zone
DIMA	Department of Mechanics and Aeronautics (University La Sapienza)
DR	Deep rolling
DTRB	Double-row tapered roller bearing
EDS	Energy Dispersive Spectroscopy
EDX	Energy Dispersive X-RAY Dispersive Spectroscopy
ESR	Electron Slag Remelting
FAG 81212	Reference type bearing for FE8_25 test rig
FCCRB	Full complement cylindrical roller bearing
FE8_25	Test rig for WEC damage
FEM	Finite Element Model
GSC	Geometric stress concentration
HNAS	High Nitrogen Austenitic Steel
HS	High speed
HV	Vickers Hardness
HW	Housing Washer
IEC	International Electrotechnical Commission
IMS	Intermediate speed
IR	Inner ring
ISQ	Instituto de Soldadura e Qualidade
LS	Low speed
MnS	Manganese Sulfide
M _{shaft}	Calculated torque value of the servomotor
N/A	Non Applicable
NaCl	Sodium chloride
Nital	Etching solution: Nitric Acid in methanol carrier
NU222	Reference type bearing for R4G test rig
OM	Optical Microscopy
OR	Outer ring
PAG	Polyalkylene glycol
PAO	Polyalphaolefin
PESR	Pressure Electron Slag Remelting
RA	Reduction of Area
R4G	Test rig for WEC damage
RCF (T)	<i>Rolling contact fatigue (testing)</i>
SCC	Steel corrosion cracking
SCH	Schaeffler
SE	Secondary Electrons
SEM	Scanning Electron Microscopy
SFEG	SCANNING FIELD EMISSION GUN
SRB	Spherical roller bearing
SW	Shaft Washer
TBD	To Be Defined
TRB	Tapered roller bearings
TRRB	Triple-row cylindrical roller bearing
UTS	Ultimate Tensile Strength
WEA	White Etching Area
WEB	White Etching Band
WEC	White Etching Crack
WSF	White Structure Flacking
WT	Wind Turbine

List of references

1. Kenneth G. Scott; David Infield; Nigel Barltrop; John Coulgate; Anabel Shahaj, (2009)Effects of Extreme and Transient Loads on Wind Turbine Drive Trains, American Institute of Aeronautics and Astronautics available from : https://www.strath.ac.uk/media/departments/eee/iee/windenergydtc/publications/Kenny_Scott_A_SME_Paper.pdf accessed: November 2014.
2. PROTEST - PROcedures for TESTing and measuring wind energy systems, FP7-ENERGY-2007-1-RTD, Deliverable D1: State-of-the-Art-Report, Date of preparation: 02.04.09.
3. R. Errichello, S. Sheng, J. Keller, A. Greco, Wind Turbine Tribology: A Recap, US Department of Energy, EERE Wind and Water Power Program, DOE/GO-102011-3496.
4. Robert J.K. Wood, AbuBakr S. Bahaj, Stephen R. Turnock, Ling Wang and Martin Evans "Tribological design constraints of marine renewable energy systems" Philosophical Transactions of the Royal Society A, 368, 4807-4827
5. W. Holweger, M.Wolf, D. Merk, T.Blass, M. Goss, J. Loosa Schwan et al., Metallurgical Transactions A, vol 76, August 1976, page 1100
6. T. B. Lund: 'Subsurface initiated rolling contact fatigue—fluence of non-metallic inclusions, processing conditions, and operating conditions', J. ASTM Int., 2010, 7, (5), 1–12;
7. K. Sugino, K. Miyamoto, M. Nagumo and K. Aoki: 'Structural alterations of bearing steels under rolling contact fatigue', ISIJ Int., 1970, 10, 98–111.
8. Grabulov, U. Ziese and H. W. Zandbergen: 'TEM/SEM investigation of microstructural changes within the white etching area under rolling contact fatigue and 3-D crack reconstruction by focused ion beam', Scr. Mater., 2007, 57, (7), 635–638.
9. R. Osterlund, O. Vingsbo, L. Vincent and P. Guiraldenq: 'Butterflies in fatigued ball bearings – formation mechanism and structure', Scand. J. Metall., 1982, 11, 23–32.
10. J. A. Martin, S. F. Borgese and A. D. Eberhardt: 'Microstructural alterations of rolling bearing steels undergoing cyclic stressing', Trans. ASME J. Basic Eng., 1966, 88, 555–567
11. K. Hiraoka, M. Nagao and T. Isomoto: 'Study on flaking process in bearings by white etching area generation', J. ASTM Int., 2006, 3, (5), 1–7.
12. W. J. Davies and K. L. Day: 'Surface fatigue in ball bearings, roller bearings, and gears in aircraft engines', Proc. Symp. on 'Fatigue in rolling contact', London, UK, March 1963, Institution of Mechanical Engineers, 23–40.
13. P. C. Becker: 'Microstructural changes around non-metallic inclusions caused by rolling contact fatigue of ball-bearing steels', Met. Technol., 1981, 8, 234–243.
14. Grabulov: 'Fundamentals of rolling contact fatigue', PhD thesis, University of Belgrade, Serbia, 2010.
15. J. Rosinski and D. Smurthwaite: 'Troubleshooting wind gearbox problems', Gear Solut., 2010, 8, 22–33.
16. M. N. Kotzalas and G. L. Doll: 'Tribological advancements for reliable wind turbine performance', Phil. Trans. R. Soc. A, 2010, 368A, (1929), 4829–4850.
17. Y. Murakami, M. Naka, A. Iwamoto and G. Chatell: 'Long life bearings for automotive alternator applications', Proc. Int. Cong. Exposit., Detroit, MI, USA, February–March 1995, SAE International, 1–14.
18. Umeda, T. Shiga and K. Ihata: 'Rolling bearing incorporated in auxiliary device for internal combustion engine', US Patent 7,618,193 B2, 2009.
19. K. Tamada and H. Tanaka: 'Occurrence of brittle flaking on bearings used for automotive electrical instruments and auxiliary devices', Wear, 1996, 199, (2), 245–252.
20. H. Mikami and T. Kawamura: 'Influence of electrical current on bearing flaking life', SAE Technical Paper 2007-01-0113, SAE International, Warrendale, PA, USA, 2007.
21. J. A. Ciruna and H. J. Szieleit: 'The effect of hydrogen on the rolling contact fatigue life of AISI 52100 and 440C steel balls', Wear, 1973, 24, 107–118.
22. J. Fitch: 'How water causes bearing failure', Mach. Lubr. Mag., Jul. 2008. Available from: <http://www.machinerylubrication.com/Read/1367/water-bearing-failure>.
23. D. Scott, B. Loy and G. H. Mills: 'Metallurgical aspects of rolling contact fatigue', P. I. Mech. Eng., 1966, 181, (315), 94–103.
24. Failures of Rolling-Element Bearings, chapter in Failure Analysis and Prevention Vol 11, 2002, ASM Handbook (ED) William T. Becker and Roch J. Shipley.
25. Roman Ritzenhoff and André Hahn (2012). Corrosion Resistance of High Nitrogen Steels, Corrosion Resistance, Dr Shih (Ed.), ISBN: 978-953-51-0467-4, InTech, Available from: <http://www.intechopen.com/books/corrosion-resistance/corrosion-resistance-of-high-nitrogen-steels>
26. <http://www.nmbtc.com/bearings/engineering/load-life/>; accessed: November 2014.

27. Tony Burton; Nick Jenkins; David Sharpe and Ervin Bossanyi.,(2011) Wind Energy Handbook, Second Edition. John Wiley & Sons, Ltd
28. Technical Trends in Wind Turbine Bearings, NTN TECHNICAL REVIEW No.76, 2008
29. PROTEST - PROcedures for TESTing and measuring wind energy systems, FP7-ENERGY-2007-1-RTD , Deliverable D1: State-of-the-Art-Report, Date of preparation: 02.04.09 [16] Berthold Schlecht; Thomas Rosenlöcher, (2008) Strategy for user orientated simulation of wind turbines to calculate realistic load conditions, IEA Meeting on Wind Turbine Drivetrain Dynamics and Reliability, Technische Universität Dresden.
30. PROTEST - PROcedures for TESTing and measuring wind energy systems, FP7-ENERGY-2007-1-RTD, Deliverable D1: State-of-the-Art-Report, Date of preparation: 02.04.09.
31. Elon J. Terrell; William M. Needelman; Jonathan P. Kyle, (2009) Current and Future Tribological Challenges in Wind Turbine Power Systems, Proc. ASME. 48951; ASME/STLE 2009 International Joint Tribology Conference:495-497.January 01, 2009.
32. Greco, A. et al. material wear and fatigue in wind turbine systems.
33. Evans, R.D. Classic bearing damage mode- TIMKEN (2011).
34. Luyckx J,(2011), "WEC failure mode on roller bearings: From observation via analysis to understanding and a solution" Proceedings of the VDI Symposium Gleit- ind Wälzlagerungen: Gestaltung, Berechnung, Einsatz, Schweinfurt, Germany, May 24-25, 2011, VDI-Berichte 2147, VDI Wissensforum, Düsseldorf, Germany, p 31-42
35. West, O. H. E., et al. "Application of complementary techniques for advanced characterization of white etching cracks." Practical Metallography 50.6 (2013): 410-431.
36. Diederichs, A. M., et al. "Electron microscopy analysis of structural changes within white etching areas." Materials Science and Technology (2016): 1-11.
37. Kang, Hosseinkhani, Rivera-Díaz-del-Castillo. Rolling contact fatigue in bearings: a multiscale overview_SKF Publications (2012).
38. Kang et al., Solute redistribution in the nanocrystalline structure formed in bearing steels, Scripta Materialia (2013).
39. Grabulov, Zandbergen ,TEM and Dual Beam (SEM/FIB) investigations of subsurface cracks and White Etching Area (WEA) formed in a deep groove ball bearing caused by Rolling Contact Fatigue (RCF)_Scripta Materialia, 2007, 57(7), 635-638. 17
40. Greco, A. et al._Material wear and fatigue in wind turbine systems. Wear 302 (2013) 1583-1591.
41. Evans, M.H., White structure flaking (WSF) in wind turbine gearbox bearings: effects of 'butterflies' and white etching cracks (WECs). Material Science and Tech.2012 vol 28.
42. Holweger W., Wolf M., Merk D, Blass T., Goss M., Loos J., Barteldes S. and Jakovics A. White Etching Crack Root Cause Investigations. Tribology Transactions, 58: 59–69, 2015
43. http://cartech.ides.com/ImageDisplay.aspx?E=73&IMGURL=%2fCarpenterImages%2fB-StainlessSteel%2f12-SS12-Type440B%2f03_SS12_TypicalRoom.gif&IMGTITLE=Typical+Room+Temperature+Mechanical+Properties
44. http://cartech.ides.com/ImageDisplay.aspx?E=72&IMGURL=%2fCarpenterImages%2fB-StainlessSteel%2f13-SS13-Type440C%2f04_SS13_TypicalRoom.gif&IMGTITLE=Typical+Room+Temperature+Mechanical+Properties
45. N.Paulus et al. «Cold and warm work of austenitic nitrogen steels», Proc.of Int.Conf «Stainless Steels 1993», Florence (Italy), 11-14 October 1993.
46. A.Rechsteiner and M.O.Spedel, "New methods for the production of high nitrogen stainless steels", Proc. Of Innovation Stainless Steel, Florence 11-14/10/1993, pp.2107-2111.
47. Li Hua-Bing et al. «JOURNAL OF IRON AND STEEL RESEARCH, INTERNATIONAL. » 2009, 16(1): 58-61.
48. Irvine, K. J. et al. (1969). J. Iron Steel Inst., 207, 1017
49. M.O.Spedel, Mat.-wiss. U. Werkstofftech. 2006, 37, n°10, pp.875-880.
50. R.Sanchez et al., Proc. of Stainless Steel '99, Sci. and Market, 1999, Chia Laguna, Vol.2, pp.353-360.
51. F.Ruffini, PhD Thesis, Università di Roma «La Sapienza», 2005.
52. Rémy, L. and Pineau, A. 1976. Twinning and Strain-Induced F.C.C.→H.C.P. Transformation on the Mechanical Properties of Co-Ni-Cr-Mo Alloys. Materials Science and Engineering, 26 (1), pp. 123-132.
53. Guler et al, Proc.of Int.Conf. HNS 2014, 144-150.
54. Michael Schymura, Alfons Fischer, International Journal of Fatigue 61 (2014) 1–9
55. L. Vitos et al. Acta Materialia 54 (2006) 3821–3826
56. Gavriljuk et al. Material Science and Engineering A (2008), 481-482, 707-712.
57. R. E. Stoltz and J. B. VanderSande: Metall. Trans. A, 11A (1980), 1033.

58. Peter J. UGGOWITZERR, R. MAGDOWSI, Markus O. SPEIDEL, "Nickel Free High Nitrogen Austenitic Steels", ISIJ International, Vol. 36 (1996). No. 7, pp. 901-908.
59. G. Svyazhin, J. Siwka and T. S. Rashev: Proc. 5th Int. Conf. on HNS, Mater., Sci. Forum, V. 318–320, Trans Tech. Pub. Ltd., Zürich, (1999), 131.
60. Satir-Kolorz, H.K. Feichtinger, M.O.Speidel, Giessereiforschung 41 (1989) 4, p.149-164
61. B.I. Medovar, et al. Arc-slag remelting of steels and alloys, Cambridge Int. Pub., Berlin (1996), 36.
62. Satir-Kolorz 1990, also reported in H. K. Feichtinger: Proc. of 3rd Int. Conf. on High Nitrogen Steels, HNS-93, Inst. of Met. Phys., Kiev, Ukraine, (1993), 45.
63. Schurmann et Kunze, 1967.
64. C.Kowanda: Solubility of nitrogen in transition metals. Proce of the intern. Conference on High Nitrogen Steel, 2003, Schaffhausen p.75-100.
65. Ridolfi M.R., O.Tassa, J.of Intermetallics (2003), 11; 1335-1338.
66. G.Saller et al. Proc.of Int.Conf. HNS 2004, 283-292.
67. A.G. Svyazhin et al. Proc.of Int.Conf. HNS 2014, 20-26.
68. Berns et al., ADVANCED ENGINEERING MATERIALS 2008, 10 No. 12.
69. R.E. Bailey et al, Hot Tension Testing, Chapter 5 in Workability Testing Techniques, Ed. George E. Dieter, ASM 1984.
70. Loos, J.; Goss, M.; Bergman, I.: Einfluss der Reibbeanspruchung auf die WEC-Bildung in Wälzlagern. In: Fachtagung der Gesellschaft für Tribologie (GfT), Göttingen, Germany, 2014
71. Loos, J.; Blass, T.; Franke, J., Kruhoeffer, W.; Bergmann, I. "Influence on Generation of White Etching Crack Networks in Rolling Bearings", TAE, 2016
72. Blass, T.; Trojahn, W.; Holweger, W.: "WEC-formation in through hardened and case hardened bearings – influence of retained austenite", CWD Aachen, Germany, 2015.
73. <http://materion.com>
74. R. Wood, rsta.royalsocietypublishing.org
75. D. Landolt et al., Electrochimica Acta, 46 (2001) 3913-3929
76. S. Mischler et al., Wear (2001) 1295-1307
77. R. Pileggi t al., Surf. And Coat. Techn. 268 (2015) 247-251
78. N. Diomidis et al., Lubrication Science 21 (2009) 53-57
79. Y. Sun et al., Surf. And Coat. Techn. 205 (2011) 4280-429
80. David G. Ullman, The mechanical design process, 2nd edition, McGraw -Hill, 1997Matayar
81. The influence of processing and metallurgical factors on fatigue, in Metal Fatigue: Theory and Design (A. Madayag, ed.) Wiley, New York, p.66)

APPENDIX - D1.1 Report with dynamic and kinetic analyses

N.P. Belfiore (DIMA)

The dynamic and kinetic analyses reported in this deliverables, according to the project objectives, is relative to the high speed shaft steel bearings and the gearbox steel bearings, which have dimension of about to 200 mm. However, such fundamental components works inside a complicated and very massive system in which the single components are mutually dynamically coupled. Therefore, it is essential to consider the dynamic behaviour of the whole Wind Turbine (WT), also by taking into account that offshore installation are much more complex and massive than onshore ones. For this reason, a theoretical study concerning the kinematic and dynamic analysis of such systems has been proposed.

The kinematic analysis is useful in order to calculate all the shaft angular velocities and the exciting frequency of the exciting pressure wave which is applied around the bearing rings.

Dynamic analysis has a fundamental importance in order to ascertain the characteristic frequencies of the WT. This aim can be reach by applying modal analysis to the structure, considering torsional and bending model of the transmission shafts and on the tower. In this case, it is possible to valuate possible coupling and dangerous modes for the system. The influence of the exciting force (wind induced vibrations, structure dynamics, gear set induced vibrations and electrical induced vibration) and of the coupled resonance mode are useful to study the different WT bearing failure modes.

D1.1.1 A brief review of the typical transmission set in offshore WT

With reference to Figure A1, a typical WT is composed of a rotor blade (1) which intercepts wind power, a rotor hub (2) which contains the mechanism and control system to adjust the blade pitch, the main bearing (4), the gearbox (5), which is used to increase the main shaft angular velocity up to a value suitable of electric power generation synchronous or asynchronous generator the latter including, obviously, the stator (7) and the rotor (8), a brake (6), the nacelle (9), which rotates around a vertical axis by means of a yaw control and wind orientation regulator (10), the tower (11) and a proper foundation (12). In this scheme there are many other components which are not represented.

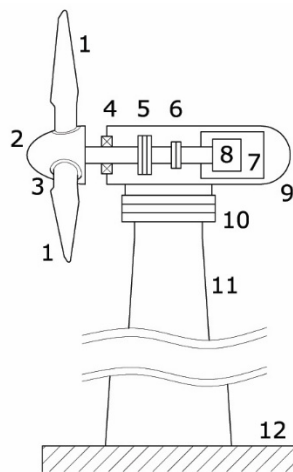


Figure A1. An approximated general scheme of a horizontal axis WT with its principal components. 1: rotor blade; 2: rotor hub; 3: blade pitch control; 4: main bearing; 5: gearbox; 6: brake; 7 and 8: generator stator and rotor; 9: nacelle; 10: yaw control (wind orientation); 11: tower; 12: foundation.

Further Nomenclature, Symbols and Definitions

Failure rate (ν): The inverse of the mean time to failure.

Repair rate (μ): The inverse of the mean time to repair.

Mean time between failure (T_F): $T_F = \frac{1}{\nu} + \frac{1}{\mu}$

Technical availability (system availability): A_T , percentage of time that an individual WT or wind farm is available to generate electricity expressed as a percentage of the theoretical maximum.

Commercial availability (turbine availability): $A_C = 1 - \frac{\lambda}{\mu}$, with $A_T < A_C$, introduced in commercial contracts between wind farm owners and WT OEMs to assess the operational performance of a wind farm project. In fact, some commercial contracts may exclude downtime for *agreed stops*, such as, for example, scheduled repair time, grid faults and severe weather.

N_0 , Number of identical samples (components) in a test set

$N_s(t)$, number surviving samples at time t

$N_f(t)$, number failed samples at time t, with $N_s(t) + N_f(t) = N_0$ at any time t.

Reliability function, $R(t) = \frac{N_s(t)}{N_0}$

Cumulative failure probability, $Q(t) = \frac{N_f(t)}{N_0}$, with $R(t) = 1 - Q(t)$

Failure density function, $f(t) = \frac{1}{N_0} \left(\frac{dN_f(t)}{dt} \right)$, obtained from $Q(t) = \frac{N_f(t)}{N_0} = \int_0^t f(t) dt$

Hazard rate (or failure rate), number of failures per unit time normalized (divided by) the number of components which are exposed to failure, $\lambda(t) = \frac{1}{N_s} \frac{dN_f(t)}{dt} = \frac{1}{R(t)} \frac{dR(t)}{dt} \cong \frac{1}{R(t)} \frac{\Delta R(t)}{\Delta t}$

Simulation of roller-race contact

Roller contact has been studied for decades, starting from Hertz Theory. Since 1926, for example, Carter (Carter, 1926) presented a theory according to which a wheel was approximated by a cylinder and the rail by an infinite half-space. The analysis was two dimensional and an exact solution was found. In 1927 Fromm (Fromm, 1927) succeeded in solving the rolling contact problem of two elastic cylinders with the same elastic constants.

More recently, some papers become classic results for rolling contact.

Bremble and Brothers wrote some interesting contributions, among which a theoretical analysis for predicting the slip-stick areas within the contact zones between the rolling elements of a roller bearing, for the condition where the cage is held stationary whilst the inner race drives the outer race through the rollers (Bremble & Brothers, 1970).

Kogut and Etsion (Kogut & Etsion, 2002) presented an elastic-plastic finite element model for the frictionless contact of a deformable sphere pressed by a rigid flat.

Raje et al. (Raje, Sadeghi, & Rateck, 2008) introduced a damage mechanics based fatigue model in conjunction with the idea of discrete material representation that takes the effect of material microstructure explicitly into account.

In this deliverable, a simpler and independent approach has been used to build a simplified model for the identification of the normal and tangent tension waves which are applied to a given point of the race. Although there are some similitudes with Raje's work, the material is, to the best of the Author, quite original.

D1.1.2 Reference bearing

AG cylindrical roller bearings NU and N are non-locating bearings and can support radial force only. FAG NU222-E-TVP2 bearings are cage type bearings which are very rigid and can support high radial load. Bearings with suffix E have a high capacity roller set and are thus designed for very high load carrying capacity. The suffix TVP2 means solid window cage made from glass fiber reinforced polyamide PA66.

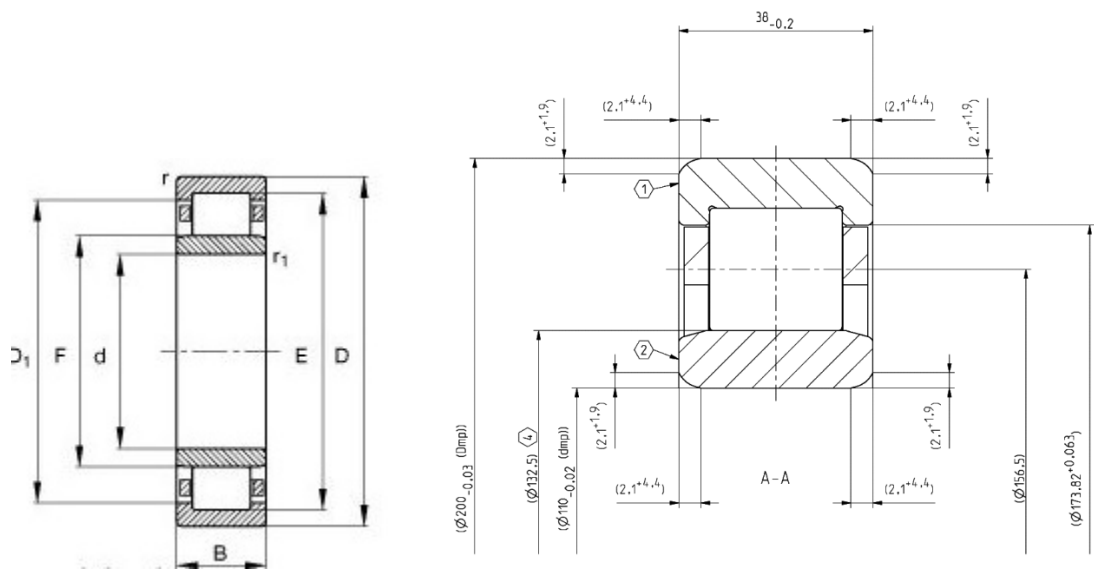


Figure A2. Reference bearing (from Schaeffler).

Table A1. Reference bearing

Type	cylindrical roller bearings, single row
Inner diameter	110 mm
Outer diameter:	200 mm
Breadth	38 mm
D1	173.8 mm
Da max	130 mm
da max	130 mm
da min	122 mm
db min	135 mm
Mass	4.84 kg
Basic static load rating, radial	365000 N
Basic dynamic load rating, radial:	345000 N
Limiting speed:	4100 r/min
Reference speed:	3300 r/min
Fatigue limit load, radial:	44000 N

D1.1.3 Kinematic analysis of roller bearings

With reference to Figure A3, $R_i = 66.25$ mm, R_g , $R_e = 90.25$ mm, and $r = 12$ mm are, respectively, as the *inner ring external radius*, the *average cage radius* (or *pitch circle radius*), the *outer ring internal radius* and the *roller radius*.

A first set of equations, at the macro scale, can be obtained by assuming, in first approximation, that a pure rolling motion occurs between the rollers and the rings,

the rollers and the rings are rigid bodies.

Under such hypothesis, a centre of the relative rotation can be defined for the three pairs roller-inner ring, roller-outer ring, and inner – outer rings, the latter being the actual centre of the or the revolute pair which the radial bearing consists of.

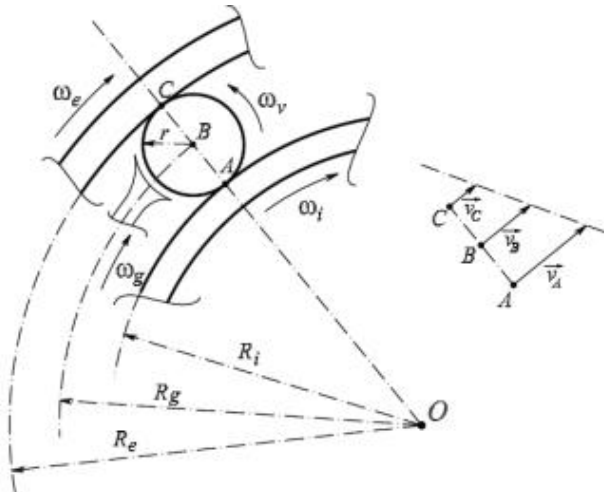


Figure A3. Kinematic analysis of a roller bearing.

The kinematic analysis is quite easy, for this simple case. For example, the velocity of the roller center, or pitch velocity, must be the average of the velocities of the contact points A and C

$$\vec{v}_B = \frac{\vec{v}_A + \vec{v}_C}{2} \quad \text{Equation 1}$$

When the outer ring is framed, of course $\vec{v}_C = \mathbf{0}$ and the pitch velocity is simply a half of the velocity of the contact point between the inner ring and the roller element. From Equation 1, it is possible to calculate, in general, the angular velocity of the cage, see also (Belfiore, Di Benedetto, & Pennestrì, 2011),

$$\omega_g = \frac{(R_i + 2r)\omega_e + R_i\omega_i}{2(R_i + r)}, \quad \text{Equation 2}$$

which becomes

$$\omega_g = \frac{R_i\omega_i}{2(R_i + r)}, \quad \text{Equation 3}$$

when the external ring is framed. In this case, the roller angular velocity

$$\omega_y = \frac{R_i}{2r} \omega_i \quad \text{Equation 4}$$

is calculated by imposing no sliding at the contact point A.

Unfortunately, the real system is much more difficult to be studies because it is composed of elastic bodies, and so the bearing will have to take into account:

- The elasticity of the rings and the rollers, especially the rings deformations
- The constraints with the cage and the outer elements
- The effects of the EHL elasto-hydro-dynamic lubrication
- Material Hysteresis and elasticity delay
- Micro-slip and creep

The study of roller ring contact has been studied by several different methods, which are well known since decades. In this report, the most important concepts will be resumed and presented by using a simplified approach. One important feature for the adopted approach is that the bearing system acts as a constraint over the single rollers; this can be justified by the fact that the whole system is composed of all the other rollers,

by the cage and also by the sealing and other components; all these elements work in order to keep the overall motion of the pseudo-rigid part as in the ideal condition, including the position of the centres of the relative motions, as represented in Figure 6; the single rollers are composed of a pseudo-rigid zone (which will obey the theory of the rigid bodies) and the peripheral compliant zones, which will be affected by significant deformations. By accepting this assumptions a simplified approach can be developed, as described in the following paragraphs.

Kinematic analysis of sliding in rollers

The configuration depicted in solid lines of Figure A3 represents the ideal case for which the rollers and the inner and outer flanges are perfectly rigid. As known, there are deformations in the roller-flanges contact zones and the Hertzian formulae can be adopted with a good approximation.

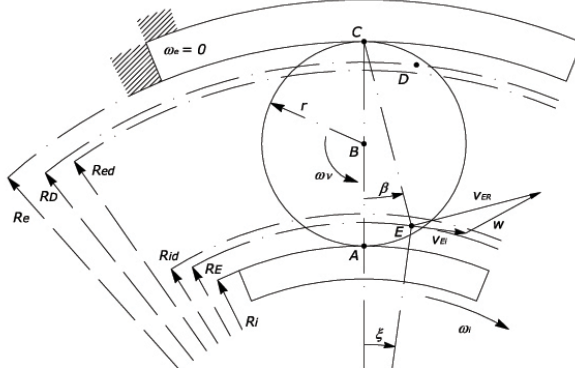


Figure A4. Schematic representation of the sliding velocity at a point E inside the contact deformation area; R_E and R_i : outer and inner flange radii; R_E and R_D : distance OE and OD ; R_{id} and R_{ed} : distance from O of the maximum deformation at the inner and outer contact sections; w : sliding velocity; v_{ER} : velocity of the roller-based point E ; v_{Ei} : velocity of the flange-based point E .

With reference to Figure A4, the inner ring is supposed rotating at speed ω_i , while the outer ring is framed. If the inner angular rotation is clockwise, then the roller angular velocity has its sense of rotation as represented in the Figure. Now, let us consider a *pseudo-rigid region* be limited, in the roller, in between the two radial distances R_{id} and R_{ed} , then it is still possible to define the roller centres of relative rotations with respect to the framed and the moving rings. In the figure, the compliant regions have been exaggerated for the sake of clarity. Point E, as depicted in the figure, is in the compliant region. For this point it is possible to define three velocities, and the Theorem of Relative Motion can be invoked:

- v_{Ei} , is the velocity of point E , when E is taken as belonging to the inner ring: such velocity is orthogonal to the OE , where O is the centre of the bearing;
- v_{ER} is the velocity of point E , when E does belong to the roller: since point C can be regarded, approximately, as the centre of relative rotation of the roller with respect to the frame, this velocity will be orthogonal to the segment EC .
- W is the sliding velocity: according to the Theorem of relative motion, such velocity will be the difference between v_{ER} and v_{Ei} .

Our interest relies on the fact that point E can be selected as belonging to the deformed surface of contact between the roller and the inner ring. Analogously, Point D can be regarded as positioned on the interface between the deformed surfaces of the outer ring and the roller.

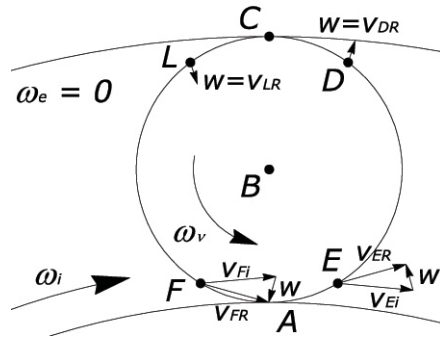


Figure A5. Sliding velocities of points E, D, L and F in four different contact points under the assumption of the existence of a pseudo-rigid part a roller and of absence of deformation in the inner ring.

Now, considering the FAG NU222-E-TVP2 bearings and by using its actual dimensions, the kinematic field appears as in Figure A5, where the sliding velocities vectors appear neither radial nor tangential, because this "picture is taken" in the course of a dynamic deformation due to the stress of the materials. Of course, the normal deformation is due to the contact normal stress σ while the tangential stress τ will be responsible for creep or micro-slip as described in the following paragraphs.

Anyway, considering the projection of the siding speed along the tangential direction, it is easy to ascertain that this component is not null. In fact, in the motion of the roller with respect to the inner ring this component has a sense which is opposite to the inlet rolling velocity U (being $U=1/2 * (V_{Ai} + V_{Ar})$). This is true for all the four points, which can be explained by considering the following reasoning. When a rigid cylinder, with radius R , complete one revolution over a rigid ring, the roller centre moves forward on an arc whose length is equal to $2\pi R$. However, the ring deformation makes the surface profiles longer than in the ideal case, and so there must be a difference which justify sliding.

If we suppose that the roller deformation is greater than the inner ring deformation, the sliding velocity w appears as in Figure A5. However, a different situation could apply when, due to the adopted materials (Young's modules), the ring deformation was greater than the roller one.

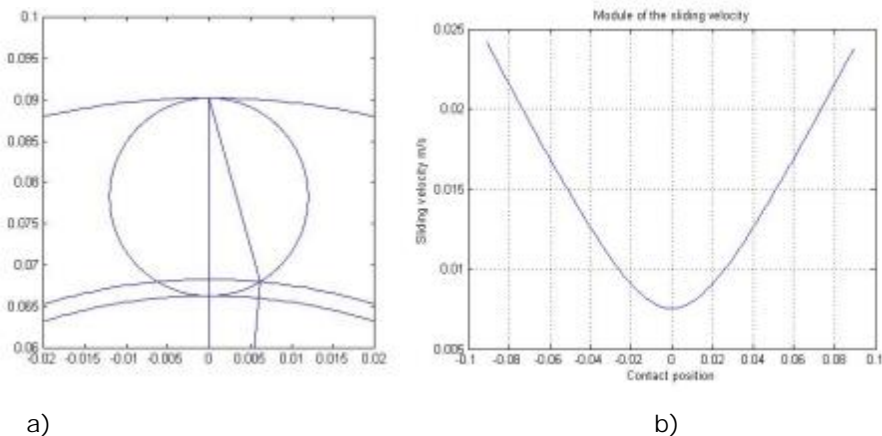


Figure A6. Figures obtained by the developed MatLab Program: a) check on the roller and ring geometry; b) sliding along the tangential interface roller-ring in the contact arc (from points F to E of the previous figures). A short MatLab Script has been encoded in order to obtain the theoretical sliding along the contact profile without taking into account the stick regions of the contact. Results are presented in Figure A6.

However, this sliding function is acceptable only when the stick regions are neglected and when the deformations are concentrated only on the roller. In this simplified approach, the obtained sliding velocity is only representative of a nonholonomic constraint which is active on the contact profiles. The module of this sliding velocity must be therefore considered as the effect of an external traction stress which affects the action that the roller exerts on the inner ring. This traction stress is due to the system constraints which force the roller to adjust all the centres of the relative motions. We will refer to this virtual traction tension as τ_k , which can be regarded, in first approximation, to be proportional to sliding w , according to a viscous elastic model for which the element dynamic balance is described by the equation

$$\tau_k = G\gamma = \eta w$$

$$\text{Equation 5}$$

where γ is the deformation angle, G is the elastic tangential module, and η is the viscosity coefficient.

If the ring compliance is taken into consideration the situation changes from that one depicted in Figure 5, to the one presented in Figure A7.

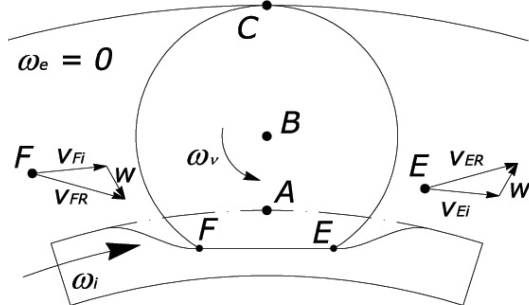


Figure A7. Sliding velocities of points E, and F in two different contact points under the assumption of the existence of a pseudo-rigid part of the ring.

In Figure A7, point A represents the instantaneous rotation centre of the roller, such a special function having been bestowed to point A by the virtual constraint composed of the whole system. Considering the triangle of the velocities for points F and E , as obtained by the application of the Relative motion Theorem, the sense of the sliding speed appears the same as that of the entraining velocity.

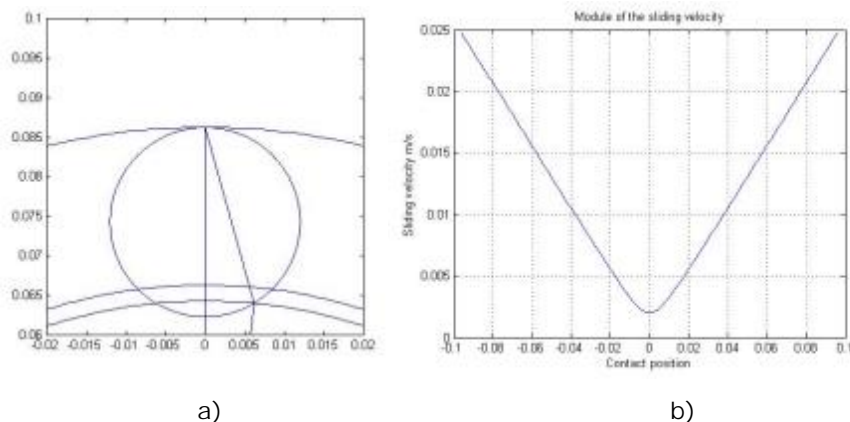


Figure A8. Figures obtained by the developed MatLab Program: a) check on the roller and ring geometry; b) sliding along the tangential interface roller-ring in the contact arc (from points F to E of the previous figures).

Figure A8 shows two diagrams obtained by applying a MatLab script. It is worth noticing that in correspondence of the central contact position the sliding speed is not generally null because the instantaneous center of the relative rotation is not coincident with the contact point.

D1.1.4 Load on rollers in roller bearings

The principal bearing of an offshore WT is subject to combined high loads and therefore they must have both radial and axial load carrying capacity. However, the greatest component of a load, generally, corresponds to the radial one. Furthermore, the main shaft angular velocity is evidently smaller than in the other common engineering applications and so the main design principles must began referring to static load conditions.

For this reason we will start the study of the principal bearing by considering only the radial component in static regime. According to this assumption, each roller is loaded, in first approximation, in static or stationary condition, and so two main resultant forces act on the roller. These two forces must be balanced and must lie on the same action line. In case of ideal material, this line of action would have the radial direction. However, during rolling, the real material always shows dissipative phenomena, such as hysteresis and elasticity delay. These two occurrences are responsible for rolling friction, which can be explained by making reference to Figure A9.

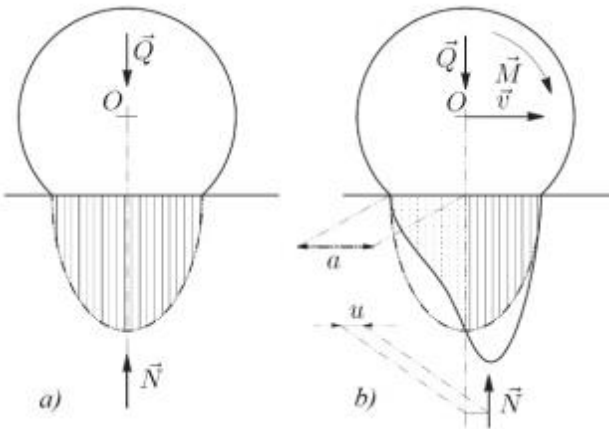


Figure A9. Pressure diagrams for static contact a) and stationary contact with a non null velocity b)

In a static contact of a roller with a plane surface (or, in a first approximation, with a surface ring), the Hertzian pressure diagram is obtained, and so symmetry guarantees that the resultant N of the normal stresses is applied along a line which is coincident with the symmetry axis (Figure A9a). If the element¹ is actually rolling, hysteresis and elasticity-delay make the pressure diagram asymmetrical because pressure will be greater in the increasing stress regions than in decreasing stress ones. In this case, the pressure is represented by a asymmetric diagram and the resultant reaction action line will be translated, by a small quantity u , toward the same direction of the velocity. This quantity is a fraction of the Hertzian contact area radius a . Consequently, a moment M is needed in order to maintain the stationary conditions. However, in the case under study, such action will be provided by the moving ring and the actual situation will be represented as in Figure A10.

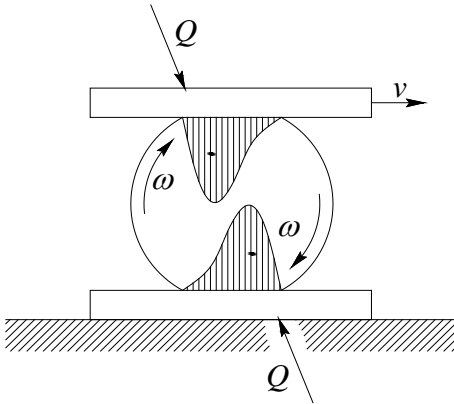


Figure A10. Introduction of a tangential component in the roller loads under stationary conditions.

Since symmetry is lost the line of action is not coincident with the symmetry axis and the action and reaction pair of forces Q is tilted with respect to the case of ideal material. However, each one of the two forces can be reduced to a normal plus a tangential component, which leads to the conclusion that tangential stresses appear on the ring and roller surfaces. Considering the rotor weight and the preload, the tangential stress appears to be an important issue in building an equivalent model for friction and wear prediction, and, more generally, for damage prediction of the component.

The generalized situation depicted in Figure A10, can be specialized as in Figure A11, where the rolling friction parameter u has been assumed, for the sake of simplicity, just equal to the Hertzian area half width a .

¹ This element in general can be a ball, a cylindrical roller, a needle roller, a spherical roller symmetrical, a spherical roller asymmetrical, a conical roller, and so on.

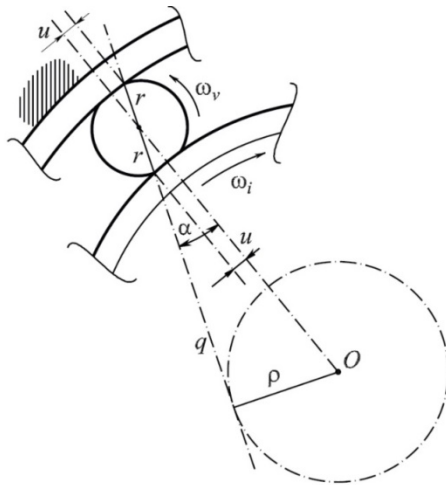


Figure A11. Friction circle and load line in a radial roller bearing

It is worth noticing that for each roller, the action line of the load is not incident to the center O of the bearing, but it is tangent to the friction circle, which has the radius

$$\rho = (R_i + r) \sin \alpha \quad \text{Equation 6}$$

Of course, this formulation represents a rough simplification of the real phenomenon which has a dynamic nature. Therefore, it must be taken into account that the above mentioned tangential stresses on the roller and ring surfaces are not constant, but will be variable. The main source of variability is simply due to the revolute motion of the main shaft, which implies that a rotating wave (composed of both normal and tangential stress) will be applied on the ring surfaces. Unfortunately, this wave is not even constant during its progress on the ring surfaces. In fact, depending on the roller position, with respect to gravity, a great variability is expected for the normal stress. Finally, impulsive torques on the shaft will induce great variability also on the tangential stresses.

Overall effects on the rings (WT main and gearbox bearings)

Considering the balance of each roller and the elasticity hysteresis, it is possible ascertain that, even though the rollers are not designed to theoretically transmit any power from a moving ring to the other ring, a small amount of power is dissipated to ground due to a tangential force T_e between the rollers and the rings. In fact, with reference to Figure 12, considering a stationary regime for rolling, there is an asymmetry in the simultaneous actions which the outer (framed) ring and the inner (rotating) ring exert on the roller. This asymmetry is due to the elasticity hysteresis which has opposite effects on the two rings because of the rolling kinematics. In order to guarantee the dynamic balance of the roller, neglecting its weight and the accelerations, the normal forces N_e have to be concentrated in the pressure centre of the normal stress distribution, which is no more symmetrical because of the elasticity delay. The two normal forces, therefore, are equivalent to a clockwise moment which must be balanced only by another moment. The balancing moment is given by the tangential adhesion of the contact region which yields, on the inner and outer rings, a traction force T_e . The two components T_e and N_e acts, on the top and bottom contact region, in such a way their resultant forces R_e are balanced, as shown in Figure A12.

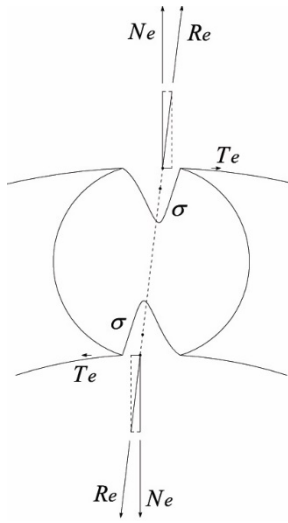


Figure A12. Resultant R_e , tangential T_e and normal N_e forces which acts on the inner and outer rings due to roller dynamic balance in stationary regime

Now, considering the contact regions, and specifically the contact between the roller and the inner ring, an attempt can be made in order to understand how the effects combine each other and how the normal and tangential stress can be represented along the contact line.

With reference to Figure A14 a), two tangential tensions can be compared.

Firstly, the tangential stress τ_k is due to the viscous-elastic action of the roller surface which is sliding on the ring surface. This stress, generated by the roller on the ring, can be regarded as the product of a viscous coefficient multiplied by the sliding velocity, directed in the sense of the sliding speed with respect to the rings. For the presented examples, the tangential stress has the same sense of the inlet rolling velocity U (in the example, such direction is directed from the left to the right hand sides).

Secondly, a tangential tension τ_E must be acts between the surfaces in order to guarantee that the roller be in dynamic balance. This action could be regarded as a rather small one, because the rolling friction coefficient is generally lower than both static and sliding friction coefficients. However, during a whole cycle the conditions may change and in some position the deformation may increase. Furthermore, the integral of all the tensions extended to the contact profile must have a net resultant which has a direction with the same sense as T_e , as appears in Figure A12. Hence, since the contribution of the viscous-elastic tangential stress τ_k is basically directed in the sense of the entering velocity, the contribution of the adhesive balancing tangential tension τ_E cannot be negligible. This contribution can be regarded, in a first approximation, as proportional to the normal stress σ multiplied by the static friction coefficient μ_0 .

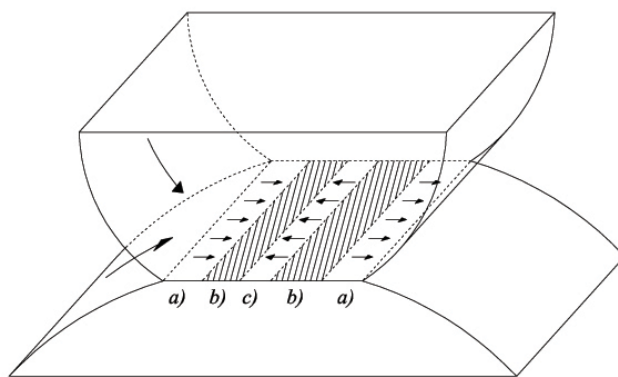


Figure A13. Slip and stick regions in the roller-ring cylindrical contact: a) slip with the same sense of the entering velocity; b) stick regions; c) slip with sense opposite to the entering velocity.

Considering the difference between the two tensions $\tau_k - \tau_E$ and the results presented in Figure 6 and Figure 8, two external region appear where the overall tension is positive (same sense as U) and a central region also

appears where the overall tension is negative – see Figure A14 b). The difference function must be compared to the maximum adhesive tension function and so five regions appear as in Figure 14 c). Two external regions with positive slip, one central region with negative slip and two intermediate regions where adhesion prevails on the tangential actions exerted by the combination of the external constraints and the roller dynamic balance – see Figure A13 and Figure A14 d).

The overall effect on the ring is depicted in Figure A15. Although the approach has been developed by assuming several approximations, more complex methods gives similar results, as those presented in (Bentall & Johnson, June 1967).

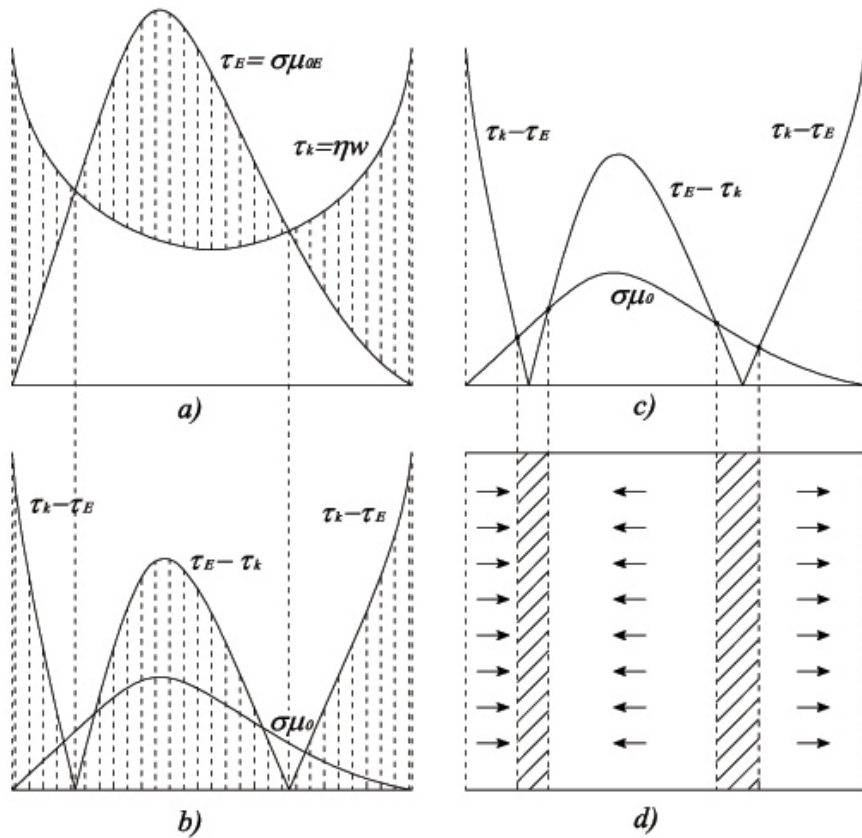


Figure A14. Qualitative distribution of: a) the tangential stress τ_e and τ_k and evaluation of their difference; b) the net tangential stress $\tau_e - \tau_k$ and adhesion tangential distribution $\sigma \mu_0$. Determination of: c) the intersection points and d) of the slip stick regions.

The normal stress is generated on the race as a wave train with highly asymmetrical wave shape, and with a pulsing waves alternated to null load. This situation represents only the variations with respect to the pre-load. The amplitude of this train is modulated by the vibrations generated by the Wind Turbine, as a whole, and by the mechanical components, such as the gearbox, which introduces some higher frequencies.

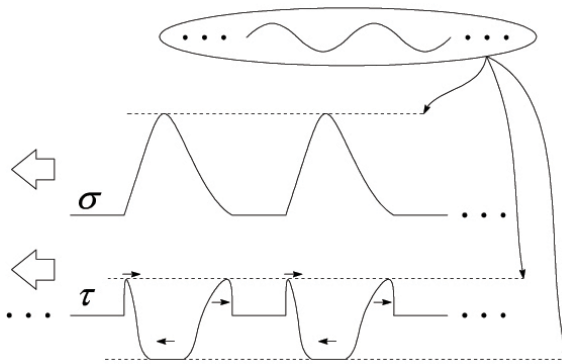


Figure A15. Qualitative representation of the normal and tangential wave train which affects the bearing races. Tangential tensions changes their direction sense with a double frequency with respect to the roller passages. Furthermore, normal and tangential amplitudes are modulated by the vibrations generated by the Wind Turbine, both flexural and torsional)

The tangential stress seems more complicated. However, it appears the possibility that the sense of direction may change during a cycle, which makes more complex the determination of the mechanism which affects wear and damage generation.

Hence it appears that the Universal Micro tribometer CETR UMT-3 could be useful to reproduce conditions that are more realistic than the simple pin-on-disk or roll-on-disk devices, where the sliding and traction directions never change their sense of motion.

Figure A16 represents only one possible concept configuration. Since the bottom wedge is softer than the top wedge, a small relative rotation between the roller and the plate will also appear.

This part of the investigation will be the subject of the activities which will follow in the next months, according to SteelWind Project schedule. In particular, in WP5, Design and set up of functional laboratory tests, the Task 5.1. Design of the test plan, will be dedicated to the actual set up of the test parameters.

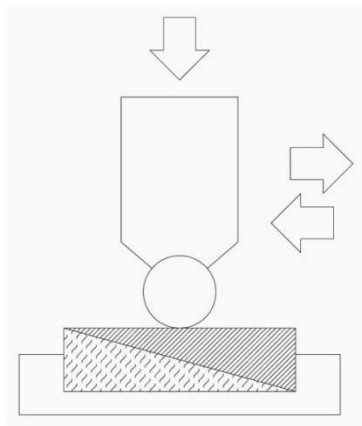


Figure A16. Idea “Zero” for a possible accelerated set which tries to imitate the real system: the sample test is a wedge which is positioned over a softer material sustaining wedge.

Roller loading on rollers in low velocity journal bearings (WT main bearings)

With reference to Figure A17, two adjacent rollers are separated by a sector whose characteristic angle is γ . If the two rings are considered as rigid with respect to the rollers, the generic i-th roller

$$\delta_i = \delta_0 \cos(i\gamma) \quad \text{Equation 7}$$

is proportional to the maximum deformation δ_0 for the rollers. However, according to Hertz formulae, and assuming P_i the load on the i-th roller, the deformation of each generic roller is equal to

$$\delta_i = k \sqrt[3]{P_i^2}$$

Equation 8

or to

$$\delta_i = k' P_i$$

Equation 9

depending on whether the rollers are cylinders or spheres.

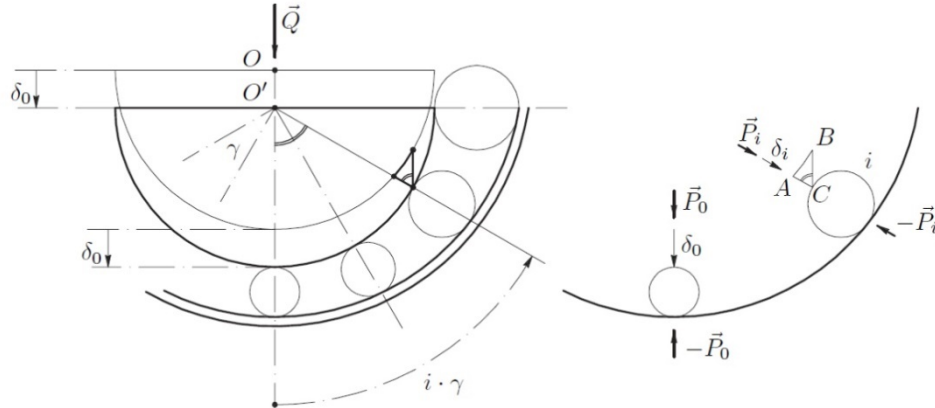


Figure A17. The shaft-bearing pair and the corresponding series of rollers, under the action of an externally applied force Q .

By substituting Equation 6 or Equation 7 in Equation 5, it is possible to obtain the load on the i -th roller, in case the latter is a ball, with

$$P_i = P_0 \cos^2(i\gamma) \quad \text{Equation 10}$$

or it is a cylinder, with

$$P_i = P_0 \cos(i\gamma) \quad \text{Equation 11}$$

Introducing the total number of rollers z , a radial load Q will be sustained by the $\frac{z}{2}$ bottom rollers, being

$$Q = \sum_{i=-\frac{z}{4}}^{\frac{z}{4}} P_0 \cos^2(i\gamma) \quad \text{Equation 12}$$

for spherical, or

$$Q = \sum_{i=-\frac{z}{4}}^{\frac{z}{4}} P_0 \cos(i\gamma) \quad \text{Equation 13}$$

for cylindrical rollers. These formulae can be modified by introducing a theoretical infinite number of infinitesimal rollers, and by using integral calculus. After little algebra, see also (Belfiore, Di Benedetto, & Pennestri, 2011), the Stribeck formula can be obtained, according to which the maximum load on a single roller (for both spherical or cylindrical roller) is never greater than

$$P_0 = 5 \frac{Q}{z} \quad \text{Equation 14}$$

However, considering that the rollers are moving between the rings, the maximum load jumps from roller to roller. Under the roller-cage perspective, each roller must sustain a cyclically variable load. As depicted in Figure 17, the roller supports the highest load when it is at the bottom. After a quarter of revolution, its load is orthogonal to the externally applied overall load Q , and therefore, it does not contribute to the global sustentation of Q . In this case, only the preload affects this roller. After another quarter of revolution the roller is in its upper position and it is opposite to the highest load configuration. In this case, the overall load is much less than the pre-load because there is a small displacement of the inner ring downward. In such a case, there is the theoretical possibility that roller-ring slip occurs.

For all these reasons it should be clear that each roller sustains a load cycle which is reasonably near to a pulsing cycle, namely, variable from about 0 to P_0 . Considering Equation 3, the frequency f_s of this exciting load is proportional to the angular speed of the main shaft, namely,

$$f_s = \frac{R_i}{2(R_i+r)} 60n,$$

Equation 15

where n is the main shaft angular velocity expressed in rpm. From the point of view of the rings.

D1.1.5 The influence of torsional vibrations of the drive train

The drive train of a turbine is composed of rotating masses and torsional elastic components and therefore vibrations characterize its dynamic behaviour. Vibrational modes can be excited by external influences at both ends of the energy transmission chain: the blades and the electric rotors. Apart from the random fluctuations of the rotor torque caused by wind turbulence, the rotor generates cyclic torque variations which represent a source of excitation. At the other end the electrical generator is connected to the grid or to another load. In particular, the synchronous generator coupled directly to the grid tends to vibrate. However, the problem also occurs in other types of generators.

The principal components of the drive train are connected as a series: the rotor hub, the rotor shaft, the gearbox, the high-speed shaft, brakes and clutches. Unfortunately, there is a great diversity of the components, for example, their mass distributions and material properties can change from model to model. Furthermore, their geometry and configuration is not simple to represent and so it is necessary to build simplified systems for the sake of dynamic and vibrational analysis. However, the most important parameters can be calculated by means of comparatively simple equivalent mechanical models called "reduced models".

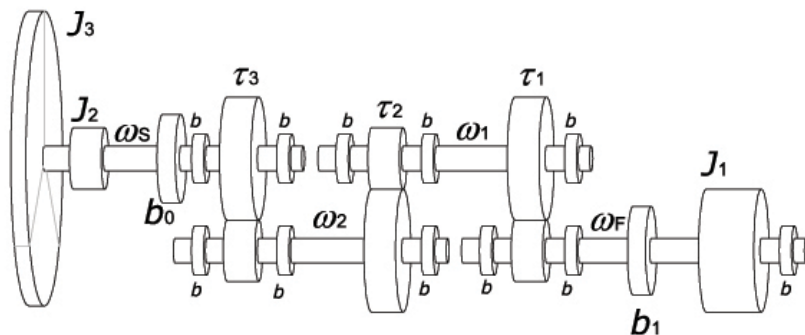


Figure A18. A simplified model of the WT shaft: b_0 = principal bearing, b_1 = high speed bearing, b = secondary bearings, J_3 = blade moment of inertia, J_2 = rotor hub moment of inertia, τ_1, τ_2, τ_3 = three reduction stages, J_1 = rotor generator moment of inertia.

A common way of performing a quite complete structural and dynamic analysis is by using FEA (Finite Element Analysis) which, nowadays, offers also parametric dimensioning and loading for the system components. However, the classical methods based on Mechanical Vibrations (with distributed or lumped parameters) still play an important role because the lumped parameters they use, and the results they offer, have a clear meaning for designer and maintenance. Furthermore, the system can be arranged in a group of equations which can be used for many reasons, such as, for only representative example, optimization, prediction, simulation and further theoretical and numerical correlated studies (tribology, multi body dynamic).

One of the possible ways of simplifying the study of the torsional vibrations of the system composed of the masses which rotate around the horizontal axis is depicted in Figure 18. First of all, the masses of the blades are represented by their equivalent moment of inertia. In fact, in offshore WT they are quite massive and they are also subject to a variety of vibrational modes. Among them, blade flexural oscillation in the rotation plane play a certain effect on the slow shaft rotation by means of an equivalent applied moment. Furthermore, the blades elasticity can be represented as a shaft connecting a virtual flywheel having moment of inertia J_3 and another flywheel having moment of inertia J_2 , the latter representing the equivalent inertia of the rotor hub. Flywheel J_2 is sustained by the slow shaft, which is sustained by the principal bearing b_0 . Now, the power enters to the gearbox. In case three speed amplification stages are adopted, for example, three epicyclic gear trains, two secondary intermediate shafts are needed before power is transmitted to the fast shaft.

However, before proceeding further, it is necessary to remember that different flywheels that are clumped on different shafts must be reduced to the same shaft. According to the principle of conservation of the kinetic energy, if we want to reduce the moment of inertia of J_1 of the generator rotor, from the fast shaft to the adjacent secondary shaft, the kinetic energy of the original system

$$\frac{1}{2}J_1\omega_F^2$$

Equation 16

must be the same of the equivalent system reduced to the slower shaft

$$\frac{1}{2}J_1^{eq1}\omega_1^2. \quad \text{Equation 17}$$

Therefore,

$$\frac{1}{2}J_1^{eq1}\omega_1^2 = \frac{1}{2}J_1\omega_F^2 \quad \text{Equation 18}$$

and so the moment of inertia of the rotor generator, reduced to the shaft 1, will be equal to

$$J_1^{eq1} = J_1 \frac{\omega_F^2}{\omega_1^2} = J_1 \tau_1^2 \quad \text{Equation 19}$$

Where

$$\tau_1 = \frac{\omega_F}{\omega_1} < 1 \quad \text{Equation 20}$$

By reducing the moment of inertia to shaft 2, and, then, to the main shaft, it is so possible to represent the generator rotor moment of inertia as it was working on the same shaft as J_2 and J_3 , namely, *reduced* to the main shaft,

$$J_1^{eqS} = J_1 \tau_1^2 \tau_2^2 \tau_3^2 \quad \text{Equation 21}$$

For the sake of simplicity, when reduced system are represented, the moment of inertia are regarded as it were all reduced to the same shaft.

Finally, the shafts which connect the reduced flywheels must be represented by means of *reduced shafts*, which must have the same torsional stiffness of the original system. As known the torsional stiffness of a circular cross section shaft can be calculated by means of well-known formulae such as

$$k_t = \frac{GJ_p}{l} \quad \text{Equation 22}$$

where G is the tangential elastic module of the material, l is the shaft length and J_p is the cross sectional polar moment of inertia. As known, for circular section having diameter equal to d ,

$$J_p = \frac{\pi d^4}{32} \quad \text{Equation 23}$$

Once the reduced model is obtained, it is possible to apply the modal analysis for achieving the main natural vibration modes and the positions oscillation nodes along the shaft.

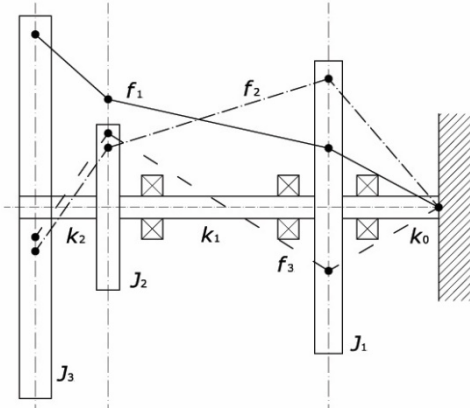


Figure A19. Qualitative representation of a simplified torsional vibration model suitable for grid coupled operation under load with synchronous generator.

Figure A19 represents a simplified model which can be studied in order to inquire about the torsional modes of the series of elements which operate in the transmission. The synchronous generator behaves as a fixed frame for the relative oscillations of the generator rotor. Hence, the first equivalent moment of inertia J_1 , which represents both the rotor generator and the gearbox rotating masses, is connected to a framed section by means of an elastic shaft which has an equivalent torsional stiffness equal to k_0 . The moment of inertia J_2 , which represents the hub rotational inertia, is then connected to J_1 by an intermediate reduced shaft, with torsional stiffness equal to k_1 . Finally, the moment of inertia J_3 , which represents the rotor and blades inertia, is connected to the hub by a reduced shaft having a torsional stiffness equal to k_2 .

This reduced system has three degrees of freedom and so the three following equations

$$\begin{aligned} J_1 \ddot{\vartheta}_1 &= -k_0 \vartheta_1 + (\vartheta_2 - \vartheta_1) k_1 \\ J_2 \ddot{\vartheta}_2 &= (\vartheta_1 - \vartheta_2) k_1 + (\vartheta_3 - \vartheta_2) k_2 \\ J_3 \ddot{\vartheta}_3 &= (\vartheta_2 - \vartheta_3) k_2 \end{aligned} \quad \text{Equation 24}$$

can be written to represent the system dynamics. Equation 14 can be rearranged in the usual matrix formulation

$$[J]\{\ddot{\vartheta}\} + [k]\{\vartheta\} = \{0\} \quad \text{Equation 25}$$

which is ready for modal analysis.

When an asynchronous generator is adopted, then the electro-mechanical interaction can be modelled by an inelastic damper, as represented in Figure A20.

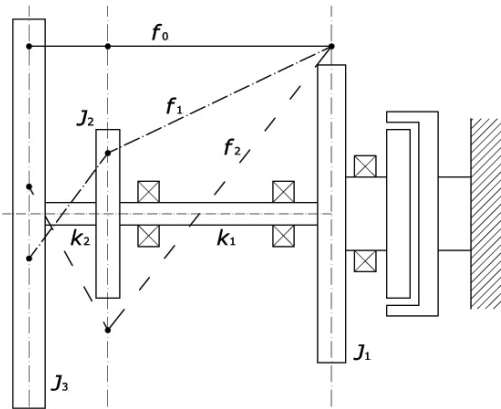


Figure A20. Qualitative representation of a simplified torsional vibration model suitable for grid coupled operation under load with asynchronous generator.

This model is also representative for idling or isolated operation (both induction and synchronous generator). The model has still three equivalent flywheels, which represent, as for the previous case, the generator-gearbox group rotational inertia, the hub inertia and the blades-rotor group inertia, respectively. However, the external section are not constrained. This change holds especially for the equivalent flywheel J_1 , which is now not constrained to the elastic equivalent shaft k_0 . The system of equations changes, and three new equations have to be written

$$\begin{aligned} J_1 \ddot{\vartheta}_1 &= (\vartheta_2 - \vartheta_1) k_1 \\ J_2 \ddot{\vartheta}_2 &= (\vartheta_1 - \vartheta_2) k_1 + (\vartheta_3 - \vartheta_2) k_2 \\ J_3 \ddot{\vartheta}_3 &= (\vartheta_2 - \vartheta_3) k_2 \end{aligned} \quad \text{Equation 26}$$

where k_0 is now missing and Equation 15 can be still used for matrix representation, provided matrix $[k]$ has been modified. As well-known from modal analysis, this circumstance ($k_0=0$) is quite a relevant one because the new system can be expressed in terms of three equations for only two variables $\vartheta_{12} = \vartheta_2 - \vartheta_1$ and $\vartheta_{23} = \vartheta_3 - \vartheta_2$ and so the null frequency appears among the three solutions of the eigenvalue problem. The solution of the eigenvalue problem provides also the amplitude of the section oscillation for each frequency. For example, with reference to Figure A4, three characteristic torsional vibrational modes are depicted for frequencies f_1 (principal), f_2 (second) and f_3 (third). One of the three modes is lost for the shaft represented in Figure 20, because the lost one corresponds to the null frequency vibrational mode, that is a rigid motion of the whole system.

The influence of the torsional vibration of the tower

Considering again Figure A13, two simplified models can be built to simulate the torsional vibrations around the yaw axis. These models are depicted in Figure A21. In particular, Figure A21 a) represents a model with only one equivalent flywheel rotating around the vertical axis. The masses are those relative to the whole system composed of the nacelle, the hub and the blades rotor, while the torsional stiffness k_y corresponds to the stiffness of the yaw drive system. In this model there is also frictional damping. Of course, this model is

able to carry out only the first natural frequency. However, this could be enough for our purpose of figuring out the influence of the vertical torsions on the bearings, and, specifically, on the fast shaft bearings. By using the model reported in Figure A21 b), the second vibrational mode can be calculated. However, this model is useful only when there is a certain amount of compliance $1/k_T$ in the tower, in relation to the nacelle and blades masses. The analysis can be performed by using again Equation 23.

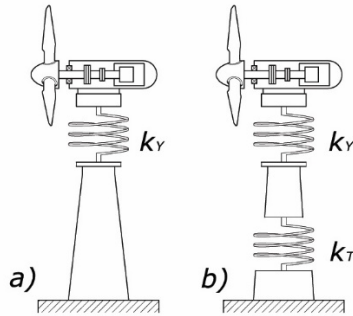


Figure A21. Two models of the study of torsional vibration around the yaw axis: a) one flywheel; b) two equivalent flywheels.

The adoption of a direct drive configuration is nowadays possible, although the adoption of a multiplication stage for the low angular velocities of the slow shaft offers several advantages. The simplest gear train is composed of two gears I and j rotating around parallel axis a_i and a_j , as represented in Figure A22.

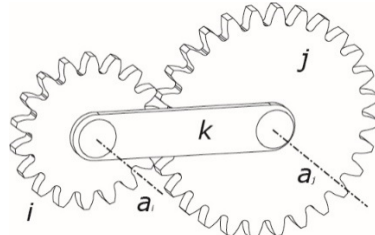


Figure A22. The basic gear transmission set, composed of two gears I and j and one gear carrier k.

For this elementary arrangement there is still the possibility of classifying the transmission according to two different categories, namely, ordinary gear trains or epicyclical gear train, depending on whether the gear carrier k is fixed or it is moving, respectively. In case the transmission is ordinary the transmission ratio τ is simply the ratio between the teeth numbers of the two gears (with the minus sign), while for the epicyclical arrangements the Willis equation can be adopted, as described next in this paragraph.

Figure A22 presents the classical configuration with external gears, and so the angular velocities of the two gears will be parallel to the same axis but they will have opposite directions. However, it is possible to arrange the two gears by using an internal configuration, as depicted in Figure A23.

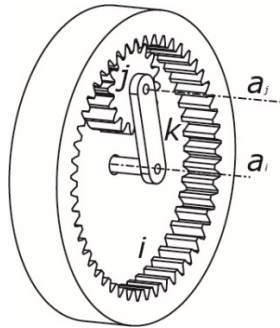


Figure A23. The basic configuration with internal gears.

When the transmission represented in Figure A23 consists in an ordinary train, the transmission ratio τ is still equal to the ratio between the numbers of teeth of the two gears, but this time with a plus sign, because the

angular velocities have the same direction. When the gears are arranged in an epicyclic configuration the Willis equation must be used.

The study of the epicyclic gear trains is important for the sake of onshore or offshore WT because epicyclic trains present many advantages with respect to the ordinary trains, among which a higher reduction/amplification factor (*ceteris paribus*). The schematic (or functional) representation of the elementary gear train with external gear is reported in Figure A24.

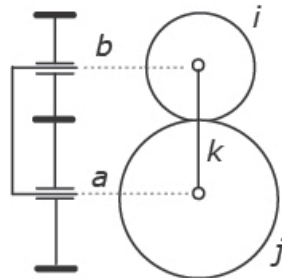


Figure A24. Elementary planetary gear-train

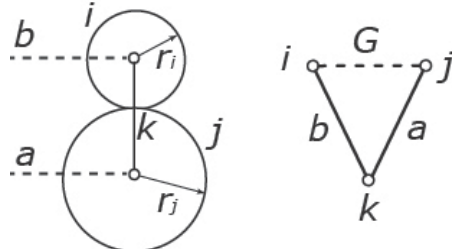


Figure A25. The elementary gear-train and the corresponding graph.

The schematic representation of the basic epicyclic transmission with internal gear is represented in Figure A26.

Graph theory allows the evaluation of the angular velocities of all the moving components, also the most sophisticated ones. However, for a single stadium of speed reduction the basic relation:

$$\omega_k = \frac{z_1 \omega_1 + z_2 \omega_2}{z_1 + z_2}$$

allows the determination of the higher frequencies.

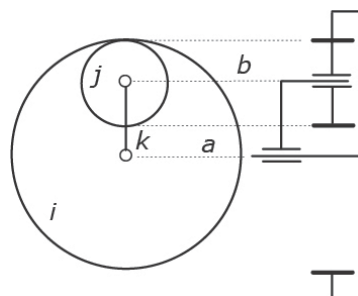


Figure A26. Elementary gear-train with internal gears.

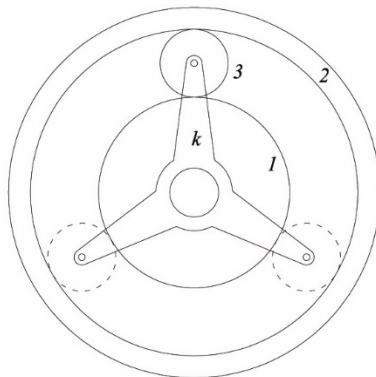


Figure A27. Single stage gearbox.

Highlights

- A simplified approach to slip-stick modelling has been presented for roller-ring contact
- This simplified approach takes into account hysteresis and elasticity delay in materials
- A general method for identifying fatigue cycles in frequency and amplitude is suggested
- Flexional and torsional effects on the main bearings but, primarily, on the gearbox bearings are considered
- A strategy to simulating the real system by lab test stand is suggested.

REFERENCES (APPENDIX)

- Belfiore, N. P., Di Benedetto, A., & Pennestrì, E. (2011). *Fundamentals of Applied Mechanics: Second Edition (in Italian)*. Milan: Casa Editrice Ambrosiana (Zanichelli).
- Bentall, R. H., & Johnson, K. L. (June 1967). Slip in the rolling contact of two dissimilar elastic rollers. *International Journal of Mechanical Sciences*, 389–404.
- Billinton, R., & Allan, R. (1992). *Reliability Evaluation of Engineering Systems: Concepts and Techniques*, 2nd Ed. New York & London: Plenum Press, ISBN-13: 978-0306440632.
- Bremble, G. R., & Brothers, B. G. (1970). An Analysis for the Determination of the Slip-Stick Areas and the Creep of Rollers in a radially loaded bearing. *Wear*, 189-201.
- Carter, F. W. (1926). On the action of a locomotive driving wheel. *Proc. R. Soc. London. A* (pp. 151-157). London: R. Soc. London.
- Fromm, H. (1927). Berechnung des Schlupfes beim Rollen deformierbarer Scheiben. *Zeitschrift für Angewandte Mathematik und Mechanik*, 7(1), 27-58.
- Kogut, L., & Etsion, I. (2002, September). Elastic-plastic contact analysis of a sphere and a rigid flat. *Journal of Applied Mechanics, Transactions ASME*, 69(5), 657-662.
- Raje, N., Sadeghi, F., & Rateick, R. G. (2008). A Statistical Damage Mechanics Model for Subsurface Initiated Spalling in Rolling Contacts. *Journal of Tribology*, 130(4), 042201-1.

Getting in touch with the EU

In person

All over the European Union there are hundreds of Europe Direct information centres. You can find the address of the centre nearest you at:

https://europa.eu/european-union/contact_en

On the phone or by email

Europe Direct is a service that answers your questions about the European Union. You can contact this service:

- by freephone: 00 800 6 7 8 9 10 11 (certain operators may charge for these calls),
- at the following standard number: +32 22999696 or
- by email via: https://europa.eu/european-union/contact_en

Finding information about the EU

Online

Information about the European Union in all the official languages of the EU is available on the Europa website at: https://europa.eu/european-union/index_en

EU publications

You can download or order free and priced EU publications at: <https://publications.europa.eu/en/publications>. Multiple copies of free publications may be obtained by contacting Europe Direct or your local information centre (see https://europa.eu/european-union/contact_en).

EU law and related documents

For access to legal information from the EU, including all EU law since 1952 in all the official language versions, go to EUR-Lex at: <https://eur-lex.europa.eu>

Open data from the EU

The EU Open Data Portal (<https://data.europa.eu/euodp/en/home>) provides access to datasets from the EU. Data can be downloaded and reused for free, for both commercial and non-commercial purposes.

The aim of this project was to increase the reliability of wind turbine, improving the properties of steel bearings by the development of a new high nitrogen austenitic steel (HNAS) functional grade replacing the 100Cr6 steel which is usually used for steel bearings production.

The work finally focused on the selection of a Carnit 90 alloy with a composition expected to withstand both dynamic loads – achieving high levels of strength - and corrosion attack of water, especially sea water when used in offshore applications. With respect to the initially experimentally tested composition, some modifications have been made in the industrial prototype production, especially in the balance of C and N, and in the content of added elements as Mo, in order to guarantee a fully austenitic microstructure, free from undesired precipitates when properly subjected to solubilizing treatment.

With the developed Carnit composition, it has been possible to produce bars (from ingot casting, PESR and forging) characterized by a good quality, in terms of absence of porosity and steel cleanliness. Besides that, the required level of strength for the bulk (300 HV, 900-1000 MPa) can be achieved after a proper solubilization heat treatment, with an excellent level of toughness in comparison with the reference materials. The operations of surface strengthening needed to enhance the surface hardness, as deep rolling in particular, were investigated and optimized on a laboratory scale. However, the surface hardness levels achieved on the components are still unsatisfying, which resulted in early failures of the prototypes in the full-scale tests.

Component testing included full-scale testing and the development of functional testing equipment aimed at creating in the conventional steel the typical features of bearing damage as butterfly defects, which are often found coupled to WEC damage.

